

Preface

This special issue contains contributions from already 4th (2007) and 5th (2008) years of the seminar *Local Mechanical Properties (Lokálne Mechanické Vlastnosti, LMV)*. Its tradition was established in 2004 when it was organized as Slovak-Czech seminar. At these days, the seminar developed into a regular international conference covering a wide range of nano/micromechanics and other local phenomena and attracting researchers from wide geographical regions.

The knowledge of local mechanical properties is a prerequisite for the proper knowledge of other local phenomena and natural relations of small scale objects. Through this knowledge one is able to model and predict global macroscopic properties of the bulk material or a structure. Availability of the measurements comes with the development of experimental techniques, computers, software and most importantly with the development of nanosciences. An important role between the experimental techniques is played by nanoindentation. This technique has encountered tremendous evolution and its abilities are still expanding.

The LMV seminar was found in 2004 as one of the results of the Slovak-Czech bilateral project proceeded in the frame of intergovernmental scientific collaboration and conducted by the Department of Materials Science, Faculty of Metallurgy, Technical University of Košice (L. Pešek) and the Department of Material Science and Technology, Faculty of Mechanical Engineering, University of West Bohemia in Plzeň (O. Bláhová). The project coordinators aimed to establish a platform for research presentations from the area which underwent a large expansion. And such a platform was missing at these days.

In 2004, the 1st Slovak – Czech seminar *Lokálne mechanické vlastnosti LMV'04* was held in Košice (December 1-2, 2004) themed “Instrumented indentation and its application”. It was attended by 22 participants from Slovak and Czech Republic, 16 papers were presented.

In 2005, the 2nd year of LMV'05 was held in Herľany near Košice (November 14-15, 2005), themed “Relation of instrumented indentation with other hardness tests and properties”. It was attended by 25 attendees from Slovak and Czech Republic, 12 papers were presented. Both first two years were organized by L. Pešek and Department of Materials Science, Faculty of Metallurgy, Technical University of Košice.

In 2006, the 3rd year LMV'06 themed “Applicability of indentation measurements” was held in Nečtiny near Plzeň (November 8-10, 2006). It was attended by 40 participants from Czech and Slovak Republic, 30 papers were presented. The main organizer became O. Bláhová and the Department of Material Science and Technology, Faculty of Mechanical Engineering, University of West Bohemia in Plzeň.

Proceedings of the 1st to 3rd years were published on CD-ROM and/or printed (ISBN 80-8073-235-3, ISBN 80-8073-405-4, ISBN 80-7043-512-7). Contributions covered problems of indentation measurements, experimental techniques, instruments, possibilities of measurements, evaluation of results, layered materials, substrates, bulk materials and thin films. Always, the seminar was complemented with an excursion and exhibition of experimental instruments. In 2006, the scope of the seminar was enlarged with themes covering non-contact local deformation imaging techniques and small punch test.

In 2007, the 4th LMV'07 was held in Brno-Šlapanice (November 7- 9, 2007) organized by Masaryk University in Brno. It was attended by 40 attendees, 28 papers were presented. Excursion to the laboratories of Institute of Physical Electronics took place. The seminar was organized by V. Buršíková and her team from Institute of Physical Electronics, Faculty of Science, Masaryk University Brno. Proceedings of the LMV'07 were published also on CD-ROM under ISBN 978-80-210-4688-7.

In 2008, the 5th LMV'08 was held in Herľany near Košice (November 3-5, 2008), organized by Department of Materials Science, Faculty of Metallurgy, Technical University of Košice. It was attended by 22 participants from Czech and Slovak Republic and Poland, 21 papers were presented. The topics of last two seminars were similarly to previous years focused on experimental techniques, instrumentation, evaluation of results on layers, thin films, particles and it covered materials like metals, alloyed systems, polymers. New areas as multi-scale modeling, models based on neural networks, properties of composite polymers, CNTs, DLCs, construction materials like cement and concrete and wood were touched. Problems solved by presented contributions were viewed from different perspectives (physical, chemical, engineering, technological). It was decided to focus preferably on small-scale mechanical properties in the next years with the clear connection either to microstructure or to the macro-scale.

All information on the seminar (also for the next years) can be tracked on <http://www.tuke.sk/lmp>. The 2007 and 2008 are the first years of the seminar for which the reviewed full-length papers are published within the special issue of *Chemické listy* journal.

Ladislav Pešek
Scientific guarantor and co-chairman of the LMV 2007 and 2008 seminars

Department of Materials Science
Faculty of Metallurgy
Technical University of Košice

Editors

prof. Ing. Ladislav Pešek, CSc. (TU Košice) edited 2007, 2008
doc. Ing. Olga Bláhová, Ph.D. (ZČU Plzeň) co-edited 2008
RNDr. Vilma Buršíková Ph.D. (MU Brno) co-edited 2007

Organizing committee

2007

doc. Ing. Olga Bláhová, Ph.D. (ZČU Plzeň)
RNDr. Vilma Buršíková Ph.D. (MU Brno)
prof. Ing. Ladislav Pešek, CSc. (TU Košice)
Mgr. Pavel Stratil (MU Brno)
Ing. Zuzana Vadasová (TU Košice)
Ing. Pavol Zubko (TU Košice)

2008

Ing. Eubomír Ambriško (TU Košice)
doc. Ing. Olga Bláhová, Ph.D. (ZČU Plzeň)
Ing. Mária Mihalíková, PhD. (TU Košice)
prof. Ing. Ladislav Pešek, CSc. (TU Košice)
Ing. Pavol Zubko, PhD. (TU Košice)

Scientific committee

2007

doc. Ing. Olga Bláhová, Ph.D. (ZČU Plzeň)
RNDr. Vilma Buršíková, CSc. (MU Brno)
prof. Ing. Jaroslav Menčík, CSc. (Univerzita Pardubice)
prof. Ing. Ladislav Pešek, CSc. (TU Košice)

2008

doc. Ing. Olga Bláhová, Ph.D. (ZČU Plzeň)
prof. Ing. Jaroslav Menčík, CSc. (Univerzita Pardubice)
prof. Ing. Ladislav Pešek, CSc. (TU Košice)

Co-Chairs

Mr. prof. Ing. Ladislav Pešek, CSc. (TU Košice)
Mrs. doc. Ing. Olga Bláhová, Ph.D. (ZČU Plzeň)

Declaration

All contributions included in this journal special issue were reviewed before publication by members of the scientific committee.

Table of Content

LMV 2007

Regular lectures

<i>V. Buršíková, O. Bláhová, M. Karásková, L. Zajičková, O. Jašek, D. Franta, P. Klapetek, J. Buršík</i>	Mechanical properties of ultrananocrystalline thin films deposited using dual frequency discharges	s98
<i>T. Fořt, T. Vítů, R. Novák, J. Grossman, J. Sobota, J. Vyskočil</i>	Testing of the impact load and tribological behaviour of W-C:H hard composite coatings	s102
<i>M. Kašparová, Š. Houdková, F. Zahálka</i>	Angle of spraying and mechanical properties of WC-Co coatings prepared by HVOF spray technology	s105
<i>J. Krajčovič, I. Jančuška</i>	Determination of the optical fibre deformation by the interferogram analysis	s109
<i>F. Lofaj, M. Ferdinandy, A. Juhász J. Menčík</i>	Nanohardness of WC/C coating as a function of preparation conditions Determination of parameters of viscoelastic materials by instrumented indentation	s112 s115
<i>J. Němeček</i>	Local micromechanical properties of cement pastes	s120
<i>J. Němeček, K. Forstová</i>	Delayed deformation recovery after nanoindentation of cement paste	s123
<i>J. Ráhel, P. Štáhel, M. Odrášková</i>	Wood surface modification by dielectric barrier discharges at atmospheric pressure	s125
<i>P. Štáhel, V. Buršíková, J. Čech, Z. Navrátil, P. Kloc</i>	Deposition and characterization of thin hydrophobic layers using atmospheric-pressure surface barrier discharge	s129
<i>A. Stoica, R. Vlădoiu, G. Musa, V. Ciupină, M. Contulov, V. Buršíková, O. Bláhová</i>	Mechanical properties of thin films deposited by TVA and G-TVA methods	s132
<i>Z. Vadasová, L. Pešek, M. Kollárová, O. Bláhová, P. Zubko</i>	Nanoindentation measurements of the intermetallic phases in galvanneal coatings	s136

LMV 2008

Invited lectures

<i>O. Bláhová, M. Špírková</i>	Local mechanical properties of organic-inorganic nanocomposite layers (Lokální mechanické vlastnosti organicko-anorganických nanokompozitních povlaků)	s140
<i>J. Menčík</i>	Determination of parameters of viscoelastic materials by instrumented indentation	s143
<i>J. Němeček, K. Forstová</i>	Micromechanical analysis of heterogeneous structural materials	s146

Regular lectures

<i>E. Ambriško, T. Kandra, L. Pešek</i>	Hodnotenie indentačných a deformačných charakteristík laserových zvarov	s150
<i>J. Bidulská, R. Kočiško, T. Kvačkaj, R. Bidulský, M. A. Grande</i>	Simulácie ECAP procesu zliatiny EN AW 2014 pomocou MKP	s155

<i>R. Bidulský, M. A. Grande, M. Kabátová</i>	Improved fatigue resistance of sintered steels via local hardening	s159
<i>O. Bláhová</i>	Investigation of local mechanical properties of zirconium alloys using nanoindentation	s163
<i>M. Březina, L. Kupča</i>	Možnosti využitia systému na odber malých vzoriek z prevádzkovaných zariadení pri hodnotení vlastností materiálov	s167
<i>V. Buršíková, Z. Kučerová, L. Zajíčková, O. Jašek, V. Kudrle, J. Matějková, P. Synek</i>	Measurement of mechanical properties of composite materials	s171
<i>L. Dajbychová, O. Bláhová, M. Špírková</i>	The influence of additives on mechanical properties of organic-inorganic coatings	s175
<i>L. Hegedúsová, J. Dusza</i>	Contact strength measurements and cone crack formation of Si ₃ N ₄ and SiC based ceramics	s178
<i>Š. Houdková, F. Zahálka, M. Kašparová, O. Bláhová</i>	Nanoindentační měření HVOF stříkaných povlaků	s182
<i>M. Garbiak, R. Chylińska</i>	Microhardness of phase constituents present in creep-resistant cast steel	s187
<i>A. Kovalčíková, J. Dusza</i>	Thermal shock resistance of SiC+Si ₃ N ₄ composites evaluated by indentation technique	s191
<i>J. Krajčovič, I. Jančuška</i>	Holografická metóda určenia Youngovho modulu pružnosti	s195
<i>F. Lofaj</i>	Localized viscous flow in the oxide and oxynitride glasses by indentation creep	s198
<i>R. Medlín, J. Říha, O. Bláhová</i>	Microstructure and local mechanical characteristics of Zr1Nb alloy after hardening	s202
<i>M. Mihalíková, L. Ambriško</i>	Stanovenie veľkosti plastickej zóny videoextenzometrickou metódou	s206
<i>J. Říha, O. Bláhová, P. Šutta</i>	Fázové zmeny slitiny Zr-1Nb a jejich vliv na lokální mechanické vlastnosti	s210
<i>J. Savková, O. Bláhová</i>	Scratch resistance of TiAlSiN coatings	s214
<i>J. Špaková, F. Dorčáková, J. Dusza</i>	Indentation load/size effect of structural ceramic materials	s218
<i>P. Zimovčák, O. Milkovič, P. Zubko, M. Vojtko</i>	Vplyv fosforu na lokálne mechanické vlastnosti a vývoj štruktúry IF ocelí	s223
<i>P. Zubko, B. Ballóková, L. Pešek, O. Bláhová</i>	Determination of mechanical properties of MoSi ₂ composites by nanoindentation	s227

Papers presented at
the 4th International Seminar on

LOCAL MECHANICAL PROPERTIES 2007

LOKÁLNÍ MECHANICKÉ VLASTNOSTI 2007

November 7th to 9th, 2007
Brno-Šlapanice, Czech Republic



Advex Instruments



Organized by the Masaryk University Brno
in cooperation with
Technical University of Košice
and
University of West Bohemia in Plzeň

2007

MECHANICAL PROPERTIES OF ULTRANANOCRYSTALLINE THIN FILMS DEPOSITED USING DUAL FREQUENCY DISCHARGES

VILMA BURŠÍKOVÁ^{a*}, OLGA BLÁHOVÁ^b, MONIKA KARÁSKOVÁ^a, LENKA ZAJÍČKOVÁ^a, ONDŘEJ JAŠEK^a, DANIEL FRANTA^a, PETR KLAPETEK^c, and JIŘÍ BURŠÍK^d

^aDepartment of Physical Electronics, Masaryk University, Kotlářská 2, 611 37 Brno, ^bUniversity of West Bohemia Plzeň, ^cMetrologic Institute, Brno, ^dInstitute of Physics of Materials, Academy of Sciences of the Czech Republic, Žitkova 22, 616 62 Brno, Czech Republic
vilma@physics.muni.cz

Keywords: ultrananocrystalline diamond, plasma enhanced chemical vapor deposition, dual frequency discharge, local mechanical properties

1. Introduction

The preparation of nanostructured (nanocomposite or nanocrystalline) diamond coatings is in a centre of a great industrial interest due to their extreme mechanical hardness and wear resistance, high bulk modulus, low compressibility, high thermal conductivity, low thermal expansion coefficient, broad optical transparency from the deep ultraviolet to the far infrared, high electrical resistivity, biocompatibility, etc^{1–9}. Their main advantage compared to the polycrystalline diamond film is, that they can be prepared with relatively low surface roughness. Smooth diamond films with crystallite size at nanometre scale offer the potential for manufacturing a wide variety of components and structures of technological importance, with enhanced mechanical and functional properties, which cannot be realized in conventional microstructures.

The mechanical properties such as hardness, wear resistance, fracture toughness, film-substrate adhesion and thermo-mechanical stability of the coating-substrate system play always a crucial role for industrial applications of the coatings^{10–13}. Therefore the main aim of the present work is to study the mechanical properties of ultrananocrystalline thin films using two different indentation techniques.

2. Experimental

The common type of microwave reactor ASTEX was used to deposit the studied films. In this reactor, microwaves are coupled into a water-cooled metal cavity through a quartz window, using an antenna, which converts the TE₁₀ microwave mode in the wave-guide to the TM₀₁ mode in the cavity. The inner chamber diameter is chosen so that only one microwave radial mode can be sustained in the cavity at 2.45 GHz. Substrates as large as 10 cm in diameter can be coated by

positioning them on a heated stage beneath the plasma ball which forms immediately above it. This reactor was modified for the dual frequency application, i.e. application of RF power to a substrate holder to achieve the so-called bias-enhanced nucleation (BEN). The RF power of 35 W (13.56 MHz) was capacitively coupled to the central graphite plate of the substrate holder. Due to different mobility of electrons and ions this resulted in dc self-bias accelerating the ions across the sheath adjacent to the graphite plate, i.e. the substrate, causing them to sub-plant beneath the surface and create a carbon-rich layer in the topmost few layers of the substrate. This had two important effects, the initial nucleation rate was greatly increased, and the resulting diamond film was registered with the underlying substrate lattice to a much greater extent, allowing deposition of films with a preferred orientation to be grown. The orientation of diamond crystallites was studied using XRD technique.

The deposition was carried out on mirror polished (111) oriented n-doped silicon substrates in the mixture of methane (CH₄) and hydrogen (H₂) changing the CH₄ concentration. The supplied microwave power was 850 W and pressure in the reactor was 7.5 kPa. The substrate temperature, estimated by means of a pyrometer with disappearing filament, was kept in the range from 1090 to 1120 K.

A Fischerscope H100 depth sensing indentation (DSI) tester and Nano Indenter XP equipped with continuous stiffness measurement (CSM) were used to study the indentation response of ultrananocrystalline diamond films.

The optical measurements were done with Horiba Jobin Yvon ellipsometer in the spectral range from 190 to 2100 nm at the incidence angles from 55° to 75° and were evaluated using a dispersion model of optical constants based on the parameterisation of densities of states (DOS)¹⁴.

3. Results and discussion

Nanostructured diamond films with different concentrations of methane (CH₄) in hydrogen (H₂) were studied in the present paper. According to Bachmann's¹⁵ C-H-O gas phase concentration triangle the polycrystalline diamond can be deposited by CVD from the CH₄/H₂ gas mixtures, when the concentration of CH₄ is in the range from 1 to 3 %.

With increasing methane concentrations, the crystal sizes decrease, until above ca. 3 % CH₄ in H₂ the gas phase and the resulted films exhibit 'nanocomposite' structure and may be considered to be an aggregate of diamond nanocrystals and disordered graphite. If BEN is employed as well as growth conditions, which favour one particular orientation, highly textured films can be produced which are very closely aligned with the lattice of the underlying substrate. In case of the BEN technique the monitoring the self-bias voltage provides important information about the diamond growth. At the beginning ions impinge on the almost clean silicon surface and the self-bias voltage is nearly constant. After the surface is step by step filled by diamond nuclei the measured voltage de-

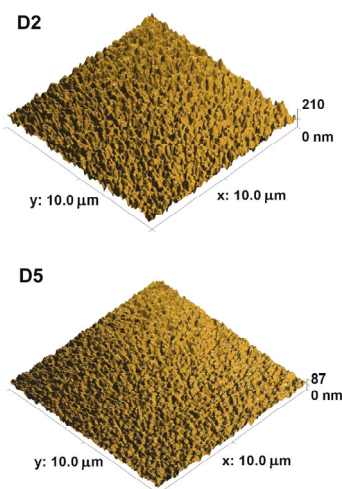


Fig. 1. AFM images of the surfaces of sample D2 (2 % CH₄ in the deposition mixture) and D5 (10.4 % CH₄ in the deposition mixture). The analysis of AFM data yielded the RMS roughness 20.7 and 8.8 nm and autocorrelation lengths of 141 and 120 nm for D2 and D5, respectively

creases. When the surface is completely covered the growth stage begins and the measured voltage is again constant. Sample D2 was deposited with 8.3 sccm of CH₄ mixed with 400 sccm of H₂, i. e. equivalent to 2.0 % of CH₄ in the gas phase. The nucleation stage was relatively long: it took 20 minutes. Sample D5 was, on the other hand, prepared from the mixture with higher C/H, 10.4 % (flow rates of CH₄ and H₂ were 41.7 and 400 sccm, respectively). The nucleation stage of the film D5 prepared with highest amount of CH₄ was 5 minutes.

In order to prepare the films with similar thickness in these two different gas mixtures the deposition time of the D2 and D5 was 28 and 15 min, respectively. AFM micrographs of the films D2 and D5 are shown in Fig. 1. They reveal a significant difference between the two films as concerns the surface topography. Especially in case of D5 the surface was relatively smooth and allowed optical measurements in the reflection mode. The analysis of AFM data yielded the RMS roughness 20.7 and 8.8 nm and autocorrelation lengths of 141 and 120 nm for D2 and D5, respectively.

Mechanical properties of the films D2 and D5 were studied by depth sensing indentation (DSI) test at several different final loads and by the continuous stiffness measurement (CSM) enabling the determination of the material properties continuously as the indenter moves into the surface, eliminating the need for unloading cycles. We studied not only the film hardness and elastic modulus, but also the film-substrate system indentation response in a wide range of indentation depths (20 to 3000 nm). Dependencies of the hardness and elastic modulus on the indentation depth obtained for samples D2 and D5 using these two techniques are shown in Figs. 2 and 3.

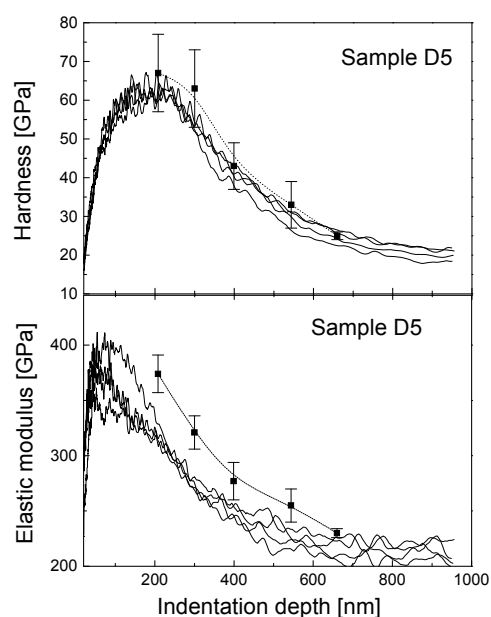


Fig. 2. Results of mechanical tests obtained on D5 using DSI and CSM method. The lines in hardness and elastic modulus dependencies belong to the selected measurements obtained using CSM technique, the scatter graphs belong to the results obtained using DSI technique

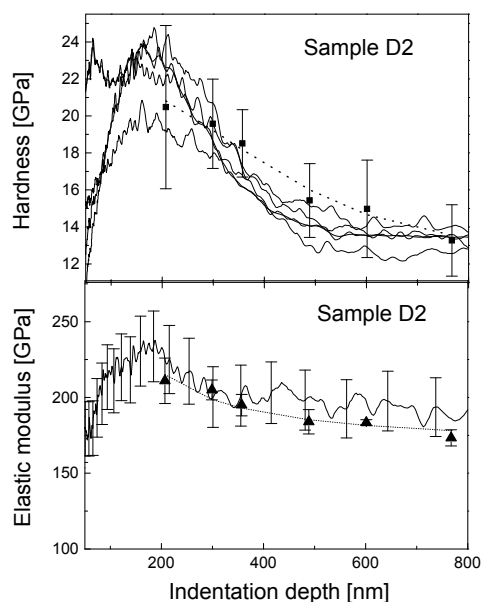


Fig. 3. Results of mechanical tests obtained on D2 using DSI and CSM methods. The lines in hardness and elastic modulus dependencies belong to the selected measurements obtained using CSM technique, the scatter graphs belong to the results obtained using DSI technique

The influence of the substrate on the measured values was negligible up to 200 nm of indentation depth. With increasing indentation depth the influence of the substrate on the measured values increased. The combined effect of the film and substrate on the measured values of composite hardness H_c was modelled according to Battacharya and Nix¹⁶. The combined influence of the film and substrate on the measured elastic modulus was calculated according to Saha and Nix¹⁷. The results obtained with both DSI and CSM methods are in good agreement. The sample D2 exhibited the hardness around 20 GPa and elastic modulus of 220 GPa. Although the film D2 was deposited in "diamond yielding mixture" the low values of mechanical parameters suggest that it is rather a composite consisting of diamond crystals embedded in a disordered graphite matrix. The fact, that the results obtained by both DSI and CSM measurement were highly scattered confirm the previous assumption. The film D5 exhibited, on the other hand, relatively high hardness and elastic modulus of 65 and 375 GPa, respectively.

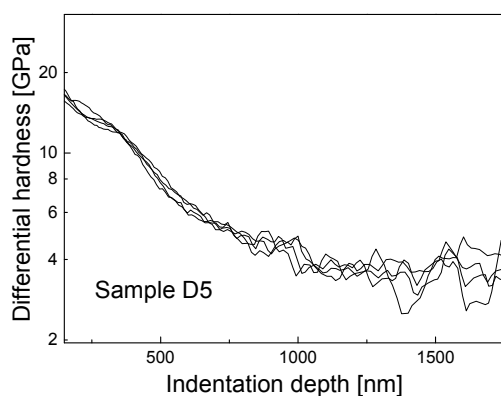


Fig. 4. Differential hardness dependence on the indentation depth obtained on D5 using the Fischerscope tester

Moreover, the film D5 exhibited high fracture toughness. In Fig. 4 the differential hardness $\partial L/\partial(h^2)$ (here L is the load and h is the indentation depth) dependence on the indentation depth is shown for sample D5 together with the SEM image of the indentation made at maximum load of 1 N. This dependence enables to visualise the crack creation, what appears on the dependence as an abrupt jump.

In case of the film D5 the ring/like through surface cracking begun (see SEM image in Fig. 5), when the indenter approached the film-substrate interface. We did not observe any cracks emanating from the indentation print corners or delamination around the indentation print even at indentation depths higher, than the film thickness.

For the evaluation of optical measurements on sample D5, the Rayleigh-Rice theory for roughness^{18,19} and the dispersion model of optical constants based on the parameterisation of densities of states (DOS) were taken into account. The dispersion model was similar to that presented earlier for diamond like carbon films^{18,19}. The refractive index was slightly lower than that of the natural diamond. The RMS

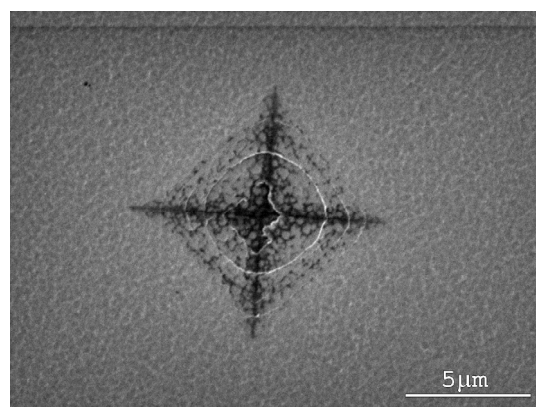


Fig. 5. SEM image of the indentation carried out at maximum load of 1 N

roughness and autocorrelation length for D5 were 9.1 and 73 nm, respectively. This is in a good agreement with the values found by AFM.

4. Conclusion

We have deposited a large set of diamond like carbon films with incorporation of silicon, oxygen and nitrogen. The optimum deposition conditions for deposition of smooth, hard, wear resistant thin films suitable for protection of the polycarbonate substrates were found. The film prepared under optimum conditions exhibited excellent fracture resistance and low intrinsic stress. The prepared films have all the properties needed for excellent protective coatings including high hardness, low friction coefficient, excellent chemical and thermal stability and transparency in the visible spectrum.

This research has been supported by Ministry of Education, Youths and Sports of the Czech Republic under project MSM0021622411 by the grant of Czech Science Foundation No. 202/07/1669 and by Academy of Science of the Czech Republic by KAN311610701.

REFERENCES

1. Erdemir A., Fenske G. R., Krauss, D. M. Gruen, McCauley T., Csencsits R. T.: *Surf. Coat. Technol.* 120-121, 565 (1999).
2. Jones A. N., Ahmed W., Hassan I. U., Rego C. A., Sein H., Amar M., Jackson M. J.: *J. Phys. Condens. Matter* 15, S2969 (2003).
3. Liu Y. K., Tzenga Y., Liu C., Tso P., Lin I. N.: *Diamond Relat. Mater.* 13, 1859 (2004).
4. De Barros M. I., Vandenbulcke L.: *Diamond Relat. Mater.* 9, 1862 (2000).
5. Hogmark S., Hollman O., Alahelsten A., Hedenqvist P.: *Wear* 200, 235 (1996).
6. Yugo S., Kanai T., Kimura T., Muto T.: *Appl. Phys. Lett.* 58, 1036 (1991).
7. Seo S.-H., Lee T.-H., Park J.-S.: *Diamond Relat. Mater.* 12, 1670 (2003).

8. Asmussen J., Reinhard D. K. (ed.): *Diamond Films Handbook*. Marcel Dekker, New York 2001.
9. May V.: *Phil. Trans. R. Soc. Lond. A* (2000).
10. Veprek S., He J. L.: *Surf. Coat. Technol.* 163-164, 374 (2003).
11. Musil J., Zeman H.: *Mater. Sci. Eng., A* 340, 281 (2003).
12. Bachmann P. K., Drawl W., Knight D., Weimer R., Messier R.: *Mater. Res. Soc. Symp. Proc. EA-15*, 99 (1988).
13. Oliver W. C., Pharr G. M.: *J. Mater. Res.* 7, 1564 (1992).
14. Ohlídal I., Franta D., Klapetek P.: *Proceedings of the 4th Seminar on Quantitative Microscopy, Braunschweig, Germany*, 124 (2000).
15. Bachmann P. K., Leers D., Lydtin H.: *Diamond Relat. Mater.* 1, 1 (1991).
16. Battacharya A. K., Nix W. D.: *Int. J. Solids Struct.* 38, 335 (2001).
17. Saha R., Nix W. D.: *Acta Materialia* 50, 23 (2002).
18. Franta D., Ohlídal I.: *Opt. Commun.* 248, 459 (2005).
19. Franta D., Ohlídal I., Buršíková V., Zajíčková L.: *Thin Solid Films* 455-456, 393 (2004).

V. Buršíková^{a*}, O. Bláhová^b, M. Karásková^a, L. Zajíčková^a, O. Jašek^a, D. Franta^a, P. Klapetek^c, and J. Buršík^d (^a Department of Physical Electronics, Masaryk University, Brno, ^b University of West Bohemia, Plzeň, ^c Czech Metrologic Institute, Brno, ^d Institute of Physics of Materials, Academy of Sciences of the Czech Republic, Brno, Czech Republic): **Mechanical Properties of Ultrananocrystalline Thin Films Deposited Using Dual Frequency Discharges**

The present paper describes the deposition of nanostructured diamond films with low surface roughness, high hardness and fracture toughness by microwave PECVD in the ASTeX type reactor from mixture of methane and hydrogen. Films were deposited on a mirror polished (111) oriented n-doped silicon substrate. The film exhibited relatively low roughness, the root mean square (RMS) of heights ranged from 20 to 9.1 nm, depending on the deposition conditions. The hardness was found to be in the range from 22 to 65 GPa and the elastic modulus ranged from 220 to 375 GPa, depending on the film structure.

TESTING OF THE IMPACT LOAD AND TRIBOLOGICAL BEHAVIOUR OF W-C:H HARD COMPOSITE COATINGS

**TOMÁŠ FOŘT^{a*}, TOMÁŠ VÍŤ^b,
RUDOLF NOVÁK^c, JAN GROSSMAN^a,
JAROSLAV SOBOTA^a,
and JIŘÍ VYSKOČIL^d**

^a Institute of Scientific Instruments, Academy of Sciences of the Czech Republic, Kralovopolska 147/62, 61264 Brno,

^b Faculty of Transportation Sciences, Czech Technical University, Na Florenci 25, 110 00, Prague 1, ^c Faculty of Mechanical Engineering, Czech Technical University, Technicka 4, 166 07, Prague 6, ^d HVM Plasma Ltd, Prague 5 Czech Republic
fortt@isibrno.cz

Keywords: PVD, DLC, impact test, pin-on-disc, friction coefficient

1. Introduction

Hard carbon based composite coatings are more and more frequently used in practical applications, such as automotive industry, where not only good adhesion and wear resistance, but also reasonable thermal stability, low wear at elevated temperatures and impact resistance are required. Diamond-like carbon coatings have a range of tribological properties that are controlled with the incorporation of additional elements such as silicon, nitrogen or metal. Considerable scientific and industrial interest is focused in nanocomposite coatings containing tungsten in the diamond-like amorphous hydrogenated carbon matrix (W-C:H). These coatings generally possess high hardness, low friction coefficients against a range of counterfaces, good wear resistance and good adhesion to a range of substrates by controlling the interlayers responsible for promoting good adhesion and control of residual stress in the coatings¹. Numerous papers deal with the tribological behaviour and properties of DLC coatings^{2,3}. Density, hardness and compressive stress of W-C:H coatings were studied as a function of composition and structure and deposition conditions⁴. The effect of slightly different hydrogen content in W-C:H coatings on microstructure, adhesion and tribological properties was studied in ref.⁵. A detailed structural characterization of W-C:H showed the existence of a submicrometer scale columnar structure and intercolumnar defects within the coating⁶. This structure could be related to failure mechanisms during tribological and wear tests. In the case of W-C:H coatings the outweighing degradation mechanism was a combination of polishing wear with micro- or nano-delamination and micro-pitting⁷. Nevertheless, no results of detailed studies of tribological parameters temperature dependency have been published yet.

The dynamic impact wear tester developed in our laboratory has been used to evaluate the impact resistance of thin

hard composite coating in dynamic loading wear applications. Impact testing of the coatings was proposed by Knotek et al in the 1990's (ref.⁸). During testing the specimen was cyclically loaded by tungsten carbide ball that impacts against the coating/substrate surface. After each the test, wear scars were evaluated by means of optical microscope and profilometer. Results of these tests show usability of coatings in dynamic load and enable to optimize the design of the coating/substrate system for the particular use. The test simulates a wide range of tribological systems. The impact test offers an important new method for determination of the fracture toughness of hard thin coatings.

2. Experimental Details

The substrates made from high speed steel were used with tempering temperature of 550 °C. They were polished with brush papers and finally with diamond pastes. The substrate hardness was 62 HRC. W-C:H coatings were deposited with combined PVD and PACVD processes. Thickness determined by calotest method was about 2 µm. The dynamic impact wear tester developed in the Institute of Scientific Instruments ASCR in collaboration with Brno University of Technology has been used to evaluate modified DLC coatings. Setting of the impact tester: impact force from 200 N to 600 N, number of impacts could be varied from 1 to 100 000. The tungsten carbide ball 5.00 mm in diameter with guaranteed geometry and surface roughness was used. After each test, wear scars were evaluated by means of profilometer Talystep (Taylor-Hobson) and confocal microscope LEXT OLS 3100 (Olympus). Impact tester has been used in our laboratory for more than two years to evaluate hard coatings produced in coating centres and both its hardware and software were improved to achieve minimum scattering of measured values caused by the device. Nowadays the range of values scattering on homogenous coating/sample system does not exceed several percent.

The coatings hardness and Young modulus were measured with nanoindenter Fisherscope H100. The results were: indentation force $F = 50$ mN, universal hardness $H_u = 6380 \pm 120$ MPa, $W_e/W_{tot} = 58$ %, $E = 151 \pm 4$ GPa. Parameters measured with higher indentation forces (up to 1 N) did not differ substantially. In order to verify the adequate mechanical properties of W-doped a-C:H coatings, the tribological performance was studied using standardized pin-on-disc CSM Instruments measuring device. The tests were carried out in the temperature range from 20 °C (room temperature, RT) to 200 °C, thus the thermal stability could be determined. The testing conditions were set as follows 5000 cycles, normal load 5 N, linear speed 0.05 m s⁻¹. The testing ball-coating contact was unlubricated and the relative air humidity at room temperature was about 40±5 %. As counterparts the ceramic Al₂O₃ balls with diameter of 8 mm were used.

The tribological performance was determined not only with respect to the friction coefficients, but from the point of

view of wear rates and free wear debris characterization as well. The coating wear rates were evaluated on the basis of cross-section wear track profile measurements, the wear rates of balls were calculated from spherical wear cap images taken from optical microscopy. The wear rates were determined as the worn volume per sliding distance and load⁹. Each tribological test was carried out three times with expected measured parameters standard deviation of about 10%. In this paper the average values of friction coefficient and wear rates are presented. To determine the dominant wear mechanism, the wear tracks were studied using optical microscopy, scanning electron microscope JEOL JSM-6460 LA and confocal microscope. Additionally, the measurements of coating hardness were taken into account.

3. Results

3.1. Impact tests

Fig. 1 shows crater volumes against the number of impacts plotted at three different impact forces. Volumes were calculated provided that the shape of the crater was approximated by a rotational paraboloid, by using the radius and the average depth of the crater measured by profilometer. Average values were calculated from at least five repetitive measurements carried under identical conditions. The wear rate was calculated using central part of the dependence (from 5 to 50 000 impacts) as a quotient of the variation of crater volume ΔV and the number of impacts. In the Tab. I the wear rates for three values of impact forces are summarized.

In the Fig. 2 the crater volume corresponding to wear rate of coating/substrate system and bare substrate is presented. In spite of this high load the coating has beneficial effect on the system wear resistance in the whole range, namely for higher number of impacts.

Table I

Wear rate of the coating/substrate system in dynamical mode for the load forces 200 N, 400 N and 600 N

F [N]	200	400	600
ΔV [mm ³]	3.4 E-8	14 E-8	23 E-8

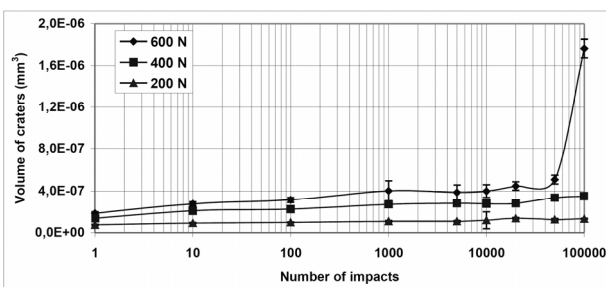


Fig. 1. Mean values of crater volume, impact force varies from 200 N to 600 N

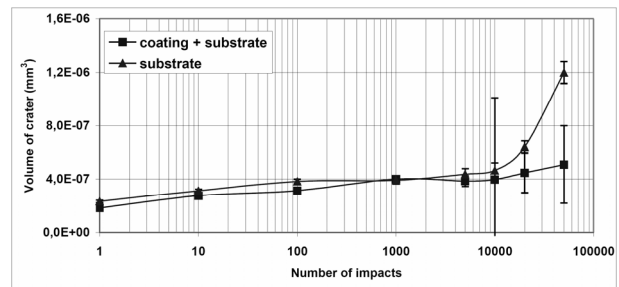


Fig. 2. Comparison of wear rate of coating/substrate system and bare substrate at 600 N

3.2. Tribological tests

The tribological measurements clearly showed high-temperature coating applicability limit. The friction coefficient at 200 °C became unstable and higher values of about 0.45 were obtained. The coating wear scars were very coarse with deep abrasive scratches that in many cases reached the substrate surface.

The typical evolution of friction coefficient with number of cycles is shown in Fig. 3. At RT the friction process is stable, short run-in could be observed and at about 500 cycles the steady-state phase was reached with average friction coefficient of about 0.1. The testing ball exhibited almost no notable surface damage, only high coverage with compact carbon-containing wear debris interlayer was observed. Thus, third body friction occurred predominantly. The calculated coating wear rate value of about $0.43 \cdot 10^{-6} \text{ mm}^3 \text{ N}^{-1} \text{ m}^{-1}$ corresponded to the low measurability limit. The wear track appeared very smooth with very low surface damage, thus, only polishing wear mechanism occurred.

At 100 °C the sliding process partially lost its stable behaviour. Up to 1500 cycles the friction coefficient exhibited unsteady evolution with higher value of about 0.5. The sliding interlayer was not compact enough and, thus, ceramic ball hard surface affected the tested coating directly. Higher amount of free wear debris were produced and this process

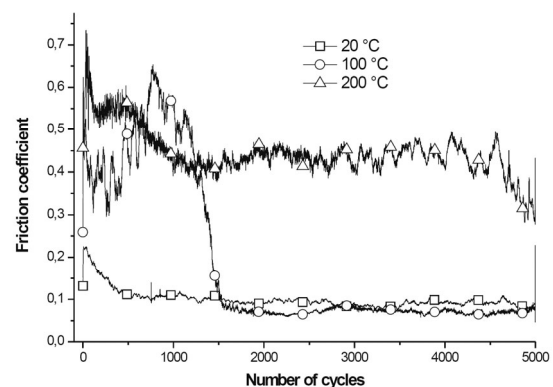


Fig. 3. Typical friction curves of Al₂O₃ ball against W-C:H coating at RT, 100 °C and 200 °C

resulted in consequent friction coefficient reduction above 1500 cycles. The ball wear scar was negligible, the contact surface exhibited partial coverage with free wear debris. The value of coating wear rate increased to $12 \cdot 10^{-6} \text{ mm}^3 \text{ N}^{-1} \text{ m}^{-1}$, maximum penetration depth was about $0.5 \mu\text{m}$ that corresponded to 50 % of total coating thickness. The wear tracks were rather coarser with many scratches parallel to the contact movement and significant effect of abrasive wear mechanism was observed. At $200 \text{ }^\circ\text{C}$ the evolution of friction coefficient was unstable reaching high value of about 0.45. The free wear debris did not affect the ball-coating interface; no compact sliding interlayer was observed. Thus, the ceramic ball surface slid directly on the tested surface and induced very high abrasive wear of coating. The coating wear rate reached the value of about $31 \cdot 10^{-6} \text{ mm}^3 \text{ N}^{-1} \text{ m}^{-1}$ and the penetration depth exceeded in some cases the coating thickness. The failure of ball surface was negligible.

4. Conclusions

The impact tests demonstrated low wear rate of the coating/substrate system in a wide range of dynamical load. Coating erosion occurred and the substrate was gradually uncovered only for the highest impact force of 600 N and the number of impacts exceeding 50 000. At 100 000 impacts approximately one half of the coating was removed.

The comparison of the wear rate coating/substrate system and the bare substrate clearly demonstrated that the coating significantly extended the lifetime of the tribological system even for high loads and high number of loading cycles.

The results of tribological testing showed the temperature limit of about $200 \text{ }^\circ\text{C}$. The increase in wear rate was probably due to lower humidity, graphitization and coating hardness reduction at elevated temperature. This phenomenon is under further investigation.

This work has been supported by grant of Czech Ministry of Industry and Trade MPO 2A-ITP1/031.

REFERENCES

1. Veverkova J., Hainsworth S. V.: *Wear* 264, 518 (2008).
2. Grill A.: *Diamond Relat. Mater.* 8, 428 (1999).
3. Erdemir A.: *Tribol. Int.* 37, 1005 (2004).
4. Pujada B. R., Janssen G. C. A. M.: *Surf. Coat. Technol.* 201, 4284 (2006).
5. Kao W. H.: *Mater. Sci. Eng., A* 432, 253 (2006).
6. Jiang J. C., Meng W. J., Evans A. G., Cooper C. V.: *Surf. Coat. Technol.* 176, 50 (2003).
7. Yonekura D., Chittenden R. J., Dearnley P. A.: *Wear* 259, 779 (2005).
8. Knotek O., Bosserhoff B., Schrey A., Leyendecker T., Lemmer, Esser S.: *Surf. Coat. Technol.* 54/55, 102 (1992).
9. Holmberg K., Mathews A.: *Coatings Tribology*, Elsevier, Amsterdam 1998.

T. Fořt^{a*}, T. Vítů^b, R. Novák^c, J. Grossman^a, J. Sobota^a, and J. Vyskočil^d (^a*Institute of Scientific Instruments, Academy of Sciences of the Czech Republic*, ^b*Faculty of Transportation Sciences, Czech Technical University, Prague*, ^c*Faculty of Mechanical Engineering, Czech Technical University, Prague*, ^d*HVM Plasma Ltd, Prague, Czech Republic*): **Testing of the Impact Load and Tribological Behaviour of W-C:H Hard Composite Coatings**

W-C:H hard composite coatings were studied. The comparison of the wear rate of the coating/substrate system and the bare substrate obtained from dynamic impact test clearly demonstrated that the coating significantly extended the lifetime of the samples even for high loads and high number of loading cycles. The obtained results will support the research and development of new metal-doped a-C:H coatings, which exhibit promising properties for future engineering applications, especially in dynamically loaded contacts.

ANGLE OF SPRAYING AND MECHANICAL PROPERTIES OF WC-Co COATINGS PREPARED BY HVOF SPRAY TECHNOLOGY

MICHAELA KAŠPAROVÁ, ŠÁRKA HOUDKOVÁ, and FRANTIŠEK ZAHÁLKA

ŠKODA VÝZKUM Ltd., Plzeň, Czech Republic
michaela.kasparova@skodavyzkum.cz

Keywords: WC-Co, HVOF spray technology, deposition angle, IFT, microhardness

1. Introduction

1.1. HVOF technology

Thermal spray technology encompasses a group of coating processes that provide functional surfaces to protect or improve the performance of a substrate or component. Many types and forms of materials can be thermally sprayed – which is why thermal spraying is used worldwide to provide protection from corrosion, wear, and heat; to restore and repair components; and for a variety of other applications. HVOF (High Velocity Oxygen Fuel spray) spray technology uses a high velocity spraying of the flame. This method was developed most of all for spraying of the cermets coatings. It is based on the special torch design where the combustion products (oxygen and kerosene) rapidly expand in the nozzle-end and consequently come to the dramatic acceleration. The powder of coated material, injected to the flame, reaches a supersonic velocity. The combustion is also accomplished by the heating for melting of the incoming powder. The melted powder particles impinge on the grit-blasting substrate and create the coating. Schematic picture of HVOF spraying is described in Fig. 1. With HVOF technology the coatings with a high adhesion, cohesion and density, with a low oxides and pores contents are created. The main advantage of HVOF technology is the deposition of cermets coatings with the hardness about 55–66 HRC that are used for the most demanding applications².

1.2. WC-Co coating

In the WC-Co sprayed coatings there are carbides homogeneously distributed in the coatings without mutual touch. That is influenced by the high part of cobalt in this sprayed system (12–17 % Co) and by the loss of the WC particles or by their dissolution in the cobalt during the spraying. In comparison with the basic powder material, the changes in the coatings composition appear due to the spraying process. The main cause is the decarburization, in other words the carbon elimination. A high flame temperature of the applied fuel increases the carbon loss during the spray process¹⁰. During this process one part of WC is diffusing to W_2C and W while generating CO and CO_2 .

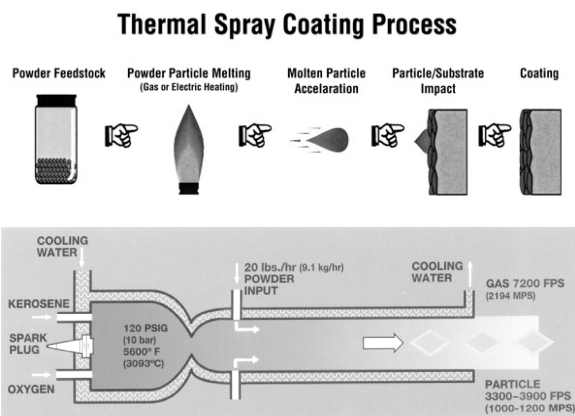


Fig. 1. The scheme of HVOF spray technology

After oxidation the process continues with W and C dissolution in cobalt. The particles impacting the substrate become cold very fast and the matrix solidifies in the amorphous or in the fine-grinded form like a supersaturated solid solution from which can precipitate W and other phases (brittle η phases Co_3W_3C , Co_6W_6C). The decarburization and arising of the brittle phases is undesirable because they decrease the ductility of Co matrix and the cermet losses its excellent properties – combination of the hard phase in the ductile basis^{2,3}.

For the creating of coatings with definite desired properties it is important to spray at optimal conditions. The most important spray conditions are the equivalent ratio (relation between oxygen and kerosene), the pressure in the combustion chamber, and the deposition distance. The next important spray condition is the angle of spraying. The stream of spray particles should impact the target surface as close to normal (deposition angle 90°) as possible. It is mentioned that the decreasing deposition angle is followed by the decrease of the coating properties like the bond strength and the coating cohesion and increase of the coating porosity. Particle impacting at angles of less than 90° creates a shadowing effect that results in increasing of the coating porosity¹.

2. Experiment

The WC-Co powder is documented in Fig. 2. The initial powder for spraying is agglomerated and sintered with chemical composition 83 % WC and 17 % Co and its grain size is 15–45 μm . The powder particles are spherical and the WC grains (white areas) are uniform distributed in the cobalt phase (grey areas). Inside of the particles are visible pores, the dark areas in the SEM picture. The material of this powder was sprayed in five different deposition angles: 90° , 75° , 60° , 45° and 30° on the steels substrate. The substrate material was

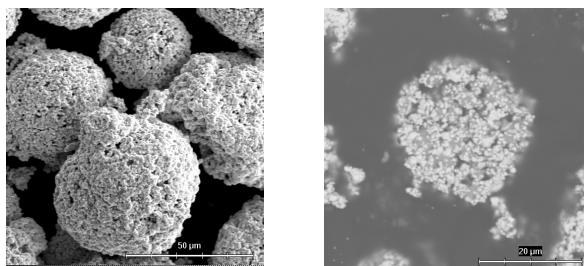


Fig. 2. SEM picture of the WC-Co powder, left: the powder surface, right: the powder cross section; the hell areas – carbides WC, the grey areas – Co matrix, dark areas – pores

the steel ČSN 11 373. The substrate surface was before spraying cleaned and roughened by grit-blasting for a good coating adhesion to the substrate. The grit-blasted medium was brown corundum in average size 1 mm.

The optimized spraying parameters are the standard parameters used in ŠKODA VYZKUM Ltd. Plzeň. On such prepared samples were measured several mechanical properties. The microhardness, indentation fracture toughness (IFT) and coating microstructure were investigated.

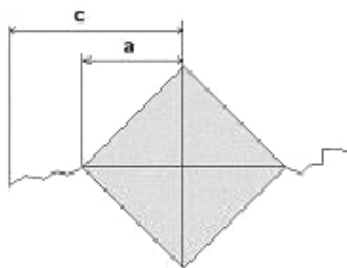


Fig. 3. Evaluation of the fracture toughness

LEM theory:	$K_{IC}=0,0134 (L/c^{3/2}) (E/H)^{1/2}$	ref. ⁵
LS theory:	$K_{IC}=0,0101 L/(ac^{1/2})$	ref. ⁶
EC theory:	$K_{IC}=0,0824 L/c^{3/2}$	ref. ⁷
LF theory:	$K_{IC}=0,0515 L/(c^{3/2})$	ref. ⁸

Here is a – $1/2$ of the diagonal length [m], c – fracture length + a [m], E/H – materials constant [–], K_{IC} – fracture toughness [MPa m^{1/2}]

The microhardness HV0.3 was measured on the coating cross sections by LECO DM-400A Hardness Tester. The used load was 300 g and the indentation time was 10 s. Altogether there were prepared 10 indentations. The lengths of diagonals were measured and then calculated for an average value. In the accordance with the Standard ČSN EN ISO 6507-4 (ref.⁴) the microhardness value was determined from the diagonal length.

The indentation fracture toughness was determined by the help of the Scratch Tester “Revetest” in the Academy of Science in Plzeň. In the cross sections were prepared 10 indentations by the Vickers diamonds indenter. The load was

selected in such manner in order to be possible to obtain cracks which start from the corners of the indents, Fig. 3. WC-Co cermet is very hard and tough therefore it was necessary to use a load of 200 N for crack creation. After these cracks were measured we determined the IFT values by using the four models below.

Microhardness and fracture toughness were evaluated on the cross sections of the samples. For sections preparation was used standard method for metallography preparation of hard metals⁹.

3. Results

3.1. Coatings microhardness

Results of microhardness testing are summarized in the Tab. I. For WC-Co coatings the typical high microhardness also corresponds to their high resistance against several wear conditions. As seen in the Tab. I and in Fig. 4, the microhardness has the tendency to decrease with lower deposition angle. For deposition angles 30° and 45° we noticed the lowest values and then it is seen an increase up to the deposition angle 90° where the microhardness is the highest. The microhardness variance between deposition angles 90° and 30° is of a significant value 145 HV0.3.

3.2. Indentation fracture toughness and microstructure

Thermally sprayed coatings show a strong anisotropy due to their lamellar structure. Because of that the lengths of cracks differ significantly in parallel and perpendicular direction with respect to coatings surface¹¹. In this experiment there were measured only parallel cracks, Fig. 5. As shown in the picture, the cracks spread parallel through the coatings from the corner of the indent.

The lengths of the cracks were specific to each deposition angle. For lower deposition angles the cracks were longer and wider. Also the indents size was different for the different deposition angles. The coatings prepared with the lower depositions angles showed a lower indents size. That is among others obvious from the results of microhardness.

The results of the indentation fracture toughness (IFT) for all used models are contained in Tab. II below. In Fig. 6 it is recorded an evident effect of deposition angle on IFT. The IFT values that are calculated according to models^{5–8} differ significantly, but they have a similar tendency. The deposition

Table I
List of microhardness values

Deposition angle	Microhardness	Standard deviation
	HV0.3	[±]
30°	1145	100
45°	1134	80
60°	1238	90
75°	1291	70
90°	1319	110

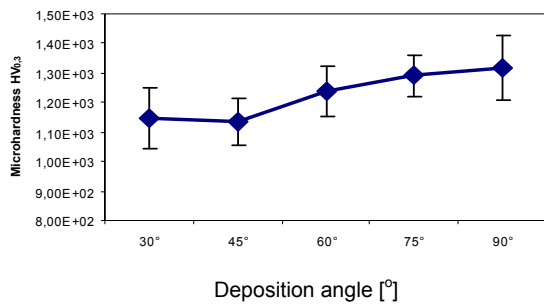


Fig. 4. Dependence of the microhardness on the deposition angle

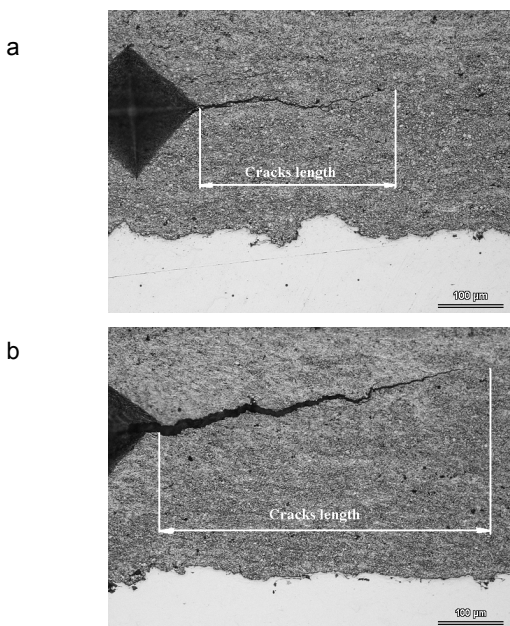


Fig. 5. Measurements of indentation fracture toughness, a) cracks in the coating sprayed under 90°, b) cracks in the coating sprayed under 30°

angle definitely influences the IFT. The trend of IFT changes is similar to the changes of microhardness. With the decreasing deposition angle decreases the indentation fracture toughness of the coatings. One disagreement in this trend of IFT measuring is only for deposition angle 60° and 75° where the IFT values are identical.

The fracture strength of WC-Co cermet depends mainly on the carbides grain contents and carbide grain size in the coating and further also on the amount of Co-binder phase. For WC-Co system exists an optimal carbide grain size and free path of cobalt binder where occurs the highest fracture strength¹². During HVOF spray process the decarburization which leads to the carbides loss might occur together probably with the carbide loss provoked by melted particle impact on the substrate. When the melted particle impinges the substrate with the high velocity it could occur a disadvantageous

Table II
Summary of IFT values

θ [°]	Indentation fracture toughness IFT [MPa m ^{1/2}]				Standard deviation [MPa m ^{1/2}]			
	LEM	LS	EC	LF	LEM	LS	EC	LF
30	0.75	0.62	1.1	0.68	0.07	0.05	0.1	0.07
45	0.87	0.72	1.3	0.78	0.30	0.10	0.4	0.20
60	1.00	0.84	1.5	0.91	0.20	0.10	0.3	0.20
75	0.98	0.83	1.4	0.88	0.30	0.20	0.4	0.30
90	1.20	0.93	1.8	1.10	0.4	0.20	0.7	0.40

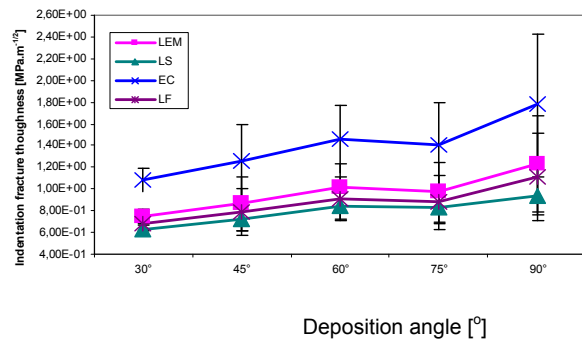


Fig. 6. Effect of deposition angle on the indentation fracture toughness

effect of some hard WC grains ejecting from the melted cobalt matrix. This undesirable effect could be higher when the deposition angle decreases and the particles impinge on the substrate in oblique direction. This assumption could explain why the IFT value decreases with decreased deposition angle.

The coatings cross sections show several differences in the microstructure. All coatings are dense without cracks and presence of oxides. The boundary between individual splats (impinged melted particles) is not identifiable and the adhesion to the substrate seems to be good. The coatings sprayed under the angles 75° and 90° show uniform carbides distribution and the pores content is low and nearly identical. The pores are small and spherical. The coatings sprayed under 60° and lowers contents more porosity in particular the coating sprayed under the angle 45°. Increase of coatings porosity can tend to decrease coating cohesion and fracture strength.

4. Conclusion

The experimental results described in this paper show that the deposition angle in the HVOF spray process plays an essential role for the resulting coating properties. The coating sprayed with 90° deposition angle shows the best mechanical properties.

The coating microhardness and indentation fracture toughness decrease with the decreasing of the deposition angle. This deterioration of mechanical coatings properties is

probably affected by WC grain loss in the coatings that are sprayed by lower deposition angle than 90°. Further effect could be assigned to coatings porosity rise and to cohesion loss in the coatings that are sprayed with the lower deposition angles.

The article was prepared thanks to the project of Ministry of Education, Youth and Physical Training of the Czech Republic MSM4771868401.

REFERENCES

1. Davis J. R. & Associates: *Handbook of Thermal Spray Technology*, ASM International, USA 2004.
2. Enžl R.: *Disertační práce*, ZČU, Plzeň 1999.
3. Loveloc H. L.: *J. Therm. Spray Technol.* 7, 357 (1998).
4. *Kovové materiály - Zkouška tvrdosti podle Vickerse - Tabulky hodnot tvrdostí*, ČSN EN ISO 6507-4, Český normalizační institut, (2006).
5. Lawn B. R., Evans A. G., Marshall D. B.: *J. Am. Ceram. Soc.* 63, 574 (1980).
6. Lawn B. R., Swain M. V.: *Mater. Sci.* 10, 2016 (1975).
7. Evans A. G., Charles E. A.: *J. Am. Ceram. Soc.* 59, 371 (1976).
8. Lawn B. R., Fuller E. R.: *J. Mater. Sci.* 10, 2016 (1975).
9. Bjerregaard L., Geels K., Ottesen B., Ruckert M.: *Metalog Guide, Struers A/S*, ISBN 80-238-3488-6 (1996).
10. Schwetzke R., Kreye H.: *J. Therm. Spray Technol.* 8, 436 (1999).
11. Houdková Š.: *Disertační práce*, ZČU, Plzeň 2003.
12. Liu B. et al.: *Mater. Chem. Phys.* 62, 35 (2000).

M. Kašparová, F. Zahálka, and Š. Houdková (*ŠKODA VÝZKUM Ltd., Plzeň, Czech Republic*): **Angle of Spraying and Mechanical Properties of WC-Co Coatings Prepared by HVOF Spray Technology**

Thermal spraying is the effective technology that produces the coatings from 50 μm to several millimeters in the thickness. In this paper the HVOF spray technology is discussed. This technology for its typical properties is most of all used for forming cermets coatings. WC-Co cermets coating was tested and its mechanical properties were studied. WC-Co coatings were sprayed with five different angles (90°, 75°, 60°, 45° and 30°). The deposition angle is very important for resulting coating properties. The deposition angle influences most of all bond strength, coating cohesion and porosity of the coating. From this case the different properties for the five different deposition angles were expected. We directed our attention at the hardness measurements and indentation fracture toughness (IFT) measurements. The results of microhardness and IFT indicate on mechanical material properties in the influence of the deposition angle.

DETERMINATION OF THE OPTICAL FIBRE DEFORMATION BY THE INTERFEROGRAM ANALYSIS

JOZEF KRAJČOVIČ
and **IGOR JANČUŠKA**

Faculty of Materials Science and Technology STU, Institute of Materials, Department of Physics, Paulínska 16, 917 24 Trnava, Slovakia
krajcov@mf.stuba.sk

Keywords: optical methods, deformation, holographic interferometry, regression analysis, Young's elasticity modulus

1. Theoretical substance of the two-exposure holographic interferometry method and its using for the Young's elasticity modulus measurement

The light waves generated by the stimulated radiation of atoms conserve not only the frequency but also the phase during the coherence time that determines the spatial coherence. Let the v is the velocity of the light wave with the wavelength λ from laser and this wave is divided into two waves u_1, u_2 with the different passed optical paths x_1, x_2 .

$$u_1 = a \sin\left(\omega t - \frac{x_1}{v}\right)$$

$$u_2 = b \sin\left(\omega t - \frac{x_2}{v}\right)$$

We can observe the interference of these two waves in the place of meeting

$$u = u_1 + u_2$$

$$u = a \sin(\omega t - kx_1) + b \sin(\omega t - kx_2)$$

where $k = \frac{2\pi}{\lambda}$ is the wave number. The amplitude of the wave u is

$$A^2 = a^2 + b^2 + 2ab \cos k(x_1 - x_2)$$

For $k(x_1 - x_2) = (2n+1)\pi$ we obtain $A = |a - b|$. If $a = b$, then the wave disappears in the place of meeting.

We can obtain the information about the object if we divide the wave from laser into two waves. The first falls on the object. This wave is reflected and dispersed by the object and falls on the holographic plate with high resolution. The second wave falls on the same plate after the reflection by the mirror. Both of the waves write the information about the object on the plate during the first exposure, see Fig. 1.

If we do the second exposure with the same plate, when the object is deformed, we obtain the picture of the object with the interference fringes, that carry the information about the object deformation¹. This fact we use for the Young's

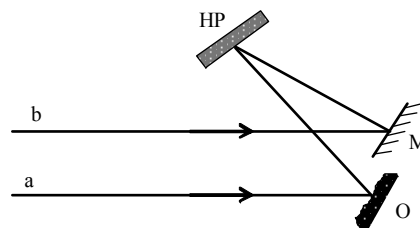


Fig. 1. An optical composition. M – mirror, a, b – parallel beams of coherent waves, HP – holographic plate, O – object

elasticity modulus determination. The down end of the material is fixed and the up end is deviated by the force F action during the second exposure. We can calculate the bend y of the loose girder end by formula.

$$y = \frac{Fl^3}{3EJ} \quad (1)$$

Where l is a distance between the fixed end and the point of the force activity, E is the Young's elasticity modulus, J is the area momentum of inertia for the perpendicular cross-section of the girder, see Fig. 2.

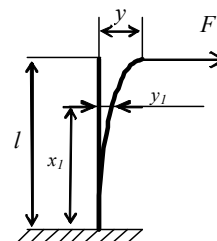


Fig. 2. Deformation of the object. l – the length of the object, y – the bend in the point of the deforming force F action, y_1 – the bend in distance x_1 from the fixed end

The bend determination needs a high accuracy, therefore the holography method is suitable. This method can determine the bend with accuracy equal to one half of the wavelength. The bend y is determined from the number $n+1$ of the interference dark fringes, that rise after two exposures and developing of the holographic plate on the picture (hologram) of the object, by the formula

$$2y = (2n+1) \frac{\lambda}{2} \quad (2)$$

If we substitute it into equation (1), we obtain the Young's elasticity modulus

$$E = \frac{4Fl^3}{3J(2n+1)\lambda} \quad (3)$$

2. Conditions of the experiment realization

We used described process of the two-exposure holographic interferometry. The round cross-section optical fibre was our researched object.

The choice of the deforming force value must be so that the dark fringes are well sumable, see Fig. 3.

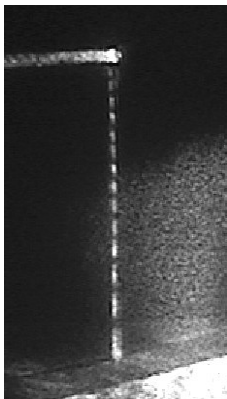


Fig. 3. Digital picture of the hologram with the well sumable interference fringes

If we substitute the area momentum J of inertia for the round cross-section with the optical fibre diameter d

$$J = \frac{\pi d^4}{64} \quad (4)$$

into equation (3), we obtain

$$E = \frac{256Fl^3}{3\pi d^4(2n+1)\lambda} \quad (5)$$

where $\lambda = 632.8$ nm for used laser.

The values of the quantities we need for using formula (5) we obtain as follows. We read the force F straight from the forcemeter scale. The accuracy depends upon the kind of the forcemeter. We measure the length l of the optical fibre after it is fixed. We use the slide rule with error 0.05 mm, but because of uncertainties that rise by fixing of the object and by determination of the force action point, we choose the accuracy 1 mm. We measure the optical fibre diameter d by means of micrometer.

We read the number of the dark fringes from hologram, see Fig. 3. It is problem to read the position of the dark fringe middle, therefore we choose accuracy of the dark fringes number 1, 0.5 or 0.25. It is depends upon specific situation.

3. The regression analysis using

One of the sources of errors is determining the position of the dark fringes middle near the point of force action. There are cases we don't observe the fringes near the point of force action, see Fig. 4.

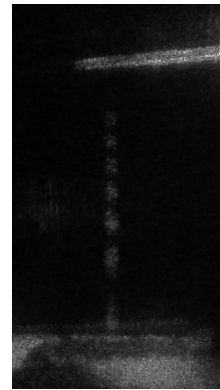


Fig. 4. Digital picture of the hologram with the bad sumable interference fringes near the point of force action

Both of the disadvantages we may eliminate by the regression analysis using. From the theory for the girder with deforming force in one point² yields, that we can use equation

$$y = -\frac{F}{6EJ}x^3 + \frac{Fl}{2EJ}x^2$$

for computing the band y_1 in distance x_1 from the fixed end. We may write simply equation

$$y = ax^3 + bx^2 \quad (6)$$

where we substitute $a = -\frac{F}{6EJ}$ a $b = \frac{Fl}{2EJ}$

Because we don't know the value of the Young's elasticity modulus, we cannot determine constants a, b directly.

We determined constants a, b by means of the least squares method for the seven pairs with regression function (6). Each pair contains the measured value of the dark fringe middle position x and the measured value of the bend y for this middle. The dependence the bend of fibre upon the position x , see Fig. 5, we saved into PC memory.

4. The measured and calculated values

We measured the values x_i by means of suitable software in the digital picture, see Fig. 4. We determined the values y_i by means of formula (2). There are the values in the Tab. I.

Table I

I	1	2	3	4	5	6	7
$x_i, \mu\text{m}$	0	3580.4	7221.1	9869.0	12005.3	13299.0	15706.0
$y_i, \mu\text{m}$	0	0.158	0.475	0.791	1.110	1.420	1.700

We determined the values of constants
 $a = -3.4429048 \cdot 10^{-13} \mu\text{m}^{-2}$, $b = 1.2226397 \cdot 10^8 \mu\text{m}^{-1}$.
 The dependence the bend y of the optical fibre upon the position x is on Fig. 5.

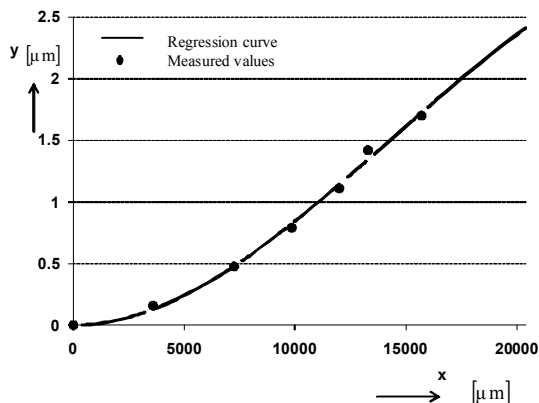


Fig. 5. Dependence the bend of the fibre upon the position – regression curve

For the known value for the distance between the fixed end and the force action point $x = 20\,400 \mu\text{m}$ we obtain $y = 2.1562269 \mu\text{m}$. This value we can substitute into equation

$$E = \frac{64Fl^3}{3\pi d^4 y}$$

that we obtained by substituting formula (4) into (1). We used values $F = 19.13 \mu\text{N}$, $l = 20.4 \text{ mm}$ and $d = 0.507 \text{ mm}$. The calculated value of the Young's elasticity modulus for the optical fibre is $E = 7.7086629 \cdot 10^9 \text{ Pa}$.

5. Conclusion

The described method enables the complex view on the deformation field distribution in the researched object without the damage of the object.

We expect the increase of the accuracy by the regression analysis using.

It is positive we can obtain the result from the holograms, that don't contain the interference fringes along the whole length of the picture.

Generally we can say the method is rather sensitive and it is suitable for researching of the larger cross-section objects from the metal and ceramic materials.

The Young's elasticity modulus of the measured optical fibre is at about 25-times lesser than the Young's elasticity modulus of steel ($E = 20 \cdot 10^{10} \text{ Pa}$).

REFERENCES

1. Balaš J., Szabó V.: *Holografická interferometria v experimentálnej mechanike*. VEDA, Bratislava 1986.
2. Pucher O. a kol.: *Pružnosť a pevnosť I*, str. 175. SVŠT, Bratislava 1987.

This work was supported by grant agency VEGA, Slovakia (grant project 1/2100/05).

J. Krajčovič and I. Jančuška (Faculty of Materials Science and Technology STU, Institute of Materials, Department of Physics, Trnava, Slovakia): **Determination of the Optical Fibre Deformation by the Interferogram Analysis**

There used the optical methods for the determination of the several solid states materials mechanical parameters. For example, we may to determine the Young's elasticity modulus by means of laser, by the two-exposure holographic interferometry method. We obtained the interferogram by means this method that contained a system of the light and dark interference fringes. Then we determined the deformation of the researched material by means of the regression analysis. We used the regression analysis for the determination of the bend in the point of the force action. Our researched material was an optical fibre of the cylinder shape.

This paper contains the describing of the used method, the measured values and the calculated values of the optical fibre Young's elasticity modulus.

NANOHARDNESS OF WC/C COATING AS A FUNCTION OF PREPARATION CONDITIONS

FRANTIŠEK LOFAJ^{a*}, MILAN FERDI-NANDY^a, and ANDRÁS JUHÁSZ^b

^a Institute of Materials Research of SAS, Košice, Slovakia,

^b Eötvös Loránd Tudomány Egyetem, Budapest, Hungary
flofaj@imr.saske.sk

Keywords: WC/C coatings, nanohardness, indentation modulus, compressive stresses

1. Introduction

Amorphous hydrogenated carbon (a-C:H) coatings, including diamond-like coatings (DLC), which are rich in sp^3 content, exhibit very high hardness, low friction and other properties, which make them attractive for hard protective and wear resistant films, coatings on magnetic storage devices, micro-electromechanical systems and others^{1,2}. The amorphous carbon films can be deposited by variety of methods including ion-beam deposition, sputtering technique, plasma enhanced chemical vapor deposition (PECVD), pulsed laser deposition and the magnetron sputtering. Magnetron sputtering is possibly the most common and in that case, Ar^+ ion bombardment of a carbon target is used and a bias voltage is applied to the substrate. However, one of the problems of such coatings is a poor adhesion of the sputtered carbon films due to high intrinsic compressive stresses. Several approaches have been developed to reduce the stresses: post-deposition annealing, formation of the multilayer films consisting of sequential rich in sp^2 and sp^3 content layers^{3,4}. Metal doped carbon coatings are also an interesting group which can be tailored into nanocomposite structure with special properties. Although DLC and various metal-doped DLC nanocomposite coatings have been extensively studied, W-doped diamond-like carbon films have received comparatively little attention. WC exhibits relatively high hardness and its combination with the properties of amorphous carbon in the nanocomposite structure results in a coating with low friction coefficient and good wear resistance⁵. However, similarly as pure DLC, W based-carbon coatings some drawbacks, including a poor adhesion with common substrate materials⁶, low fracture toughness (35 J m^{-2} , ref.⁷) and the effect of hydrogen in the structure on the friction behavior of sp^2 rich coating. There are only a few studies on carbon based coatings without the influence of hydrogen. Some aspects of the tribological behavior of such non-hydrogenated metal containing DLC coating studied here by Camino⁸, Yang^{9,10}, Zeng¹¹ and Konca¹². The hardness values ranging from 1600 HV to 3300 HV were obtained despite relatively high sp^2 content by increasing bias voltage from 20 V to 90 V (ref.⁹) due to nanocomposite structure¹⁰. Thus, the purpose of the work is to investigate the process of the deposition conditions on the formation and nanohardness of non-hydrogenated WC/C coatings.

2. Experimental procedure

The studied WC/C films were deposited on the polished high speed steel (HSS) and Si (100) substrates using combined PVD-PECVD techniques. The substrates were cleaned by the Ar ions prior to the deposition. In some cases, a Ti sublayer was deposited using an electron gun. Then, the vapors of the W and C from a precursor were introduced into the main chamber, they were ionized and accelerated toward the substrate with the negative bias. The main deposition parameters were total gas pressure in the chamber, bias voltage applied to the substrate and current density at the substrate surface. Four series of coatings were prepared varying these parameters to optimize the conditions. Thin Ti interlayer has been deposited on the substrate in at the beginning in several cases to achieve better adhesion with the substrate. Later, Ti layer was excluded and the WC/C film was deposited directly on the substrate. Phase composition was investigated using X-ray diffraction. Film thickness was measured and the surface morphology and structure were studied in SEM on the broken cross sections. The elastic properties of the films were conducted using a nano-indenter UMIS 2000. The hardness and the reduced elastic modulus of the films were measured with a Berkovich tip, which was forced into the coating using a coil and magnet assembly. The maximum load was up to 1 mN or 5 mN in 20 steps followed by a 5 sec dwell and unloading in 10 steps. Nanohardness was determined from the penetration depth at the maximum load and the reduced elastic modulus from the unloading part of the curve according the method of Oliver and Pharr. At least 15 indentations were performed automatically for each coating and the average values were calculated.

3. Results and discussion

The variation in the deposition conditions and the coating thicknesses are summarized in Tab. I. At the beginning (sample designated as #13), Ar carrier gas was used which resulted in the total pressure up to 4 Pa. Ti sublayer was also deposited in this case. However, the coating delaminated from the substrate in small chips, which covered significant parts of the substrate. The repetition without Ti sublayer and without Ar revealed slightly better adhesion. Thus, subsequent coat-

Table I
Deposition condition for the studied WC/C coatings

Sample	Total pressure [Pa]	Bias [kV]	Beam current [mA cm^{-2}]	Thickness [nm]
#13, Ar	4	3.8	1	300
#20	1	5	1	200
#24	2	5	0.8	700
#21	0.8	4.5	1.2	200

ings were produced without Ar and Ti at under total pressure in the range from 0.8–2 Pa. Bias voltage was in the range from 3.8 up to 5 kV and the beam current varied from 0.8 up to 1.2 mA cm⁻².

The reduction of the pressure and bias increase (#20) did not solve the delamination problem, therefore we varied the beam current and the thickness (i.e. longer deposition time) of the coating. Though not fully optimized, the best results from the viewpoint of coating stability were obtained in the case of sample #21 under the lowest total pressure and highest beam current. X-ray diffraction indicated the presence of broad diffuse peaks and identified WC which suggests that the produced coatings are nanocomposites. The morphology of this coating #21 is illustrated in Fig. 1. In contrast to all other coatings it is very smooth and almost featureless. Preliminary AFM study showed surface relief of less than 10 nm on Si wafer and up to 25 nm on the polished steel substrate. The cross section at the broken edge of the coating in Fig. 1 shows globular features with the size of 10–20 nm, which also supports the presence of nanocomposite structure. However, more detail TEM study is necessary to reveal the structure of the coating unambiguously.

Nanohardness tests were initially performed with the maximum load of 1 mN to be within the limit 10% of the film thickness and to avoid substrate effects. However, the scatter among the obtained values exceeded 100% and it was reduced to acceptable level only when the load was increased to 5 mN. Typical penetration depth under those conditions was around 120 nm, which means that the obtained values are lower than they should be because of the influence of softer substrate. Fig. 2 shows several loading-unloading curves obtained on a coating #21. The scatter of the curves, though still significant, is acceptable. The absence of pop-ins indicates sufficient adhesion. The results of the measurements are summarized in Tab. II.

The average nanohardness of the studied coatings is within the range from 20 GPa to 24 GPa and the reduced elastic modulus in the range from 265 GPa up to 320 GPa with significant scatter (up to 50% in some cases).

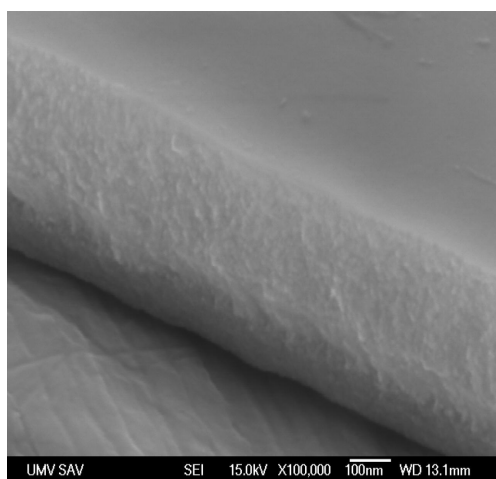


Fig. 1. The morphology and the cross section of the WC/C coating on steel substrate (sample #21) by SEM

Table II
Summary of the nanoindentation tests

Sample	Hardness [GPa] (min. – max.)	Elastic modulus [GPa] (min. – max.)
#13	24.1 ± 9.5 (16.9–45.8)	323 ± 96 (203–489)
#20	21.5 ± 3.1 (18.0–25.7)	318 ± 24 (297–355)
#24	19.9 ± 2.1 (17.7–22.9)	265 ± 12 (251–277)
#21	20.1 ± 11.9 (7.1–38.9)	266 ± 128 (106–350)

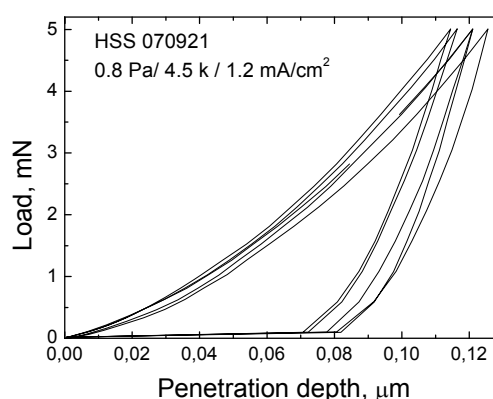


Fig. 2. Indentation curves in sample #21

Such a large scatter of the data seems to be the result of the compressive stresses developed during deposition in the layers and level of their relaxation.

The obtained hardness corresponds to the values for many other coatings and the true hardness of the studied coating can be increase when measured at smaller penetration depth and without the compressive stresses. The presence of such stresses is a principal problem for the nanoindentation measurements because the level of these stresses can be in the range from 1 GPa to 6 GPa (ref.^{3,4}), which is in the same order of magnitude as the measured values. Obviously, additional investigations are the unbiased values of nanohardness from the studied coatings and to reduce the compressive stresses.

4. Conclusions

Current study on the nanohardness of WC/C coatings prepared by a PECVD method emphasizes the problems with delamination and nanohardness measurements resulting from the presence of large compressive stresses developed during deposition. These stresses can be slightly reduced via modification of the deposition conditions, especially total pressure

and current density. Nearly optimized conditions for WC/C coating preparation were obtained and provided nanocomposite microstructure with the nanohardness of around 20 GPa and reduced elastic modulus of 266 GPa. However, additional TEM investigations are necessary to confirm the presence of nanoparticles in the coatings and further work on the reduction of the compressive stresses and improvement of coating adhesion.

REFERENCES

1. Grill A.: Surf. Coat. Technol. 94–95, 507 (1997).
2. Liu Y., Gubisch M. et al.: Tribology Int. 39, 1584 (2006).
3. Gioti M., Logothetidis S., Chariditis C.: Appl. Phys. Lett. 73, 184 (1998).
4. Patsalas P., Logothetidis S., Kelires P. C.: Diamond Rel. Mat. 14, 1241 (2005).
5. Liu Y., Gubisch M., Hild W., et al.: Thin Solid Films 488, 140 (2005).
6. Bewilogua K., Cooper C.V., Specht C., et al.: Surf. Coat. Technol. 127, 224 (2000).
7. Wang J. S., Sugimura Y., Evans A. G., et al.: Thin Solid Films 325, 163 (1998).
8. Camino D., Jones A. H. S., Mercks D., Teer D. G.: Vacuum 52, 125 (1999).
9. Yang S., Camino D., Jones A. H. S., Teer D. G.: Surf. Coat. Technol. 124, 110 (2000).
10. Yang S., Li X., Renevier N. M., Teer D. G.: Surf. Coat. Technol. 142–144, 85 (2001).
11. Zeng X. T., Zhang S., Ding X. Z., Teer D. G.: Thin Solid Films 420–421, 366 (2002).
12. Konca E., Cheng Y.-T., Weiner A. M., et al.: Surf. Coat. Technol. 200, 3996 (2006).

F. Lofaj^a, M. Ferdinandy^a, and A. Juhász^b (^a *Institute of Materials Research of SAS, Košice, Slovakia*; ^b *Eötvös Loránd Tudomány Egyetem, Budapest, Hungary*): **Nanohardness of WC/C Coating as a Function of Preparation Conditions**

A set of thin WC/C coatings had been prepared by the PECVD technique from W and C precursors under different conditions on high speed steel and Si wafer substrates. The nanohardness and indentation modulus and microstructure of these films prepared were investigated in order to establish the correlations between the preparation conditions and mechanical properties. The main problem identified after deposition were high compressive stresses causing film delamination. The modification of the total pressure with slightly increased bias and beam current density resulted in the reduction of delamination. Very large variations in the indentation hardness and indentation modulus were also attributed to the presence of high local compressive stresses. The average hardness of the coating prepared under optimized condition was around 20 GPa and indentation modulus around 265 GPa.

DETERMINATION OF PARAMETERS OF VISCOELASTIC MATERIALS BY INSTRUMENTED INDENTATION

JAROSLAV MENČÍK

University of Pardubice, Jan Perner Transport Faculty,
Studentská 95 532 10 Pardubice, Czech Republic
jaroslav.mencik@upce.cz

Keywords: viscoelastic material, instrumented indentation, rheological models

1. Introduction

Instrumented indentation, called also nanoindentation if very low loads are used, provides information about mechanical properties from indenter load and depth measured during loading and unloading (Fig. 1). Today, these methods are well established for elastic-plastic materials like metals or ceramics. They can also be used for characterisation of polymeric and other materials whose response to load depends also on time. However, specific features of their behaviour must be taken into account in the test preparation and data processing. The pertinent methods are still under development. This paper gives a brief review of basic formulae for instrumented indentation into elastic-plastic materials, then it explains the load response of viscoelastic materials and presents the pertinent formulae, with emphasis on indentation testing. Also, a practical test procedure is described.

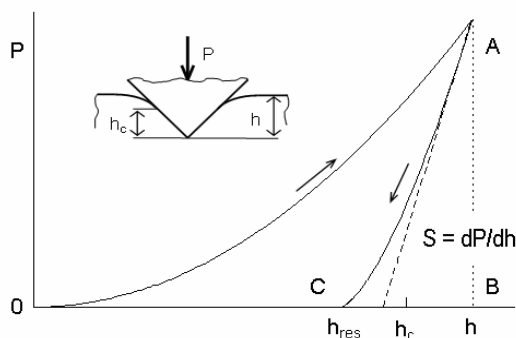


Fig. 1. Load-depth curves of an indentation test – a schematic. P – indenter load, h – displacement (penetration), h_c – contact depth

2. Basic formulae for indentation testing of elastic-plastic materials

In instrumented indentation, hardness H is defined as the mean contact pressure, and calculated by dividing the indenter load P by the projected contact area A :

$$H = \frac{P}{A} \quad (1)$$

The contact area is calculated from contact depth h_c , which is obtained from the total indenter displacement h , indenter load P and contact stiffness $S = dP/dh$ at the beginning of unloading (Fig. 1), usually by the formula proposed by Oliver and Pharr¹:

$$h_c = h - \varepsilon \frac{P}{S} \quad (2)$$

where ε is a constant ($\varepsilon \approx 0.75$). The stiffness S is determined from the regression function, mostly of power-law type,

$$P = c(h - h_{\text{res}})^m \quad (3)$$

fitted to the upper part of unloading curve; c , m and h_{res} are regression constants (h_{res} corresponds to the residual depth of imprint after unloading). For Berkovich indenter (a three-sided pyramid often used in nanoindentation), the contact area is approximately $A = 24.5 h_c^2$; more accurate results $A(h_c)$ are obtained by indenter tip calibration.

Equation (2) has proved good for elastic materials, where the ratio of the depth of permanent imprint after unloading, h_{res} , and the total depth under load, h , is less than 0.7. For more ductile materials, with $h_{\text{res}}/h > 0.7$, however, Equation (2) gives lower values h_c than actual. For these cases, Bec et al.² have recommended the relationship

$$h_c = 1,2 \left(h - \frac{P}{S} \right) \quad (4)$$

a discussion to both approaches can be found in paper³.

In addition to hardness, also the elastic modulus can be calculated from the contact stiffness and contact area:

$$E_r = \frac{\sqrt{\pi}}{2\beta} \frac{S}{\sqrt{A}} \quad (5)$$

E_r is the reduced modulus, related with the elastic modulus E and Poisson ratio ν of the specimen (no subscript) a indenter (subscript i) as

$$\frac{1}{E_r} = \frac{1-\nu^2}{E} + \frac{1-\nu_i^2}{E_i} \quad (6)$$

β is a correction for the indenter tip shape (for Berkovich indenter, $\beta \approx 1.05$).

3. Theoretical background for testing of viscoelastic materials

The response of some materials, such as polymers, is more complex, as it depends not only on the load magnitude, but also on its duration and time course. The indenter continues penetrating into the specimen even under constant load (part D of the curve in Fig. 2). Such materials are called viscoelastic or viscoelastic-plastic. In this case, hardness (I) is no more a constant, but decreases with the time under load, $H = H(t)$.

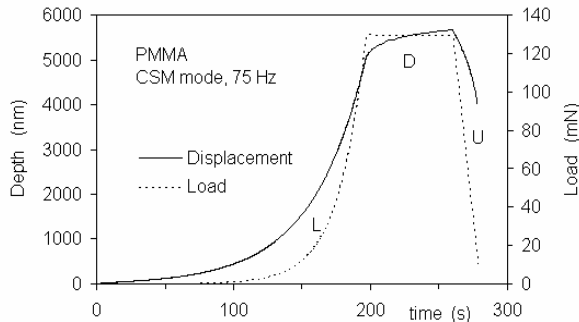


Fig. 2. Time course of a nanoindentation test into PMMA [4]; L – loading, D – dwell under constant load, U – unloading

Moreover, due to delayed deforming, also the unloading part of the $P-h$ curve is sometimes distorted (Fig. 3); it is more convex than in elastic materials, sometimes with a bulge or even a “nose” at the beginning of unloading. The determination of contact stiffness by a conventional manner from the slope of the unloading curve thus could lead to an error in the determination of contact stiffness S , and thus to an error in the contact depth and area, as well as in the elastic modulus and hardness. If the time-dependent effects are not negligible, a special approach is needed. This paper will deal with procedures for viscoelastic materials and monotonic loading and unloading. The determination of viscoelastic properties under harmonic loading can be found in Menčík et al.⁴. The characterisation of viscoelastic-plastic properties, typical by the occurrence of time-independent permanent deformations, will be the topic of another paper.

The delayed deforming in indentation tests can be accounted for in various ways. In order to avoid the distortion of unloading curve (Fig. 3), it is recommended to insert a dwell (with constant load) between the loading and unloading period. According to Chudoba and Richter⁵, the influence of delayed deforming on the unloading curve may be neglected if the creep velocity has decreased so that the penetration depth at the end of dwell grows not faster than 1% per minute. Some disadvantage of this approach is that the indenter depth at the beginning of unloading (after the dwell) is larger than at the end of loading, and this results in larger contact area and lower apparent hardness.

Therefore, some authors recommend to use relatively fast loading followed immediately by fast unloading, and to calculate the contact depth and elastic modulus using the ef-

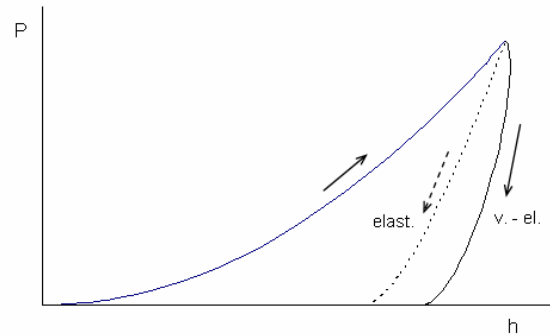


Fig. 3. Load-depth diagram for elastic and viscoelastic (v.-el.) material; note the differences between unloading curves

fective contact stiffness S , defined by the following expression proposed by Ngan and Tang⁶:

$$\frac{1}{S} = \frac{1}{S_{app}} + \frac{\dot{h}_d}{|\dot{P}_u|} \quad (7)$$

S_{app} is the apparent stiffness, obtained by the common Oliver and Pharr procedure¹ from the unloading curve, \dot{h}_d is the indenter velocity at the end of dwell, and \dot{P}_u is the load decrease rate at the beginning of unloading (Fig. 3); the units are N/m, m/s and N/s, respectively.

However, the results can also be influenced by viscoelastic deforming during the load increase phase. Moreover, it is generally insufficient to characterise materials that flow permanently under load, only by means of a single value of hardness or elastic modulus. The time-dependent properties must be described in a more appropriate way. Usually, rheological models consisting of springs and dashpots are used, such as the Kelvin or Maxwell model and their combinations (Fig. 4). The parameters in these models, suitable as material characteristics, can be obtained by fitting the time course of penetration depth by a suitable creep function, depending on the material, indenter shape and loading history.

The commonly used formulae are based on the approach proposed by Lee and Radok⁷, which uses the elastic solution, but replaces the elastic constants by a viscoelastic hereditary integral operator; cf. Johnson⁸ or Oyen⁹.

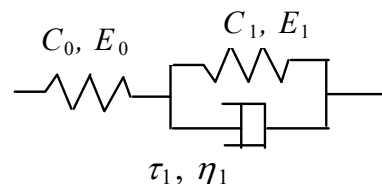


Fig. 4. Standard Linear Solid

The relationship between indenter load and depth of penetration into an elastic or viscoelastic material under monotonic loading can be expressed generally as

$$f[h(t)] = K \psi(P, J, t) \quad (8)$$

where f is some function of the indenter shape and penetration, K is a constant characterising the indenter geometry, and $\psi(P, J, t)$ is a function depending on the load magnitude and history, on material parameters, and on time. For spherical indenter (subscript s),

$$f_s = h^{3/2}; \quad K_s = 3 / (8\sqrt{r}) \quad (9)$$

r is the indenter tip radius. For pointed indenters (conical, Berkovich or Vickers, subscript c),

$$f_c = h^2; \quad K_c = \pi / (4 \tan \alpha) \quad (10)$$

α is the semiangle of indenter tip or of equivalent cone (for Berkovich and Vickers indenter, $\alpha = 70.4^\circ$). The function ψ for penetration of a rigid indenter into ideally elastic materials is

$$\psi = P \frac{1-\nu}{G} \quad (11)$$

G is the shear modulus and ν is Poisson ratio. The general formula for linearly-viscoelastic materials (and a rigid indenter) is

$$\psi(t) = \int_0^t J(t-u) [dP/du] du \quad (12)$$

where $J(t)$ is the so-called creep compliance function, depending on the material model used, t is time, and u is a dummy variable for integration. For constant load after step change from 0 to P , the function ψ is simply the product of load and creep compliance function $J(t)$,

$$\psi(t) = P J(t) \quad (13)$$

However, step load is impossible to realise; there is always some period of load increase. For ramp loading with constant load rate, $R = dP/dt = \text{const}$, it holds

$$\psi(t) = R \int_0^t J(t-u) du \quad (14)$$

The penetration under constant load P following the ramp load lasting t_R can be described by the function

$$\psi(t) = R \int_0^{t_R} J(t-u) du \quad (15)$$

where t_R is the duration of load increase. Formula (15), valid for $t > t_R$, was obtained as the sum of two loads growing with the constant rate R : the first load starts at $t=0$, while the other, acting in the opposite direction, starts at time t_R . Thus, for $t > t_R$, the load is constant, $P = R t_R$.

The application of the above formulae can be illustrated on a relatively universal model, consisting of a spring connected in series with a Kelvin-Voigt unit, which is a spring in parallel with a dashpot. For this model, called Standard Linear Solid (Fig. 4), the creep compliance function is

$$J(t) = C_0 + C_1 [1 - \exp(-t/\tau_1)] \quad (16)$$

where C_0 and C_1 are compliance constants, and τ_1 is so-called retardation time. This is a time constant of the system, related to the compliance C_1 of the spring and viscosity η_1 of the dashpot in the Kelvin-Voigt body as $\tau_1 = \eta_1 C_1$. A more complex response can be approximated using more Kelvin-Voigt units in series,

$$J(t) = C_0 + \sum C_j [1 - \exp(-t/\tau_j)] \quad (17)$$

($j = 1, 2, \dots, n$). The instantaneous compliances C_j (and C_0) are related to the shear moduli G_j and Poisson ratios ν_j by

$$C_j = (1 - \nu_j)/G_j \quad (18)$$

The springs can also be characterised by means of tensile moduli E , related to the shear moduli as

$$E_j = 2(1 + \nu_j) G_j \quad (19)$$

However, only G_0 and E_0 correspond to the actual (instantaneous) elastic modulus of the material. The other constants C_1, C_2, \dots just characterise delayed deforming. The “moduli” G_1, G_2, \dots or E_1, E_2, \dots do not represent additional stiffnesses, but reciprocals of additional, time-dependent compliances.

Indentation creep under constant load P following ramp loading (with constant load rate) lasting $t_R = P/R$, can be described by the function derived by Oyen⁹:

$$\psi(t) = P \{ C_0 + C_1 [1 - \rho_1 \exp(-t/\tau_1)] \} \quad (20)$$

or, for a generalised standard linear solid (15),

$$\psi(t) = P \{ C_0 + \sum C_j [1 - \rho_j \exp(-t/\tau_j)] \} \quad (21)$$

In expressions (20) and (21), ρ_j is so-called ramp correction factor, calculated as⁹

$$\rho_j = (\tau_j/t_R) [\exp(t_R/\tau_j) - 1] \quad (22)$$

Note that the formulae (20) and (21), valid for $t \geq t_R$, differ from those for step loading, based on Eqs. (16) and (17), only by the factors ρ_j at the exponential terms. For fast loading, with the load increase very short compared to the retardation time, $t_R \ll \tau_j$, the ramp correction factor is close to 1; it attains 1.025 for $t_R/\tau_j = 0.05$ and 1.05 for $t_R/\tau_j = 0.1$, and grows rapidly for higher ratios t_R/τ_j .

REMARK. Creep compliance function (17) can also be written in another form⁹:

$$J(t) = C_0' - \sum C_j \exp(-t/\tau_j) \quad (23)$$

where

$$C_0' = C_0 + \sum C_j \quad (24)$$

C_0' expresses the asymptotic compliance, corresponding to very long loading ($t \rightarrow \infty$), in contrast to C_0 , which characterises the instantaneous compliance, i.e. the immediate reaction to sudden loading. [The form (23) is usual in computer programs for the finite element analysis of viscoelastic response.] Similarly, Eq. (21) can be written as follows

$$\psi(t) = P [C_0' - \sum C_j \rho_j \exp(-t/\tau_j)] \quad (25)$$

In the limit case with $j = 1$, formulae (23) and (25) reduce to equations (16) and (20) for Standard Linear Solid.

4. Practical part

A suitable procedure for the determination of material parameters is as follows. The indenter is loaded quickly (with the constant load rate R) to the nominal load P , then kept under this load for a relatively long time, and unloaded quickly. From the unloading curve, the contact stiffness can be determined, either directly as $S = dP/dt$ if the indenter velocity at the end of dwell was negligible, or using correction (7). The contact area A , necessary for the determination of instantaneous elastic modulus E_0 from the unloading curve via Eqs. (5) and (6), is calculated from the contact depth h_c , determined by Eq. (2) from the depth h at the beginning of unloading.

The dwell under constant load is used for the determination of constants in rheological (spring and dashpot) models. Depending on the model, the function $\psi(t)$, defined by Eq. (20) or (21), is inserted into (8), together with the function f and constant K , chosen from Eq. (9) or (10) with respect to the indenter shape. This function $f[h(t)]$ is then used to fit the measured $h(t)$ data.

The constants C_0 , C_1 , τ_1 , ρ_1 , etc. can be obtained by minimising the sum of squared differences between the measured and calculated $h(t)$ values. A suitable tool for this purpose is Solver, available in some universal computer programs, such as Excel. However, the actual procedure must be modified for the following reason. The constants C_j appear in Eqs. (20), (21) and (25) only together with the constant ρ_j (as product $C_j\rho_j$), or together with the constant C_0 (as C_0' , cf. Eq. (24)). Thus, the regression fitting of experimental data can yield the correct values of $C_j\rho_j$ and C_j' , while the individual values of constants C_j can be wrong. The constants C_j , however, are the genuine material parameters, independent of the loading history, and must be determined accurately. Their correct values can be obtained using a simple three-step data processing, based on the verified fact that the retardation times τ_j can be determined correctly for any mathematical form of the model (25).

In the first step of the procedure, the $h(t)$ data obtained by indentation during the constant-load part of the test are fitted by the function (25), with all constants C_0' , C_1 , τ_1 , ρ_1 , etc. considered as “free”. In this way, the retardation times τ_j are obtained. Then, the ramp correction factors ρ_j are calculated from Eq. (22) for these times τ_j and the duration t_R of the load increase. These values ρ_j are then inserted as fixed constants into Eq. (25) or (21), and the curve fitting, now searching for the remaining constants C_0 , C_1 , τ_1 , etc. is done again. Computer modelling has shown that this procedure yields correct results.

REMARK. Due to viscoelastic deformations, the indenter depth at the end of dwell is larger than at the end of load increase, so that also the contact area is larger. This can influence the calculated value of the constant C_0 . For this reason (and for a check), it is recommended to determine this constant (and elastic modulus E_0) using also a separate test with fast loading followed immediately by unloading.

From the compliances C_0 , C_1 , etc., it is also possible to calculate the values of G_0 , G_1 , etc. for the (chosen) value of Poisson ratio ν . In an ideal case, the instantaneous shear modulus G_0 is related to the (instantaneous) tensile modulus

E_0 from the unloading curve as $G_0 = E_0/[2(1+\nu)]$. If the calculated parameters do not fulfil this condition, it is an indication that a correction is necessary, e.g. for the delayed deforming during the load increase period.

When looking for a suitable model, one should be aware that very complex models, with more than about 6–7 regression constants, can sometimes cause problems in the search for their accurate values, and a compromise between the model complexity, accuracy and “robustness” may be necessary. A similarly good fit is sometimes obtained for various arrangements of springs and dashpots. The model complexity should also respect the amount of experimental data available, especially regarding the test duration. If the measurement lasts only several tens of seconds, it is impossible to obtain accurate information about the behaviour under a load lasting several hours or more.

Finally, it should be reminded that Eqs. (16), (17), (20) and (21) are only valid for reversible viscoelastic deformations, which occur under a spherical indenter (sometimes even under pointed indenter¹⁰) if sufficiently low load is used. For higher loads, also plastic deformations appear. The characterisation of viscoelastic-plastic materials with permanent deformations exceeds the scope of this paper and will be the topic of another work¹¹.

5. Summary

Mechanical properties of viscoelastic materials with time-dependent response can be determined by instrumented indentation, which continuously measures indenter load and displacement. The paper has explained the principle of the method as used for elastic-plastic materials, gave the basic formulae for expressing the load response of visco-elastic materials by means of spring-and-dashpot models, and described a procedure for the indentation testing and the determination of material parameters.

This work was supported by the grant Agency of Czech Republic, project GAČR No. 103/05/2066.

REFERENCES

1. Oliver W. C., Pharr G. M.: *J. Mater. Res.* 7, 1564 (1992).
2. Bec S., Tonck A., Georges J.-M., Georges E., Loubet J. L.: *Philos. Mag.*, A 74, 1061 (1996).
3. Fujisawa N., Swain M. V.: *J. Mater. Res.* 21, 708 (2006).
4. Menčík J., Rauchs G., Bardon J., Riche A.: *J. Mater. Res.* 20, 2660 (2005).
5. Chudoba T., Richter F.: *Surf. Coat. Technol.* 148, 191 (2001).
6. Ngan A. H. W., Tang B.: *J. Mater. Res.* 17, 2604 (2002).
7. Lee E. H., Radok J. R. M.: *J. Appl. Mechanics* 27, 438 (1960).
8. Johnson K. L.: *Contact Mechanics*. Cambridge University Press, Cambridge 1985.
9. Oyen M. L.: *Philosophical Magazine* 86, 5625 (2006).
10. Lu H., Wang B., Ma J., Huang G., Viswanathan H.: *Mechanics of Time Dependent Materials* 7, 189 (2003).
11. Menčík J., He L. H., Swain M. V.: *J. Mech. Behav. Biomed.* 2, 318 (2008).

J. Menčík (*University of Pardubice, Jan Perner Transport Faculty, Pardubice, Czech Republic*): **Determination of Parameters of Viscoelastic Materials by Instrumented Indentation**

Deformation of viscoelastic materials depends on the load magnitude and history. Hardness is not constant, but decreases with the time under load. Universal description of the response is possible by means of rheological models consisting of springs and dashpots. The constants in these models can be obtained from the time course of penetration of an indenter loaded by constant force. In real tests it is also necessary to respect the period of the load increase to the nominal value, and to make a correction of the contact stiffness and area, determined from the unloading curve. The paper explains the principles of instrumented indentation, brings the formulae for indenter penetration into viscoelastic material under increasing and constant load, and describes a practical procedure for measurement and data processing.

LOCAL MICROMECHANICAL PROPERTIES OF CEMENT PASTES

JIRÍ NĚMEČEK

*Faculty of Civil Engineering, Czech Technical University in Prague, Thákurova 7, 166 29 Praha 6, Czech Republic
jiri.nemecek@fsv.cvut.cz*

Key words: cement paste, C-S-H gel, nanoindentation, grid indentation, ESEM

1. Introduction

Cement is the widespread building material whose impact to the environment is enormous. Therefore, investigation of its behavior and proper numerical modelling on all scales is desirable. The overall behavior of any material is directly dependent on the microstructure and its individual phase properties. Modern constitutive models for composite materials try to respect this fact and link the overall material response with its micro-level. The development of various experimental techniques in the past decades made possible to access mechanical properties of various materials at submicron length scales. Nanoindentation plays an important role among them. This technique is based on the direct measurement of the load-displacement relationship. The depth of penetration starts from the level of nanometers. Although, nanoindentation was originally developed and used mainly for studying homogeneous materials like metals, coatings, films, glass, and crystal materials, the evolution of this method allows us to use it also for materials like concrete and other cementitious composites. The major studies can be found^{1,2,6}. However, the interpretation of measured data is more complicated due to the large heterogeneity of cementitious composites. We will focus on cement paste (which is the base material of all cementitious composites) in the following.

2. Testing strategies

In contrast to usual indentation on metals, for example, cement paste is much more complex and also time-dependent material. From the microstructural point of view, cement paste is a heterogeneous material with several material phases. The most important are the hydrated phases (C-S-H gels that exist in two morphologies- high and low density², Portlandite, Ettringite and other minor phases), anhydrous phases (rest of clinker minerals) and porosity. Cementitious materials exhibit also significant creep that can affect evaluation of their elastic properties using standard procedures. This difficulty can be overcome by using long dwelling periods at the peak load. The material properties in this study are assessed for hydrated phases which occupy majority of the specimen volume.

There are basically three testing strategies to assess micromechanical properties of individual phases in a heterogeneous material:

- Producing of large number (grid) of indents that are larger than the characteristic phase dimension with subsequent statistical evaluation of overall material properties of all affected phases that were indented (phase compound).
- Statistical indentation in which indents are produced over a large area but the dimension of a single indent is smaller than the characteristic dimension of individual phase. Subsequent deconvolution techniques can be employed for assessment of the individual phase properties^{3,4}.
- Pointed indentation to a specific material phase with indent dimension smaller than the characteristic dimension of the tested phase. In this case, intrinsic properties of the phase (including intrinsic phase porosity) are obtained.

In this study, all three aforementioned approaches have been used and elastic properties evaluated by Oliver and Pharr method⁵ compared.

3. Test samples

Alite (tricalcium silicate) paste samples were prepared. Water to cement ratio was 0.4. Samples were cured in water in 20 °C for 5 month. High degree of hydration can be supposed for such matured sample. Then the sample was dried and polished to achieve flat surface with the roughness 10–20 nm (RMS measured by AFM over 30×30 μm area).

4. Results

For the first approach (A), a large grid of 100 indents was produced over the hydrated phases of cement paste. Indents lying in anhydrous phases were identified in ESEM and excluded from the study. The final depth of indents was around 700 nm (Fig. 1a) which yielded in the surface dimension around 4 μm. Such indents' dimension affects usually more than one material phase and thus causes a physical homogenization (averaging) of properties. Overall modulus of elasticity for all the affected phases (mainly C-S-H gels and Portlandite) was measured to be 23.3 ± 3.1 GPa.

For the second approach (B), 400 small indents (around 200 nm in depth, Fig. 1a) were produced with mutual distances 5 μm in between. The total area covered by indentation was 100×100 μm. The dimensions of indents was chosen to be below the characteristic phase dimension and therefore measurement provided information on (i) heterogeneity of the material properties and (ii) characteristic (intrinsic) material properties over the studied area. Results of indentation moduli are presented in the form of histogram in Fig. 1b. Several peaks defining mean values of indentation modulus for distinct phases can be found in this histogram from which it

could be possible to deconvolute it^{3,4}. Comparison of the morphology taken in ESEM and the map of moduli is shown in Fig. 2. Very good correlation of the data was achieved. Areas of hard clinkers and their surroundings created by HD C-S-H can be easily recognized.

For the third approach (C), small indents similar to those used in (B) were pointed into one specific cement phase that is usually referred as high-density C-S-H gel². This phase appears specifically around anhydrate clinker grains and it can be recognized in optics or in ESEM like a 5–10 μm rim around (Fig. 3). This pointed indentation resulted in much narrower histogram (Fig. 1b) of indentation moduli. Such a fact proves the existence of a homogeneous-like material phase within the tested length scale. The indentation modulus of this phase was 38.6 ± 2.6 GPa.

5. Summary

It was proved that nanoindentation can be used for assessment of intrinsic phases' properties of cement paste. The direct way of pointed indentation is possible only in some cases provided the phase can be easily distinguished in the microstructure. This was achieved for high-density C-S-H gel for which the elastic indentation modulus was assessed. If the

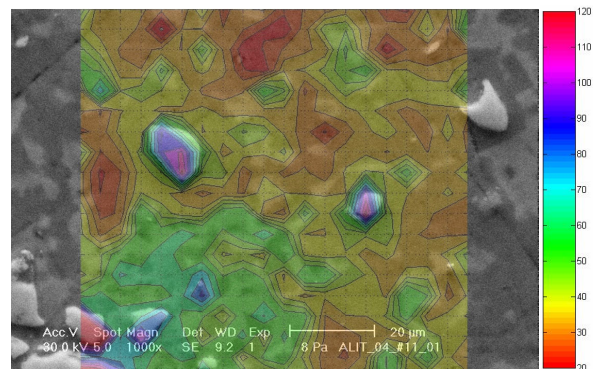


Fig. 2. Map of the indentation modulus placed over the ESEM image of the same area of cement paste

direct measurement is not possible, statistical grid indentation can be used and individual phase properties can be deconvoluted from histogram plotted for all phases. Peaks in the histogram can be attributed to mean properties of individual material phases. For comparison, overall properties of the phase compound can be measured using grids with large indents.

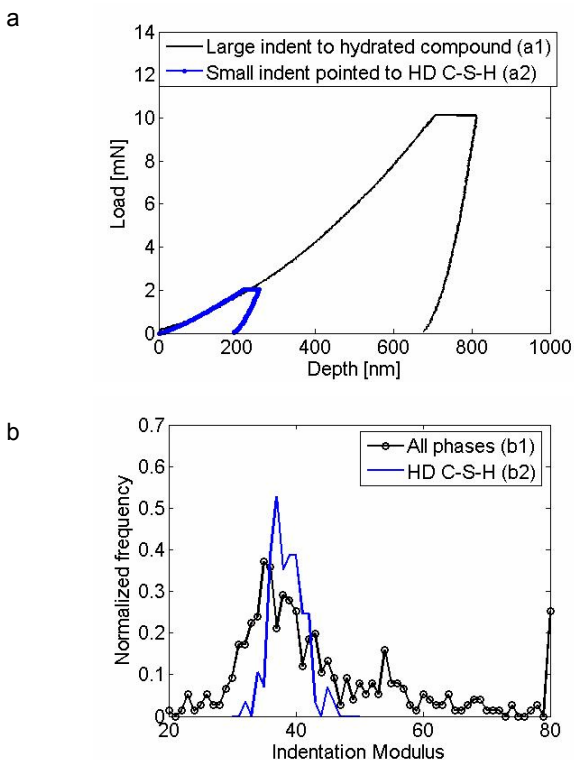


Fig. 1. (a) Load-depth curve for large indent (a1: $P_{\max}=10$ mN) covering all hydrated phases of the cement paste and small indent (a2: $P_{\max}=2$ mN) with the size below the characteristic phase size. (b) Histogram of indentation moduli in GPa. (b1) Measurement over $100 \times 100 \mu\text{m}$ area, (b2) pointed indentation to HD C-S-H

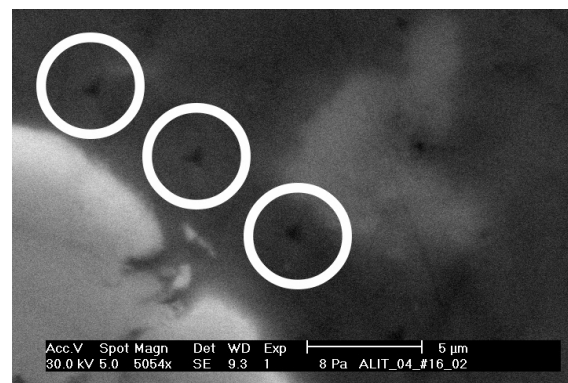


Fig. 3. ESEM image of pointed indentation around clinker grain to HD C-S-H (indents are circled)

Support of the Czech Grant Agency (No. 103/06/1856) and Ministry of Education of the Czech Republic (MSM 6840770003) are gratefully acknowledged.

REFERENCES

1. Constantinides G., Ulm F. J., Van Vliet K.: *Mater. Structures* 36, 191 (2003).
2. Constantinides G., Ulm F. J.: *Cem. Concr. Res.* 34, 67 (2004).
3. Constantinides G., Ulm F. J.: *J. Mech. Phys. Solids* 55, 64 (2007).
4. Constantinides G., Chandran K. S. R., Ulm F. J., Van Vliet K. J.: *Mater. Sci. Eng., A* 430, 189 (2006).
5. Oliver W. C., Pharr G. M.: *J. Mater. Res.* 7, 1564 (1992).
6. Velez K., et al.: *Cem. Concr. Res.* 31, 555 (2001).

J. Němeček (*Faculty of Civil Engineering, Czech Technical University in Prague, Czech Republic*): **Local Micro-mechanical Properties of Cement Pastes**

This paper focuses on experimental investigations of cement paste and its local elastic properties. The paper shows the complexity of cement microstructure and concerns on different approaches used for investigation of such heterogeneous material in submicron length scale. Three approaches are tested and results from nanoindentation and also ESEM are compared. Intrinsic material properties are assessed for high density C-S-H phase. Grid indentation with small indents is used for evaluation of properties for this and other phases. Overall elastic properties are measured for the whole hydrated compound using grid indentation with large indents.

DELAYED DEFORMATION RECOVERY AFTER NANOINDENTATION OF CEMENT PASTE

JIRÍ NĚMEČEK*
and KATEŘINA FORSTOVÁ

Faculty of Civil Engineering, Czech Technical University in Prague, Thákurova 7, 166 29 Praha 6., Czech Republic
jiri.nemecek@fsv.cvut.cz

Keywords: nanoindentation, AFM, delayed recovery, cementitious materials, time dependence

1. Introduction

Hardened cement paste is a heterogeneous material. Several phases can be distinguished at its microlevel. Namely, we can find products of hydration (C-S-H gels, Portlandite and others), unhydrated clinkers and pores. All of them occur at micron and submicron length scale.

Generally, we can distinguish between two types of deformations – reversible (e.g. elastic deformation or temperature change) and irreversible (cracking, chemical shrinkage, other inelastic deformations). All these deformations can be observed and also measured at macrolevel but for all phases' compound. Slightly different situation is at microscale where some deformations, for example cracking, can be easily detected (e.g. by ESEM). Also different material phases can behave very differently. For instance, viscous deformation can be attributed almost purely to hydrated phases (mainly C-S-H gels) while clinkers are mostly elastoplastic. Avoiding some discontinuities (cracking) we can split microlevel deformations to elastic part that is fully reversible, plastic part that is irreversible and causes permanent deformation in time and viscous deformation that is time dependent. The question is how to separate them from microscopic measurements.

Overall microlevel deformations can be successfully measured by nanoindenter at its tip up to full load removal whereas deformations after unloading can be scanned with atomic force microscope (AFM) or other type of scanning probe microscope (SPM). Nanoindentation is the only experimental technique that enables direct measurement of mechanical response of individual material phases at submicron scale even for such heterogeneous system like cement paste¹. In this process a very small tip is brought to the sample surface producing an imprint. Load versus depth of penetration diagram (Fig. 1) is measured through the whole loading, holding and unloading process. Loading and holding parts of the diagram contain elastic, plastic and viscous deformations whereas the unloading part is usually supposed to be elastic and elastic constants are extracted from this part using semi-analytical elastic solutions².

On the other hand, SPM provides exact three-dimensional morphological information of the material surface, (i.e. after indentation, possible fracture surfaces, cracks,

etc.) and can be used to construct delayed recovery of the deformation.

Separation of individual types of the deformation is a difficult task even at microlevel due to complicated stress states under indenter probe during loading. However one can utilize simplified stress state after full unloading. At this stage, the delayed deformation recovery (caused mainly by viscoelastic effects) takes place.

2. Test samples and measurements

Cement paste sample was prepared for this study from ordinary Portland cement CEM I–42.5 with water/cement ratio 0.4. The sample was cured in water for 34 days. Before nanoindentation the sample surface was polished to achieve a flat surface with maximum roughness 10–20 nm. For the sake of comparison, additional measurements were performed on fused silica copper and polyethylene samples.

3. Methods

Nanoindentation was used for performing a single imprint and the final penetration depth (at load release) was taken as a base (time 0) for subsequent considerations. SPM called 'in-situ imaging' was used for surface scanning after the load removal (Fig. 2). 'In-situ imaging' is a patented technology of Hysitron® that uses the same tip (Berkowich in our case) for indentation as well as for surface scanning. Indents were scanned several tens of minutes after the load removal. The evolution of maximum depth was monitored and evaluated in time. Results were normalized with respect to the base depth (at time 0) for comparison purposes. Also final penetration depth was kept similar for all materials (close to 100 nm) for comparisons except for polyethylene (around 500 nm) where a smaller penetration depth was difficult to achieve.

4. Results

Measurements proved the existence of the delayed recovery of the deformation on all samples. As expected, the smallest recovery (almost negligible) was observed on fused silica (Fig. 3). Cement sample evolved strongly in time and the deformation had descending (approximately logarithmic) trend. Similar behavior was found on copper, although the descent was less rapid and deformations stabilized relatively soon (Fig. 3). This could be attributed to the smaller viscous deformation of copper compared to cement paste. It can be supposed that the deformation approaches to the final plastic deformation that is irreversible and that was accumulated in the sample during the whole loading process. Polyethylene was found to have the largest delayed deformation recovery. It might be caused (i) by the viscous nature of the polyethyl-

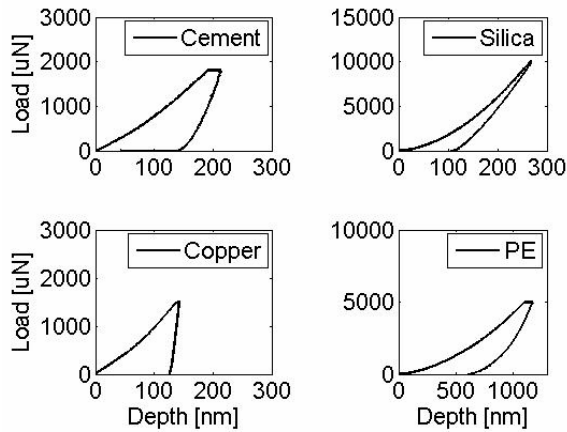


Fig. 1. Load vs. depth diagram from nanoindentation on cement paste, fused silica, copper and polyethylene

ene itself and (ii) by the higher force (and corresponding stress) used for its loading.

5. Summary

The delayed recovery of the deformation after load removal was studied on four materials. It appears that fused silica shows a very little change in deformation and can be considered as almost non-viscous material. In contrast, cement and copper exhibit viscous behavior. For copper, the

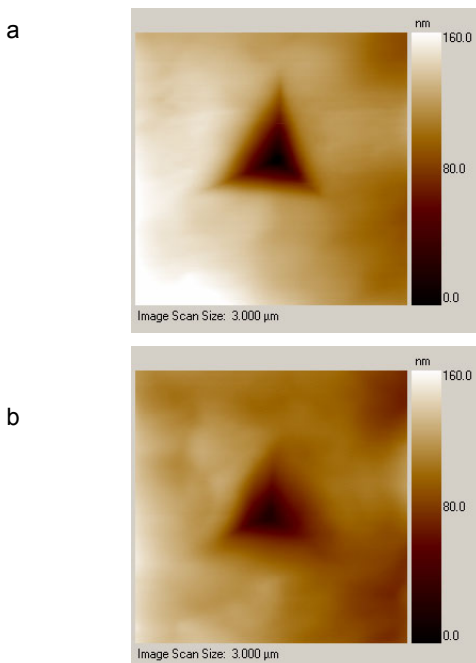


Fig. 2. SPM image of the imprint in time = 146 s (a) and in time = 4772 s after load removal (b) measured on cement sample

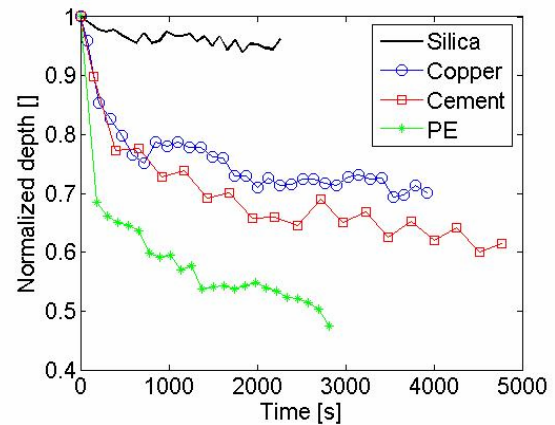


Fig. 3. Comparison of the delayed deformation recovery for fused silica, copper, cement paste and polyethylene after load removal

recovery was smaller and is in the order of minutes to an hour for the given load level. However, for cement sample the evolution of the deformation does not approach to the final value at this time period. This finding points out the higher viscosity of this material. Polyethylene sample was also studied and its behaviour was found to have similar trend like for cement paste but the deformations were more pronounced.

This study is a first step to the further research on cement samples that will lead towards separation of the viscous and plastic deformations and extraction of relevant parameters of constitutive models.

Support of the Czech Grant Agency (No. 103/06/1856) and Ministry of Education of the Czech Republic (MSM 6840770003) are gratefully acknowledged.

REFERENCES

1. Constantinides G., Ulm F. J.: *Mater. Structures* 36, 191 (2003).
2. Oliver W. C., Pharr G. M.: *J. Mater. Res.* 7, 1564 (1992).

J. Němeček and K. Forstová (*Faculty of Civil Engineering, Czech Technical University in Prague, Czech Republic*): **Delayed Deformation Recovery After Nanoindentation of Cement Paste**

In this study, the delayed recovery of the deformation after unloading of indented cement paste was investigated. Comparison with different types of materials (fused silica, copper and polyethylene) was also performed. The aim of the work was to determine how the material deforms after the load release as a stepping stone for separation of viscous and plastic parts of the deformation. Such knowledge is very important for further modeling of nanoindentation and for accessing of inelastic material properties at cement microlevel.

WOOD SURFACE MODIFICATION BY DIELECTRIC BARRIER DISCHARGES AT ATMOSPHERIC PRESSURE

JOZEF RÁHEL^{a,*}, PAVEL ŠTÁHEL^b,
and MÁRIA ODRÁŠKOVÁ^a

^a Univerzita Komenského, Mlynská dolina F2, 842 48 Bratislava, Slovak Republic, ^b Masarykova Univerzita, Kotlářská 2, 611 37 Brno, Czech Republic
rahel@gimmel.ip.fmph.uniba.sk

Keywords: dielectric barrier discharges, wood, activation, deposition, surface energy

1. Introduction

Like other biological materials, wood is susceptible to environmental degradation¹. Interaction of wood with water can lead to dimensional instability and accelerated bio as well as weathering degradation. Because of this, the surface of wood has to be protected to prolong its durability. Majority of paint and wood adhesives are water-based. Water wetting is an important parameter for bond formation. In general wood exhibited a good wettability by water, nevertheless some woods of high lignin content (like oak) are hard to wet. A chemical treatment of the wood surface that promotes better wettability or provides new bonding sites, should improve adhesive bond performance. The same effect can be achieved using the plasma treatment. Majority of tests have been performed at low pressure, however these processes are very cost consuming². This constraint can be overcome by the treatment of plasma generated at atmospheric pressure³, which effect on improving the wetting and adhesion properties of various polymer materials have been extensively studied for last 10 years. The surface activation was carried out using coplanar barrier discharge⁵ in the ambient air to obtain wettable surface suitable for easy painting. Our results in activating the hydrophobic oak surface will be presented in this paper.

By choosing a suitable composition of discharge gas, the hydrophobic surface properties of wood can be obtained too⁴. In presented study, plasma assisted deposition of hydrophobic coatings was performed directly on the surface of poplar veneer by surface barrier discharges at atmospheric pressure from the mixture of nitrogen containing HMDSO vapors. We will present these results as well.

2. Experimental

For hydrophobization study the samples of poplar veneer with dimension 700 × 130 × 0.5 mm were used. The sample surface was sanded by sandpaper of 150-grit.

Plasma activation study (creating a hydrophilic surface) was performed on oak heartwood samples with the dimensions of 50 × 15 × 5 mm. The oak was chosen because of its

known low surface energy (36.1 mJ m⁻²) resulting in poor water wettability.

The deposition of thin hydrophobic layer was carried out by surface barrier discharge (SBD) at atmospheric pressure⁶. The surface discharge was created on the surface of the mica dielectric plate, fully covered with metal electrode on one side. The opposite side of the mica plate was in contact with metal electrode consisting of 11 connected rotating rods of 9 mm. The rods were 10 cm long. The whole arrangement was placed in deposition chamber. The SBD electrodes were energized by 5 kHz sinusoidal high voltage generator LIFETECH VF 700. The poplar veneer strip was drawn with controlled speed through the chamber between the metal electrodes and the dielectric mica plate. The discharge appeared along the substrate surface in the decreasing initial electric field from the side of the rod metal electrodes. The surface power density was kept at 1.1 W cm⁻² in all cases. Configuration of the reactor is shown in Fig. 1.

The layers were deposited from mixture of nitrogen with different amount of hexamethyldisiloxane (HMDSO) vapors. The flow rate of nitrogen was kept at 6 l min⁻¹ in this study and the HMDSO flow rate varied between 0.06 and 0.4 g min⁻¹ in order to optimize the coating properties. Plasma activation of wooden samples was done by the coplanar surface barrier

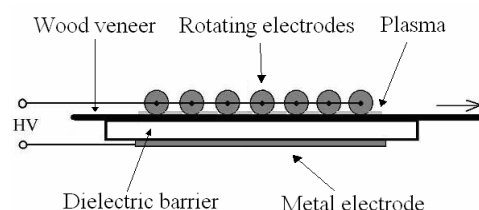


Fig. 1. Scheme of deposition reactor based on Surface Barrier Discharge

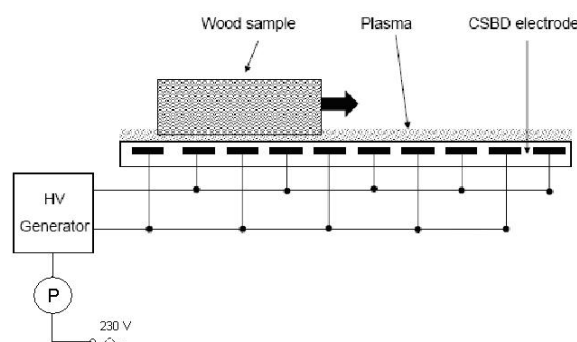


Fig. 2. Scheme of the reactor based on Coplanar Surface Barrier Discharge

discharge⁵. The coplanar surface barrier discharge electrodes consisting of 15 pairs of silver strip electrode embedded 0.5 mm below the surface of 96 % Al₂O₃ ceramics were energized by 14 kHz sinusoidal voltage, supplied by HV generator LIFETECH VF 700. The mutual distance of the 200 mm long and 2 mm wide silver strip electrodes was 1 mm. The electrode system was mounted inside the closed reactor chamber equipped with a moving sample holder (Fig. 2).

The surface of oak samples was sanded by sandpaper of 150-grit before the surface energy measurement and by 100-grit before the water uptake time measurement. Wood samples were mounted to the moving sample holder and conveyed to the intimate contact with the plasma generated above the ceramics surface. Plasma activation was done in ambient air with an average plasma power density 2.2 W cm⁻² and exposure time of 5 s. The wood moisture content was within the range of 7–8 % in all cases.

The surface properties of plasma treated and untreated wooden samples were investigated by means of the sessile drop technique using the Surface Energy Evaluation System (SEE System, <http://www.seesystems.wz.cz>). The contact angles were measured directly from the images of the solid/liquid meniscus of a liquid drop set on a solid surface taken with CCD camera. The value of wood total surface free energy γ_s and its disperse γ_s^d and polar γ_s^p components was calculated by means of Owens-Wendt method⁶ expressed as:

$$(1 + \cos \Theta) \gamma_L = 2\sqrt{\gamma_L^d \gamma_s^d} + \sqrt{\gamma_L^p \gamma_s^p}$$

were Θ is the contact angle of the test liquid with the sample, γ_L is total surface energy of the test liquid, γ_L^d is dispersion component and γ_L^p is polar component of the testing liquid. γ_s^p and γ_s^d are dispersive and polar components of the surface energy of the tested sample. In the case of characterization of hydrophobic coatings deposited in SBD the contact angle was measured with following testing liquids: water, glycerol, ethylene glycol, formamide, diiodomethane, α -bromonaphtalene. In the case of characterization of plasma activated samples the contact angle was measured with water, diiodomethane and α -bromonaphtalene. Water is a representative of polar liquid, diiodomethane and α -bromonaphtalene are non-polar testing liquids. Two combinations of water + diiodomethane and water + α -bromonaphtalene were used as a test liquid pairs for evaluation of surface free energy of activated samples using Owens-Wendt method.

The water uptake time was measured as the time from the impact of the droplet to its complete penetration into the wood surface (no optical reflection can be seen). For this test one half of each wooden sample surface was activated by plasma while the second half was left untreated. The water droplet of 50 μ l was put on the plasma activated part of sample and second one on untreated part of oak surface. According to the method described⁷ the uptake time was evaluated for 15 oak samples.

3. Results

Highly hydrophobic thin layers were deposited on the

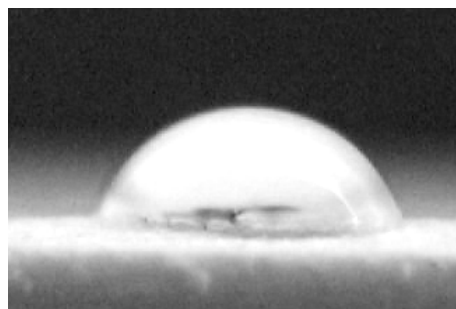


Fig. 3. Water droplet on the surface untreated poplar veneer

poplar veneer surface in order to protect it against water penetration. Organosilicon monomer (HMDSO) mixed with nitrogen was used as a working gas during the plasma deposition to create protective hydrophobic layer. Water droplet on untreated poplar veneer surface is shown in Fig. 3. After the plasma deposition the contact angle increased from 63° to 120° which proves the hydrophobic nature of deposited layer (see Fig. 4). The concentration of monomer and also deposition time were varied to obtain optimal deposition conditions and also surface properties. Fig. 5 shows the total surface free energy as a function flow rate of HMDSO. Total surface free energy exponentially decreases with increasing monomer flow rate. The most hydrophobic layer were deposited when the deposition time was 120 s. Fig. 6 shows the total surface energy and its polar and dispersion part as a function flow rate of HMDSO. In this case the deposition time was 42 s. The dispersion component quickly decreases with the increasing flow rates HMDSO, however polar part remains almost constant. Similar behavior was obtained also for samples with different deposition times.

The results of plasma activated oak surfaces are summarized in Tab. I. The value of total free surface energy increased from 40 to 74 mJ m⁻², mainly due to the rise of its polar component. The results of water uptake time measurement are shown in Tab. II.

The uptake time reduced from 675.8 to 61.5 s after the plasma treatment, the mean relative reduction of uptake time was 88 ± 7 %. Our result is in the same order of magnitude as those declared⁷. Fig. 7 shows a plane view of the treated (left sample) and untreated (right sample) oak samples 10 s after the dropping of water droplet on sample surface. Water wets

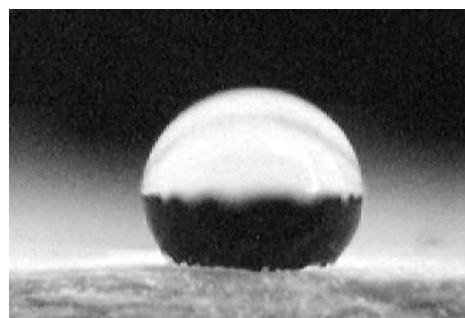


Fig. 4. Water droplet on the poplar veneer after coating

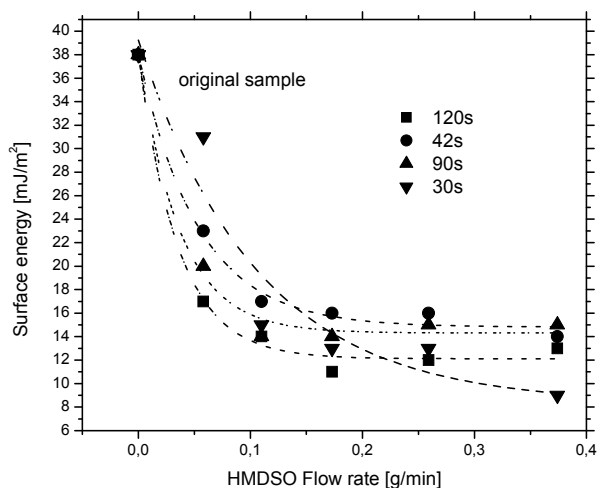


Fig. 5. Total surface free energy as a function of HMDSO flow rate. Flow rate of nitrogen 6 l min^{-1} was kept constant in all cases

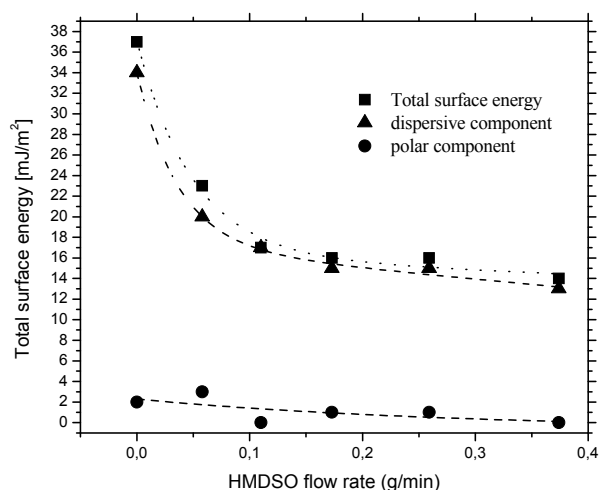


Fig. 6. Total surface free energy γ^{tot} and its dispersive γ^{d} and polar γ^{p} parts a function of HMDSO flow rate. Flow rate of nitrogen 6 l min^{-1} was kept constant in all cases

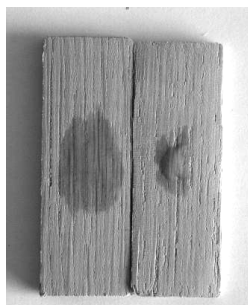


Fig. 7. Plane view on plasma treated (left) and untreated (right) oak samples 10 s after placing $50 \mu\text{l}$ water droplet on the surface

Table I

Total surface free energy γ^{tot} and its dispersive γ^{d} and polar γ^{p} parts of oak surface (in radial section) before and after the plasma treatment

Testing liquid	Water and diiodomethane		Water and α -bromonaphtalene	
[mJ m^{-2}]	original	activation	original	activation
γ^{tot}	40.71	74.26	42.36	73.80
γ^{d}	39.56	45.40	41.40	44.43
γ^{p}	1.15	28.26	0.96	29.37

Table II

Water uptake time of plasma activated (T_{A}) and untreated (T_0) oak in radial section

	Untreated oak T_0 [s]	Treated oak T_{A} [s]	$(1 - T_{\text{A}} / T_0) 100$ %
1	317	56	82
2	1850	90	95
3	606	45	93
4	231	42	82
5	949	75	92
6	379	61	84
7	1072	90	92
8	1190	41	97
9	154	45	70
10	1421	61	96
11	1078	84	92
12	333	54	84
13	463	68	85
14	443	47	89
15	501	65	87
Mean	732.6	61.5	88 ± 7

preferentially in direction of the surface capillaries.

Comparing the energy consumption⁷, system based on volume barrier discharge needs 0.1 kWh m^{-2} , however system based on DCSBD, needed only about 0.03 kWh m^{-2} of wood surface. The system based on DCSBD offers a considerably better efficiency. Moreover the plasma treatment in DCSBD is completely independent on the thickness and electrical conductivity of the treated wood material.

Highly hydrophobic plasma polymer coatings were deposited on the wood substrate in surface barrier discharge from the mixture of HMDSO monomer with nitrogen. The total surface free energy of sample decreased from 37 mJ m^{-2} before coating wood to about $12\text{--}17 \text{ mJ m}^{-2}$ (after the plasma deposition).

The plasma activation of wooden surfaces in diffuse surface barrier discharge was tested. The total surface energy increased from 40 to 74 mJ m^{-2} after plasma treatment.

The plasma activation of wood in DCSBD promotes a better adhesion and efficiency than competitive systems.

This research has been supported by Ministry of Education, Youths and Sports of the Czech Republic under project MSM0021622411 and by Academy of Science of the Czech Republic by KAN101630651.

REFERENCES

1. Denes A. R., Young R. A.: *Holzforschung* 53, 632 (1999).
2. Denes A. R., Tshabala M. A., Rowell R., Denes F., Young R. A.: *Holzforschung* 53, 318 (1999).
3. Podgorsky L., Bousta C., Schambourg F., Maguine J., Chevet B: *Pigm. Resin Tech.* 31, 33 (2001).
4. Bente N., Avramidis G., Forster S., Rohwer E. G., Viol W.: *Holz als roh-und werkstoff* 62, 157 (2004).
5. Simor M., Rahel J., Vojtek P., Cernak M.: *Appl. Phys. Lett.* 81, 2716 (2002).
6. Rehn P., Wolkenhauer A., Bente M., Forster S., Viol W.: *Surf. Coat. Technol.* 174, 515 (2003).
7. Bursikova V., Stahel P., Navratil Z., Bursik J., Janca J.: *Surface energy evaluation of plasma treated materials by contact angle measurement.* Masaryk University, Brno 2004.

J. Ráhel^a, P. Stáhel^b, and M. Odrášková^a
(^a *Univerzita Komenského, Bratislava, Slovak Republic;*
^b *Masarykova Univerzita, Brno, Czech Republic*): **Wood Surface Modification by Dielectric Barrier Discharges at Atmospheric Pressure**

The effect of plasma treatment at atmospheric pressure on surface properties of wooden samples is investigated in this work. Plasma activation of wooden surface was studied in diffuse coplanar surface barrier discharge created in air to obtain wettable surface. Plasma deposition of hydrophobic coatings directly on the surface of wooden materials using surface barrier discharge created in pure nitrogen with small admixture of hexamethyldisiloxane was investigated too. Surface properties of plasma treated wooden samples were studied using the sessile droplet technique to identify surface free energy of treated and untreated samples.

DEPOSITION AND CHARACTERIZATION OF THIN HYDROPHOBIC LAYERS USING ATMOSPHERIC-PRESSURE SURFACE BARRIER DISCHARGE

PAVEL ŠTAHEL*, **VILMA BURŠÍKOVÁ**,
JAN ČECH, **ZDENĚK NAVRÁTIL**, and
PETR KLOC

Masarykova Univerzita, Kotlářská 2, 611 37 Brno, Czech Republic
pstahel@physics.muni.cz

Keywords: surface barrier discharge, hydrophobic layers

1. Introduction

The plasma technologies became very promising technique for surface engineering of solids. The wide spread low-pressure plasma applications^{1–7} have to use expensive vacuum systems. That approach requires batch processing and inhibits the application of low-pressure plasma in larger industrial scale for treatment of low-cost materials, where in-line treatment of materials is necessary.

Several advantages of the surface modification of low-cost materials provide atmospheric-pressure plasma processing. The most significant advantages are: the expensive vacuum system is not necessary, processing times are reduced, and the scalability of plasma applications towards large-surface processing is simpler than in low-pressure plasma applications.

Recently, mainly atmospheric-pressure corona discharge or volume barrier discharge (VBD) devices are used for surface treatment of polymeric materials. In the case of VBD the requested plasma conditions are achieved only in small-volume plasma channels – streamers – developing perpendicularly to the surface of material. In that case the plasma is in a very limited contact with the surface resulting in low processing speeds, typically in the order of 1 m min^{-1} . Moreover, the localized arcing may result in the formation of pinholes in the material being treated. The using of atmospheric-pressure glow discharge (APGD) can surpass these disadvantages, however APGD is very sensitive to gas purity and optimization of electrode arrangement. These facts limit the applicability of APGD⁸.

In this work the surface barrier discharge operated at atmospheric pressure was used for deposition of thin protective hydrophobic films on paper substrates.

This work has to demonstrate good protective properties of the films deposited by means of this technique. Variation of colorimetric parameters of paper substrates such as whiteness or yellowness caused by plasma deposition and the evolution of these parameters under intensive UV irradiation is shown too.

2. Experimental

The fluorinated (Teflon-like) materials are widely used for their low surface energy and low wettability. As precursor for thin film deposition the octafluorocyclobutane C_4F_8 was used. The CF_4 (ref.⁷) or fluorotrimethylsilane⁸ are reported in the literature as precursors too. The surface barrier discharge at atmospheric pressure was used for the deposition process. The discharge was ignited on the surface of the insulating mica plate, which was fully covered with metal electrode from one side, while the opposite side of the plate was covered with moving paper sample pressed to mica with rod electrode. The rod electrode consists of nine 100 mm long rotating rods, connected together with 9 mm spacing⁹. Between each two rods of the electrode two gas inlets were placed. The whole arrangement was placed into deposition chamber. The paper strips were carried through the discharge chamber with controlled speed. The surface power density was set within the range 0 to 1.0 W cm^{-2} . In this study the deposition time 90 s was kept constant as well as the concentration of C_4F_8 in nitrogen, i.e. 0.5 slpm of C_4F_8 in 10 slpm of pure nitrogen. As a substrate the filter paper was used. The discharge was studied by means of the optical emission spectroscopy. The discharge spectra were recorded using the Jobin-Yvon TRIAX 550 monochromator, equipped with the liquid nitrogen cooled CCD detector. The total surface free energy of samples γ^{TOT} and its components γ^{LW} , γ^{AB} , γ^+ , γ^- were investigated by means of the sessile drop technique using the Surface Energy Evaluation System (<http://www.advex-instruments.cz/>). The contact angles were measured directly from the CCD camera images of the solid/liquid meniscus of a sessile drop set on a solid surface. The samples surface free energy and its components were calculated according to Lifshitz-Van der Waals/acid base approach reported in¹⁰. UV irradiation degradation tests were performed in device equipped by high-pressure Hg lamp with 40 mW cm^{-2} . The temperature of samples during degradation tests was kept constant ($40 \text{ }^\circ\text{C}$). The wetting properties were studied by means of industrial grade permeability tests consistent with the ISO 9073-8:1995 standard. Chemical composition of deposited films was investigated by means of infrared spectroscopy.

3. Results

In the past we have reported on the formation of hydrophobic protective films on paper surfaces to make it resistant against water penetration¹¹.

A typical spectrum of the discharge created in mixture of nitrogen and C_4F_8 is shown in Fig. 1.

The spectrum is plotted in the range 300–500 nm, because above 500 nm only the second spectral order was registered. The spectra consist of the molecular bands of second positive system of nitrogen ($\text{C } ^3\Pi_u \rightarrow \text{B } ^3\Pi_g$). In case of octafluorbutane admixture intensive bands of CN violet system

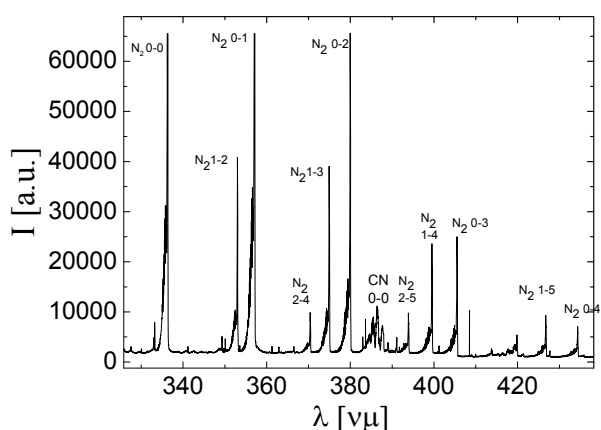


Fig. 1. Emission spectrum of the surface discharge created in nitrogen with admixture of C_4F_8

(${}^2\Pi \rightarrow {}^2\Sigma$) at 388 nm and 422 nm were observed. The vibrational temperature was calculated from the bands of second positive system of nitrogen ($\Delta v = -2$, heads 0–2, 1–3 and 2–4). The vibrational temperature varied only slightly with discharge power density variation and its estimated value was at about 2100 K in all cases. Fig. 2 shows dependencies of the whiteness W and yellowness Ye of samples in their as-deposited state as a function of the discharge power density.

Solid lines are used as a guide of eyes. Yellowness of the sample increases and whiteness decreases with increasing discharge power density. Sample colour slightly changes, however changes are caused not only by creation of film on the surface but also by thermal and UV degradation of substrate during the deposition process. The electrodes were heated by the discharge and were not cooled with any external cooling system. The electrode temperature was different for different power densities – at higher power density the temperature of electrode was higher.

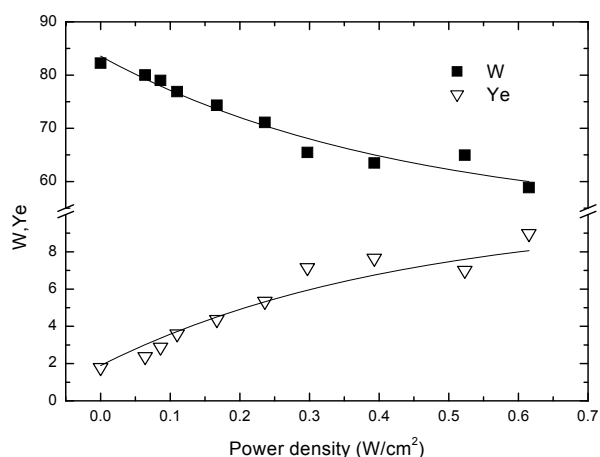


Fig. 2. Dependence of the whiteness W and yellowness Ye of as deposited samples on the power density. Solid lines represent exponential decrease fit

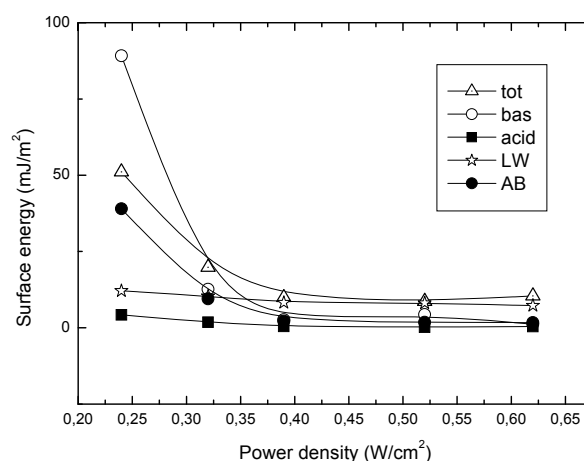


Fig. 3. Dependence of total surface energy γ^{TOT} and its components γ^{LW} , γ^{AB} , γ^+ , γ^- plotted as a function of power density

In Fig. 3 the dependence of total surface energy γ^{TOT} and its components γ^{LW} , γ^{AB} , γ^+ , γ^- is plotted as a function of power density. Samples deposited at higher power density than 0.35 W cm^{-2} show similar surface hydrophobic properties, however samples deposited at lower power density exhibit high surface energy.

In these cases surface properties are more in virtue of plasma treatment than deposition of teflon-like surface layer.

The untreated sample is shown as reference and it is rather different than samples after thin film deposition i.e. surface of the untreated sample and sample deposited at the lowest power density is polar, however surface of coated sample is non-polar.

In Fig. 4 the variation of colorimetric parameters under UV irradiation is shown. For degradation test we used high pressure Hg lamp with 40 mW cm^{-2} . Whiteness of uncoated samples strongly decreases with increasing UV irradiation time. Samples coated with Teflon-like film exhibit significantly lower degradation than uncoated sample. Samples deposited at lower power densities exhibit less protective properties than samples deposited at higher power densities. Yellowness Ye shows also similar behavior.

4. Conclusion

Thin films of highly hydrophobic properties were prepared by means of atmospheric-pressure surface barrier discharge deposition technique. The films were prepared using different power densities from the mixture of octafluorocyclobutane – C_4F_8 with nitrogen.

The colorimetric parameters as whiteness and yellowness of samples in their as-deposited and UV irradiated states were studied. The coated samples exhibited considerably higher UV irradiation resistance than the uncoated ones. It is possible to use similar type of films as hydrophobic, transparent and highly effective UV irradiation protective coating on different kind of solids.

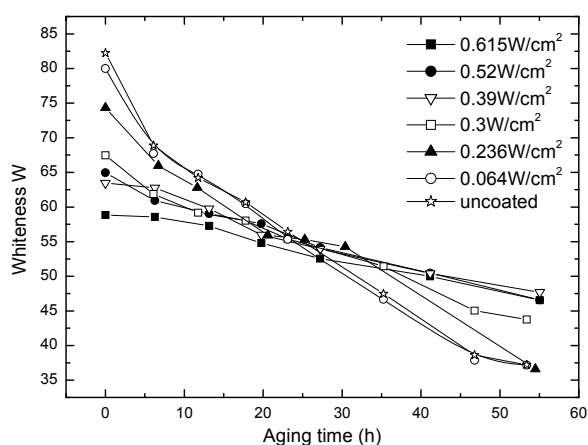


Fig. 4. Aging effect of samples under UV irradiation. Samples were deposited at different discharge power densities

This research has been supported by Ministry of Education, Youths and Sports of the Czech Republic under project MSM0021622411 and the Grant Agency of the Academy of Sciences of the CR under project KAN 101 63 0651.

REFERENCES

1. Denes A. R., Young R. A.: *Holzforschung* 53, 632 (1999).
2. Hua Z. Q., Sitaru R., Denes F., Young R. A.: *Plasmas and Polymers* 2, 196 (1998).
3. Behnisch J.: *Plasma Processing of Polymers*, In: R. d'Agostino, P. Favia, F. Fracassi (ed.), *Plasma Processing of Polymers*, *NATO ASI Series*. 346, 345 (1996).
4. Mahlberg R., Niemi H. E. M., Denes F., Rowell R. M.: *Int. J. Adhesion* 62 *Adhesives* 18, 283 (1998).

5. Sahin H. T., Monolache S., Young R. A., Denes F.: *Cellulose* 9, 171 (2002).
6. Navarro F., Davalos F., Denes F., Cruz L. E., Young R. A., Ramos J.: *Cellulose* 10, 411 (2003).
7. Belgacem M. N., Blayo A., Gandini A.: *J. Colloid Interface Sci.* 182, 431 (1996).
8. Prat R., Koh Y. J., Babukutty Y., Kogoma M., Osakazaki S., Kodama M.: *Polymer* 41, 7355 (2000).
9. Sřahel P., Burřiková V., Šira M., Navrátil Z., Kloc P., Janča J.: *J. Adv. Oxid. Technol.* 2, 228 (2006).
10. Good R. J.: *Contact Angle, Wettability and Adhesion* (K. L. Mittal, ed.) 3 (1993).
11. Burřiková V., Sřahel P., Janča J.: *Czech. J. Phys.* 52, D866 (2002).

P. Sřahel, V. Burřiková, J. Čech, Z. Navrátil, and P. Kloc (*Masarykova Univerzita, Brno, Czech Republic*): **Deposition and Characterization of Thin Hydrophobic Layers Using Atmospheric-Pressure Surface Barrier Discharge**

The modern technologies often require modification of solid material surfaces with keeping desired bulk properties. To control the surface properties of solids the atmospheric-pressure plasma can be very useful. In this work the thin hydrophobic protective films were deposited on the paper surface using atmospheric-pressure surface barrier discharge. Films were deposited from the mixture of the nitrogen with C₄F₈. The plasma properties were investigated by means of optical emission spectroscopy. The properties of samples were investigated by means of colorimetric measurements such as whiteness, yellowness or brightness tests. The surface energy of the thin films was investigated by means of contact angle measurements. The sample properties were measured in as-deposited state and in UV-exposed state.

MECHANICAL PROPERTIES OF THIN FILMS DEPOSITED BY TVA AND G-TVA METHODS

**ADRIAN STOICA^a, RODICA VLĂDOIU^b,
GEAVIT MUSA^b, VICTOR CIUPINĂ^b,
MIRELA CONTULOV^b, VILMA
BURŠÍKOVÁ^a, and OLGA BLÁHOVÁ^c**

^a Department of Physical Electronics, Faculty of Science, Masaryk University, Kotlářská 2, 611 37 Brno, Czech Republic, ^b Department of Physics, Ovidius University, 124 Mamaia Av., 900527 Constanța, Romania, ^c University of West Bohemia Plzeň, Czech Republic
stoica@mail.muni.cz

Keywords: Thermionic Vacuum Arc, Gaseous Thermionic Vacuum Arc, DLC coatings, nanoindentation

1. Introduction

Studies of discharges in the anodic vapors are founded on the discovery of new types of discharge, which can be produced in vacuum conditions in the vapors of any materials. Thermionic Vacuum Arc (TVA) can generate intense plasma in the vapors of the evaporating anode material¹. Even intense plasma of the refractory materials is obtained easily. Due to their high melting points, instead of crucible, as anode are used rods of refractory materials. Few other technologies can compete with TVA thin film deposition of materials like C, W, Mo, Nb, Ta, Re, etc.^{2–5}. Peculiar to the Thermionic Vacuum Arc (TVA) is the fact that it is generating its own neutral atoms in a continuous manner maintaining an equivalent pressure in which a low voltage arc type discharge takes place.

One of the most convenient fields of application of TVA thin film deposition technique is the nanostructured carbon thin films synthesis. In fact, due to the high variety of the obtained structures of the carbon (not mentioning the huge number of applications) we are encountering a new field of science.

The extension of Thermionic Vacuum Arc technology to coatings using gases or evaporable liquids instead of solid materials is of great interest, the number of materials used for TVA deposition could dramatically increased.

2. Experimental systems

The Thermionic Vacuum Arc (TVA) is a heated cathode vacuum arc discharge in the vapors of the anode material in high vacuum conditions. The electrons, emitted from a heated tungsten cathode, are accelerated towards the anode, by a d.c. high voltage applied across the electrodes. This type of arc offers the unique opportunity to generate energetic ions, with a controlled value of the directed energy, which are bombarding the condensing thin film on the substrate. The ions are just

those of the depositing atoms on substrate^{6,7}. In this way the substrate bombarding ions are generated just from the atoms of the depositing material, no any other gas being present in the vacuum chamber during the process.

The experimental arrangement used for Thermionic Vacuum Arc (TVA) electrodes configuration is shown in Fig. 1. There is no cooling system for either the anode or the cathode, because it is important to avoid as much as possible any cooling of the electrodes, in order to minimize the energy loss in the deposition process.

This discharge can be established in vacuum between a heated cathode and a anode mounted at a small distance in front of cathode. For convenient applied d.c. voltage across the cathode and anode, a melted spot appears on the anode surface and a continuous evaporation of the anode material from this melted spot is established due to the accelerated electrons emitted from the cathode and incident on anode. Consequently, in vacuum, a steady state density of the metal vapors appears in the interelectrode gap. The value of the equivalent pressure of the metal vapors depends mainly on the power of the accelerated electron beam from the cathode.

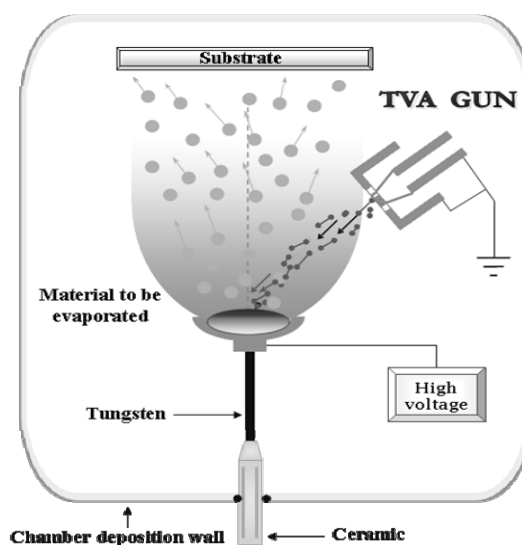


Fig. 1. Thermionic Vacuum Arc experimental set-up

At further increase of the applied high voltage, suddenly a bright discharge appears in the interelectrode space in the vapors of the anode material, with a simultaneous decrease of the voltage drop over the electrodes and with a significant increase of the current. Since the cathode of TVA is at earth potential and vacuum vessel also, it results that the plasma has a potential accelerating ions towards against the vacuum vessel wall. This potential is roughly equal with the cathode potential fall (see Fig. 2).

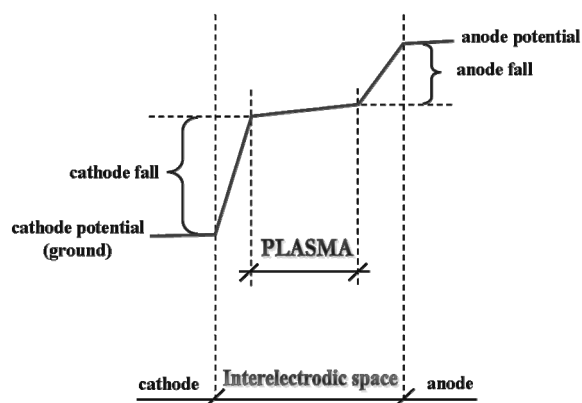


Fig. 2. Potential distribution in the cathode–anode space

In these circumstances, besides the evaporated neutral atoms, on the sample are also incident energetic ions. So, the thin film is growing under the bombardment of ions of the material to be deposited. This is a major advantage in obtaining high purity thin films because the discharge is ignited in vacuum and the film is bombarded during its growing with own atoms which are ionized⁸.

TVA technology offers following advantages for thin layer depositions: high rate of evaporation up to 100 nm s^{-1} ; no buffer gas is necessary; very low thermal energy transfer; deposited thin film layers are smooth, compact and of very fine structures; very stable discharge conditions; no cathode impurities can be found in deposited thin films; low mechanical stress of the deposited layer and very good adherence.

The second new type of discharge – Gaseous Thermionic Vacuum Arc (G-TVA) consists from a heated thermionic cathode (as in the case of TVA) while the anode is a disk type sintered powder piece tightly bounded to a stainless steel tubing connected adequately to the gas supply bottle (Fig. 3). The anode consists from a stainless-steel piece with a diameter of 16–25 mm, provided with a tubing necessary to connect this anode to an out vacuum chamber gas sources. Inside of the hole of the stainless steel piece is mounted a disk of sintered metal powder with an average size of $100 \mu\text{m}$.

The most important part of the experimental arrangement is the gas inlet, which is provided with a special sieve capable of limiting and simultaneously spreading spatially the flow of gas. Thus, a high pressure gradient is obtained between the end of the gas inlet and the chamber walls.

A peculiarity of the G-TVA discharge is the critical value of the interelectrode distance. Indeed, for small distance, a cold cathode discharge can ignite. For distances higher than this critical distance we will have a real G-TVA discharge because only if the cathode is heated the discharge can ignite. In this case, the G-TVA discharge is sustained by the thermo-electron emission current from the cathode. The Gas-TVA is the only deposition method using precursor material in the gas state that forms localized plasma in vacuum. This is a very important feature of the technique, as the substrate material can be placed away from the plasma, thus avoiding overheating.

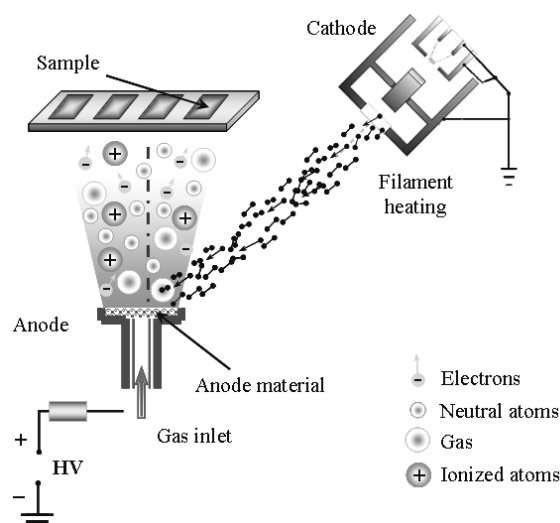


Fig. 3. Schematically configuration of the electrodes in the case of G-TVA

3. Results on mechanical properties

The mechanical properties of carbon thin film were studied using two different types of indentation methods: the depth sensing indentation test (DSI) based on analysis of the loading/unloading hysteresis (Fischerscope H100 equipped with a Vickers four-sided diamond pyramid) and the continuous stiffness measurement (CSM) method (NanoIndenter XP Berkovich with three-sided diamond pyramid). The continuous stiffness measurement system applies a load to the indenter tip to force the tip into the surface while simultaneously superimposing an oscillating force with the force amplitude generally several orders of magnitude smaller than the nominal load. Material properties are determined continuously as the indenter moves into the surface, eliminating the need for unloading cycles.

The studied carbon films were deposited on silicon or

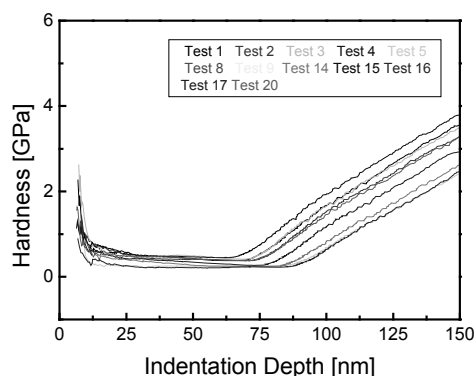


Fig. 4. The dependence of the hardness of 75 nm thin polymer-like carbon film on silicon substrate prepared using G-TVA method

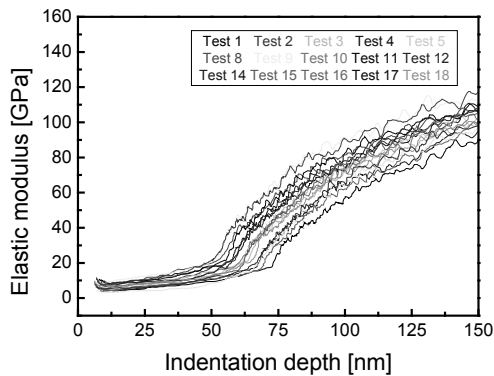


Fig. 5. The dependence of the elastic modulus of 75 nm thin polymerlike carbon film on silicon substrate prepared using G-TVA method

glass substrates. The indentation tests were made at several different depths from near surface through film-substrate interface up to bulk of the substrate. This enabled us to obtain information about the indentation response of the whole film-substrate in a wide range of testing conditions. An example of the indentation response of soft polymer-like carbon film deposited on silicon substrate using the G-TVA method is shown in Figs. 4 and 5. The results were obtained by the continuous stiffness measurement (CSM). At least 20 tests were made at different places on the samples. The reproducibility of the obtained material parameters evidenced the good homogeneity of the prepared films. However, the film thickness was in the range from 70 to 80 nm as it can be seen from the abrupt change on hardness curves. In case of a soft film on relatively hard substrate, the measured hardness is not significantly influenced by the substrate hardness up to 50 % of the film thickness. In case of the elastic modulus this value is lower, it is approximately 20 %.

The described methods enable to prepare carbon films with wide range of mechanical properties. The second example shows results obtained on hard carbon film deposited by the TVA method. The loading-unloading curves obtained on

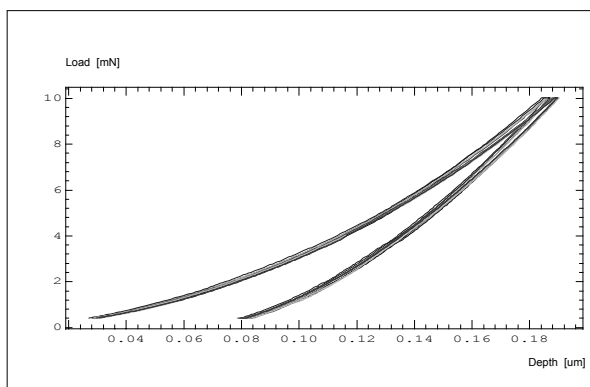


Fig. 6. Loading-unloading dependences obtained at maximum load of 10 mN on DLC film prepared using TVA method

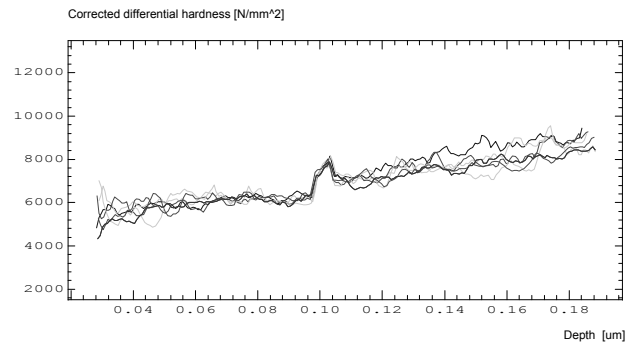


Fig. 7. Differential hardness dependences on the indentation depth obtained on DLC film prepared using TVA method

hard diamond-like film using the depth sensing indentation technique are shown in Fig. 6. The loading-unloading curves were well reproducible proving the surface homogeneity of the films.

We studied also the dependence of the differential hardness on the indentation depth. The differential hardness H_{dif} is given by the relation

$$H_{\text{dif}} = \frac{\partial L}{\partial A} = \frac{\partial L}{k \partial (h^2)} \quad (1)$$

where L is the applied load, A is the contact area between the indenter and the film material, k is geometric constant and h is the indentation depth. H_{dif} represents the ratio of the small load increase and the corresponding change in contact area (in case of Vickers indenter it is given simply by the product of geometric constant k and the square of the given indentation depth h). This value is very sensitive to any changes in the tested material.

The differential hardness dependence (Fig. 7) showed us, that the hard DLC films contain two parts with slightly different properties. The abrupt jumps on the differential curves are related to the boundary between these two parts created by change in conditions during the deposition.

4. Conclusions

DLC films were successfully prepared by the new method (G-TVA) using CH_4 as precursor. The technique is based on the ignition of cathodic arc plasma in the vapors of the material of interest, similar to the Thermionic Vacuum Arc (TVA) method. The results confirm our initial hypothesis that G-TVA might be a useful tool for high quality thin film depositions.

The G-TVA extends the applicability of the classical TVA technique to the deposition of thin films from gas precursors.

It was demonstrated the capability of the Gas-TVA technique to produce adherent, hydrogenated DLC films of relatively high sp^3 content.

The G-TVA deposition technique has opened up a new area of research for the synthesis of new materials. Further work on plasma diagnosis and also on surface characterization of the films obtained using this technique is envisaged.

REFERENCES

1. Musa G., Surdu Bob C., Lungu C. P., Ciupina V., Vlădoiu R.: *J. Optoelectronics Adv. Mater.* 9-4, 867 (2007).
2. Vlădoiu R., P.Lungu C., Mustata I., Bursikova V., Bursik J.: *J. Optoelectronics Adv. Mater.* 9-4, 1087 (2007).
3. Surdu-Bob C., Musa G., Buck V., Mustata I., Filipov O., Poukhovoi A.: *J. Optoelectronics Adv. Mater.* 9-8, 2657 (2007).
4. Surdu-Bob C., Musa G., Vlădoiu R., Lungu C. P.: *J. Optoelectronics Adv. Mater.* 9-8, 2660 (2007).
5. Musa G., Mustata I., Ciupina V., Vlădoiu R., Prodan G., Vasile E., Ehrich H.: *Diamond Related Mater.* 13, 1398 (2004).
6. Musa G., Mustata I., Blideran M., Ciupina V., Vlădoiu R., Prodan G., Vasile E., Ehrich H.: *Acta Phys. Slovaca* 55-4, 417 (2005).
7. Musa G., Mustata I., Blideran M., Ciupina V., Vlădoiu R., Prodan G., Vasile E.: *J. Optoelectronics Adv. Mater.* 5-3, 667 (2003).
8. Musa G., Ehrich H., Mausbach M.: *J. Vac. Sci. Technol.* 12(5), (1994).

A. Stoica^a, R. Vlădoiu^b, G. Musa^b, V. Ciupina^b, M. Contulov^b, V. Buršíková^a, and O. Bláhová^c (^a *Department of Physical Electronics, Faculty of Science, Masaryk University, Brno, Czech Republic*, ^b *Department of Physics, Ovidius University, Constanța, Romania*, ^c *University of West Bohemia Plzeň, Czech Republic*): **Mechanical Properties of Thin Films Deposited by TVA and G-TVA Methods**

The Thermionic Vacuum Arc (TVA) plasma is a powerful technique able to growth thin films using solids as precursor in vacuum conditions. A large range of materials, even refractory metals were successfully deposited using this technique. In this paper an extension of TVA method from gases (G-TVA) for DLC synthesis is reported. The novelty consists in using a flow of methane, instead of the carbon rod used as anode in the classic TVA method. This expands enormously the applicability of the TVA technique for the synthesis of thin films from solids to gas precursors. The mechanical properties of the films deposited were investigated. The described methods enable to prepare carbon films with wide range of mechanical properties from polymer-like carbon up to hard diamond-like carbon.

NANOINDENTATION MEASUREMENTS OF THE INTERMETALLIC PHASES IN GALVANNEAL COATINGS

ZUZANA VADASOVÁ^a, LADISLAV PEŠEK^{a*}, MÁRIA KOLLÁROVÁ^b, OLGA BLÁHOVÁ^c, and PAVOL ZUBKO^a

^a Faculty of Metallurgy, TU of Košice, Park Komenského 11, 042 00 Košice, Slovakia, ^b Research and Development Centre, U. S. Steel, Košice, Slovakia, ^c West Bohemian University, Plzeň, Czech Republic
ladislav.pesek@tuke.sk

Keywords: nanoindentation, intermetallic phases, galvannealing

1. Introduction

Galvannealed IF-HS steel sheets are presently the subject of interest in automotive as well as steel industry for higher corrosion resistance, and considerably higher strength with excellent formability¹. These coatings may contain one or more of four possible iron-zinc phases of low thickness². The mechanical properties of these phases haven't been in detail investigated. Thus the depth sensing indentation is a suitable method for measurements of mechanical properties of these phases.

2. Experimental details

IF steel (galvanized) was used for the experiment. One sample was prepared from this galvanized steel and next the steel was additionally annealed in the furnace at 450 and 500 °C at 10 and 60 s holding times, respectively. The steel thickness was 0,85 mm and average thickness of the zinc layer was 13,5 μm. We marked these samples as R456 and R501. Then cross-sectional samples were prepared via classical metallographic method. All samples were investigated via scanning electron microscopy (SEM) and energy dispersive X-ray microanalysis (EDX) to determine the composition of individual intermetallics³.

Nano Indenter XP with Berkovich indenter was used for the hardness and indentation modulus measurement. Load control mode was chosen and the load of 10 mN was used. Firstly the galvanized sample was measured and the mechanical properties of both, steel substrate and zinc layer were evaluated. Then two galvannealed samples were measured. Twenty indentations in each intermetallic phase were performed on the samples. In the case of thin Γ layer the load of 5 mN was used because of achieving the appropriate results from smaller indents.

3. Results and discussion

Firstly the mechanical properties namely the hardness and indentation modulus of galvanized steel were measured. Twenty indentations in both, steel and zinc layer (η -phase) have been performed. The load of 10 mN was used. The measured values of the indentation hardness H_{IT} and the elastic modulus E_{IT} are in the Tab. I.

Then two galvannealed samples were measured using load control mode. Approximately twenty indentations into each intermetallic layer were performed using the load of 10 mN.

Table I
Hardness and modulus values of galvanized steel and zinc layer

R – zakl	Average hardness [GPa]	Average modulus [GPa]
Steel substrate	2,13	200
Zinc layer	0,72	102

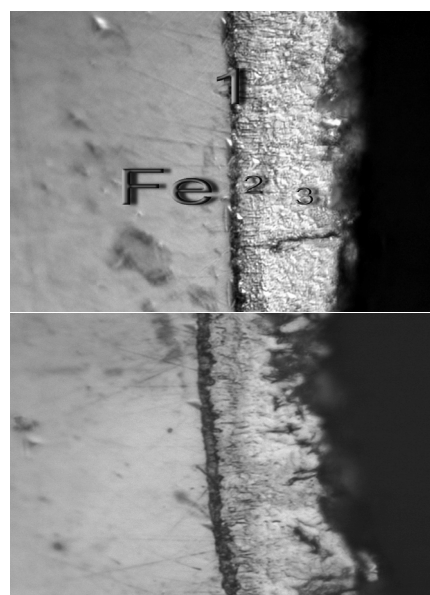


Fig. 1. Steel with visible zinc layer - illustration of marking of measured intermetallic layers

We named the intermetallic phases using the numbers instead of Greek alphabet, Fe – steel substrate, 1 – Γ layer, 2 – $\Gamma+\delta$ layer, 3 – δ layer see Fig. 1 and Table II. There is a great difference between hardness of intermetallic layers of galvannealed steel when compare with zinc layer of galvanized steel.

Table II
Hardness and modulus values of individual intermetallic phases for each measured sample

	R - zakl		R 456				R 501			
	steel	zinc layer	steel	1	2	3	steel	1	2	3
H_{IT} [GPa]	2,13	0,72	2,44	1,36	4,58	3,33	2,39	1,11	5,12	4,46
E_{IT} [GPa]	199,8	102,1	204,3	129,3	159,0	116,9	215,2	106,3	138,4	120,9

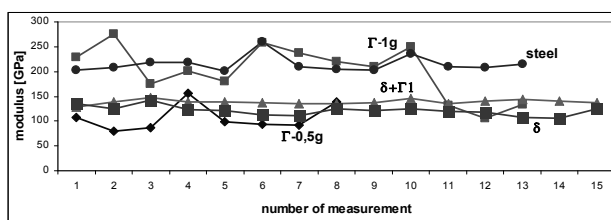


Fig. 2. Elastic modulus measured by Nano Indenter XP – sample R456

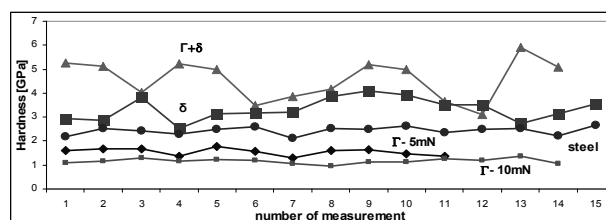


Fig. 3. Hardness measured by Nano Indenter XP – sample R501

Table III
The averages values of indentation hardness, comparison of literature³ and measured values

	HV	H_{IT} -calculated	E_{IT} - measured		H_{IT} - measured		
			450 °C/60 s	500 °C/10 s	450 °C/60 s	500 °C/10 s	
η	52	0,56	η	102	0,72		
	39	0,42					
	71	0,77					
ζ	208	2,25	ζ				
	117	1,26					
	177	1,91					
δ1	358	3,87	δ	117	121	3,33	4,46
	273	2,95					
δ0	270	2,92	δ+Γ1	159	138	4,58	5,12
Γ1	505	5,46	Γ	129	106	1,36	1,11
Γ	326	3,52	Fe	204	215	2,44	2,39
Fe	104	1,12					

The average values of the indentation hardness and elastic modulus are in the Tab. II. The same measurement was performed for the second sample. The hardness and indentation modulus of the phases have the same trend as that for the first sample.

As you can see in Fig. 1, the indents in Γ layer are so expansive that they interfere into the base material but also into the $\Gamma+\delta$ phase. The thickness of Γ layer is varying from 500 to 2200 nm for used temperatures of annealing and holding times moreover this layer is not continuous and there are some discontinuities^{3,4}.

Thus the load of 5 mN was used for reaching the appropriate properties of this thin layer. According to literature data the hardness of the Γ layer is much greater than the hardness of the others intermetallic layers. In our experiment the values

for the Γ layer are the lowest ones. But as can be seen in the Fig. 2 the values for the modulus of each layer are typical for Fe-Zn. More experiments with lower loads are needed for achieving the appropriate values of the mechanical properties of the Γ layer. It is evident that the hardness of intermetallic layers decreases with the decrease of the content of the Fe in the layer, except of the Γ layer.

When the load of 10 mN was used for the measurements of the thin Γ layer, the hardness values reach the steel hardness values. Bigger part of each indent interferes into the base material and only little area reach the layer. Also the values of the modulus are typical for the steel. But in the case of 5 mN load, the hardness and modulus values are as low as for the first sample, see Tab. II.

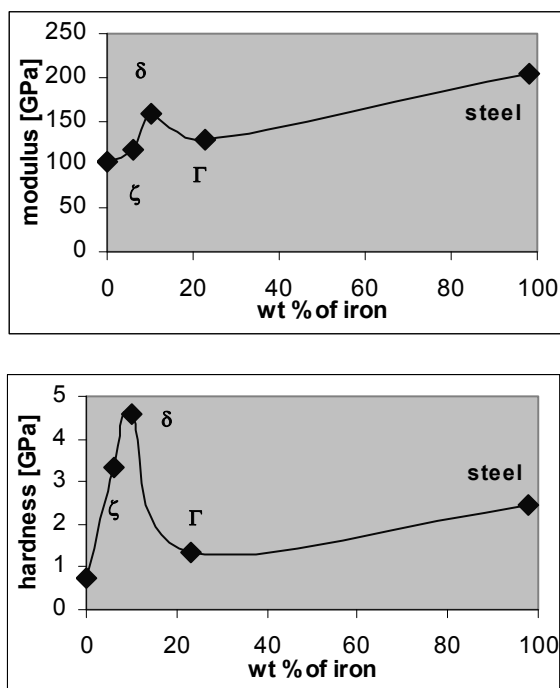


Fig. 4. Indentation hardness and indentation modulus values in dependence of the weight percentage of the iron in zinc layers, sample 456

When compare to the literature value for Vickers measurements using 250 mN load and converted into H_{IT} values and H_{IT} values from our indentation measurements there are not great differences, see Tab. III.

In the Fig. 4 it can be seen that the course of indentation hardness and indentation modulus are not in accordance with the course of the weight percentage of the iron in the intermetallic layers. Such as the Γ layer possesses the highest percentage of the iron, low values of the hardness and modulus are measured in our experiment.

4. Conclusions

Depth sensing indentation is a suitable method for the detail experimental identification of local mechanical properties of intermetallic layers in zinc coating on galvanized steel sheet.

There are not great differences in the Vickers microhardness values converted into the indentation hardness and measured values of H_{IT} using depth sensing indentation method.

The annealing has the meaningful influence on the mechanical properties of the zinc layer which is transformed into the intermetallic layers. The formation of intermetallic layer causes the increase in hardness and elastic modulus.

The change in the used annealing temperatures and holding times does not have great influence on the mechanical properties of Intermetallic layers. Values for both samples are quite similar.

The weight percentage of the iron in the intermetallic layers is not in accordance with the indentation hardness and indentation modulus of these layers.

This work was supported by the SK-CZ project SK-132/CZ-109 and partly by the project MŠMT ČR: MSM4977751303.

REFERENCES

1. Bakshi S. D., Dutta M., Baudyopadhyay N., Rajesh N.: Surf. Coat. Technol. 201, 4547 (2007).
2. Marder A. R.: Prog. Mater. Sci. 45, 191 (2000).
3. Kollárová M.: *Dizertačná práca*. Ústav materiálového výskumu SAV v Košiciach, Košice 2005.
4. Kollárová M., Džupon M., Leško A., Parilák L.: Metalurgija 46, 9 (2007).

Z. Vadasová^a, L. Pešek^a, M. Kollárová^b, O. Bláhová^c, and P. Zubko^a (^aFaculty of Metallurgy, TU of Košice, Slovakia, ^bResearch and Development Centre, U. S. Steel, Košice, Slovakia, ^cWest Bohemian University, Plzeň, Czech Republic): **Nanoindentation Measurements of the Intermetallic Phases in Galvanneal Coatings**

The paper deals with indentation measurements of hardness of the intermetallic phases in the galvanneal coatings. Galvannealed IF-HS steel sheets are presently the subject of interest in automotive as well as steel industry for higher corrosion resistance, and considerably higher strength with excellent formability. These coatings may contain one or more of four possible iron-zinc phases of low thickness. The mechanical properties of these phases haven't been in detail investigated. Thus the depth sensing indentation is a suitable method for measurements of mechanical properties of these phases.

Papers presented at
the 5th International Seminar on
LOCAL MECHANICAL PROPERTIES 2008
LOKÁLNE MECHANICKÉ VLASTNOSTI 2008

November 3rd to 5th, 2008

Košice – Herľany, Slovak Republic



organized by Technical University of Košice
in cooperation with
University of West Bohemia in Plzeň



2008

s139

LOKÁLNÍ MECHNICKÉ VLASTNOSTI ORGANICKO-ANORGANICKÝCH NANOKOMPOZITNÍCH POVLAKŮ

OLGA BLÁHOVÁ^a
a MILENA ŠPIRKOVÁ^b

^a NTC ZČU, Univerzitní 8, 306 14 Plzeň, ^b ÚMCH AV ČR, v.v.i., Heyrovského nám. 2, 162 06 Praha 6, Česká republika
 blahova@ntc.zcu.cz, spirkova@imc.cas.cz

Klíčová slova: organicko-anorganické povlaky, nanoindentace

Úvod

Použití materiálů na bázi makromolekulárních látek na mechanicky, tepelně, chemicky a elektricky namáhané strojní a elektrotechnické výrobky vyžaduje dobrou znalost jejich strukturního uspořádání, mechanických, chemických a jiných vlastností a zpracovatelských procesů.

Polymery se svými vlastnostmi výrazně odlišují od materiálů kovových; příčinou je jejich rozdílná strukturní stavba, proto je důležité hodnotit jejich strukturu i vlastnosti nejen v makroskopickém měřítku, ale i na submikronové úrovni. To je nezbytné především při vývoji a hodnocení nových typů materiálů, zejména ve formě povlaků.

Rízení struktury v submikronovém měřítku umožňuje připravovat nanokompozitní materiály s řízenými vlastnostmi, což je umožněno širokým výběrem organických monomerů, kovových alkoxidů a rozpouštědel. Z ekologického hlediska je důležité, že rozpouštědlem může být voda nebo její směs s alkoholy.

Organicko-anorganické (O-A) materiály nabízejí velké množství potenciálních nebo již technologicky zvládnutých aplikací: používají se jako optické nátěry, biomateriály, membrány, jako ochranné povlaky proti poškrábání, korozi, oxidaci, apod.

Praktické aplikace O-A povlaků vyžadují znalost hlavních materiálových charakteristik, především mechanických vlastností (pevnost, houževnatost, mikrotvrdość, apod.). O-A materiály jsou systémy značně složitě, je tedy nutná multidisciplinární charakterizace, u povlaků zvláště se zřetelem na povrchové vlastnosti. Mechanické vlastnosti povlaků odrážejí celou řadu faktorů ovlivňujících konečný stav celého systému.

Pro určení tvrdosti a modulu pružnosti samotného povlaku, bez vlivu substrátu, je nutno použít instrumentovanou zkoušku tvrdosti při malých zatíženích. V tomto příspěvku je hodnocen vliv druhu a množství plniva (přírodní, nemodifikovaný montmorillonit a koloidní oxid křemičitý).

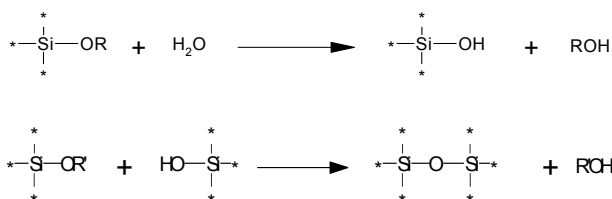
Hodnocené povlaky byly připravované s cílem vytvořit anti-odrazové, anti-reflexní nebo anti-statické vrstvy odolné proti vlivům okolního prostředí (vlhkost, působení částic ...).

Experimentální materiál

Nové typy O-A povlaků jsou vyvíjeny v ÚMCH¹. Hodnocené povlaky byly připraveny z organokřemičitého prekurzoru [3-(glycidyl oxy) propyl] methyldiethoxysilanu (GMDES) a oligomerního triaminu s koncovými primárními aminoskupinami (Jeffamine T403) a přidáním siliky nebo montmorillonitu Na⁺. Nanokompozitní povlaky byly vytvářeny dvěma nezávislými reakčními mechanismy: anorganické struktury vznikaly tzv. sol-gel procesem zahrnujícím dva následné procesy: (kyselou) hydrolyzu alkoxy skupin a (bazickou) polykondenzaci prekurzoru GMDES.

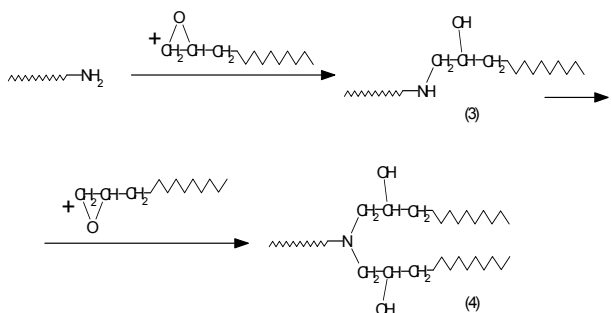
Organická polymerní síť byla vytvářena adičními reakcemi glycidylových skupin GMDES s aminoskupinami příslušného Jeffaminu T403. Reakční prostředí tvořila směs voda–propan-2-ol (7:3 – hmotnostně), HCl sloužila jako katalyzátor hydrolyzy sol-gel procesu, Jeffamine nejdříve působil jako katalyzátor polykondenzace sol-gel procesu při laboratorní teplotě, poté – za zvýšené teploty – jako reakční složka při tvorbě organické polymerní sítě. Vznikly transparentní, ve většině případů bezbarvé nebo slabě nažloutlé produkty ve formě volných nátěrových filmů nebo povlaků na skle. Tloušťka se pohybovala okolo 100 μm.

Anorganická síťová výstavba (sol-gel proces):



kde R je alkyl, ROH je hydroxyl skupina nebo alkyl, * je buď (aktivní) alkoxylová nebo hydroxylová skupina nebo nějaká jiná skupina v procesu netečná.

Organická síťová výstavba:



Hodnocené vzorky:

<i>O-A</i>	O-A matrice (GMDES a T403)
<i>S</i>	O-A matrice se silikou 20 hm.% (GMDES, T403 a SiO ₂)
<i>M</i>	O-A matrice s montmorillonitem Cloisite Na ⁺ 1 hm.% (GMDES, T403 a MMT Na)
<i>S1-S8</i>	O-A matrice se silikou 0–40 hm.% (GMDES, T403 a SiO ₂)

Experimentální metody

V ÚMCH je proces vzniku a struktura připravených povlaků hodnocena využitím spektroskopie NMR (nukleární magnetická rezonance)^{1,2}. Struktura hybridních O-A nanokompozitních povlaků byla studována pomocí metod SAXS a WAXS (maloúhlového a širokoúhlového rozptylu paprsků X)¹⁻⁴. Morfologie povrchů nátěrových filmů byla sledována pomocí AFM (mikroskopie atomových sil) za použití kontaktního i bezkontaktního režimu^{1,5}. Teplotní závislosti obou složek komplexního smykového modulu byly hodnoceny metodou dynamické mechanické termální analýzy⁶. Byly testovány pevnostní charakteristiky vzorků ve formě volných nátěrových filmů: ze závislosti napětí – deformace byly určeny tažnost, pevnost a houževnatost^{1,7}. Dalším ze způsobů hodnocení kvalitativních vlastností povlaků je „scratch test“, který byl prováděn pomocí AFM s přítlakovou silou řádově 100 nN (cit.⁵).

Indentační experimenty byly uskutečněny použitím přístroje MTS NanoIndenter XP s použitím metody CSM (kontinuální měření tuhosti). Tato metoda je založená na principu superpozice velmi malé sinusoidní síly s lineárně rostoucí zátěžnou silou. Odezva indentoru při dané frekvenci a fázovém posunu mezi silou a posunutím indentoru je měřená průběžně jako funkce hloubky vtisku. Vyhodnocení odezvy vede k určení kontaktní tuhosti *S* v závislosti na hloubce vtisku. Mechanické vlastnosti pak mohou být určeny ze vztahu:

$$S = 2\beta E_r \sqrt{\frac{A_c}{\pi}} \quad (1)$$

kde A_c je projekční kontaktní plocha mezi indentorem a vzorkem při maximální síle, β je konstanta závislá na druhu indentoru a E_r je redukovaný modul pružnosti:

$$1/E_r = (1 - \nu_m^2)/E_m + (1 - \nu_i^2)/E_i \quad (2)$$

kde E_i (1140 GPa) a ν_i (0,07) jsou elastické vlastnosti indentoru, E_m a ν_m jsou elastické vlastnosti zkoumaného vzorku. V práci byla předpokládána hodnota Poissonova čísla pro hodnocený materiál 0,35. Modul pružnosti vzorku je pak vypočten ze vztahů $(1 \text{ a } 2)^3$. Tvrdost H jako podíl zátěžné síly P a kontaktní plochy A_c :

$$H = P/A_c = cP/h_c^2 \quad (3)$$

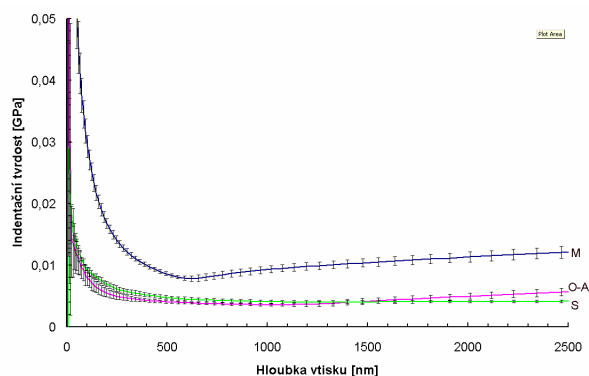
kde c je geometrická konstanta a h_c je kontaktní hloubka vtisku při maximálním zatížení. Parametry měření: amplituda 5 nm, oscilační frekvence 75 Hz, změna hloubky vlivem teploty $<0,05 \text{ nm s}^{-1}$, maximální hloubka vtisku 2,5 μm .

Výsledky měření

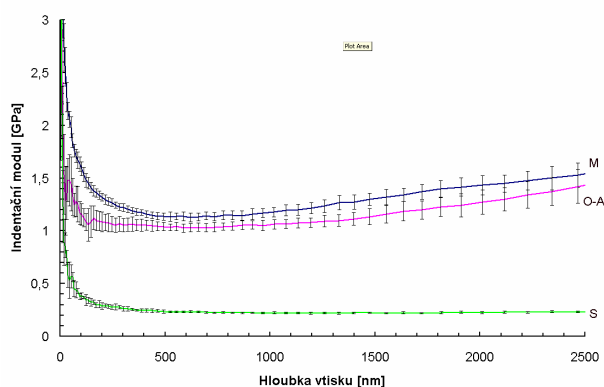
Na obr. 1. a obr. 2. jsou hloubkové průběhy indentační tvrdosti a indentačního modulu pružnosti vzorků *O-A*, *S* a *M*. Průběhy tvrdosti a modulu pružnosti s hloubkou nejprve klesají od povrchu. Tento pokles v malých hloubkách je pozorovatelný ve všech polymerních systémech⁹ a může být způsoben velikostním efektem, resp. vlivem zaoblení indentoru a způsobem kalibrace⁸. Při homogenní tloušťce vrstvy 100 μm maximální hloubka vtisku (2,5 μm) dosahuje 2,5 % tloušťky vrstvy. Ovlivnění naměřených hodnot substrátem v okolí lokálního minima křivek je tedy minimální.

Povlak *S* se silikou měl stejnou nanotvrdost jako povlak *O-A* bez plniva, ale došlo k poklesu indentačního modulu pružnosti. Povlak *M* s přidavkem montmorillonitu měl stejný indentační modul jako povlak bez plniva, ale vyšší nanotvrdost.

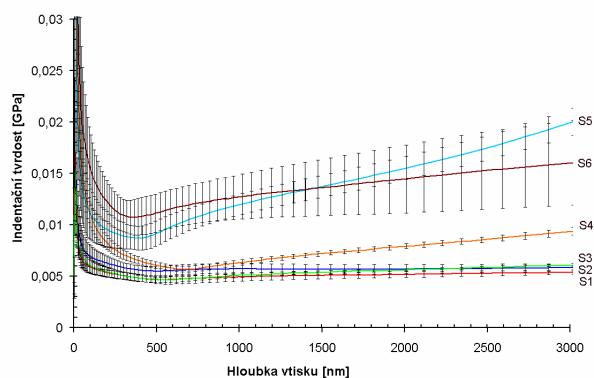
V člancích^{10,11} byla hodnocena drsnost povrchu těchto vzorků a byly provedeny tribologické zkoušky metodou „pin-on-disc“. Bylo zjištěno, že povlaky se silikou mají mnohem nižší míru opotřebení než povlaky s montmorillonitem, přestože měly menší tvrdost. Proto byly dále hodnoceny



Obr. 1. Průběh indentační tvrdosti v závislosti na hloubce proniknutí indentoru vzorků *O-A*, *S*, *M*



Obr. 2. Průběh indentačního modulu pružnosti v závislosti na hloubce proniknutí indentoru vzorků *O-A*, *S*, *M*



Obr. 3. Průběh indentační tvrdosti v závislosti na hloubce vtisku vzorků S1 až S6

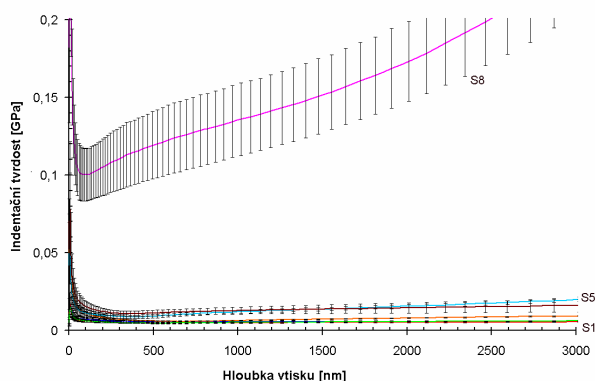
povlaky s různým množstvím tohoto plniva.

Na obr. 3. je hloubkový průběh indentační tvrdosti vzorků S1 až S6. Tvrdost s hloubkou nejprve klesá. Hodnoty charakterizující povlak byly určeny z lokálních maxim křivek a jsou uvedeny v tab. I. Výraznější vliv má obsah aditiva nad 20 %.

Tabulka I

Hodnoty indentační tvrdosti a indentačního modulu pružnosti povlaků s různým obsahem SiO₂

Vzorek	Obsah plniva [%]	H_{IT} [MPa]	E_{IT} [MPa]
S1	0	5,48 ± 0,47	483 ± 61
S2	0,5	4,66 ± 0,43	457 ± 49
S3	5	4,64 ± 0,27	438 ± 22
S4	10	5,69 ± 0,28	737 ± 23
S5	20	8,70 ± 1,15	1034 ± 92
S6	30	10,74 ± 1,72	966 ± 119
S8	40	100,23 ± 16,81	3890 ± 422



Obr. 4. Průběh indentační tvrdosti v závislosti na hloubce vtisku vzorků S1 až S8

Na obr. 4. je hloubkový průběh indentační tvrdosti vzorků S1 až S8. Obsah aditiva 40 % má značný vliv na hodnotu tvrdosti. Ovšem velký rozptyl naměřených hodnot svědčí o velké nehomogenitě povlaku.

Závěr

Tato práce obsahuje výsledky nanoindentačních analýz hybridních O-A nanokompozitních povlaků bez plniva a s přidáním montmorillonitu a koloidního oxidu křemičitého. Přidání 0,5 % oxidu křemičitého zlepšilo odolnost povlaků proti opotřeby, přestože se nezvýšila tvrdost. Proto byly hodnoceny vzorky s vyšším obsahem tohoto aditiva. Výsledky doplňují poznatky získané jinými metodami¹⁻⁷ a přispějí tak k optimalizaci vytváření těchto povlaků vzhledem k aplikacím vyžadujícím zvýšenou odolnost proti opotřeby.

LITERATURA

- Špírková M. et al.: Surf. Coat. Int., B 86, 187 (2003).
- Špírková M. et al.: Nano '03, Brno, 2003. str. 109–114, Brno 2003.
- Brus J. et al.: Macromolecules 37, 1346 (2004).
- Špírková M. et al.: J. Appl. Polym. Sci. 92, 937 (2004).
- Špírková M. et al.: J. Appl. Polym. Sci. 102, 5763 (2006).
- Špírková M. et al.: Prog. Org. Coat. 61, 145 (2008).
- Špírková M. et al.: Surf. Eng. 24, 268 (2008).
- Fisher-Cripps A. C.: Introduction to Contact Mechanics, Springer Verlag, New York 2000.
- Hu Y. et al.: Polym. Test. 25, 492 (2006).
- Farkačová T. et al.: Vrstvy a povlaky 2004. Dubnica nad Váhom, str. 195–200. ZTS – MATEC, 2004.
- Farkačová T. et al.: Vrstvy a povlaky 2005. Trenčín, str. 40–45. Digital Graphics, 2005.

Práce byla podpořena projektem IAA400500505 Grantové agentury Akademie věd České republiky a výzkumným záměrem MŠMT MSM 4977751303.

O. Bláhová^a and M. Špírková^b (^aNTC ZČU Plzeň, ^bÚMCH AV ČR Praha, Czech Republic): Local Mechanical Properties of Organic-Inorganic Nanocomposite Coatings

The paper deals with the determination of local mechanical properties of hybrid organic-inorganic epoxy-based coatings. Examined specimens were prepared from functionalized organosilicon precursors, oligomeric di- or triamines and colloidal silica particles. The mechanical properties were studied by nanoindentation technique. Tests were performed to study influence of additives on indentation hardness and indentation modul.

DETERMINATION OF PARAMETERS OF VISCOELASTIC MATERIALS BY INSTRUMENTED INDENTATION.

PART 2: VISCOELASTIC-PLASTIC RESPONSE

JAROSLAV MENČÍK

University of Pardubice, Studentská 95, 53210 Pardubice,
Czech Republic
jaroslav.mencik@upce.cz

Keywords: mechanical properties, instrumented indentation, nanoindentation, viscoelasticity, plastic deformations

1. Introduction

This paper is a continuation of the article „Determination of parameters of viscoelastic materials by instrumented indentation“¹. That article has explained the principles of instrumented indentation and brought basic formulae for indentation testing of elastic-plastic materials (with instantaneous response to load), as well as for the description of load response of viscoelastic materials, where the deformations depend not only on the load magnitude, but also on its duration. In Practical part, recommendations were given for the preparation of indentation tests into viscoelastic materials and for the evaluation of results. The article was limited to reversible deformations, which disappear fully during some time after unloading. Often, however, also irreversible deformations occur, e.g. under concentrated load or in materials whose response has viscous character. In this paper, the formulae for indentation response will be extended to irreversible deformations. Advice will be given for tests arrangement and data evaluation, and the proposed procedure will be illustrated on a practical example.

2. Theoretical part

Viscoelastic materials are typical by deformations depending not only on the load magnitude, but also on its duration and time course. As shown in¹, the relationship between indenter load P and depth h of its penetration into a specimen from such material under monotonic loading can generally be expressed as

$$f[h(t)] = K \psi(P, J, t) \quad (1)$$

where f is some function of the indenter shape and penetration, K is a constant characterizing the indenter geometry, and $\psi(P, J, t)$ is a function depending on the load magnitude and history, on material parameters, and on time; J is so-called creep compliance function. For pointed indenters (conical, Vickers or Berkovich)

$$f = h^2; \quad K = \pi / (4 \tan \alpha) \quad (2)$$

α is the semi-angle of indenter tip or of equivalent cone (for

Berkovich and Vickers indenter, $\alpha = 70.4^\circ$). The load response of viscoelastic materials is usually described by models assembled from springs and dashpots. Rheological parameters for a viscoelastic model-body consisting of a spring in series with several Kelvin-Voigt units (a spring in parallel with a dashpot), can be obtained relatively easily from the time course of indenter penetration under constant load. For this case^{1,2},

$$\psi(t) = P \{ C_0 + \sum C_j [1 - \rho_j \exp(-t/\tau_j)] \} \quad (3)$$

C_0 represent the instantaneous compliance, while the constants C_1, \dots, C_j pertain to the individual Kelvin-Voigt bodies, and, together with the retardation times τ_j characterize the time-dependent processes. ρ_j is so-called ramp correction factor, which takes into account the fact that the load increase was not infinitely short, but lasted t_R . According to Oyen²,

$$\rho_j = (\tau_j / t_R) [\exp(t_R / \tau_j) - 1] \quad (4)$$

The irreversible deformations can be time-independent or time-dependent. The time-independent (plastic) behaviour can be modelled by a plastic element (a slider) in the rheological model, and the time-dependent irreversible deformations can be described by a dashpot arranged in series with other elements. The plastic element is characterised by hardness H_0 (or yield strength Y), which is – together with the Young modulus E_0 for instantaneous elastic response – contained in the constant C_0 . Time-dependent irreversible deformation is characterised by a dashpot of viscosity η_v , with the creep compliance function

$$J(t) = c_v t \quad (5)$$

where the viscous compliance c_v is related to the dynamic viscosity as $c_v = 1/\eta_v$.

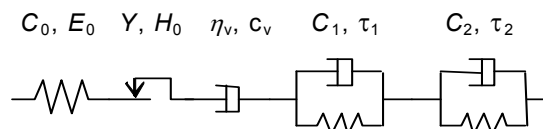


Fig. 1. Viscoelastic-plastic model “spring + plastic element + dashpot + 2 Kelvin-Voigt bodies”

The response function for a universal viscoelastic-plastic body, consisting of a spring, a dashpot and several Kelvin-Voigt units in series (Fig. 1), loaded by a constant force P , is

$$\psi(t) = P \{ C_0 + c_v(t - t_R/2) + \sum C_j [1 - \rho_j \exp(-t/\tau_j)] \} \quad (6)$$

the term $t_R/2$ expresses the fact that the irreversible viscous deformations during the load increase from 0 to P are smaller than they would be if the full force P acted for the time t_R (they correspond to the average force $P/2$).

3. Procedure for the determination of viscoelastic-plastic properties

Parameters, characterizing viscoelastic properties, can be estimated from a simple five-step procedure (Fig. 2). In the first step (I, duration t_R), the indenter is quickly loaded to the nominal load P . Then, a long dwell under this load follows (step II), then rapid unloading to a very low load P_u (step III), followed by a long time under this load (IV), and unloading to zero (V). The response during dwell II provides the base for the determination of viscoelastic parameters, while the back-creep in the low-load dwell IV serves for the verification of the duration of reversible viscoelastic processes and of the necessary number of Kelvin-Voigt elements (determined in step II). The parameters of instantaneous elastic and plastic deforming are best obtained from a separate load-unload test.

The loading in step I should be as quick as possible in order to reduce the time-dependent processes during this period. A constant load rate ($dP/dh = \text{const}$) is recommended here, because the ramp correction factor ρ , Eq. (4), corresponds to this case. However, if the duration of load increase is short, the viscoelastic deformations during this time are small, and the details of the load increase $P(t)$ are not very important. The dwell II under constant load should be sufficiently long so that all reversible viscoelastic processes have died away and their duration can be assessed. The unloading III should be fast and the constant load P_u in the following period IV should be very low, only such that the indenter remains in contact with the specimen and can serve as a sensor to measure the deformation recovery (back-creep). The period IV should last about the same time as period II.

The processing of measured $h(t)$ data starts with the determination of constants in the creep compliance function from the dwell II. The practical procedure will be illustrated on a test with a pointed indenter and response function (6). Inserting this function together with equation (2) into Eq. (1) gives

$$h^2(t) = PK\{C_0 + c_v(t - t_R/2) + \sum C_j [1 - \rho_j \exp(-t/\tau_j)]\} \quad (7)$$

where P is the nominal load and $K = \pi/(4 \tan\alpha)$, with the indenter tip semiangle α .

The constants C_0 , c_v , C_1 , τ_1 , ρ_1 , etc. can be obtained by minimizing the sum of the squared differences between the measured and calculated $h^2(t)$ values. However, the actual procedure must be modified. In equation (7), several terms appear that do not depend on time: C_0 , $c_v t_R/2$ and C_j . Regression analysis cannot determine them individually, but only as a whole; otherwise incorrect values could be obtained. More-

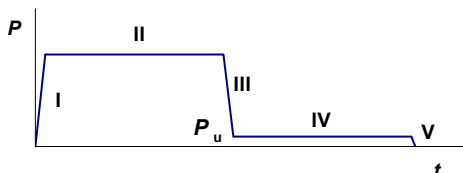


Fig. 2. Five-step loading-unloading scheme for obtaining the viscoelastic-plastic parameters; P – indenter load, t – time

over, the terms $C_j \rho_j$ also occur here, as well as the ramp correction factors ρ_j , which depend on the retardation times τ_j that are also unknown. From a curve-fitting point of view, equation (7) corresponds to the expression

$$h^2(t) = PK [B + c_v t - \sum D_j \exp(-t/\tau_j)] \quad (8)$$

where

$$B = C_0 - c_v t_R/2 + \sum C_j; \quad D_j = C_j \rho_j; \quad j = 1, 2, 3 \dots (9)$$

The determination of material parameters proceeds in three steps:

Step 1. Calculation of regression constants B , c_v and D_j , as well as the retardation times τ_j by fitting the $h^2(t)$ data from period II by the regression function (8).

Step 2. Calculation of the ramp correction factors ρ_j from Eq. (4) for the known duration t_R of load increase and the retardation times τ_j . Then, the constants C_j are found as $C_j = D_j/\rho_j$.

Step 3. Determination of C_0 from Eq. (9) as

$$C_0 = B + c_v t_R/2 - \sum C_j \quad (10)$$

Similar procedures can be used for other models and indenters. It is recommended to try and evaluate several models; analysis of the back-creep during the low-load dwell (step IV) can be helpful here.

The above data-processing has separated the time-dependent deformations from the instantaneous ones, characterized by the compliance C_0 . Now it is necessary to decompose C_0 into the reversible elastic component and irreversible plastic component. These components may be characterized by instantaneous elastic modulus E_0 and hardness H_0 , which are determined in a similar way like in elastic-plastic materials, i.e. from the loading and unloading curves, as described in¹. If the unloading in step III is sufficiently quick, the “fast” contact stiffness S could be obtained. However, this stiffness corresponds to the larger depth at the end of dwell, and the pertinent hardness will be lower than the “instantaneous” one. Therefore, it is better to determine S , E_0 and H_0 in a separate test, with fast loading followed immediately by fast unloading.

4. Experimental part

The above method was used for the determination of viscoelastic-plastic parameters of tooth enamel³. A human tooth was embedded into epoxy resin and cut and polished with a diamond paste. The tests were done with a UMIS-2000 nanoindenter and a diamond Berkovich indenter. The experiments were divided into two groups; one served for obtaining viscoelastic parameters from the creep data, and the other was for the determination of the instantaneous elastic modulus and hardness.

In the first group, six tests were made using the five-step loading scheme (Fig. 2). The indenter was loaded to the nominal load $P = 250$ mN, which was then held constant for 975–1145 s. Then it was unloaded to $P_u = 5$ mN, kept constant 938–1110 s and then unloaded to zero. The load increase (step I) and decrease (step III) lasted about 20 s each. The characteristic depths varied between 1.83–1.96 μm under nominal load 250 mN, and between 1.40–1.33 μm after

unloading to 5 mN; the details are given in³.

The load-displacement curve during dwell II was approximated by four models:

Spring + one Kelvin-Voigt body,
Spring + two Kelvin-Voigt bodies,
Spring + dashpot + one Kelvin-Voigt body,
Spring + dashpot + two Kelvin-Voigt bodies.

Model d), depicted in Fig. 1, was described by the equation (7) or (8) with $j = 2$, while the model c) was only with $j = 1$, and the models a) and b) were without the dashpot (c_v). The constants B , c_v , D_1 , D_2 , τ_1 and τ_2 were found by minimizing the sum of the squared differences between the squares of the measured and calculated depth, $\Sigma[h_m^2(t_j) - h_c^2(t_j)]^2 = \min$. The solver in Microsoft Excel was used for the minimization. Then, the ramp correction factors ρ_1 , ρ_2 and the constants C_0 , C_1 , C_2 were found. For better judgement of individual approximations, the relative differences between measured and calculated values, $\Delta_{rel,j} = [h_m(t_j) - h_c(t_j)]/h_m(t_j)$, were also calculated and plotted.

The best approximation was obtained by the model (d) “spring + dashpot + 2 Kelvin-Voigt bodies” (Fig. 3). A very good fit was also obtained by the model (b) “S + 2 KV”. The model (c) “S + D + KV” was worse, and the model (a) “S + KV” has not corresponded to the measured curve. The back-creep after unloading has confirmed suitability of the model (d) and the retardation times, which were approximately $\tau_1 \approx 20$ s, $\tau_2 \approx 200$ s.

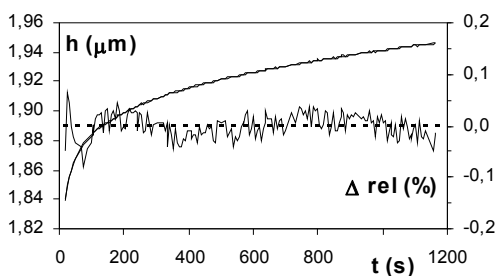


Fig. 3. Indenter penetration into tooth enamel under constant load during dwell II³. Measured values are plotted together with those calculated for model “S + D + 2 KV”; the differences can be seen only in the diagram of relative residuals Δ_{rel} . h – depth, t – time

Elastic modulus E and hardness H , determined in six separate load-unload tests using the formulae numbered (1)–(4) in¹, were in the range: 96–102 GPa for E , and 4.0–4.6 GPa for H . All measurements are described in paper³, which also contains all important values.

Hardness and elastic modulus characterize the instantaneous response. As such, they are related to the compliance C_0 . Hainsworth et al.⁴ and Malzbender et al.⁵ have derived the following relationships for the loading curve under a pointed indenter:

$$P = kh^2; \quad k = E \left(\Phi \sqrt{E/H} + \Psi \sqrt{H/E} \right)^{-2} \quad (11)$$

with constants $\Phi = 0.202$ and $\Psi = 0.638$. The combination with the instantaneous part of Eq. (7), $h^2 = PKC_0$, gives³:

$$C_0 = \frac{4 \tan \alpha}{\pi} \frac{1}{E_r} \left(\Phi \sqrt{E_r/H} + \Psi \sqrt{H/E_r} \right)^2 \quad (12)$$

where E_r is the reduced modulus, related to the elastic modulus of the specimen (E) and the indenter (E_i) as $1/E_r = (1 - \nu^2)/E + (1 - \nu_i^2)/E_i$; ν is Poisson’s ratio. The value of C_0 for the tooth enamel, calculated from the measured values H and E (resp. E_r), differed from the instantaneous compliance C_0 , obtained by fitting the creep data via Eq. (12), by less than 4 % (ref.³). This demonstrates the possibility of using the formula (12) for verification of parameters in viscoelastic-plastic models.

5. Conclusions

Mechanical properties can be determined by instrumented indentation, where the indenter load and displacement are measured continuously during loading and unloading. The load response of viscoelastic-plastic materials can be described by means of rheologic models, consisting of springs and dashpots. In this paper, following the first part¹, formulae were given for the description of indentation response of these materials. Also a five-step test procedure, combined with a fast load-unload test, was proposed for experimental determination of viscoelastic-plastic parameters. The use of the method has been illustrated on indentation testing of human-tooth enamel.

The work was supported by the Grant Agency of Czech Republic, project No. GAČR 103/08/1340.

REFERENCES

1. Menčík J.: Chem. Listy, in print.
2. Oyen M. L.: Philosophical Magazine 86, 5625 (2006).
3. Menčík J., He L. H., Swain M. V.: J. Mech. Behav. Biomed. 2, 318 (2009).
4. Hainsworth S. V., Chandler H. W., Page T. F.: J. Mater. Res. 11, 1987 (1996).
5. Malzbender J., With de G., Toonder den J.: J. Mater. Res. 15, 1209 (2000).

J. Menčík (Department of Mechanics, Materials and Machine Parts, Jan Perner Transport Faculty, University of Pardubice, CZ-53210 Pardubice, Czech Republic): **Determination of Parameters of Viscoelastic Materials by Instrumented Indentation. Part 2: Viscoelastic-Plastic Response**

The load response of viscoelastic-plastic materials can be described by rheologic models, consisting of springs and dashpots. This paper, which follows the first part, published in Chemické listy earlier¹, gives formulae for description of indentation response of these materials. Also a five-step test procedure, combined with a fast load-unload test, was proposed for experimental determination of viscoelastic-plastic parameters by instrumented indentation. The use of this method has been illustrated on testing of human-tooth enamel.

MICROMECHANICAL ANALYSIS OF HETEROGENEOUS STRUCTURAL MATERIALS

JIRÍ NĚMEČEK
and KATEŘINA FORSTOVÁ

ČVUT v Praze, Fakulta stavební, Thákurova 7, 166 29 Pra-
gue 6, Czech Republic
jiri.nemecek@fsv.cvut.cz, katerina.forstova@fsv.cvut.cz

Keywords: heterogeneous materials, cement, fly-ash,
nanoindentation, ESEM, AFM

1. Introduction

Micromechanical analysis of any material involves several subsequent steps that cannot be omitted. The first one includes microstructural observations and determination of phases. This step can be performed with the aid of many experimental techniques. Among others, the most common technique is electron microscopy (ESEM) and atomic force microscopy (AFM). These techniques allow qualitative as well as quantitative investigation of individual material phases at small volumes near or at the sample surface. As a complementary computational technique, image analysis can give valuable results for the phase distribution based on the separation of pixel colors.

The second step is the measurement of intrinsic properties of individual material phases. These measurements can be provided exclusively by nanoindentation which is a technique that can directly access mechanical properties at small dimensions starting from several tens of nanometers (depending on the sample and the probe).

The third step involves up-scaling of the properties to the higher level (mesolevel)⁶. Several analytical or numerical homogenization techniques can be employed to reach this goal.

2. Heterogeneity of structural materials

We can find several types of heterogeneity at microscale of structural materials. The first type of heterogeneity comes from mixing of components that do not chemically react in the matrix like sand, fibers, and other additives. Such heterogeneity is usually known in advance and is given by the mixing proportions. The second type of heterogeneity comes from chemical reactions that are evolving after the mixing of components. As a result of these reactions, new phases are produced and it is hard to rigorously define their volumes and distribution. Formation of the new phases includes fully reacted matrix, unreacted grains of the raw material and interfacial zones with different chemical and also mechanical properties^{1,2}. Structural materials based on cement or waste materials (like fly-ash, furnace slag, etc.) usually include both types of the heterogeneity.

3. Test samples

As an example of structural materials, two types of samples were selected: cement paste (CP) and alkali-activated fly-ash (AAFA). Cement paste (as the main component of cementitious composites) is formed by mixing the cement powder (granulated clinker minerals) with water. Subsequent chemical reaction (hydration) follows to form new products. The main components that can also be distinguished in ESEM are hydrated products containing mainly calcium-silica hydrates (C-S-H gels) and calcium hydroxide Ca(OH)₂ (CH, Portlandite), unreacted clinker grains and capillary pores (see Fig. 1). Samples used in this study were created from Portland cement CEM-I 42,5R, locality Mokrá, mixed with water in water-cement ratio = 0.5 by weight and cured in water for approximately 1 year.

The second samples were produced from granulated fly-ash (coal power-plant, Mělník) activated by addition of 6–10 % of Na₂O and cured 4–16 hours at 60–90 °C. After the

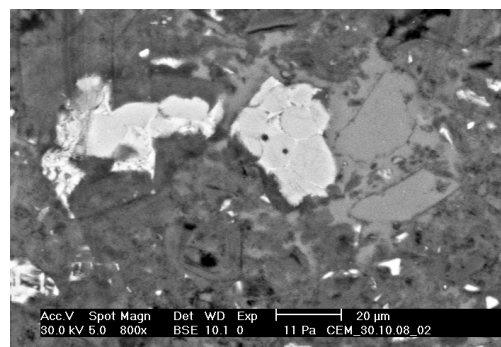


Figure 1. ESEM image of hydrated cement paste. Dark areas = pores; dark grey = C-S-H gels; light grey = Portlandite; light areas = unreacted clinkers

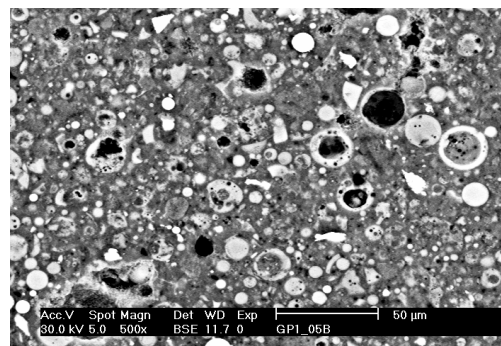
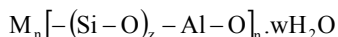


Figure 2. ESEM image of AAFA. Light and light grey areas = unreacted or partly reacted fly-ash grains; dark grey areas = polymer zone; dark areas = pores

activation, polymerization takes place to form 2–3 dimensional Si-O-Al-O chains as follow



The microstructure of resulting AAFA is shown in Fig. 2.

4. Nanoindentation

In order to identify intrinsic material properties of the test samples, nanoindentation was employed. Two nanoindenters were used. Namely, Hysitron Tribolab was used for small indents (up to 10 mN) due to its high resolution and possibility of surface scanning and CSM Nanohardness tester was used for standard indentation with larger forces (up to 500 mN).

Since we are dealing with heterogeneous microstructure, interpretation of the results is more complicated than for a single phase material. We have to employ also special testing strategies to be able to correctly interpret experimental results. There are basically three strategies that can be used:

- Producing of large number of indents that are larger than the characteristic phase dimension with subsequent statistical evaluation of overall material properties of all affected phases that were indented (phase compound).
- Grid indentation in which indents are produced over a large area but the dimension of a single indent is smaller than the characteristic dimension of individual phase. Subsequent deconvolution techniques can be employed for assessment of the individual phase properties^{3,4}.
- Pointed indentation to a specific material phase with indent dimension smaller than the characteristic dimension of the tested phase. In this case, intrinsic properties of the phase (including intrinsic phase porosity) are obtained.

All three strategies were applied for the studied case and results compared.

The above mentioned deconvolution includes identification of the number of material phases (n) in the material. This number is usually known in advance from separate analysis (like EDX). Therefore, we are in fact looking for a finite number of n peaks in the histogram of mechanical properties from the whole set which serves like an overall probability function. We can deconvolute n probability functions from the overall one by defining n separate intervals with the individual probability function related to a single material phase. These functions are usually constructed using normal (Gauss) distribution⁴.

5. Results on cement paste

A large grid of 100 indents was produced over the arbitrarily selected region of the cement paste. Relatively large indents possibly affecting more than one material phase were prescribed (maximum force 10 mN). The final depth of indents was around 700 nm (Fig. 3) which yielded in the surface dimension around 4 μm . Such indents' dimension causes physical homogenization (averaging) of properties in this volume. Since the majority of indents were performed in the hydrated products and indentation to clinkers was rare, in-

dents lying in unhydrous phases were not considered for further evaluation. Thus, results are valid and identified for the hydrated phase compound. Overall modulus of elasticity for all the affected phases (mainly C-S-H gels and Portlandite) was measured to be 23.269 ± 3.093 GPa. Properties of clinker minerals are usually measured separately in its pure unreacted state⁸.

Although the results indicate small deviations, they must be considered as mean values of the whole compound. Identification of individual phases is not possible in this case.

Substantially larger number of indents is necessary to cover heterogeneity of the sample when using small indents. 400 indents in four series were prescribed to the maximum load of 2 mN (Fig. 4). On the other hand, we were able to identify individual material phases from histogram plotted for

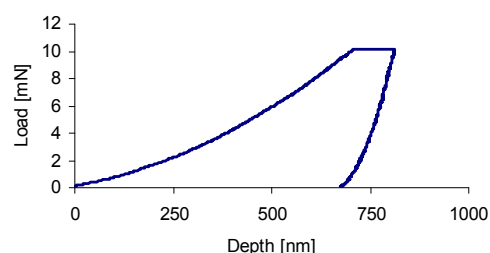


Figure 3. Large indent (10 mN) into hydrated compound of cement paste

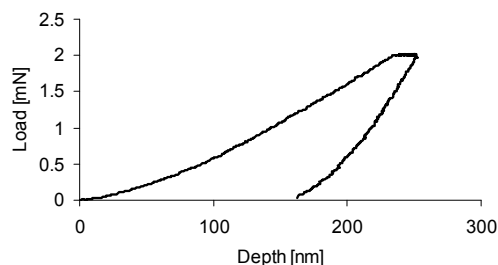


Figure 4. Small indent (2 mN) in cement paste

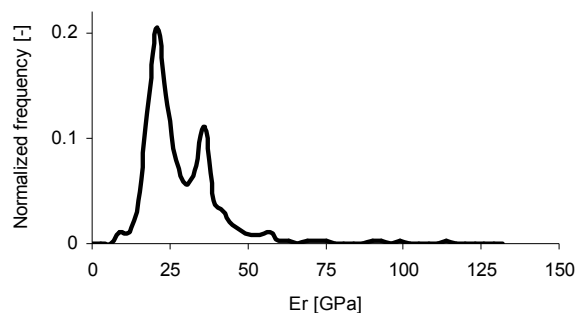


Figure 5. Histogram of reduced moduli in cement paste

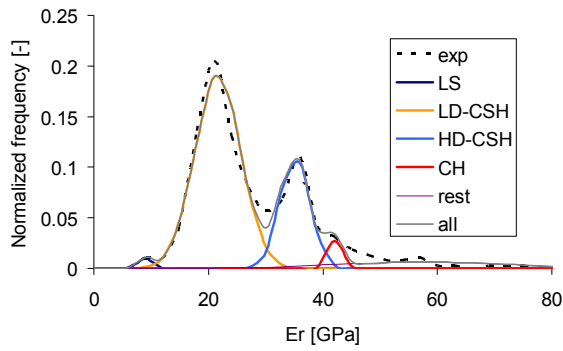


Figure 6. Deconvolution of individual phases in cement paste

reduced modulus⁵, for example (Fig. 5). Several identifiable peaks can be found in this histogram that can be attributed to individual phases.

We decided to apply deconvolution into 5 phases in Fig. 5. These phases were following: low stiffness phases (LS); low density C-S-H gels (LD-CSH); high density C-S-H gels (HD-CSH); Portlandite (CH) and the rest (rest). Experimental histogram of all phases as well as individual phase distributions are depicted in Fig. 6. Mean values and standard deviations of normal distributions for individual phases can be found in Tab. I.

Pointed indentation to a specific phase is in general possible based on the assumption that the phase can be distinguished in optical microscope or in a scanner prior to indentation. In case of cement paste, such a phase can be a clinker or high density C-S-H gel that is formed mainly as a rim around the clinker grain. Other phases cannot be found in such a way. Therefore, we tried to identify directly HD C-S-H by pointed indentation. Small deviations were found which shows on indentation to a homogeneous-like phase. The results of reduced moduli were 38.6 ± 2.57 GPa. This value corresponds fairly well with results obtained by deconvolution from histogram (Tab. I).

Table I

Results from deconvolution and image analysis of cement paste

	LS	LD-CSH	HD-CSH	CH	Rest
Mean E_r , GPa	7.45	20.16	33.59	40.74	55.75
s.d.	0.85	3.90	2.47	0.92	14.62
f_j , %	1	64	24	3	8
f_j^{IA} , %	7.9 ± 6		82 ± 5.3	4.6 ± 2.8	5.5 ± 2.4

E_r stands for reduced modulus; f_j stands for volume fraction received from deconvolution; f_j^{IA} stands for volume fraction received from image analysis

6. Results on alkali-activated fly-ash

Similar approach was used also for the investigation of AAFA samples. First, a matrix of 100 large indents to 100 mN was prescribed. Second, matrices with 100 indents up to 2 mN were tested on four arbitrary places (i.e. 400 indents all together). The difference of the histogram of reduced moduli is depicted in Fig. 7. It can be seen that the distribution of large indents is much narrower and some of the peaks are missing. It clearly shows physical homogenization produced already during the indentation. Obtained results are moreless mean values of the polymer and fly-ash compound. On the other hand, histogram of small indents is wider and contains results from several individual phases.

We decided to apply deconvolution into 5 phases in Fig. 7. These phases were following: low stiffness phases (LS); polymeric phases (GP); partly polymerized zones (partGP); partly activated fly-ash (partFA); and the rest, mainly nonreacted fly-ash (rest). Experimental histogram of all phases as well as individual phase distributions are depicted in Fig. 8. Mean values and standard deviations of normal distributions for individual phases can be found in Tab. II.

Pointed indentation was not possible in case of AAFA because we were not able to distinguish a specific phase prior to indentation.

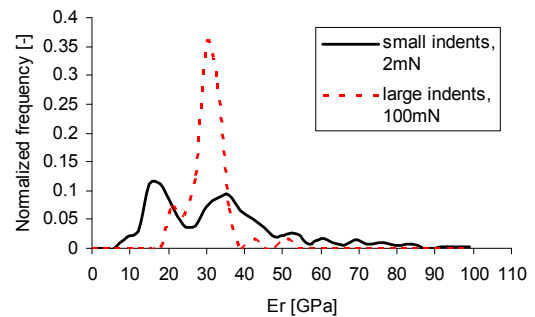


Figure 7. Histogram of reduced moduli in AAFA

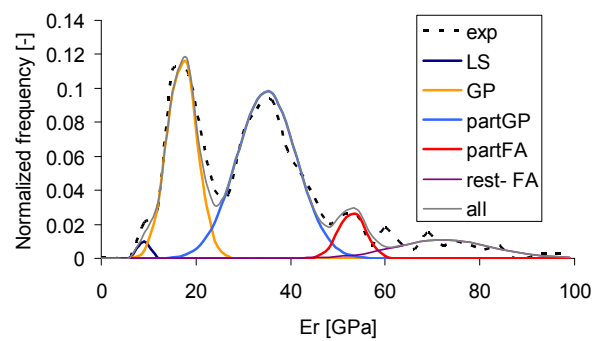


Figure 8. Deconvolution of individual phases in AAFA

7. Validation of results using image analysis

In order to validate our results from deconvolution, we employed also image analysis. Our aim was to separate material phases from ESEM images based on the pixel color. Multiple back-scattered electron images were taken in ESEM and thresholded (20 images for CP and 4 images for AAFA). Results of thresholding is summarized in Tabs I and II. It can be concluded that good correlation in terms of similar volume fractions was obtained for cement paste samples but for the low stiffness phase. However, results from image analysis include (i) pores that cannot be mechanically determined and (ii) deviation of the value indicate large scatter in the set of 20 images. That means that irregular pore structure cannot be sufficiently determined by means of mechanical testing. For the AAFA samples, the correlation is good for the main phases (GP, partGP) but again LS phase is not in good agreement with results from image analysis in which a pore structure is determined rather than the solid phase. It also seems that image analysis overestimates fly-ash phases (partFA and rest). This can be attributed to not sufficiently high number of images (only four were analyzed).

Table II
Results from deconvolution and image analysis of AAFA

	LS	GP	part GP	part FA	Rest
Mean E_r , GPa	7.15	15.53	33.50	51.49	70.85
s.d.	0.65	3.01	6.18	2.76	10.29
f_j , %	1	32	51	7	9
f_j^{IA} , %	4.2±1.5	23.7±2	45.3±4		26.8±2

E_r stands for reduced modulus; f_j stands for volume fraction received from deconvolution; f_j^{IA} stands for volume fraction received from image analysis

8. Conclusions

Micromechanical analysis using different testing strategies was demonstrated on two examples- cement paste and alkali activated fly-ash. For both cases, grid indentation using large indents give mean values with small deviations of a material compound. Mechanical properties are homogenized by the indenter from several phases. In case of using small indents, intrinsic phase properties are obtained in the form of

property histogram. Subsequently, individual phase properties can be deconvoluted from this histogram.

Pointed indentation to a specific material phase is the best solution but it can be performed only if the following conditions are satisfied: the phase is easily identifiable in optical microscope or it can be morphologically determined before indentation (e.g. by surface scanning). Otherwise, indents cannot be pointed to this phase even if the indent's size is smaller than the measured volume.

Support of the Czech Grant Agency (No. 103/06/1856) and Ministry of Education of the Czech Republic (MSM 6840770003) are gratefully acknowledged.

REFERENCES

1. Constantinides G., Ulm F.J., Van Vliet K.: *Mater. Struct.* 36, 191 (2003).
2. Constantinides G., Ulm F. J.: *Cem. Concr. Res.* 34, 67 (2004).
3. Constantinides G., Ulm F. J.: *J. Mech. Phys. Solids* 55, 64 (2007).
4. Constantinides G., Chandran K. S. R., Ulm F. J., Van Vliet K. J.: *Mater. Sci. Eng., A* 430, 189 (2006).
5. Oliver W. C., Pharr G. M.: *J. Mater. Res.* 7, 1564 (1992).
6. Šmilauer V., Bittnar Z.: *Cem. Concr. Res.* 36, 1708 (2006).
7. Vandamme M., Ulm F.-J.: *Int. J. Solid. Structur.* 43, 3142 (2006).
8. Velez K.: *Cem. Concr. Res.* 31, 555 (2001).

J. Němeček and K. Forstová (*Czech Technical University, Civil Engineering Faculty, Prague, Czech Republic*):
Micromechanical Analysis of Heterogeneous Structural Materials

This contribution is dedicated to the methodology used in the micromechanical analysis of heterogeneous materials. It is applied to two cases of structural materials: cement paste and alkali activated fly-ash. The paper contains several approaches how to test and evaluate data from nanoindentation. It is shown that different size of indents must be followed by different interpretation of results. In case of using small size indents it is possible to derive individual material phase properties by means of deconvolution from property histogram. Indentation to a specific phase can be used only in limited number of cases provided this phase can be determined optically or by scanning before the test. Nanoindentation results were also compared with similar results obtained from image analysis.

HODNOTENIE INDENTAČNÝCH A DEFORMAČNÝCH CHARAKTERISTÍK LASEROVÝCH ZVAROV

LUBOMÍR AMBRIŠKO^a, TOMÁŠ KANDRA^b a LADISLAV PEŠEK^a

^a Technická univerzita v Košiciach, Hutnícka fakulta, Katedra náuky o materiáloch, Park Komenského 11, 043 85 Košice,

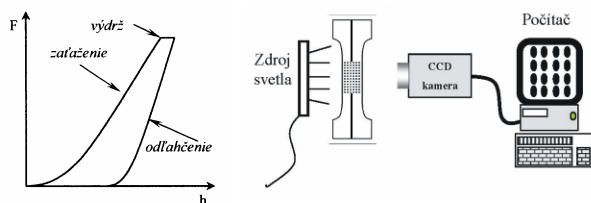
^b KOVOHUTY, a.s., Ulica 29. augusta 586, 053 42 Krompachy, Slovensko

lubomir.ambrisko@tuke.sk, ladislav.pesek@tuke.sk

Kľúčové slová: inštrumentovaná tvrdosť, videoextenzometria, laserové zvary

1. Úvod

Metóda DSI (Depth Sensing Indentation), inštrumentovaná tvrdosť, je založená na princípe priebežného monitorovania sily a hĺbky vpichu. Indentor je zaťažovaný silou, ktorá sa zvyšuje od nuly až po zvolenú maximálnu hodnotu F_{max} . Po dosiahnutí maximálnej sily nastáva fáza výdrž (môže, ale nemusí byť) a nasledovné odľahčenie. Výsledkom skúšky je indentačná krivka ako závislosť zaťažujúca sila F – hĺbka vpichu h (obr. 1). Z nej sa dá určiť tvrdosť a ďalšie mechanické vlastnosti¹.



Obr. 1. Indentačná krivka

Obr. 2. Princíp videoextenzometrie²

Videoextenzometria je bezkontaktná metóda, ktorej princípom je snímanie obrazu pomocou CCD (Charge-Coupled Device) snímača z povrchu skúšobného telesa (obr. 2). Teleso je osvetlené nebodovým zdrojom svetla. V snímanej oblasti sú vhodne nanosené kontrastné body (čierne body na svetlom povrchu vytvárajú požadovaný kontrast). Kontinuálnym snímaním v čase a zaznamenávaním súradníc ťažísk týchto bodov pomocou príslušného softvéru je možné vyhodnocovať deformácie medzi jednotlivými bodmi³.

Cieľom tohto príspevku je stanoviť indentačné a deformačné charakteristiky laserových zvarov a vzťahy medzi nimi.

2. Materiál a metodika práce

Pre experimenty boli použité zvary odobraté z hlbokotážnych laserovo zváraných prístrihov na mieru produkcie firmy Arcelor. Hrúbky a mechanické vlastnosti základ-

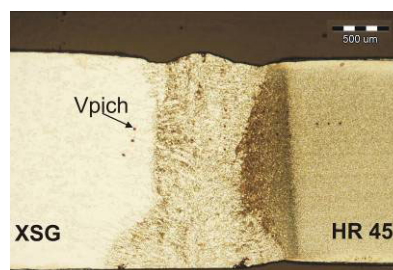
ných materiálov sú uvedené v tab. I a ich chemické zloženie je uvedené v tab. II.

Tabuľka I
Mechanické vlastnosti použitých ocelí

Akosť	Hrúbka [mm]	R_e [MPa]	R_m [MPa]	A [%]
XSG	1,95	182	299	45,2
HR 45	1,80	382	493	24,7

Tabuľka II
Chemické zloženie použitých ocelí

	Chemické zloženie [%]					
	C	S	N_2	Mn	P	Si
XSG	0,0013	0,0105	0,0017	0,082	0,011	0,006
	Al	Ni	Sn	Nb	V	Ti
HR 45	0,055	0,013	0,003	0,001	0,002	0,040
	C	S	N_2	Mn	P	Si
	0,1562	0,004	0,003	0,654	0,013	0,010
	Al	Ni	Sn	Nb	V	Ti
	0,035	0,015	0,005	0,001	0,002	0,001

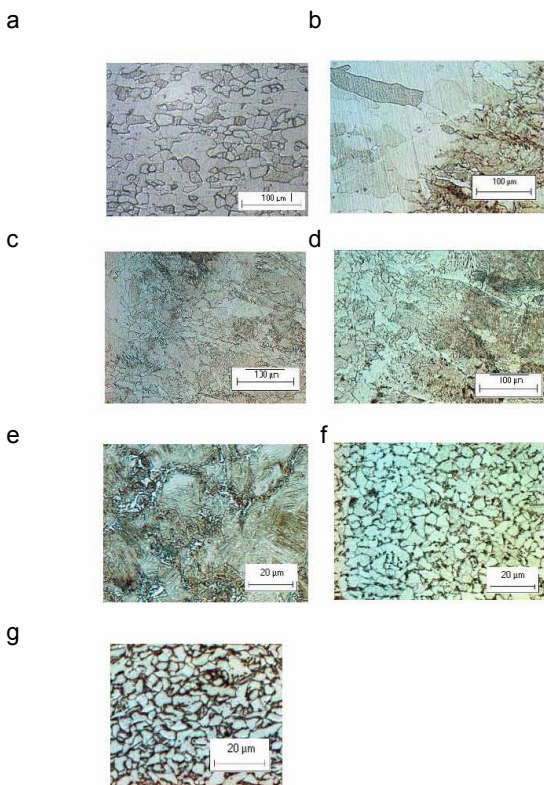


Obr. 3. Makroštruktúra zvarového spoja

Makroštruktúra zvarového spoja je zobrazená na obr. 3. Priemerná šírka TOO na strane ZM XSG je 0,43 mm, na strane ZM HR 45 je 0,41 mm. Mikroštruktúra jednotlivých oblastí je na obr. 4 a) – g).

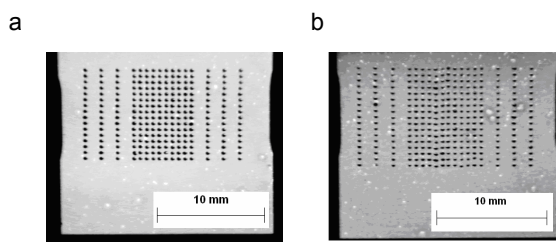
Indentačné charakteristiky laserových zvarov boli stanovené metódou DSI, určili sme: indentačnú tvrdosť (H_{IT}), Martensovu tvrdosť (HM), deformačnú indentačnú energiu celkovú (W), deformačnú indentačnú energiu elastickú (W_{el}) a deformačnú indentačnú energiu plastickú (W_{pl}). Indentácie na výbruse v rovine kolmej k osi zvaru boli realizované na zariadení Shimadzu DUH 202 Vickersovým indentorom pri zaťažení 490 mN (50 g), do jednotlivých oblastí zvarového spoja a základných materiálov, v línii rovnobežnej s povrchom plechu. V každej oblasti boli urobené 3 vpichy.

Deformačné charakteristiky: priečna deformácia ε_x (kolmo ku smeru zaťažovania) a pozdĺžna deformácia ε_y (v smere zaťažovania) pozdĺžne zvarových základných materiálov XSG a HR 45 boli stanovené videoextenzometrickou metódou. Skúšobné telesá na statickú skúšku ťahom boli vyrobené tak, že zvar bol rovnobežný s osou telesa, v tomto smere boli telesá zaťažené pri statickej skúške v ťahu. Pred samotným nanášaním kontrastných bodov, bol na povrch vzoriek nanesený tenký plastický film bielej farby, ktorý slúži na zvýšenie kontrastu medzi pozadím a kontrastnými bodmi (obr. 5). Minimálna vzdialenosť medzi stredmi bodov bola 0,6 mm a veľkosť bodov 0,44 mm.

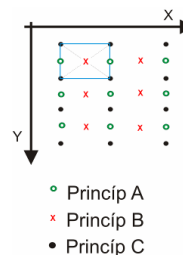


Obr. 4. Mikroštruktúra zvarového spoja (poradie XSG–ZVAR–HR 45); a) Základný materiál XSG tvorený feritickou nerovnomernou štruktúrou s výraznou textúrou po tvárnení za studena (♦ZM1-XSG, označenie podľa legendy obr. 8 a 9). b) Oblasť zhrubnutia feritického zrna. Nerovnomerná štruktúra (■Zhrubnuté zrna). c) Prechod polygonálneho feritu do oblasti tvorenej acikulárnym feritom (▲TOO1). d) Prechod z oblasti natavenia tvorenej acikulárnym feritom (×ZK) do oblasti tepelne ovplyvnenej na strane materiálu HR 45, kde vidieť bainitickú štruktúru. e) Detail, bainitická štruktúra – tepelne ovplyvnená oblasť materiálu HR 45 (*TOO2 – 1.časť). f) Oblasť prehriatia materiálu HR 45 do intervalu teplôt $A_1 - A_3$, kde vplyvom následného rýchleho ochladenia nastalo rovnomerné vylúčenie perlitu vo forme chumáčov na hraniciach feritických zŕn (+TOO2 – 2.časť). g) Jemnozrná rovnomerná feriticko-perlitická štruktúra základného materiálu HR 45 (–ZM2-HR 45)

Deformačné charakteristiky boli stanovené na dvoch skúšobných telesách: na medzi pevnosti a pre okamih tesne pred roztrhnutím (perforácia), ktoré sa líšili počtom nanesených bodov (PZZ-1 – 256 bodov, PZZ-2 – 324 bodov). Pre



Obr. 5. Konfigurácie nanesených kontrastných bodov; a) PZZ-1, b) PZZ-2



Obr. 6. Princípy VDTK

hodnotenie nameraných výsledkov bol vyvinutý program VDTK, ktorý bol využitý pre off-line hodnotenie deformačných charakteristik. Program VDTK poskytuje možnosť výberu z troch spôsobov výpočtu deformácií (obr. 6, A – úseky, B – elementy, C – posunutia). Deformácia na základe spôsobu A (v čase t , v smere Y) sa počíta ako relatívne predĺženie úsekov ohraničených kontrastnými bodmi (plné body na obr. 6). Výsledkom je hodnota deformácie, ktorá sa priradzuje zeleným bodom (prázdne body). Rovnako platí aj pre smer X . V prípade spôsobu B sa hodnota deformácie, vypočítaná ako priemerná hodnota deformácií rovnobežných susedných úsekov, priradí stred celého elementu (červený krížik). Spôsob C poskytuje možnosť výpočtu deformácie priamo pre kontrastné body z hodnôt ich posunutí u_x , u_y . Pre nekonečne malý prírastok deformácie platí:

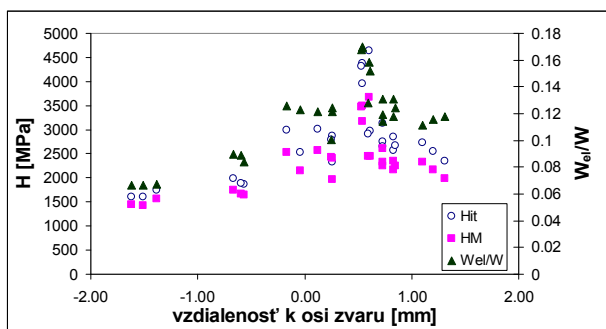
$$d\varepsilon_x = \frac{\partial(du_x)}{\partial x} \quad d\varepsilon_y = \frac{\partial(du_y)}{\partial y}$$

3. Výsledky experimentov

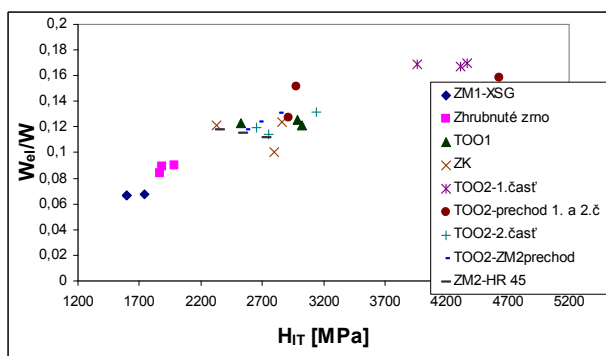
V jednotlivých oblastiach zvarového spoja bola vyhodnotená veľkosť Martensovej tvrdosti (HM), indentačná tvrdosť (H_{IT}) a pomer energií spotrebovanej na elastickú deformáciu a celkovej spotrebovanej energie (W_{el}/W); akumulovaná elastická energia môže byť významnou pri iniciácii a šírení trhlin. Priebehy jednotlivých veličín v závislosti od polohy voči osi zvaru sú zobrazené na obr. 7. Maximálna hodnota tvrdosti bola nameraná v TOO na strane materiálu HR 45 (obr. 8). Ide o oblasť, kde vplyvom zvaracieho cyklu došlo k ohrevu materiálu HR 45 nad teplotu A_{c3} a pri následnom chladnutí sa v štruktúre vylúčil bainit (obr. 4e). Zaujímavosťou je, že minimálne hodnoty tvrdosti neboli namerané v oblasti zhrubnutia feritického zrna, ale v základnom mate-

riáli XSG. Medzi hodnotami Martensovej a indentačnej tvrdosti bola zistená lineárna závislosť⁴.

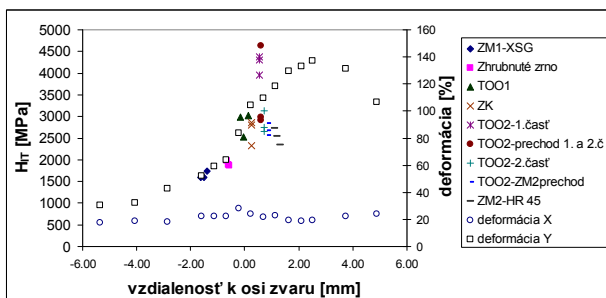
Pri obidvoch skúšobných telesách s pozdĺžnym zvarom nastala iniciácia lomu na strane materiálu HR 45, kde bola nameraná aj maximálna pozdĺžna deformácia ϵ_y . V čase perforácie bola maximálna deformácia na strane materiálu HR 45 približne dvakrát väčšia ako na strane materiálu XSG. Maximálna priečna deformácia ϵ_x bola nameraná v oblasti zhrubnutia feritického zrna. Pribeh deformácie cez oblasť maximálnej nameranej deformácie (po šírke skúšaného telesa), v závislosti od vzdialenosti k osi zvaru je znázornený na obr. 9.



Obr. 7. H_{IT} , HM a W_{el}/W v závislosti od vzdialenosti k osi zvaru



Obr. 8. Závislosť podielu elastickej indentačnej energie W_{el}/W od H_{IT}



Obr. 9. Pribeh deformácie (princíp C) a H_{IT} po šírke telesa PZZ-1perf

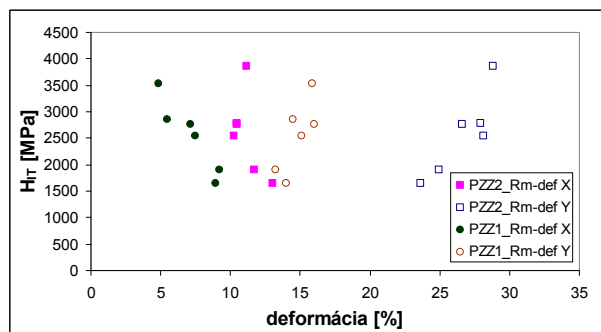
Deformácie ϵ_x a ϵ_y sme stanovili na medzi pevnosti a v okamihu tesne pred vznikom trhliny (perforáciou plechu). Na obr. 10 a 11 sú zobrazené závislosti tvrdosti H_{IT} od deformácie pre jednotlivé skúšobné telesá. Priemerné hodnoty boli priradené jednotlivým oblastiam zvarového spoja na základe ich vzdialenosti od osi zvaru. Dosiahnuť rovnakú hodnotu deformácie pri maximálnej sile na dvoch telesách je obťažné, pretože ťahový diagram je na F_{max} plochý. Hodnoty deformácii u PZZ-1 sú preto iné než u PZZ-2 a závislosti ϵ_x a ϵ_y pre jednotlivé telesá v obr. 10 sú rozdielne. Stav tesne pred perforáciou je definovateľný jednoznačnejšie a pre obe telesá tiež ľahšie porovnateľný, preto výsledky telies PZZ-1 a PZZ-2 lepšie súhlasia (obr. 11).

Vzťah medzi H_{IT} a lokálnou deformáciou má lineárny charakter pre jednotlivé skupiny bodov, obr. 10 a 11.

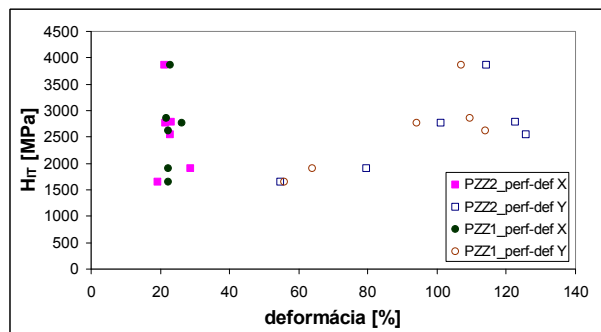
V rôznych miestach priečného prierezu skúšobného telesa je rôzna štruktúra a teda aj rôzna tvrdosť a rôzna schopnosť sa deformovať, susedné prierezy sú však rovnaké. Deformácia priečna ϵ_x pritom nie je po priereze vo svojom rozvoji obmedzovaná, pretože dva susedné prierezy majú, prechádzajúc cez ich šírku, rovnakú štruktúru. Deformáciu pozdĺžnu ϵ_y v danom mieste ovplyvňuje ale iná deformácia v susednom mieste toho istého prierezu.

Na medzi pevnosti je mäkkší materiál schopný sa viac rovnomerne deformovať v priečnom smere (väčšie hodnoty ϵ_x). Pre pozdĺžnu deformáciu ϵ_y platí opačne: tvrdší materiál sa deformaoval viac než materiál mäkkší.

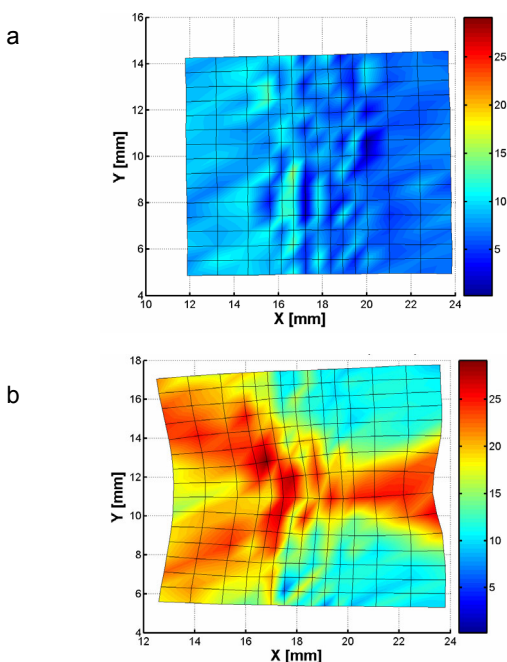
Porušenie (perforácia) nastáva na strane materiálu HR 45 (viď maximum na krivke „deformácie Y“ na obr. 9). V tom okamihu ostatné časti namáhaného prierezu (rôzne



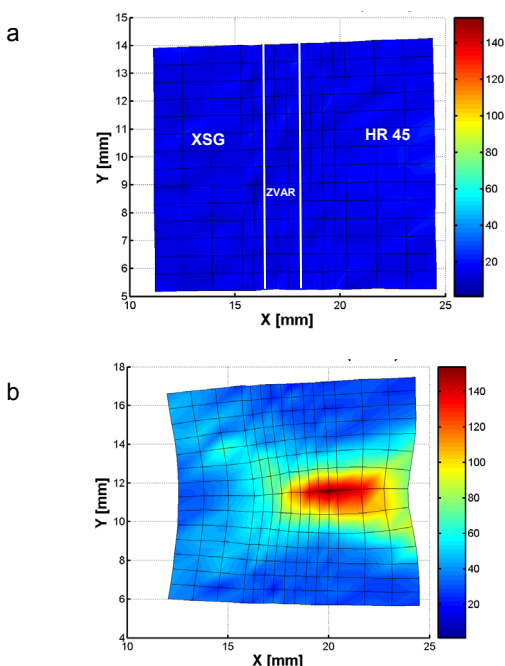
Obr. 10. Závislosť H_{IT} od deformácie (princíp C) na medzi pevnosti



Obr. 11. Závislosť H_{IT} od deformácie (princíp C) pred perforáciou



Obr. 12. Mapy rozloženia priečnej deformácie (princíp C) pre PZZ-1; a) ϵ_x [%] na R_m , b) ϵ_x [%] pred perforáciou



Obr. 13. Mapy rozloženia pozdĺžnej deformácie (princíp C) pre PZZ-1; a) ϵ_x [%] na R_m , b) ϵ_x [%] pred perforáciou

časti zvarového spoja) majú nevyčerpanú zásobu svojej plasticity, a preto je ich príslušná deformácia menšia, než by im prislúchalo v okamihu porušenia.

Tesne pred porušením (perforáciou) je priečna deformácia ϵ_x cca 20 % pre všetky, rôzne tvrdé, oblasti zvarového spoja. Pre pozdĺžnu deformáciu ϵ_y platí podobne ako na medzi pevnosti: tvrdší materiál sa deformoval viac než materiál mäkkší.

Na obr. 12 a 13 sú znázornené mapy pozdĺžnej a priečnej deformácie telesa PZZ-1. Rozloženie pozdĺžnych deformácií na medzi pevnosti je homogénne, hodnoty priečných deformácií lepšie vizualizujú polohu zvaru. Stupnica na pravej strane jednotlivých máp nie je rovnaká pre všetky obrázky.

Na PZZ-1 pred perforáciou boli vyhodnotené deformačné charakteristiky tromi spôsobmi. Tab. III uvádza porovnanie maximálnych hodnôt deformácií. Pre porovnanie bolo vybraté miesto výskytu maximálnej deformácie. Hodnoty ϵ_x pre spôsoby A a B sa líšia o 5 %, pre B a C o 4 % a pre spôsoby vyhodnocovania C a A sa líšia o 1,3 %. Hodnoty ϵ_y pre spôsoby A a B sa líšia o 1,3 %, pre B a C o 11 % a pre spôsoby vyhodnocovania C a A sa líšia o 12 %.

Tabuľka III
Porovnanie spôsobov výpočtu deformácií

Spôsob	ϵ_x [%]	ϵ_y [%]
Úseky (A)	29,4	155
Elementy (B)	27,9	153
Posunutia (C)	29,0	137

4. Záver

Zvar je vždy potenciálne najslabším miestom konštrukcie, preto poznať lokálne vlastnosti jeho jednotlivých oblastí je dôležité. Maximálne tvrdosti H_{IT} a HM boli namerané v tepelne ovplyvnenej oblasti na strane materiálu HR 45. Minimálna H_{IT} bola nameraná v základnom materiáli XSG. Podiel W_{el}/W spočiatku lineárne rastie s H_{IT} a dosahuje maximálne hodnoty pre oblasť $H_{IT} = 4000\text{--}4500$ MPa. Ďalším zvyšovaním H_{IT} podiel W_{el}/W nerastie.

Najväčšia priečna deformácia tesne pred porušením bola nameraná v oblasti zhrubnutia feritického zrna (28 %). Porušenie sa iniciovalo na strane materiálu HR 45, kde bola nameraná aj maximálna pozdĺžna deformácia (137 %).

Rozvoj deformácie ϵ_y v určitej oblasti zvarového spoja je ovplyvňovaný rozvojom deformácie v susednom mieste daného prierezu, ktoré má inú štruktúru a iné vlastnosti. Na medzi pevnosti ako aj pred perforáciou rastúca pozdĺžna deformácia ϵ_y má za následok nárast tvrdosti H_{IT} . Rozvoj deformácie ϵ_x po priečnom priereze skúšobného telesa nie je obmedzený susedným prierezom a preto mäkkší materiál je schopný sa viac deformovať. Oblasti zvaru s rôznou tvrdosťou H_{IT} sa v priečnom smere v okamihu lomu deformujú (ϵ_x) rovnako.

Príspevok vznikol pri riešení projektu VEGA No. 1/4149/07 a APVV – 0326 – 07.

Autori príspevku ďakujú firme Noble International Senica s.r.o., ktorá poskytla experimentálny materiál.

LITERATÚRA

1. Fischer-Cripps A. C.: *Nanoindentation*. Springer, New York 2002.
2. Gazdag Š., Pešek L.: *Dehnungsfelder und Lokalisation der Dehnungen in dünnen Stahlblechen*, 13, *Internationaler Studententag der Metallurgie, Leoben 2005*, s. 149–156.
3. Spinka O.: *Videoextensometer ME46*, Messphysik Laborgeräte, GmbH, Fürstenfeld 2000.
4. Pešek L., Vadasová Z., In: „*Lokální mechanické vlastnosti 2006*“, Plzeň – Nečtiny, 8.-10. 11. 2006, ZČU v Plzni, s. 126–133.

E. Ambriško^a, T. Kandra^b, and L. Pešek^a (^a *Technical university of Košice, Faculty of metallurgy, Department of material science*, ^b *KOVHUTY, a.s., Krompachy, Slovakia*):
Evaluation of Indentation and Deformation Characteristics of Laser Welds

Two progressive methods were used for evaluation of indentation and deformation characteristics of laser welds. Depth sensing indentation techniques (DSI) is used for determination of local mechanical properties of laser welds. Mechanical properties such as indentation hardness (H_{IT}), Martens hardness (HM), total indentation energy (W), elastic indentation energy (W_{el}) and plastic indentation energy (W_{pl}) for each individual regions of the weld had been established. Videoextensometry was used to determine longitudinal and transversal components of the normal strain. Relations between indentation and deformation characteristics had been established.

SIMULÁCIE ECAP PROCESU ZLIATINY EN AW 2014 POMOCOU MKP

JANA BIDULSKÁ^a, RÓBERT KOČIŠKO^a, TIBOR KVAČKAJ^a, RÓBERT BIDULSKÝ^b a MARCO ACTIS GRANDE^b

^a Katedra tvárnenia kovov, Hutnícka fakulta, Technická univerzita v Košiciach, 042 00, Košice, Slovensko, ^b Politecnico Torino, Alessandria Campus, 15 100, Alessandria, Italy
 jana.bidulska@tuke.sk, robert.kocisko@tuke.sk,
 tibor.kvacaj@tuke.sk, robert.bidulsky@polito.it

Kľúčové slová: Al zliatina, mechanické vlastnosti, ECAP, MKP, DEFORM 2D

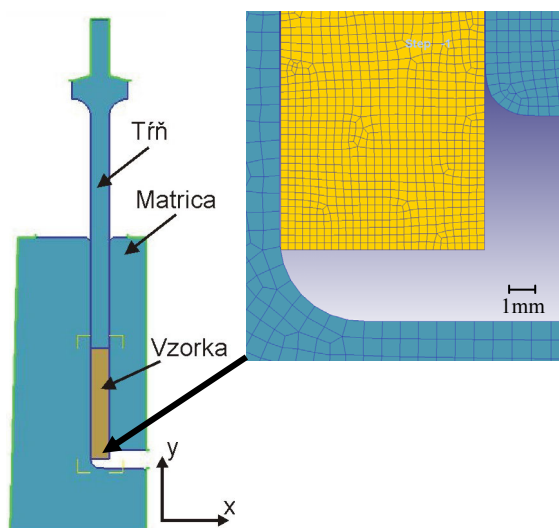
1. Úvod

Equal Channel Angular Pressing (ECAP) – pretlačovanie cez kanál rovnakého prierezu je pomerne jednoduchá SPD (Severe Plastic Deformation) metóda na získavanie UFG (Ultra Fine Grain) štruktúry na úrovni 70–500 nm (cit.¹). Táto metóda, ktorú v roku 1977 vynášiel Segal², je schématicky zobrazená na obr. 1. Princíp tejto spracovateľskej metódy spočíva v pretlačovaní vzorky cez špeciálnu maticu, ktorá obsahuje dva navzájom sa krížiace kanály (vertikálny a horizontálny) rovnakého prierezu. ECAP matica je definovaná: priemerom, uhlom Φ – uhol medzi kanálmi, ktorý sa najčastejšie pohybuje od 90° do 120° a uhlom ψ – uhol na vonkajšom rohu matrice. Efektívna deformácia po N prechodoch sa počíta podľa vzťahu (1):

$$\varepsilon_N = \frac{2N}{\sqrt{3}} \cdot \cot \varphi \quad (1)$$

kde N je počet pretlačení, φ uhol medzi kanálmi.

V súčasnej dobe, vďaka rýchlo rozvíjajúcej sa výpočtovej technike sa vo veľkej miere používajú softvérové produkty pre analýzu tvárniacich procesov. Tie nám poskytujú lokálne detailné informácie o priebehu plastickej deformácie v materiáli, týkajúce sa distribúcie deformácie, rýchlosti deformácie, napätí, ako aj informácie o vonkajšom zaťažení tvárniacich nástrojov. Na matematické simulácie sa používajú rôzne softvérové produkty, ako napr. Ansys, Forge, Marc, SuperForm, SuperForge a Deform. Softvérový produkt Deform 2D a Deform 3D (cit.³), je založený na MKP (Metóda Konečných Prvkov). Deform 2D je vhodný na riešenie osov symetrických úloh v oblasti veľkých objemových plastickej deformácií. Umožňuje súhrn interakcií medzi deformáciou, tepelným spracovaním, transformáciami a difúziou. Vhodným nástrojom, ktorý predstavuje veľkú výhodu oproti iným spomenutým simulačným produktom, je automatický generátor siete (AGS). Najdôležitejší vstupný údaj pre matematickú simuláciu tvárneného materiálu je napäťovo-deformačná kriv-



Obr. 1. Geometria ECAP matrice s detailom na hustotu siete

ka (σ - ε), od ktorého závisí presnosť výpočtu. Tento údaj je možné použiť buď z programovej databázy, alebo z experimentálne stanovenej krivky σ - ε . Experimentálne krivky σ - ε sa získavajú z laboratórnych skúšok tvárnosti: ťahom, krutom, resp. tlakom.

Predmetom príspevku je porovnanie výsledkov matematických simulácií ECAP procesu materiálu EN AW 2014, ktorého krivky spevnenia boli do programu Deform 2D implementované pomocou výberu krivky σ - ε z programovej databázy a experimentálne stanovenej závislosti σ - ε .

2. Materiál a experimentálne metodiky

Pre experimentálne štúdium bola použitá hliníková zliatina EN AW 2014.

Boli použité nasledovné experimentálne metodiky:

- experimentálna závislosť σ - ε pre materiál EN AW 2014 bola získaná po aplikácii nasledovného tepelne-deformačného cyklu:
 - valcovanie vstupného materiálu za tepla na laboratórnej valcovacej stolici DUO 210 pri teplote 460 °C,
 - tepelné spracovanie: rozpúšťacie žihanie pri teplote 520 °C s časom výdrže 2,5 h, s následným kalením do vody.

Statická skúška v ťahu bola realizovaná na zariadení FP 100/1 pri rýchlosti zaťaženia $v = 0,15 \text{ mm min}^{-1}$, čo zodpovedá rýchlosti deformácie $\dot{\varepsilon} = 2,5 \cdot 10^{-4} \text{ s}^{-1}$, v súlade s STN 420310 (STN EN 10002-1).

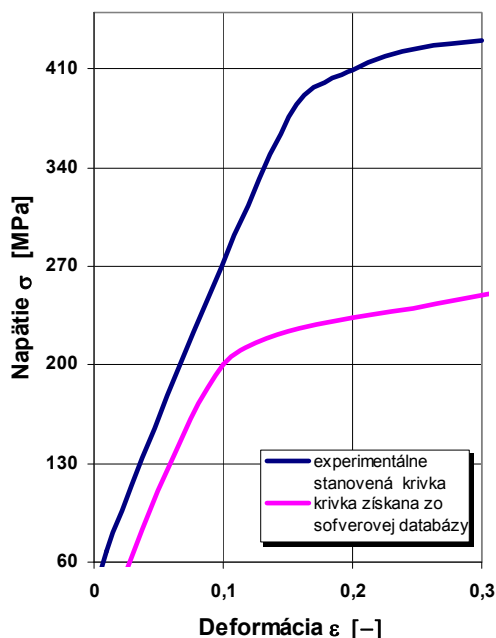
- matematické simulácie v SW produkte DEFORM 2D.

Geometria ECAP matrice pre simuláciu je zobrazená na obr. 1. Pozostáva z kruhového kanála s priemerom $\phi = 10 \text{ mm}$,

uhla medzi kanálmi $\Phi = 90^\circ$, vonkajším polomerom $R = 5$ mm a vnútorným polomerom $r = 0$ mm. Vzorka bola v tvare tyče s priemerom $\phi = 10$ mm o dĺžke $l = 60$ mm. Dĺžka trňa bola $l_{\text{trňa}} = 105$ mm, ktorý mal v procese pretlačovania konštantnú rýchlosť 1 mm s^{-1} . Trecie podmienky medzi jednotlivými objektmi boli definované podľa Coulomba, s koeficientom trenia $f = 0,12$. Teplota pretlačovania bola 20°C . Oblasť riešenia úlohy ECAP zariadenia (matrica, trň a pretlačovaná vzorka) boli popísané konečnoprvkovou sieťou v tvare štvoruholníkov. Hustota siete určuje presnosť výpočtu a čas výpočtu. Ak je objekt popísaný veľmi malým počtom elementov, tak výpočet je z hľadiska strojového času krátky, ale presnosť výpočtu je veľmi malá. Naopak, ak je hustota siete príliš vysoká, strojový čas sa niekoľkonásobne predĺži,

Tabuľka I
Materiálové charakteristiky vzorky a nástrojov

Vzorka	Databáza	Experiment
Plastické	údaje z σ - ε kriviek	
Youngov modul, MPa	68900	70000
Elastické		
Poissonova konštanta	0,33	0,33
teplotná expanzia, K^{-1}	$2,2 \cdot 10^{-5}$	$2,2 \cdot 10^{-5}$
tepelná vodivosť, $\text{kW m}^{-1} \text{K}^{-1}$	180,2	180,2
Tepelné		
tepelná kapacita, $\text{kJ kg}^{-1} \text{K}^{-1}$	2,433	2,433
Kritérium porušenia	Cockcroft-Latham	



Obr. 2. σ - ε krivky spevnenia

prícom presnosť výpočtu je zbytočne vysoká. Vzhľadom na geometriu a veľkosť jednotlivých objektov je potrebné zvoliť optimálnu hustotu siete. Vzhľadom na čas výpočtu a jeho presnosť autori⁴⁻⁶ odporúčajú, že je postačujúce vzorku s priemerom $\phi = 10$ mm popísať približne 20 elementmi. V simulovanom prípade bola vzorka s priemerom $\phi = 10$ mm a dĺžke $l = 60$ mm pokrytá pomocou 3000 elementov, čo predstavuje 28 elementov na priemer vzorky, ako je to v detailnom zábere vidieť na obr. 1. Na styčných plochách bola sieť zhustená, čo umožnilo lepšie popísať zložitú geometriu napr. v oblasti polomerov.

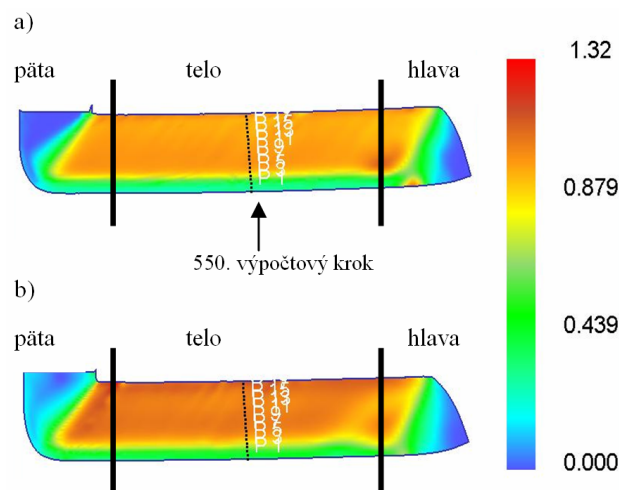
Nástroje ECAP zariadenia, t.j. matrica a trň boli v matematickej simulácii popísané ako elastické objekty, ktorým bola priradená materiálová charakteristika nástrojovej ocele. Materiálová charakteristika nástrojovej ocele vysoko prevyšuje materiálovú charakteristiku tvárneného materiálu. Vzorka bola popísaná ako elasto-plastický objekt, ktorého materiálové charakteristiky sú: $R_{p0,2} = 157$ MPa, krivka σ - ε , Youngov modul pružnosti a tepelné vlastnosti.

Výsledky matematických simulácií ECAP procesu na materiáli EN AW 2014 boli porovnávané na základe dvoch prístupov pre voľbu krivky σ - ε : krivka vybraná z programovej databázy podľa normy EN a krivka dosadená z experimentálnych skúšok. Priebeh obidvoch kriviek σ - ε je zobrazený na obr. 2, z ktorého vyplýva rozdiel v hodnotách napätí. V tab. I sú uvedené materiálové charakteristiky oboch vzoriek.

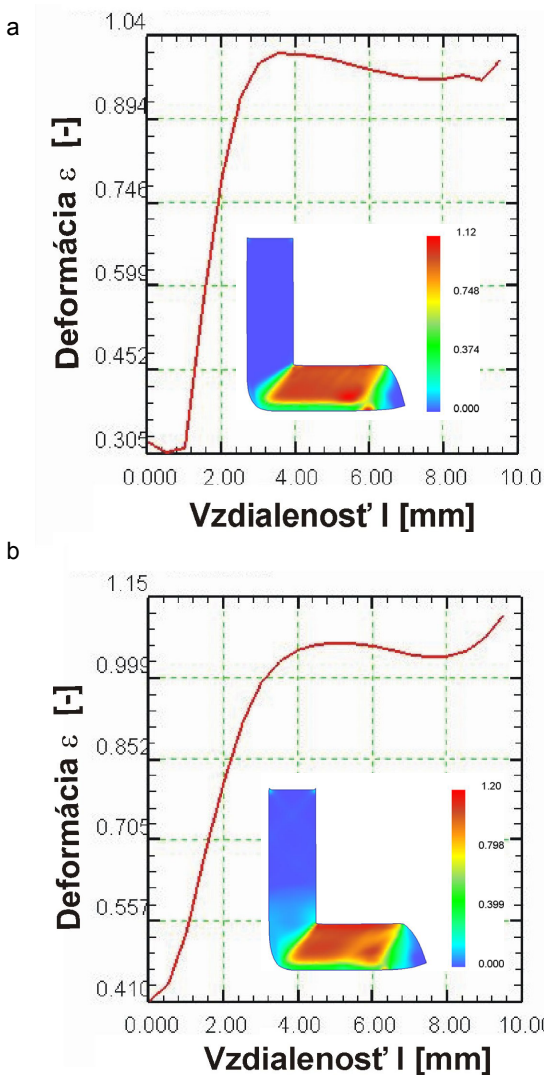
3. Analýza dosiahnutých výsledkov

Rozloženie intenzity plastickej deformácie po jednom ECAP prechode pre obe sledované materiálové charakteristiky je zobrazené na obr. 3.

Na obr. 3 vidieť, že intenzita plastickej deformácie je nerovnomerne rozložená po priečnom priereze aj po dĺžke vzorky. Po dĺžke vzorky je možné intenzitu plastickej deformácie rozdeliť do troch základných oblastí: hlava – nerovno-



Obr. 3. Distribúcia a intenzita plastickej deformácie vo vzorke pre: a) materiál definovaný z databázy, b) materiál definovaný na základe experimentálne stanovenej krivky σ - ε



Obr. 4. Distribúcia intenzity plastickej deformácie po priečnom priereze vzorky v 550. výpočtovom kroku pre: a) materiál definovaný z databázy, b) materiál definovaný na základe experimentálne stanovenej σ - ε krivky

mernosť deformácie je spôsobená nerovnomerným tokom materiálu pri prechode z vertikálneho kanála do horizontálneho, telo – ustálený stav plastickej deformácie, päta – nerovnomernosť deformácie je spôsobená neúplným pretlačením vzorky cez kanál. Nerovnomernosť intenzity plastickej deformácie sa najviac koncentruje do spodnej časti vzorky. Podobné výsledky boli dosiahnuté aj v iných prácach⁴⁻⁷. Materiálové vlastnosti po ECAP spracovaní sa výlučne robia len z oblasti tela.

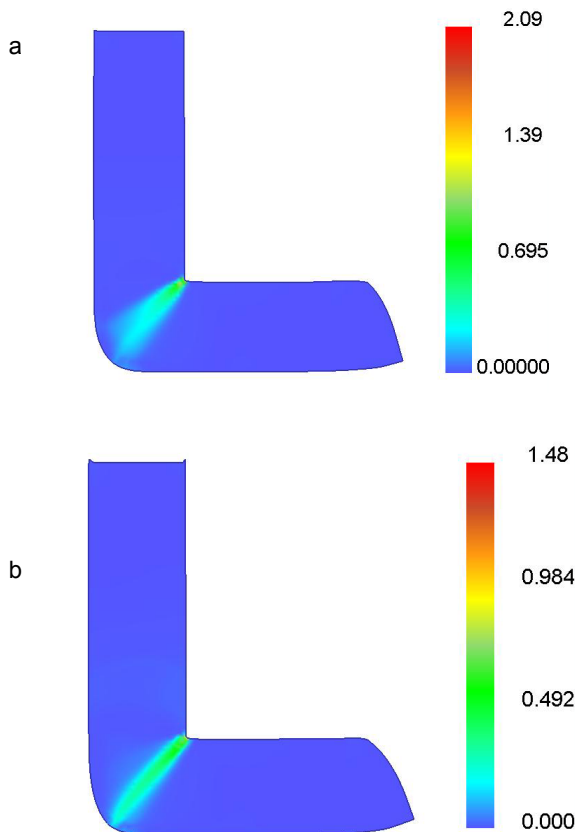
Na obr. 4 je zobrazená distribúcia intenzity plastickej deformácie po priečnom priereze vzorky v 550. výpočtovom kroku (v ustálenom pásme plastickej deformácie) pre obidve sledované materiálové charakteristiky.

Lokálne zmeny v distribúcii plastickej deformácie sú

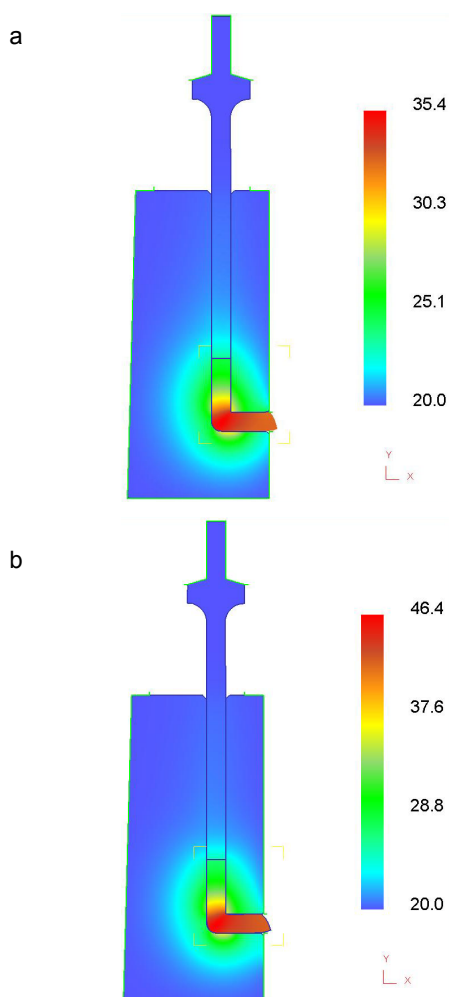
pozorované len v oblasti dolného polomeru, kde v hĺbke 1 mm pod povrchom vzorky je rozdiel efektívnej deformácie $\approx 0,1$. To znamená, že vstupné údaje napäťovo-deformačných kriviek nemajú podstatný vplyv na distribúciu a intenzitu plastickej deformácie po priečnom priereze.

Na obr. 5 je zobrazená distribúcia intenzity rýchlosti plastickej deformácie pre obidve sledované materiálové charakteristiky. Rýchlosť deformácie vymedzuje oblasť plastickej deformácie resp. zónu plastickej deformácie (ZPD)⁶. Na obr. 5 jednoznačne vidieť, že rýchlosť plastickej deformácie je sústredená v úzkom pásme – v zóne plastickej deformácie (ZPD). Dôležitosť ZPD z hľadiska rozloženia plastickej deformácie po celej vzorke potvrdili aj autori^{4,5}. Lokálne zmeny z hľadiska porovnania obidvoch sledovaných materiálov sú evidentné aj v závislosti na rýchlosti deformácie. Rýchlosť deformácie je rozdielna v kroku 550, kde v materiáli z databázy bolo dosiahnuté v oblasti vnútorného polomeru rýchlosti deformácie vyššej o 29 %, v porovnaní s druhým prípadom. Tento rozdiel už nie je možné zanedbať.

Na obr. 6 je zachytený vývoj teploty v ECAP procese. Z obr. 6 vyplýva nárast teploty v priebehu procesu z pôvodnej teploty okolia na 35,5 °C pre materiál definovaný z databázových údajov a na 46 °C pre materiál s experimentálne stanovenu materiálovou charakteristikou. Nárast teploty súvisí



Obr. 5. Distribúcia intenzity rýchlosti plastickej deformácie po priečnom priereze vzorky v 550. výpočtovom kroku: a) materiál definovaný z databázy, b) materiál definovaný na základe experimentálne stanovenej krivky σ - ε



Obr. 6. Vývoj deformačného tepla a ohrev tvárniacich nástrojov pre: a) materiál definovaný z databázy, b) materiál definovaný na základe experimentálne stanovenej krivky σ - ϵ

s premenou časti práce plastickej deformácie na teplo. Rozdiel teplôt závisí na krivkách spevnenia, reprezentuje nezanedbateľný vplyv, avšak teplota vzorky ani v jednom prípade nedosiahla úroveň nástupu uzdravovacích procesov skúmaného materiálu. V simulácii sa uvažovalo aj s prestupom tepla, čím môžeme sledovať aj ohrev tvárniacich nástrojov, tak ako to vidieť na uvedenom obrázku. Teplota tvárniaceho nástroja by nemala presiahnuť jeho popúšťaciu teplotu.

4. Záver

Detailný rozbor výsledkov simulácie ECAP procesu

hliníkovej zliatiny EN AW 2014 pomocou simulačného programu DEFORM 2D ukázal, že z hľadiska predikcie jednotlivých premenných počas tvárnenia materiálu bol v niektorých prípadoch (intenzita rýchlosti plastickej deformácie a teploty) značný rozdiel, ak bol materiál zadaný zo softvérovej databázy, alebo definovaný na základe experimentálne stanovenej krivky σ - ϵ . Spôsobené zmeny sa môžu vysvetliť lepším poznaním materiálových charakteristík zo skúšky ťahom, pretože materiál v sebe nesie všetky stopy predchádzajúcich technologických operácií a použitie údajov z programu DEFORM 2D nemusí v plnej miere zodpovedať experimentálnemu materiálu. Z tohto dôvodu je nevyhnutné pri simulácii procesu vychádzať z poznania materiálových charakteristík, ktoré sa získajú pomocou laboratórnych skúšok.

Autori ďakujú agentúre APVV (Projekt APVV-20-027205) za podporu.

LITERATÚRA

1. Kvačkaj T., Zemko M., Kuskulič T., Kočiško R., Besterčí M., Dobatkin S.V., Molnárová M.: *High Temp. Mater. Process.* 26, 147 (2007).
2. Segal V. M., Reznikov V. I., Drobyshevskiy A. E., Kopylov V. I.: *Russian Metal.* 1, 99 (1981).
3. Kvačkaj T.: *Acta Metallurgica Slovaca* 2, 160 (2002).
4. Kvačkaj T., Zemko M., Kočiško R., Kuskulič T., Pokorný I., Besterčí M., Sulleiová K., Molnárová M., Kováčová A.: *Kovove Mater.* 45, 249 (2007).
5. Kočiško R., Zemko M., Kuskulič T., Kvačkaj T., Kováčová A.: *Acta Metallurgica Slovaca* 13, 397 (2007).
6. Li S., Bourke M. A. M., Beyerlein I. J., Alexander D. J., Clausen B.: *Mater. Sci. Eng.* 382 A, 217 (2004).
7. Leo P., Cerri E., De Marco P. P., Roven H. J.: *J. Mater. Proc. Techn.* 182, 207 (2007).

J. Bidulská^a, R. Kočiško^a, T. Kvačkaj^a, R. Bidulský^b, and M. Actis Grande^b (^aDepartment of Metals Forming, Faculty of Metallurgy, Technical University of Košice, Košice, Slovakia ^bPolitecnico Torino, Alessandra Campus, Alessandria, Italy): **Simulations of ECAP Process of EN AW 2014 Using FEM**

The finite element method (FEM) is a proven and reliable technique for analyzing various forming processes, including heat treatment and ECAP. The plastic deformation behaviour of the materials during the ECAP process with a round die corner angle (90°) and a frictionless condition was investigated using the commercial two-dimensional rigid-plastic finite element code (DEFORM 2D). The main aim of the present work were provided information concerning the distribution of effective strains, strain rates, effective stresses and temperatures in the EN AW 2014 material.

IMPROVED FATIGUE RESISTANCE OF SINTERED STEELS VIA LOCAL HARDENING

RÓBERT BIDULSKÝ^a, MARCO ACTIS GRANDE^a, and MARGITA KABÁTOVÁ^b

^a Politecnico Torino, Alessandria Campus, 15100 Alessandria, Italy, ^b Institute of Materials Research, Slovak Academy of Sciences, 040 11 Košice, Slovakia
 robert.bidulsky@polito.it, actis.grande@polito.it, mkabatova@imrnov.saske.sk

Key words: prealloyed sintered steel, shot peening, fatigue, fracture

1. Introduction

The current status of powder metallurgy marked demands for either a reduction of costs or a sensible increase in properties. This concept applies, especially in the automotive sector, where the average weight of PM parts per car is now nearly 10 kg and a growth of 37 % is assumed to be reached in 10 years¹. The increase of properties could affect the design as well as the customer's demands but can be obtained only through new tendency and technological innovation and/or through the application of either new or adapted solutions.

Modification of density and microstructure, via classical route as pressing and sintering, can be successfully achieved for the fatigue limits of powder metallurgy steels at about 300 MPa average², this means that secondary operations are generally necessary to reach the higher fatigue properties. If compared to wrought steels^{3–5}, fatigue behavior of sintered steels is more complicated and depends on some factors related to sintered microstructures, such as pore agglomerates⁶. Fatigue properties of sintered steels depend on plasticity and strength of microstructures, as well as porosity. The pores act as crack initiators, the distribution of stress is inhomogeneous across the cross section of the investigated material and reduces the effective load bearing area. Both the morphology and distribution of pores have a significant effect on the mechanical behavior of powder metallurgy steels. Two types of porosity are typically observed in sintered materials^{7,8}: interconnected and isolated porosity. Interconnected porosity has more pronounced effect on properties than isolated porosity. Relationship to strength is expressed by ratio between fatigue strength and tensile strength. Ratio between fatigue strength and tensile strength, σ_C/R_m , is close to 0.38 (ref.⁹).

A suitable modification of functional surfaces may determine a sensible upgrade in the required properties of low alloyed steel. Shot peening is an industrial process often used to improve the component properties^{10–13}, especially fatigue life and fatigue strength.

In powder metallurgy area, shot peening is a relatively new technological solution for higher strength sintered materials, especially in fatigue performance. Nakazawa et al.¹⁴ tested the sub gear (in order to replace forging by powder

metallurgy) through the addition of the shot peening operations; the bending fatigue strength (parts were tested using test rig and motored engine test) was improved by 30 %. Additional researchers evaluated results Ancorsteel 1000 B with 2 % copper and 0.9 % graphite and showed that by optimising the controlled shot peening parameters, the endurance limit of sintered steel powder metal alloys can be raised by 16 % and 22 % (ref.¹⁵). Automotive components such as gears, sprockets and connecting rods are excellent candidates for powder metallurgy and controlled shot peening.

The aim of this work is to determine the effect of local hardening cause by surface modification on the fatigue failure resistance. Fatigue strength was evaluated by Wöhler curves for the plane bending fatigue tests on unnotched specimens of as-sintered and shot peened alloys.

2. Material and experimental procedure

Commercially pre-alloyed water-atomised Höganäs Fe-(Cr, Mo) powder (Astaloy CrL, which contains 1.5 % Cr and 0.2 % Mo) was used as base material. The other commercial raw materials were CR 12 graphite powder and HW wax powder as lubricant. Graphite was added in mixture as 0.5 % and 0.7 %. Final powder mixtures were homogenized in a Turbula mixer. Two different specimen types, compacted at 600 MPa to a green density of $\sim 7.0 \text{ g cm}^{-3}$, were prepared: “dog-bone” tensile (ISO 2740) and fatigue (ISO 3928) specimens. Formulation and processing parameters of the tested alloys are presented in Table I.

Sintering was carried out in laboratory tube furnace in an atmosphere of pure gases 75 % N₂ + 25 % H₂. The sintering temperature was 1180 °C for 60 minutes. Heating and cooling rates were 10 °C min⁻¹. The surface modifications were carried out on laboratory testing apparatus. Parameters of testing apparatus were steel granulate S11 with diameter $d_z = 0.6 \text{ mm}$, angle between shot stream and peened surface 90°, shot velocity $v_{7000} = 71 \text{ m s}^{-1}$. Specimens were tested in static tensile test on a ZWICK 1387 machine, extension rate = 0.1 mm min⁻¹. Fatigue tests were carried out in symmetric plane bending at $R = -1$, using SCHENCK PWON testing apparatus. The maximum cycle number was 10⁷. Batches of 15 specimens were tested.

Table I
Formulation and processing parameters

Material	State	Sintering [°C min ⁻¹]
Astaloy CrL + 0.5C	as-sintered	1180 / 60
Astaloy CrL + 0.5C	shot-peened	1180 / 60
Astaloy CrL + 0.7C	as-sintered	1180 / 60
Astaloy CrL + 0.7C	shot-peened	1180 / 60

The profile surface roughness, Ra, was measured by Hommel Tester T1000 profilometer.

Light and scanning microscopy were employed for microstructural evaluations. For optical microscopy, samples were individually mounted, mechanically polished and finally etched at room temperature using a Nital reagent. Scanning microscopy was carried out using SEM JEOL 7000F.

3. Results and discussions

3.1. Surface roughness

The implementation of plastic deformation via shot peening caused profile unevenness. The profile unevenness was expressed by the arithmetical mean deviation of the profile surface roughness; R_a . The profile surface roughness is the average arithmetical deflection of all unevenness from the central line in the measured length^{16–18}. The average results from 5 measurements of the profile surface roughness are presented in Table II.

Table II
Average values of surface roughness

Material	State	R_a [μm]
Astaloy CrL + 0.5C	as-sintered	1.31 ± 0.17
Astaloy CrL + 0.5C	shot-peened	7.56 ± 0.23
Astaloy CrL + 0.7C	as-sintered	1.32 ± 0.19
Astaloy CrL + 0.7C	shot-peened	7.21 ± 0.21

3.2. Properties and microstructures

Mechanical properties of prealloyed sintered Astaloy CrL steels are presented in Fig. 1.

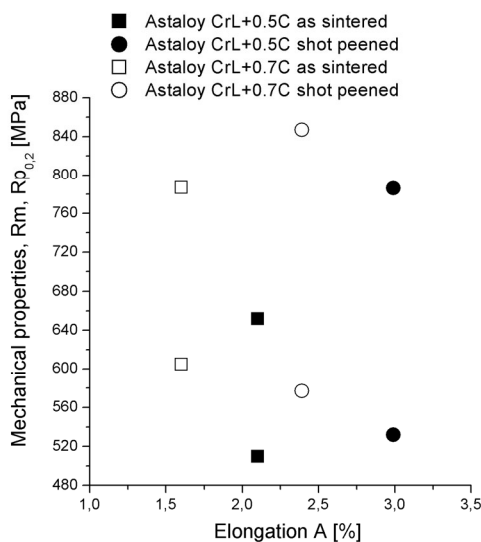


Fig. 1. Mechanical properties of investigated materials

The

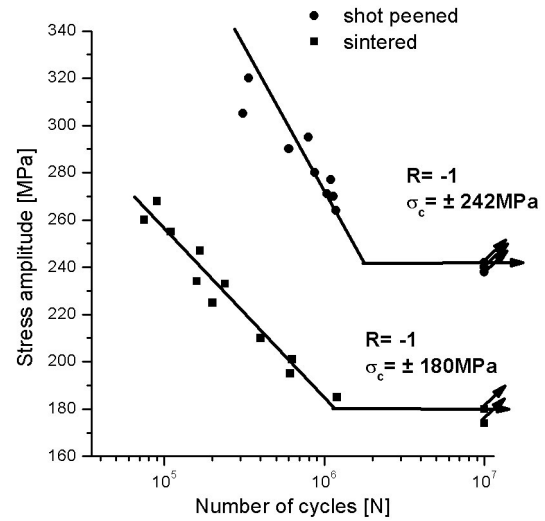


Fig. 2. S-N diagram for Astaloy CrL + 0.5 C steels

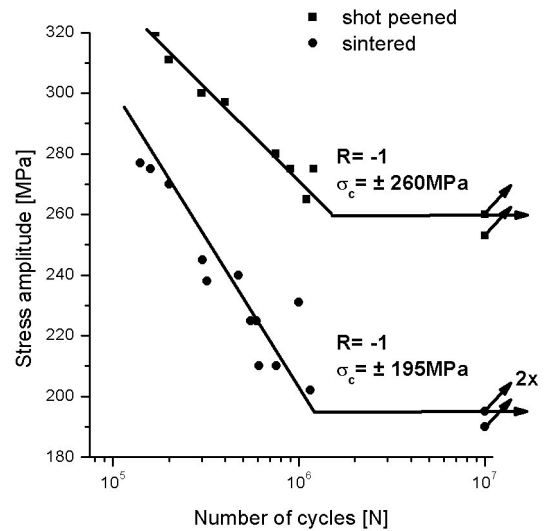


Fig. 3. S-N diagram for Astaloy CrL + 0.7 C steels

S-N curves of investigated materials are presented in Fig. 2 and 3.

Prealloyed Astaloy CrL with 0.7 % C is a material with good combination of mechanical properties and fatigue strength. The observed rankings in fatigue strength of the as-sintered and shot peened states are readily explained by the different microstructures due to different processing conditions. Microstructure of Astaloy CrL with 0.5 % C consist of mainly fine pearlite with areas of ferrite and bainite, Fig. 4.

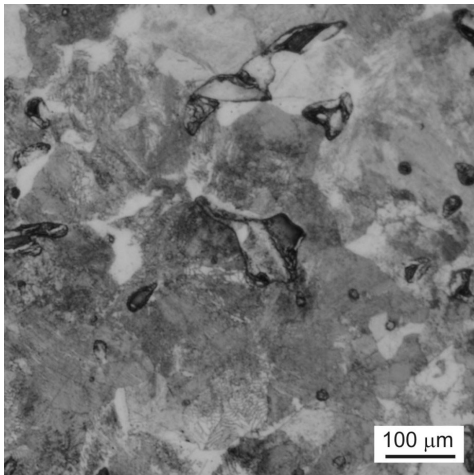


Fig. 4. The representative microstructure of Astaloy CrL + 0.5 C

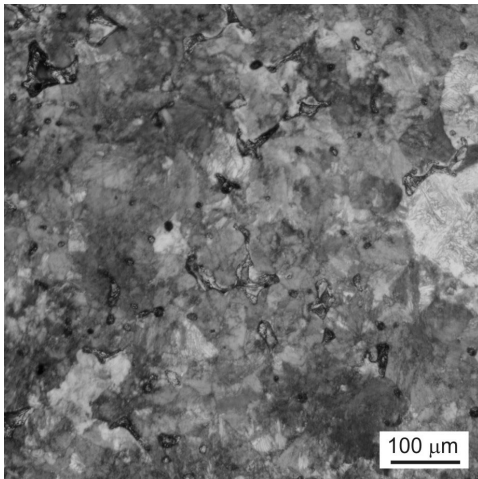


Fig. 5. The representative microstructure of Astaloy CrL + 0.7 C

The microstructure of Astaloy CrL with 0.7 % C consist of predominate upper bainite with small areas of pearlite, Fig. 5.

3.3. Local hardening

The detailed research of local area showed that the effects of local hardening caused by surface modification via shot peening exhibit higher hardness. Microhardness profiles, Fig. 6, confirmed the important role of microstructure constituents. The presence of bainite in specimens with higher graphite contents exhibited higher value of microhardness (the blank circle); on the other hand, the dominant presence of fine pearlite determined lower microhardness in the range $HV_{0.025} = 200\text{--}250$. The highest microhardness values located at average value of $25\ \mu\text{m}$ from outer surface. This corresponds to the details focused on local hardened area.

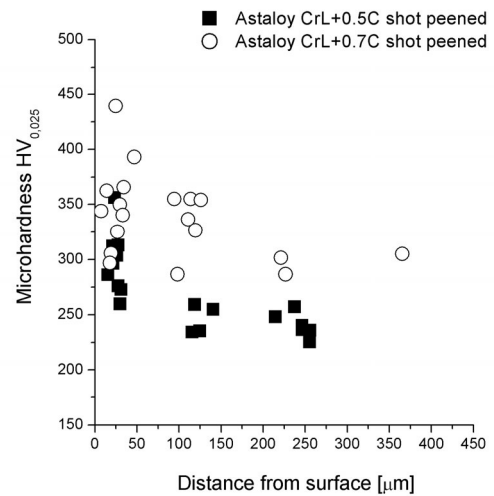


Fig. 6. Microhardness profiles of shot peened specimens

The modification of functional surfaces of investigated steels increased the mechanical and fatigue properties by means of stronger segments on the surfaces of specimens due to something close to a fully densified surface layer, as well as by the elimination of the detrimental effect of pores near the surface; the result was the decrease of crack propagation, Fig. 7.

On the other hand, the creation of a rough surface (represented by values of R_a) and notch production increasing strain localization caused the formation of local distribution secondary cracks, thus decreasing the tensile strength. The role of weak interfaces seems to be considered as a significant factor. Mechanical properties are controlled by the mechanisms of fracture in sintering necks. Characteristic for a duc-

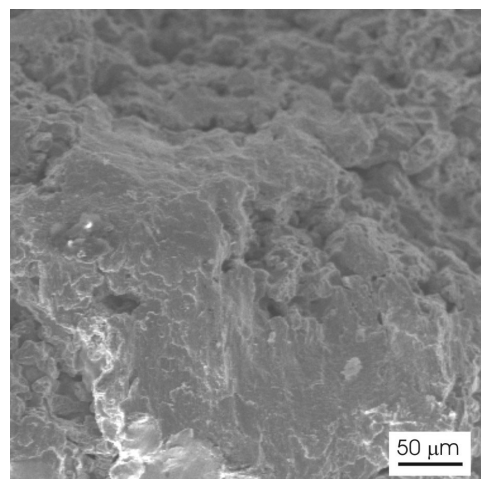


Fig. 7. Detail of local hardened area

tile fracture are the nucleation, coalescence and growth of voids within the sintering necks. Such voids are often nucleated at small brittle inclusions in the neck region. Shot peening has positive effect for fatigue endurance but it has also been demonstrated that negative results may arise^{19,20}. It is therefore important, in the future, to evaluate the parameters of shot peening.

4. Conclusion

The detailed research of local area has showed that the effect of local hardening causes by shot peening exhibits non-uniform distribution. The modification of functional surfaces of investigated steels increased mechanical and fatigue properties by means of stronger segments on the surfaces of specimens due to something close to a fully densified surface layer, as well as by the elimination of the detrimental effect of pores near the surface. The number and distribution of such inclusions might control the final mechanical properties. Further research in this area may lead eventually to the publication of a design specification for sintered shot peened components. Controlled shot peening seems to be most effective on higher hardness and higher density powder metallurgy components.

R. Bidulský thanks the Politecnico di Torino, the Regione Piemonte, and the CRT Foundation for co-funding by the fellowship.

REFERENCES

1. Cremer I.: *EURO Powder Metallurgy 2007, Toulouse, 15.-17. 10. 2007*, EPMA, Shewsbury, 2007, (without ed.) p. 1, (Plenary lecture).
2. Technical trends: *Met. Powder Rep.* 59, 26 (2004).
3. Nový F., Palček P., Chalupová M.: *Kovove Mater.* 43, 447 (2005).
4. Nový F., Činčala M., Kopas, P., Bokůvka O.: *Mater. Sci. Eng., A* 462, 189 (2007).
5. Nový F., Petrevec M.: *Letná škola únavy materiálův 2008, Žilina-Oščadnica, 8.-12.9.2008*, (Bokůvka O., ed.), p. 10 (lecture). EDIS, Žilina 2008.
6. Moon J. R.: *Powder Metall. Progr.* 2, 63 (2002).
7. Khorsand H., Yoozbashizade H., Habibi S. M., Janghorban K., Nangir A., Rethani S. M. S.: *Met. Powder Rep.* 57, 32 (2002).
8. Bacova V., Draganovska D.: *Mater. Sci.* 40, 125 (2004).
9. Mihaliková M., Buršák M., Michel J., Kovalová K.: *J. Metals, Mater. Minerals* 15, 53 (2005).
10. Kniewald D., Brezinová J., Guzanová A.: *Communications* 6, 37 (2004).
11. Buršák M., Mamuzič I., Mihaliková M.: *Metalurgija* 43, 101 (2004).
12. Menapace C., Messner C., Costa P., Straffelini G., Molinari A.: *Powder Metall. Progr.* 2, 18 (2002).
13. O'Brien R. C.: *Met. Powder Rep.* 43, 744 (1988).
14. Nakazawa K., Nagata T., Motooka N.: *Powder Metallurgy 2006 World Congress, Bexco Busan, Korea, 24-29. 9. 2006*, (Eun K. Y., Kim Y. S., ed.) p. 756 (extended abstract).
15. Technical trends: *Met. Powder Rep.* 59, 48 (2004).
16. Bidulská J., Kvačkaj T., Bodák V.: *Hutnicke Listy* 57, 11 (2002).
17. Bidulská J., Kvačkaj T., Bodák V., Rakučiak R.: *Acta Metallurgica Slovaca* 8, 211 (2002).
18. Bidulská J., Kvačkaj T., Bodák V.: *Ocelové pásy 2001, Ostrava, 25.-27. 9. 2001*, Rožnov pod Radhoštěm, Czech, (Bořuta J., Kiša M., Kovář J., Kuře F., ed.), p. 187 (lecture).
19. Nový F., Chalupová M., Činčala M., Bokůvka O.: *Acta Mechanica Slovaca* 11, 189 (2007).
20. Mihaliková M., Kovalová K., Michel J.: *Materiálové Inžinierstvo* 11, 13 (2004).

R. Bidulský^a, M. Actis Grande^a, and M. Kabátová^b
^a Politecnico Torino, Alessandria Campus, Alessandria, Italy, ^b IMR SAS, Kosice, Slovakia): **Improved Fatigue Resistance of Sintered Steels Via Local Hardening**

The aim at the present paper was to find out how the local hardening via surface modification and also microstructures affect the fatigue characteristics of the considered sintered materials. Two different systems were prepared: as-sintered and shot peened prealloyed sintered (Astaloy CrL based) steels with addition of 0.5 and 0.7 % C. Fatigue tests were carried out in symmetric plane bending at $R = -1$. The detailed research of local area showed local hardening caused by surface modification via shot peening. Local hardening exhibit positive effect on the fatigue failure resistance, due to a surface something close to a fully densified surface layer obtained by shot peening, as well as by the elimination of the detrimental effect of pores near the surface.

INVESTIGATION OF LOCAL MECHANICAL PROPERTIES OF ZIRCONIUM ALLOYS USING NANOINDENTATION

OLGA BLÁHOVÁ

*New Technology Research Centre, University of West Bohemia, Univerzitní 8, 306 14, Czech Republic
blahova@ntc.zcu.cz*

Key words: Zr alloys, LOCA, Nanoindentation

1. Introduction

Zirconium alloys are used in nuclear industry, mainly because of their low thermal neutron cross section, for their good mechanical properties and corrosion resistance. These alloys are widely used in production of nuclear fuel cladding tubes serving as the first barrier between the fuel and the surrounding environment. Zirconium shows high affinity to hydrogen, oxygen and nitrogen, forming stable hydrides, oxides, nitrides and interstitial solid solutions. The presence of oxygen and hydrogen has great influence on properties of the microstructure. Oxygen stabilizes the α phase, enlarges the α domain in the phase diagram and causes interstitial solid solution forming. Hydrogen stabilizes the β phase, causes higher solubility of oxygen in Zr at temperatures between 800–1200 °C, influences the redistribution of oxygen and causes the decrease of $\alpha - \beta$ transformation temperature.

The problem of oxide peeling on pure Zr is solved by the addition of suitable alloying elements Cr, Fe, Ni (stabilizing the β phase), which do not dissolve in the zirconium matrix and form small inclusions of intermetallic phases. Addition of Sn (stabilizing the α phase) reduces the adverse effect of nitrogen. Zirconium alloys were developed in this way, having coherent oxide layer, which do not have tendency to peel. In order to improve mechanical and corrosion properties, other alloy elements can also be added: Al (stabilizing the α phase), Nb, Cu, V and Mo (stabilizing the β phase). High corrosion resistance is attained by softening the structure with soft precipitates of β -Nb on grain boundaries and also in the matrix.

During the fuel cycle in water-cooled reactors, the outer region of the cladding tube is in contact with the cooling medium (water) with the temperature of 320 °C and pressure of 16 MPa. During the operation, oxidation of Zr occurs and hydrogen is released (part of it is absorbed into the alloy). The forming oxide creates a barrier between metal and water and slows corrosion rate. Improvement in physical, mechanical, technological and corrosion properties requires development of new alloys offering longer fuel burn up cycle, a possibility to use higher quality fuel and enhanced safety.

Loss of coolant accident (LOCA) can occur in water-cooled reactors when, due to a broken pipe, water flows out. The loss of moderator occurs within ten seconds or less and the nuclear fission stops immediately. Temperature of the cladding increases to approximately 1000 °C, which results in

high temperature oxidation (HTO). The reaction between steam and cladding surface occurs. The reactor emergency system floods the reactor with water in short time and rapidly cools down the cladding tubes.

During the heating period, the structure of the material transforms: the α phase (hcp) changes to the high temperature β phase (bcc). The maximum amount of oxygen, which can be dissolved in the β phase, depends on temperature. The exposure to high temperature atmosphere is accompanied by oxygen and hydrogen uptake. Part of oxygen forms the oxide layer during oxidation and the remaining part dissolves in the metal. The amount of oxygen dissolved in the metal depends on temperature: the higher the temperature, the higher the amount of oxygen dissolved in the metal. Oxygen concentration gradient occurs with higher concentration levels under sample surface.

Due to the rising oxygen content, the β phase transforms back to hcp α -Zr(O), α phase stabilized by oxygen, even at higher temperatures, which is not changed by further cooling. During the cooling period, the remaining β phase transforms to hcp α phase (usually called prior $\beta^{1,2}$) and β phase stabilizing elements (H, Fe and Cr) diffuse to the non-transformed β phase. Thus the α phase lamellas are formed which are depleted of these elements, despite the fact that the maximal admissible concentration of oxygen in β at higher temperatures is exceeded¹. Hydrogen causes the precipitation of hydrides during cooling. Faster cooling promotes the formation of ZrH (γ), while the slower one leads to formation of ZrH_{2-x}.

The microstructure of the material after HTO and after the cooling consists of the oxide layer ZrO₂, oxygen stabilized α -Zr(O) and α phase enriched with H, Fe and Cr which create precipitates. The α -Zr(O) layer is very brittle and thus the α phase is the only factor responsible for remaining ductility and toughness of the material. The character of the α -Zr(O) layer depends on the chemical composition of the alloy. Zr-alloys containing Sn (α stabilizer) form uniform layers, whereas in alloys containing Nb (β stabilizer), the layer is non-uniform and acicular^{1,2} (see Fig. 1).

2. Experimental

The samples were small tubes with the length of 30 mm and outer diameter of 9 mm and 0.6 mm wall thickness, which are identical to actual cladding tubes. Chemical composition: 1.0–1.1 % Nb, 3 ppm H, 20 ppm N, 100 ppm C, 840 ppm O. The course of LOCA was simulated in laboratory conditions in UJP Praha². Samples were heated at 950 °C, 1000 °C, 1050 °C, 1150 °C and 1200 °C in steam for different time, see Tab. I. After the HTO stage and hardening in water with ice, the tubes were cut to 3 mm-thick rings and then embedded in resin or in conductive substance (for following SEM analyses) and polished. Samples were examined by X-Ray diffractometer equipped with high-temperature chamber³, scanning electron microscope with EDAX⁴ and by Nanoindenter XP.

Table I
Experimental samples and measured mean values

Sample temperature [°C] / time [min]	H_{IT} [GPa]	E_{IT} [GPa]
950 / 0	2.88 ± 0.27	111.1 ± 2.6
950 / 3	2.93 ± 0.16	111.3 ± 4.4
950 / 6	3.21 ± 0.24	106.1 ± 3.0
950 / 9	3.40 ± 0.20	115.3 ± 3.7
950 / 15	3.19 ± 0.17	105.5 ± 2.7
1000 / 9	3.61 ± 0.34	106.7 ± 5.4
1000 / 15	3.69 ± 0.35	110.0 ± 5.3
1050 / 0	3.32 ± 0.25	107.7 ± 4.5
1050 / 3	3.53 ± 0.24	109.1 ± 3.8
1050 / 6	3.63 ± 0.23	110.3 ± 4.3
1050 / 9	3.95 ± 0.24	113.5 ± 3.9
1100 / 3	3.76 ± 0.28	108.9 ± 2.9
1100 / 6	3.98 ± 0.28	113.8 ± 5.1
1100 / 9	4.11 ± 0.24	112.4 ± 3.9
1100 / 15	3.82 ± 0.21	108.7 ± 3.3
1150 / 0	3.14 ± 0.27	111.3 ± 3.8
1150 / 3	3.98 ± 0.22	113.0 ± 3.7
1150 / 9	4.62 ± 0.24	118.8 ± 4.2
1200 / 3	4.67 ± 0.20	116.1 ± 3.0
1200 / 6	4.61 ± 0.38	106.9 ± 1.9
1200 / 9	5.44 ± 0.33	116.4 ± 3.6
1200 / 15	4.98 ± 0.29	106.9 ± 3.0

The instrument enables to perform instrumented indentation where the displacement of indenter and load data are recorded during the loading and unloading periods ($F-h$: indentation curve). The indentation hardness H_{IT} and indentation modulus of elasticity E_{IT} were measured by the IIT (Instrumented Indentation Testing) method⁵:

$$H_{IT} = \frac{F_{\max}}{A_p}$$

where F_{\max} is the maximum load; A_p is the projected contact area of the indent.

$$E_{IT} = \frac{1 - (\nu_s)^2}{\frac{1}{E_r} - \frac{1 - (\nu_i)^2}{E_i}}$$

where the indices i and s are related to properties of the indenter or sample material (modulus of elasticity, Poisson ratio) and E_r is reduced modulus of elasticity:

$$E_r = \frac{S \cdot \sqrt{\pi}}{2 \cdot \beta \sqrt{A_p}(h_c)}$$

where S denotes contact stiffness (the initial slope of the unloading curve), β is correction constant for the indenter tip shape (for Berkovich indenter: $\beta \approx 1.034$), A_p is the projec-

tion of contact area and h_c is contact depth:

$$h_c = h - \varepsilon \frac{P_{\max}}{S}$$

where ε is constant dependent on the indenter geometry⁶.

Nanoindentation measurements were performed with the Berkovich indenter with the load of 8 mN. The indents were made in three parallel rows with the starting point at the oxide – metal interface and the distance of 5 μm between each other. They were documented by using an optical microscope or a SEM. The min – max intervals were recorded (Fig. 1), with the assumption that they correspond with the α phase properties, then mean values were calculated.

Calculated values of indentation hardness and modulus of elasticity of the α (prior β) phase are shown in Tab. I. and Fig. 2 and 3.

The indentation hardness generally increases with the temperature of exposure. It depends on higher oxygen content⁴. The indentation modulus of elasticity is nearly constant: 111.4 GPa \pm 4.2 GPa (standard deviation is approximately 4 % from mean value).

Ratio of measured values of indentation modulus of elasticity E_{IT} and indentation hardness H_{IT} (ref.⁷) is shown

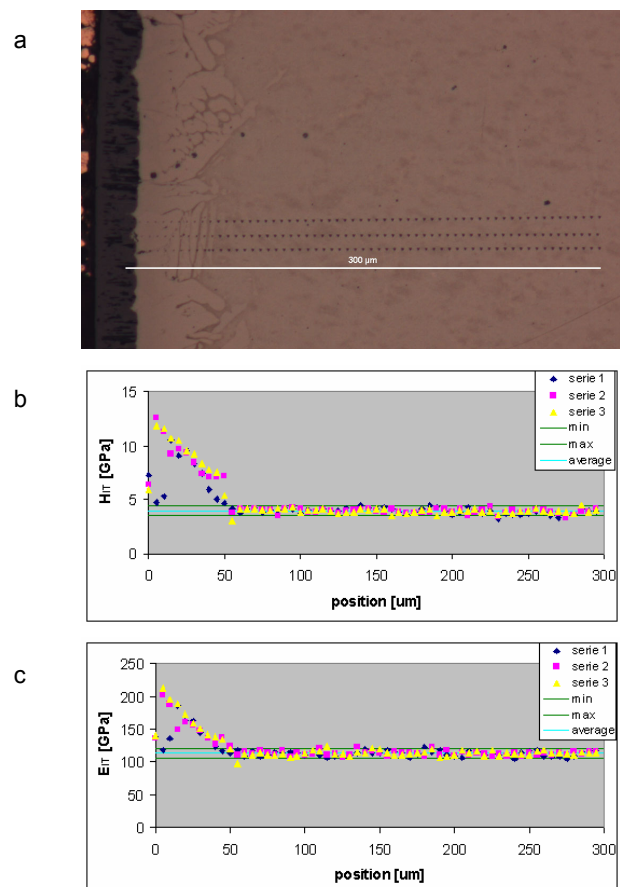


Fig. 1. a) Micrograph of sample with exposition temperature 1050 °C and time 9 min, b) measured value of indentation hardness, c) measured value of indentation modulus of elasticity

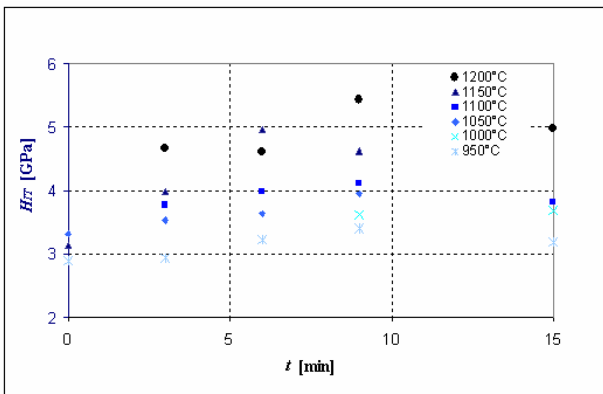


Fig. 2. Indentation hardness of samples with different exposition temperature vs. exposition time

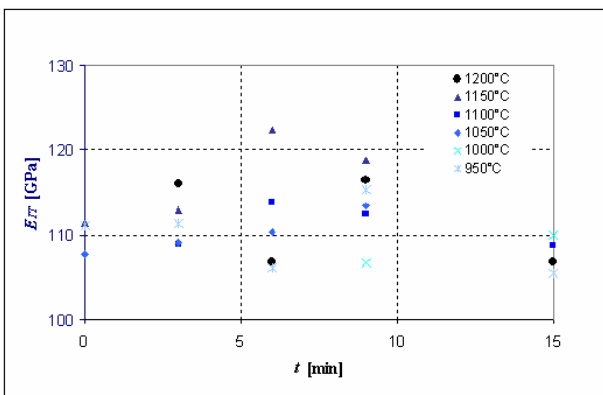


Fig. 3. Indentation modulus of elasticity of samples with different exposition temperature vs. exposition time

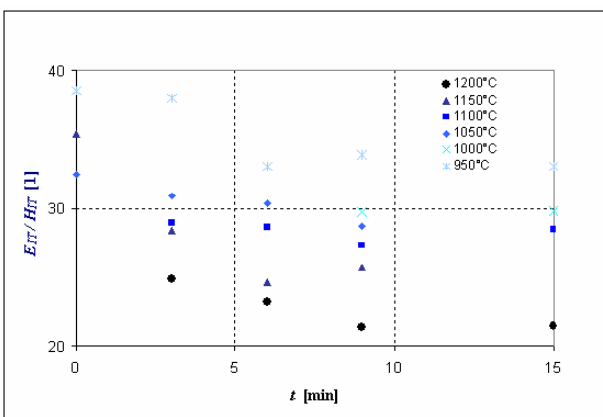


Fig. 4. Ratio of measured values of indentation modulus of elasticity E_{IT} and indentation hardness H_{IT} vs. exposition time

in Fig. 4. This ratio mostly decreases with the temperature of exposure.

Samples were measured at UJP Praha by the pressure testing method at 135 °C and ductility was determined². Sam-

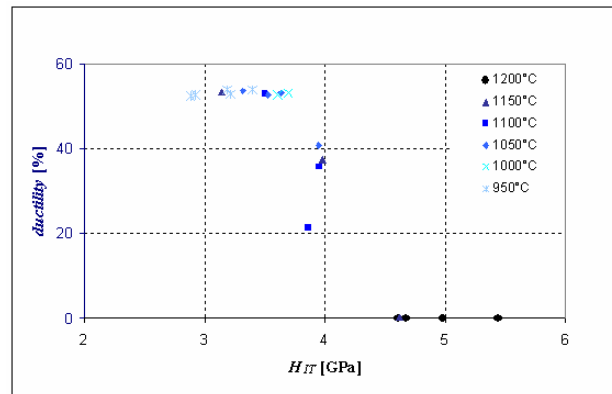


Fig. 5. The ductility vs. indentation hardness of samples with different exposition temperature

ples are brittle when their hardness is more than 4 GPa (see Fig. 5).

3. Conclusion

This paper is based on long-time investigation and characterization of mechanical and related properties of a new Zr1Nb alloy. The samples were analysed using nanoindentation method.

The indentation hardness of the α (prior β) phase was determined and it was found out that indentation hardness increases with the temperature of exposure. On the contrary, the indentation modulus of elasticity is nearly constant so that ratio indentation hardness and indentation modulus decreases with the temperature of exposure.

The indentation hardness correlates with ductility measured by the pressure testing method.

This work was supported by project MPO ČR no. 2A – ITP1/03 and project Kontakt – AIP no. MEB 080869.

REFERENCES

1. Chung H. M.: Nucl. Eng. Technol. 37, 327 (2005).
2. Vrtílková V. et al.: Vliv rozpouštění oxidu vytvořeného na povlakové trubce ze Zr-slitin na termomechanické vlastnosti povlakové trubky po vysokoteplotních přechodech, *Výzkumná zpráva 1164* (Research report). UJP Praha a. s., Praha 2005.
3. Říha J., Bláhová O., Šutta P.: Fázové změny slitiny Zr-1Nb a jejich vliv na lokální mechanické vlastnosti (Phase Changes in the Zr-1Nb Alloy and Their Impact on the Local Mechanical Properties). In this issue.
4. Medlín R., Říha J., Bláhová, O.: Microstructure and Local Mechanical Characteristics of Zr1Nb Alloy after Hardening. In this issue.
5. ISO 14577-1:2002, Metallic materials – Instrumented indentation test for hardness and materials parameters – Part 1: Test method.
6. Oliver W. C., Pharr G. M.: J. Mater. Res. 7, 1546 (1992).

7. Zubko P., Pešek L., Besterčí M., Vadasová Z.: *Kovove Mater.* 47, 39 (2009).

O. Bláhová (*New Technology Research Centre, University of West Bohemia, Plzeň*): **Investigation of Local Mechanical Properties of Zirconium Alloys Using Nanoindentation**

Samples from Zr1Nb alloy were tempered after various temperatures and various times prior to hardening. This process simulated the LOCA (Loss Of Coolant Accident) conditions when, due to a broken pipe, water flows out. The loss of moderator occurs and temperature of the cladding increases, which results in high temperature oxidation. The emergency system floods the reactor with water in short time and rapidly cools down the cladding tubes.

This paper presents the evaluation of local mechanical properties on samples after this simulation process. The indentation hardness and indentation modulus of elasticity were evaluated by nanoindentation method.

MOŽNOSTI VYUŽITIA SYSTÉMU NA ODBER MALÝCH VZORIEK Z PREVÁDZKOVANÝCH ZARIADENÍ PRI HODNOTENÍ VLASTNOSTÍ MATERIÁLOV

MARTIN BŘEZINA a ĽUDOVÍT KUPČA

VUJE, a.s., Okružná 5, 918 64 Trnava, Slovenská republika
brezina@vuje.sk, kupca@vuje.sk

Kľúčové slová: odber vzoriek, malé vzorky, small punch test, skúšky mechanických vlastností

1. Úvod

Prevádzkovatelia rôznych zariadení často riešia otázku možnosti ďalšej prevádzky zariadenia, predĺženia jeho plánovanej životnosti, prípadne aktuálnu potrebu analyzovať defektoskopické nálezy. Tieto otázky je možné zodpovedne vyriešiť len odberom časti materiálu konštrukcie alebo daného zariadenia a jeho detailnou analýzou.

Tradičný odber skúšobného materiálu u prevádzkovaných zariadení predstavuje popri nutných odstavkách aj nevhodný zásah do celistvosti hodnotenej časti, a to či už sa jedná o odber strojným obrábaním, teplotným delením alebo aj inými spôsobmi. Tieto deštruktívne metódy zvyčajne vyžadujú následnú opravu odobratého miesta, vrátane tepelného spracovania a celého radu nedeštruktívnych kontrol. Často sa pritom práve toto miesto môže stať zdrojom problémov pri ďalšej prevádzke.

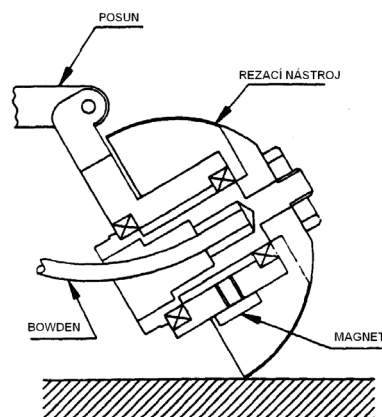
V prípade, že je potrebné získať reálne informácie o stave daného zariadenia (napr. bude výpočtovo stanovené vyčerpanie životnosti, resp. potreba analyzovať indikácie alebo defekty) je možné namiesto vyrezania a výmeny celého komponentu odobrať z najkritičnejších miest miniatúrne vzorky, ktoré nezmenia jej pevnosť ani životnosť, ale poskytnú dostatočné množstvo informácií. Pomocou špeciálnych techník je možné na takýchto malých vzorkách vykonať prakticky všetky analýzy potrebné pre posúdenie danej komponenty. Tento spôsob odberu malých vzoriek nazývaný tiež SSam (Surface Sampling) nielenže negatívne neovplyvní dané zariadenia, ale zvyčajne tiež nevyžaduje žiadne dodatočné operácie (zváranie, brúsenie). Príkladom praktického využitia takého princípu bol odber vzoriek z tlakových nádob reaktorov JE V-1 v Jaslovských Bohuniciach, realizovaný firmou Rolls-Royce¹. V tomto prípade bolo použité jednoúčelové zariadenie vyvinuté iba pre danú potrebu.

Zariadenie SSamTM-2 firmy Rolls-Royce, ktoré v súčasnosti vlastní VUJE, a.s., je koncipované ako univerzálny systém určený na odber vzoriek z rôznych zariadení bez výrazného poškodenia povrchu a bez nutnosti miesto odberu opravovať alebo upravovať. V kombinácii s metódou Small Punch Test, vyvinutej pre stanovovanie mechanických vlastností na malých vzorkách, ponúka široké možnosti získavania informácií o stave a vlastnostiach materiálov zariadení, a to aj počas ich prevádzky.

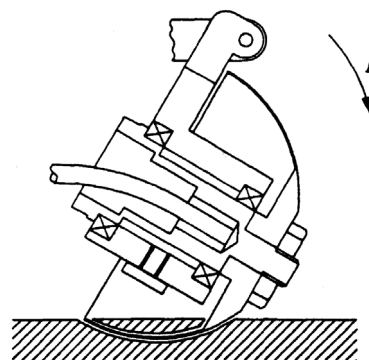
2. Popis systému odberu vzoriek

Princíp odberu vzorky zariadením SSamTM-2 je založený na rýchlej rotácii rezného nástroja v tvare dutej pologule okolo osi súmernosti a jeho pomalého zasúvania po kruhovej dráhe do rezaného materiálu. Os posunu nástroja je kolmá na os rotácie gule tak, že rezný nástroj sleduje dráhu hrany nástroja (viď obr. 1 a 2). Rezný nástroj je vyrobený z ocele a má tvar dutej pologule o priemere \varnothing 50,8 mm a hrúbke steny 0,25 mm. Povrch nástroja je pokrytý vrstvou kubického nitridu bóru (CBN). Hrúbka vrstvičky CBN je 0,18 až 0,20 mm, čo značí, že teoreticky je minimálna šírka rezu 0,61 až 0,65 mm. V závislosti na veľkosti nepravidelnosti tvaru nástroja, je skutočná šírka rezu približne 0,67 mm (cit.2).

V odberovej hlavici, ktorá má priemer 70 mm a dĺžku 520 mm je umiestnený rezný nástroj, jeho pohony, vzduchový valec na upínanie v rúrach a dva vzduchové valce pre núdzové vytiahnutie nástroja z rezu pri odbere vzoriek v nedostupných miestach (napr. v rúrach).



Obr. 1. Princíp odberu vzoriek – poloha na začiatku odberu



Obr. 2. Princíp odberu vzoriek – poloha ku koncu odberu



Obr. 3. Odberová hlavica na servisnom stojane

Vzorky je možné odoberať bez chladenia, alebo s chladením vodou. Pre tento prípad je hlavica vybavená prívadom a spätným odsávaním chladiacej kvapaliny. Použitie chladenia skráti dobu odberu, ale aj bez chladenia nedochádza k prehriatiu odobratej vzorky.

Odberovú hlavicu položenú na servisnom stojane je vidieť na obr. 3. Detailný pohľad na hlavicu pri odbere vzoriek je na obr. 4. V tomto prípade je hlavica upevnená pomocou magnetických držiakov.

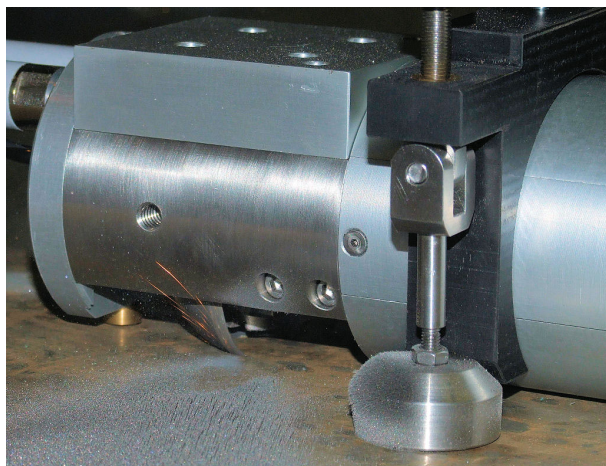
Vďaka flexibilnému systému upevňovania odberovej hlavice je možné odoberať vzorky z vonkajšieho aj vnútorného povrchu zariadení a komponentov. V prípade potrubia je možné získať vzorky z vnútorného povrchu od priemeru potrubia \varnothing 75 mm a až zo vzdialenosti 4000 mm od vstupu.

Veľkosť a tvar odobratých vzoriek závisí na geometrii v mieste odberu. Z rovinatej plochy je možné odobrať vzorky hrubé až 2,8 mm. V prípade odberu vzorky z vonkajšieho povrchu potrubia maximálna možná hrúbka vzorky rastie, v prípade vnútorného povrchu klesá. Doba odberu vzorky závisí na geometrii v mieste odberu (vonkajší resp. vnútorný povrch), nastavenej hĺbke odberu, na materiáli, z ktorého sa vzorka odoberá a tiež na tom, či je použité chladenie.

Výhodou použitia uvedeného odberového zariadenia je:

- minimálny zásah do hodnoteného komponentu,
- nie je potrebná ďalšia úprava povrchu v mieste odberu,
- možnosť odberu vzoriek na neprístupných miestach,
- prakticky nulové ovplyvnenie odobratej vzorky.

Odobraté vzorky je možné analyzovať klasickými meto-



Obr. 4. Detail hlavice pri odbere vzorky



Obr. 5. Odobratá vzorka po elektroiskrovom delení

dikami a postupmi, ale aj postupmi špeciálne vyvinutými na vyhodnocovanie malých vzoriek metódou SPT (Small Punch Test).

Z odobratých vzoriek je potom možné stanoviť:

- chemické zloženie,
- základné mechanické vlastnosti – medzu sklzu, medzu pevnosti, tvrdosť,
- prechodovú teplotu krehký – húževnatý stav,
- únavové charakteristiky,
- mikroštruktúrne a submikroštruktúrne vlastnosti,
- mieru citlivosti voči medzikryštalickej korózii a pod.

Rozsah analýz a z toho vyplývajúca potreba na počet odobratých vzoriek závisí na hodnotenom zariadení, použitom konštrukčnom materiáli a požadovaných výsledkoch. Rovnako aj delenie získaných vzoriek, ktoré sa vykonáva elektroiskrovou drôtovou rezačkou, musí vždy vychádzať z analýz, ktoré sa budú vykonávať. Pretože zvyčajne sa požaduje stanoviť aj základné mechanické vlastnosti, je delenie orientované tak, aby bolo možné získať maximálny počet vzoriek pre skúšku SPT. Pre zvyšné skúšky je spravidla možné využiť odrezky a zvyšky po delení a tiež vzorky po SPT skúškach. Príklad delenia odobratej vzorky je na obr. 5.

3. Stanovenie mechanických vlastností metódou small punch test

V súčasnosti sa prejavuje snaha o zjednodušenie skúšania, pri súčasnom zabezpečení požadovanej presnosti a vierohodnosti výsledkov. Jedným z možných riešení je miniaturizácia vzoriek. Súčasne so zmenšovaním štandardných skúšobných telies sú vyvíjané aj nové typy skúšok plne nahradzujúcich bežne používané skúšky. Jedným z takýchto možných riešení je použitie tzv. SPT skúšky (Small Punch Test).

Vo svete sa začalo rozširovať použitie SPT skúšky na hodnotenie základných mechanických vlastností rôznych zliatin^{3,4}. Jej výhody upútávajú pozornosť stále väčšieho množstva výskumných pracovníkov.

Najväčšie z týchto výhod sú:

- nízka spotreba originálnych skúšobných materiálov,
- relatívne jednoduché vyhodnocovanie výsledkov skúšky,
- použitie univerzálnych a jednoduchých skúšobných zariadení,

- uniformita vzoriek pre všetky určované vlastnosti materiálov,
- nízka aktivita ožiarených vzoriek.

Parametre tejto skúšky sa však zatial medzi jednotlivými autormi líšia. Najviac odlišností je v nasledovných oblastiach:

- veľkosť a tvar vzorky,
- druh razného nástroja,
- konfigurácia skúšobného prípravku,
- počet vzoriek pre získanie spoľahlivého výsledku.

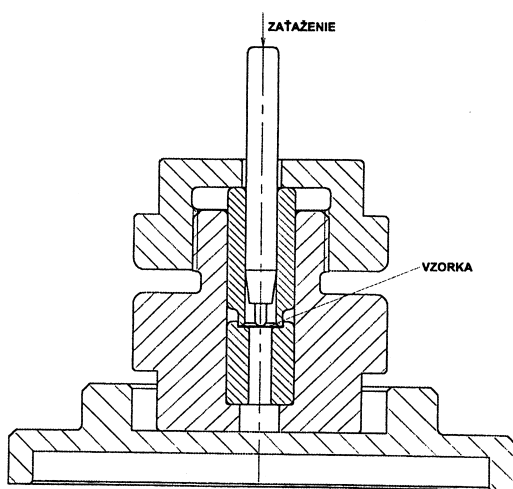
Z toho dôvodu v súčasnosti prevláda veľká snaha o normalizáciu tejto metódy, a to nie len v Japonsku a USA, ale aj v Európe. Za týmto účelom vznikla aj medzinárodná skupina CEN21 – European Committee for standardization: CEN Workshop 21 – Small Punch Test Method for Metallic Materials⁵.

Napriek popísaným rozdielom v postupe skúšania, princípom SPT skúšky je vždy prienik špeciálneho razníka cez plochú vzorku, ktorá je uchytená medzi pridržiavačom a maticou (obr. 6). Použitím pomerne jednoduchého zariadenia so záznamom zaťažovacej sily a deformácie je možné získať údaje o základných mechanických vlastnostiach. Typický priebeh sily a deformácie pri skúške tvárneho materiálu je na obrázku 7. Skúšky pri nízkych teplotách sa realizujú pomocou tekutého dusíka alebo dusíkových pár v špeciálne pre tento účel zhotovených zariadeniach a skúšky pri vyšších teplotách v špeciálnej peci, ktorá je súčasťou skúšobného zariadenia.

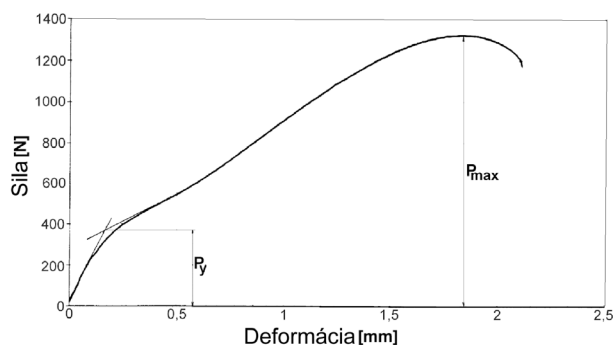
Použitím jednoduchého záznamového zariadenia pre záznam vzájomných priebehov parametrov „zaťaženie – deformácia“ je možné z výsledkov SPT skúšky zisťovať:

- medzu sklzu a medzu pevnosti materiálu zodpovedajúcu výsledkom zo štandardnej ťahovej skúšky,
- prechodovú teplotu krehkého a húževnatého lomu porovnateľnú s výsledkami získanými pomocou Charpyho skúšky vrubovej húževnatosti,
- prípadne aj lomovú húževnatosť.

Vzorky pre typ zavedenej SPT skúšky, ktorá sa používa vo VUJE, a. s., majú tvar malého kotúča s priemerom $\varnothing 8$ mm a hrúbkou 0,5 mm.



Obr. 6. Schéma skúšobného usporiadania



Obr. 7. Typický priebeh pri SPT skúške tvárneho materiálu

Určitou nevýhodou SPT skúšky sú jej vysoké nároky na uniformitu a kvalitu prípravy vzoriek. Pri ich výrobe sa musí zabezpečiť:

- vysoká kvalita povrchu vzoriek,
- konštantná hrúbka vzorky s toleranciou $\pm 0,005$ mm,
- rovnobežnosť skúšaných plôch vzorky.

Najväčšou výhodou SPT skúšky sú malé rozmery skúšobnej vzorky a to hlavne v prípade nedostatku skúšobného materiálu. Napr. pri skúšaní ožiarených vzoriek je veľkou výhodou nižšia aktivita, z dôvodu ich malého objemu. Malé rozmery skúšobných vzoriek sú výhodné aj pri ožarovaní v energetických reaktoroch. Geometria vzoriek, predovšetkým ich hrúbka, tiež umožňuje presnejšie hodnotenie degradácie vlastností v oblasti teplom ovplyvnenej zóny materiálu v blízkosti zvaru⁶.

4. Príklady využitia odberového zariadenia a SPT skúšky

Odber vzoriek s následnou komplexnou analýzou vlastností vrátane stanovenia mechanických vlastností pomocou SPT skúšky bol realizovaný pri hodnotení vlastností materiálov potrubných trás a iných zariadení vo firme Duslo, a.s.^{7,8}. Zariadením SSamTM-2 boli odobraté vzorky zo základného materiálu aj zvarových spojov. Z každej odobratej vzorky boli elektroiskrovým delením získané 3 ks polotovarov o rozmeroch $\varnothing 8 \times 0,6$ mm potrebných pre skúšku SPT. Z týchto polotovarov boli precíznym mechanickým odbrosovaním vyrobené skúšobné telieska s finálnymi rozmermi $\varnothing 8 \times 0,5 \pm 0,05$ mm. Zvyšky odobratých vzoriek po elektroiskrovom delení boli využité pre meranie mikrotvrdosti a metalografickú analýzu. Týmto spôsobom bolo možné posúdiť stav materiálu zariadenia bez nutnosti hrubého zásahu spojeného s odberom vzoriek pre „klasické“ mechanické skúšky.

Rozsiahle využitie SPT skúšky vo VUJE sa realizovalo v rámci tzv. Nového programu overovacích vzoriek (NPOV), ktorý slúžil na monitorovanie stavu a zmien vlastností materiálov tlakovej nádoby reaktora JE V-1 počas prevádzky, po regeneračnom žíhaní a následnom ožarovaní. Tento program bol realizovaný na JE v Jaslovských Bohuniciach a bol koordinovaný medzinárodnou agentúrou MAAE (cit.⁹). Porovnaním získaných výsledkov mechanických vlastností jednotlivých stavov materiálov pomocou štandardizovaných postupov

a výsledkov SPT skúšky bola v rámci tohto programu overená aj spoľahlivosť skúšania týmto novým postupom¹⁰.

Najrozsiahlejšie využitie SPT skúšok našlo uplatnenie v tzv. Zdokonalenom programe overovacích vzoriek (ZPOV), ktorý je určený na monitorovanie aktuálneho stavu vlastností materiálu tlakových nádob reaktorov JE V-2 v Jaslovských Bohuniciach počas prevádzky¹¹. V rámci prípravy tohto programu bolo vyrobených a do reaktorov zavezených niekoľko tisíc SPT vzoriek, ktoré sa budú po ožiarení v určených intervaloch vyhodnocovať.

5. Záver

Využitie špeciálneho odberového zariadenia SSam-2TM od firmy Rolls-Royce v kombinácii s SPT skúškou, ale aj jednotlivito, má veľa možností využitia pri hodnotení reálneho stavu zariadení a ich komponentov v prevádzke, a to nielen na jadrových zariadeniach.

LITERATÚRA

1. Kupča E., Březina M.: *Metallography methods application on the scoop samples from the reactor pressure vessels WWER-440 in Jaslovské Bohunice NPP V-1*. Microstructural Science, vol. 26, ASM International, Materials Park, Ohio, USA, 1998.
2. Rolls-Royce: *SSamTM-2 Surface Sampling System*. Operational manual.
3. Lucas G. E.: *Metall. Mater. Trans. A* 21, 1105 (1990).
4. Corwin W. R., Rosinski S. T., van Walle E. (ed.): *Small Specimen Test Techniques*, ASTM STP 1329, West Conshohocken 1997.
5. *CEN Workshop Agreement 21* „Small Punch Test Method for Metallic Materials“, Part B: A Code of Practice for Tensile and Fracture Behaviour.
6. Petzová J., Kupča, E., Březina M.: *Lokální mechanické vlastnosti 2006. Nečtiny 8. - 10. 11. 2006*. Zborník prednášok. Západočeská univerzita v Plzni, s. 134–140.
7. Březina M. a kol.: *Stanovenie mechanických vlastností potrubí parovodov v Duslo Šaľa*. Technická správa VUJE č. 0360/20/2007, august 2007.
8. Březina M. a kol.: *Analýza vlastností materiálu VT ohrievača napájacej vody ČP 3*. Technická správa VUJE č. 0360/20/2007, september 2007.
9. *MAAE: TC Project RER/9/035* „Skúšky Round-Robin pre ožarovanie, krehnutie, žihanie a ďalšie krehnutie zvarového kovu TNR typu VVER 440/230 Viedeň, november 1996.
10. Petzová, J. a kol.: *Výsledky hodnotenia materiálov TNR pomocou SPT skúšky na malých vzorkách v rámci programu NPOV*, výskumná správa VÚJE, ev. č. 0360/37/2004, december 2004.
11. Kupča, E. A kol.: *Zdokonalený program overovacích vzoriek materiálov tlakových nádob reaktorov typu VVER-440/213 pre 3. a 4. blok JE V-2*. Technická správa VUJE ev. č. 0360/22/2008.

**M. Březina and E. Kupča (VUJE, a.s., Trnava, Slovakia):
Implementation possibilities of the small specimen sampling system for evaluation of material properties from components under operation**

In the paper, there is described a surface sampling system which is used for cutting of small specimens from operating equipments without undesirable affects. The sampling system SSamTM-2 made by Rolls-Royce Company uses a special rotating tool, which cuts off small scoop samples. The paper describes the evaluation possibilities of taken samples to determine mechanical properties using SPT (Small Punch Test) samples, chemical composition and microstructure of materials with the aim to determine the residual lifetime of the component, mechanisms and causes of failures, etc.

MEASUREMENT OF MECHANICAL PROPERTIES OF COMPOSITE MATERIALS

VILMA BURŠÍKOVÁ^a, ZUZANA KUČEROVÁ^a, LENKA ZAJÍČKOVÁ^a, ONDŘEJ JAŠEK^a, VÍT KUDRLE^a, JIŘINA MATĚJKOVÁ^b, and PETR SYNEK^a

^aDepartment of Physical Electronics, Masaryk University, Kotlářská 2, 611 37 Brno, ^bInstitute of Scientific Instruments, Academy of Sciences of the Czech Republic, Královopolská 147/62, 612 64 Brno, Czech Republic
vilmab@physics.muni.cz

Keywords: nanocomposites, carbon nanotubes, polyurethane, hardness, storage modulus, loss modulus, indentation creep

1. Introduction

Composite materials or composites are multiple-phase materials that exhibit a significant proportion of the properties of all constituent phases such that a better combination of properties is realized. Those phases must be chemically and physically dissimilar and separated by a distinct interface. There are two categories of constituent materials: the matrix and the reinforcement or the dispersed phase. In a composite, at least one portion of each kind is required. The properties of composites are a function of the properties of the constituent phases, their relative amounts and the geometry of the disperse phase (i.e. the shape of the particles, the particle size distribution and orientation).

2. Nanocomposites

In contrast to conventional composites, where the reinforcement is on the order of microns, nanocomposites are reinforced with filler with at least one dimension that is less than 100 nm. Although some nanofilled composite have been used for more than 100 years (e.g. carbon black or fumed silica filled^{1,2}), the discovery of carbon nanotubes become a new great challenge for nanocomposite research and industry. According to³, six following characteristics distinguish the nanocomposite from the classic filled systems: particle-particle correlation (orientation and position) arising at low volume fractions (<0.001); large number density of particles per particle volume (106–108 particles/ μm^3); extensive interfacial area per volume of particles (103–104 $\text{m}^2 \text{mL}^{-1}$); short distances between particles (10–50 nm at 1.8 vol.%); comparable size scales among the rigid nanoparticle inclusion, distance between particles and the relaxation volume of the polymer chains.

The interfacial region has different properties than the

bulk material because of its proximity to the surface of the filler. Nominally, the spatial extent of this perturbed matrix is thought to extend into the bulk one to four times the radius of gyration of the matrix, R_g , which has a value of around tens of nanometers. Because of the increased number of particles, the distance between particles in the nano-filled system is comparable to the size of the interfacial region (10 nm). Thus, the relative volume fraction of interfacial material to bulk is drastically increased. This implies a necessity to optimize the properties of the interfacial region in nanocomposites. On the other hand, this region is a source of many potentially novel properties of nanocomposites derived from the interface. It can influence the mechanical properties of the nanocomposites as well as their conductivity and percolation behavior.

The final microstructure and properties of the carbon nanotubes (CNT)-based polymer composite will depend on how the CNTs will distribute, disperse and orient. The CNT orientation state determines the anisotropic functionality. Properties of composites are significantly better, if CNTs are oriented in one direction, than if they are oriented randomly^{4,5}. Another challenge in fabrication of the CNT-based polymer composites is the homogeneous dispersion of the CNTs in the polymer matrix so that it has uniform properties and can efficiently handle load transfer during structural excitation^{4,6,7}. It is a significant challenge in fabrication of the CNT-based polymer composites because the CNTs, in their manufactured state, cluster together in any suspension due to strong Van der Waals forces. Many techniques such as application of ultrasonic bath or chemical modification of the CNT surface have been attempted to separate and disperse CNTs in polymer resins to various degree of success^{4,8–10}. There are four important parameters that will describe the suspension characteristics: CNT dispersion, concentration, aspect ratio and orientation¹¹. The importance of dispersion and orientation of CNTs is obvious from the above paragraph. The CNT concentration and aspect ratio determine how easily CNTs can move and interact with each other to build interconnecting network which can transfer heat and electrons. There are three general ways of dispersing nanofillers in polymers. The first way is direct mixing of the polymer and the nanoparticles either as discrete phases or in solution. The second way is *in-situ* polymerization in the presence of nanoparticles and the third is *in-situ* formation and *in-situ* polymerization. These are so-called hybrid composites¹².

Carbon nanotubes are increasingly being used in nanocomposite preparation as a filler of many different matrices, ceramics, metal, polymer and also in clay-polymer composites^{13–16}. With their high strength, high modulus, light weight and high aspect ratio they seem to be ideal filler. However, they are held in bundles a do not disperse easily, they are inert with low wettability and that hinders their full utilization as a filler. It has already been reported that functionalization of CNTs greatly improves their dispersion in a matrix and consequently the properties of the composite¹⁷. In this work the preparation of the polyurethane (hereafter PU) composite with nanotubes is described. Both unmodified and modified multi-

walled CNTs (hereafter MWCNTs) were used. The structure and properties of composite with both kinds of filler are compared. The functionalization of MWCNTs in inductively coupled plasma ICP is also reported.

3. Mechanical properties of the composites

There are several basic problems associated with the determination of the mechanical properties of composite film consisting of hard particles and viscoelastic-plastic matrix. The evaluation of material parameters such as elastic modulus and plastic hardness of the viscoelastic-plastic film is problematic because these materials exhibit also a significant time dependent plastic deformation (creep). If we load such system to a maximum load and then keep penetration depth constant, the load will relax under some plastic or viscoelastic response (anelastic – time dependent plastic deformation). Two different indentation methods were used to study the mechanical properties of the composites.

A Fischerscope H100 depth sensing indentation (DSI) tester was used to study the indentation response of composites on glass substrates. Several different testing conditions were used in order to find the optimum procedure allowing the suppression of the influence of the time dependent indentation response of CNT-filled PU composite on a glass substrate. The loading period of 20 s was followed by a hold time of 20 s or 60 s, an unloading period of 20, 5 or 1 s and finished after holding the minimum load for 20 or 60 s. The tests were made for several different indentation loads in order to study the composite mechanical properties of the film/substrate system from near surface up to film-substrate interface. The applied load varied from 1 to 1000 mN. An example of the time dependence of the load is shown in Fig. 1.

In the case of the second, dynamic method, the CSM ultrananoindenter (UNHT) was used. The indentation measurement was based on the application of an oscillating force superimposed to the increasing indentation load in which the transfer function between the load and indentation depth pro-

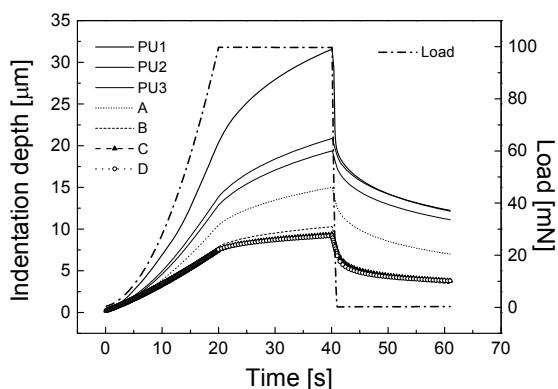


Fig. 1. Comparison of the time dependence of the load with the time dependence of the indentation depth for 3 different types of polyurethane matrices PU1-PU3 and four composites marked A,B,C,D, reinforced by CNTs

vides a method of calculating storage and loss modulus of the material.

The PU-CNT nanocomposite preparation was as follows. Appropriate amounts of CNTs, polyol, diluter and anti-static agent were weighted out, stirred well manually, glass balls ensuring the mechanical perturbation were added and the whole mixture was ultrasonicated for 60 minutes. Than isocyanate was added and the mixture was stirred once more. After that it was poured onto glass substrate surrounded by the frame. Liquid in the frame created a flat level and let dried at the laboratory temperature. After 48 hours the composite was dry enough to be removed from the frame. The chemicals weight rate was 7 : 2 : 1 (polyol : isocyanate : diluter) and the CNT concentration in composites was 0.1 wt%.

4. Results

In Fig. 1 the testing conditions (dependence of the applied load on the time) used and the corresponding time dependences of the indentation depth are illustrated for several studied samples.

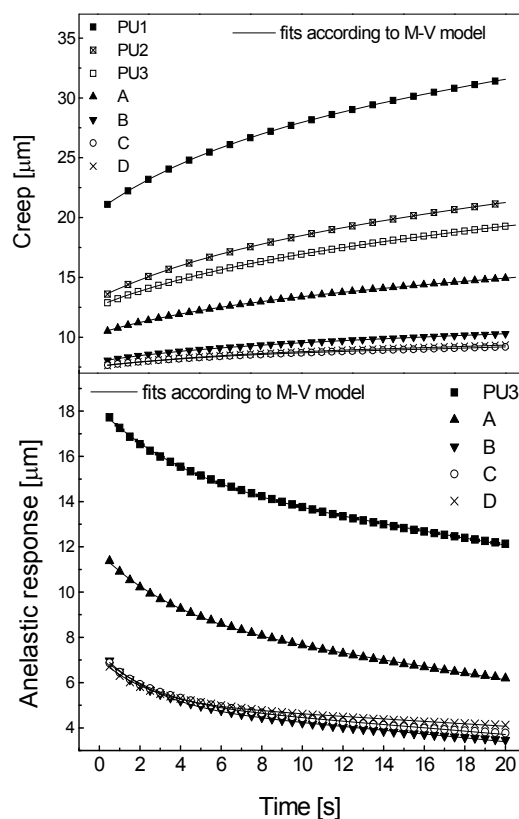


Fig. 2. Experimental indentation creep and relaxation data fitted with Maxwell-Voigt (M-V) rheological model obtained for pure PU samples and PU-CNT nanocomposites

The mechanical properties of PU depend substantially on its preparation conditions, it is well-known that the composition of PU can be varied to produce hard and stiff to soft and rubbery materials. In Fig. 1, the indentation responses of three different PU coatings to the applied load change in time are shown. The substrate material was glass. Using the indentation study, we have found that mechanical properties of PU coatings depend not only on the preparation mixture, but also on the amount of chemicals used for the preparation, i.e. they are dependent on the coating thickness. Probably it is caused by different solidification process at the surface, which is in contact with air and in the bulk of the material. In case of the sample PU1, which was thicker than 300 μm , there was a harder skin at the surface and the hardness in the bulk decreased of one order of magnitude. In case of samples PU2 and PU3 with thicknesses lower than 300 μm the solidification process was more homogeneous, and the differences in surface and bulk properties are less. The hardness of the most thin and stiff PU matrix P3 was 22 MPa, its indentation modulus E_{IT} was 1.14 GPa, the loss modulus E_L was 0.15 GPa.

The PU matrix was in each case softer than the multi-wall carbon nanotube (MWCNT) containing PU (samples A,B,C,D) and showed more significant indentation creep. The unloading cycle showed for PU coatings sudden rush decrease in indentation depth. The composite film A consisting of non-modified nanotubes in polyurethane matrix exhibited slightly higher resistance against indentation compared to P3. However, the COOH activated carbon nanotubes in case of sample B (0.05 % of MWCNT) and sample C (0.1 % of MWCNT) substantially improved the PU matrix properties. The COOH functionalisation of MWCNTs increased the composite resistance against indentation and creep and resulted in better relaxation (anelastic response) ability (see Fig. 1 and Fig. 2). The homogeneity of the composite was improved from the point of view of the indentation test and the scatter in measured values decreased. The activation of the carbon nanotubes improved the hardness and the elastic modulus of the pre-

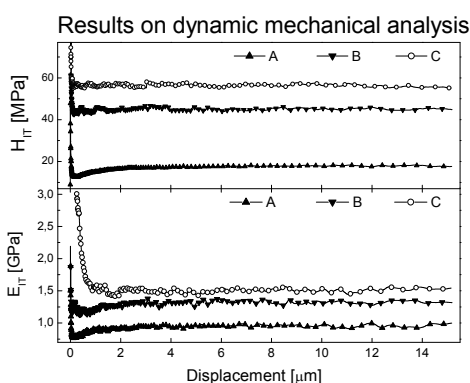


Fig. 3. Dependence of the hardness and the elastic modulus on the indentation depth for nanocomposites A, B and C; A – nanocomposite consisting of nonmodified nanotubes in PU matrix, B – COOH activated carbon nanotubes – 0.05 % of MWCNT, C – COOH activated carbon nanotubes – 0.1 % of MWCNT

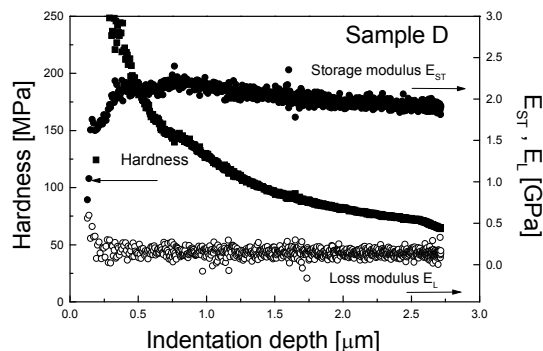


Fig. 4. Results on dynamic mechanical analysis of nanocomposite sample D. Dependence of the hardness, storage and loss modulus, E_{ST} and E_L on the indentation depth for nanocomposite D. D – nanocomposite consisting of plasma modified carbon nanotubes in PU matrix – 0.1 % of MWCNT

pared samples. These results were proven also by dynamic mechanical analysis. Results on the depth dependence of the hardness and elastic modulus are shown in Fig. 3, it is obvious, that the functionalised CNTs offer much better mechanical properties.

In case of sample D (0.1 % of MWCNT), the capacitively coupled low pressure glow discharge was used to activate the MWCNT fillers. The MWCNTs were treated with r.f. power 15 W of at the frequency of 13.56 MHz in mixture of oxygen and argon. From Fig. 1 and Fig. 2 it is evident, that the effect of this treatment on the properties of the PU/CNT composite is of the same quality as in case of commercial COOH treated CNTs.

In Fig. 4 the viscoelastic properties of composite filled with plasma modified CNTs (sample D) are characterised using dynamic mechanical analysis. The hardness of sample determined using this analysis was 65 MPa, the storage modulus E_{ST} was 1.95 GPa, the loss modulus E_L was 0.12 GPa and the loss factor ϕ was 2.8° . An increase in the hardness approaching the surface region was observed in each case of prepared coatings.

Moreover, we analysed the time dependent mechanical properties of the prepared coatings using several mechanical models (Kelvin-Voigt, Voigt, Maxwell-Voigt) The four-element Maxwell-Voigt model was found to be the most suitable approach to describe the time-dependent behaviour of the prepared coatings as it is shown in Fig. 2. In this model, the material response is described by serial combination of Maxwell model and Kelvin-Voigt model.

5. Conclusion

Complex mechanical characterization of MWCNT/PU composites was done. Four types of coatings were compared. The coating with commercial pure MWCNT filler exhibited viscoelastic properties as the PU matrix, but its mechanical

properties such as hardness, elastic modulus and creep resistance were slightly improved. Two different concentrations of MWCNTs commercially functionalized with COOH group were studied. These composites showed improved mechanical properties, and the modified nanotubes proved to be much better fillers than the unmodified MWCNTs due to stronger filler-to-matrix attachment. Because the modified nanotubes seem to be much more convenient composite filler, the first experiments with nanotube modification have been carried out. Modification using inductively coupled discharge in argon and oxygen mixture was successful and the mechanical properties of the composite were increased at the same level as in case of the commercially COOH functionalized MWCNT fillers.

This research has been supported by Ministry of Education, Youths and Sports of the Czech Republic under project MSM0021622411, by the grant of Czech Science Foundation No. 202/07/1669 and by Academy of Science of the Czech Republic by KAN311610701.

REFERENCES

1. Bueche A. M.: *J. Polym. Sci.* 25, 139 (1957).
2. Kuriakose B., De S. K., Bhagawan S. S.: *J. Appl. Polym. Sci.* 32, 5509 (1986).
3. Vaia R. A., Wagner D. H.: *Framework for nanocomposites*. *Materials today*, p. 32–37, 2004.
4. Thostenson E. T., Chou T.-W.: *J. Phys. D: Appl. Phys.* 35, L77–L80 (2002).
5. Liang Z., Ravi S. K., Kevin B., Zhang C., Wang B., Kramer L.: In *International SAMPE symposium and exhibition*, p. 1627–1634, 2003.
6. Geng H., Rosen R., Zheng B., H. Shimoda H., Fleming L., Liu J.: *Adv. Mater.* 14, 1387 (2002).
7. Allaoui S., Bai H. M., Cheng, Bai J. B.: *Compos. Sci. Technol.* 62, 1993 (2002).
8. Schadler L. S., Giannaris S. C., Ajayan P. M.: *Appl. Phys. Lett.* 73, 3842 (1998).
9. Wagner H. D., Lourie. O., Feldman Y., Tenne R.: *Appl. Phys. Lett.* 72, 188 (1998).
10. Shaffer M. S. P., Fan X., Windle A. H.: *Carbon* 36, 1603 (1998).
11. Fan Z., Advani. S. G.: *Polymer* 46, 5232 (2005).
12. Callister W. D.: *Materials Science and Engineering: An Introduction*. Wiley and Sons, New York 2000.
13. Du J.-H., Bai J., Cheng H.-M.: *eXPRESS Polym. Lett.* 1, 253 (2007).
14. Curtin W. A., Sheldon B. W.: *CNT-reinforced ceramics and metals* 7, 44 (2004).
15. Gao F.: *Mater. Today* 7, 50 (2004).
16. Valentini L., Kenny J. M.: *Polymer* 46, 6715 (2005).
17. Xiong J., et al.: *Carbon* 44, 2701 (2006).

V. Buršíková^a, Z. Kučerová^a, L. Zajíčková^a, O. Jašek^a, V. Kudrle^a, J. Matějková^b, and P. Synek (^a*Department of Physical Electronics, Masaryk University, Brno, Czech Republic*, ^b*Institute of Scientific Instruments, Academy of Sciences of the Czech Republic, Brno, Czech Republic*): **Measurement of mechanical properties of composite materials**

The aim of the present work was the study of mechanical properties of MWCNT/PU. Four types of coatings were compared. Two different concentrations of MWCNTs commercially functionalized with COOH group were prepared and studied. These composites showed improved mechanical properties compared to PU, and the modified nanotubes proved to be much better fillers than the unmodified MWCNTs due to stronger filler-to-matrix attachment. Because the modified nanotubes seem to be much more convenient composite filler, the first experiments with nanotube modification have been carried out. Modification using inductively coupled discharge in argon and oxygen mixture was successful and the mechanical properties of the composite were increased at the same level as in case of the commercially COOH functionalized MWCNT fillers.

THE INFLUENCE OF ADDITIVES ON MECHANICAL PROPERTIES OF ORGANIC-INORGANIC COATINGS

LENKA DAJBYCHOVÁ^a, OLGA BLÁHOVÁ^a, and MILENA ŠPÍRKOVÁ^b

^a *New Technology Research Centre, University of West Bohemia, Univerzitní 8, 306 14 Plzeň, Czech Republic,* ^b *Institute of Macromolecular Chemistry, Academy of Sciences of the Czech Republic, 162 06 Praha 6, Czech Republic*
blahova@ntc.zcu.cz

Keywords: nanocomposite materials, hybrid organic-inorganic, nanocomposite coatings, nanoindentation

1. Introduction

The continuous development of all industries creates demand for increasingly sophisticated materials that would meet the required properties – mechanical, thermal, chemical etc. – as accurately as possible. This gives rise to new types of materials, for example in the form of thin coatings. Thin films of a new type have been developed, including hybrid organic – inorganic (O-I) nanocomposite materials that can be widely used in various applications. O-I films are applied to various substrates. They are extensively prepared due to the fact that their final properties can be appropriately adjusted using a wide selection of organic monomers, metal alkoxides and solvents. O-I products are used as optical paints, biomaterials, membranes, as protective coating against scratches, corrosion, oxidation, etc. In terms of environment protection, it is important that water or its mixture with alcohols can be used as a solvent.

Their proper use requires good knowledge of the structural arrangement of the material. Due to the different structure of their composition, the mechanical properties of polymers significantly vary from those of metallic materials. The rapid development of technologies has made it possible to assess the structure and properties of substances not only in the macroscopic scale, but allowed us to reach the nm-scale as well. The final condition of the whole system depends on mechanical properties of thin layers and, therefore, the practical applications of O-I films require proper knowledge of such properties. The most important characteristics of coatings include hardness and modulus of elasticity. These properties are derived from the dependence of indenter penetration on the applied load (indentation curve). This paper focuses on the analysis and characterization of selected O-I films. Surface hardness was determined using nanoindentation tests and the effect of the amount of filler (colloidal silica) was assessed.

2. Experimental Material

[3-(Glycidyoxy)propyl] trimethoxysilane (GTMS, Fluka); diethoxy[3-(glycidyoxy)propyl]-methylsilane (GMDES, Fluka), oligo(oxypropylene) diamines and triamine, Jeffamine D-230, D-400 and T-403 (D230, D400 and T403 Huntsman Corporation, USA), colloidal silica (SiO₂ 40% solution in water; *d* = 29 nm; Ludox AS-40, Aldrich, propan-2-ol (Lachema, Czech Republic) and hydrochloric acid, 38% (Lachema, Czech Republic) were used as received. Functionalised organosilicon precursors (GTMS, GMDES or GTMS and GMDES) were mixed with water, propan-2-ol, and possibly with colloidal silica particles and stirred for 24 h at ambient temperature.

The pH of the mixture was adjusted to 4 with dilute HCl. Then a solution of the respective oligomeric amine (D230, D400 or T403) in aqueous alcohol was added. The reaction mixture was stirred at ambient temperature for 1 h or 2.5 h. Due to the alkaline nature of Jeffamine, pH of the resulting reaction mixture increased to 8 – 9.

Then the reaction mixture was spread on glass or modified polypropylene sheets with constant thickness using a bar coater with a 300 μm gap. The sheets were immediately placed into an oven and kept at 80 °C (2 h) and 105 °C (1 h). The thickness of the final coatings was 150 ± 10 μm (ref.^{1–3}).

Nanocomposite coating consists of an organic polymeric matrix and inorganic nanostructures.

It is a hybrid organic-inorganic product. The glassy coating is formed at moderate temperatures: the inorganic section was formed by the so-called sol-gel process consisting of two consecutive steps – acid hydrolysis and basic polycondensation of organosilicon precursors at laboratory temperatures.

Subsequently, an organic matrix was formed using the process of staged polyaddition at temperatures of 80 and 105 °C. Nanofillers were added to the reaction system in the form of dispersion before the organic polymeric network was created (ref.^{1–3}).

Coatings were prepared at the Institute of Macromolecular Chemistry AS CR in Prague. Based on previous studies of the preparation process and the multidisciplinary characterization, a system where the basic components included [3-diethoxy3-(glycidyoxy) propyl]methylsilane (GMDES) and oligo(oxypropylene) triamine (T403) was chosen.

The resulting products are colorless and optically clear, remarkably smooth. Part of the products was applied to glass and part to metal, then peeled off after becoming dry, thus producing a separate film^{1–3}.

3. Nanoindentation Measurement

The assessment of recorded indentation curves provides a substantial volume of information used to review the plastic, elastic and fracture properties, both of the layer-substrate systems and separate layers (values of nanohardness, modulus

of elasticity, energy consumed for indentation, its elastic and plastic components). The indentation tests were performed using a Berkovich indenter and the Nano Indenter XP device. The Nano Indenter XP device is equipped with a module allowing to perform the measurement using an optional CSM module that makes it possible to recognize deep changes in mechanical properties from a single indent.

Using the Nano Indenter XP, deep changes in nanohardness and the indentation modulus of elasticity were measured for samples with different content of silica. Furthermore, samples applied to glass O-I-G and foils O-I-F were compared.

Fig. 1 and 2 show a typical indentation curves for O-I-F composite layers (Figure 1 for an additive-free sample and Fig. 2 for a sample with 25% of an additive). Maximum indentation depth was 2 μm . The indentation curves indicate that the additives increase layer resistance to indenter penetration.

The values of hardness and modulus of elasticity are compared at a depth of 2 μm and listed in Tables I and II. Fig. 3 and 4 show the hardness profile, and Fig. 5 and 6 the modulus of elasticity, for samples applied to glass and foil. Samples in the form of foils confirm the increasing hardness and modulus of elasticity with a higher content of the additive. With coatings applied to glass, however, this trend is not so clearly demonstrable. The measurement was probably af-

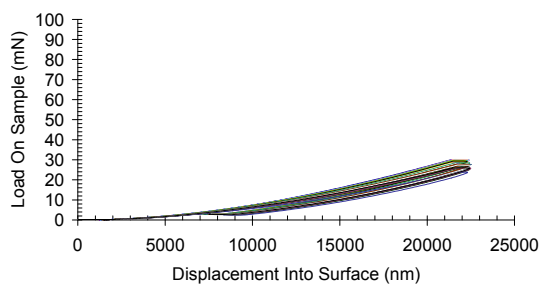


Fig. 1. Nanoindentation curves for the sample without additive

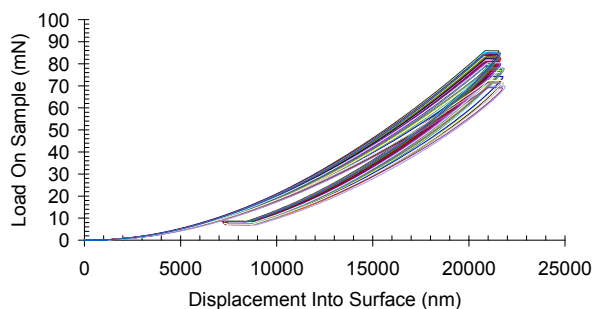


Fig. 2. Nanoindentation curves for the sample with 25% additive

Table I
Modulus of elasticity and hardness of coatings applied to glass

	Additive	H_{IT} [MPa]	E_{IT} [MPa]
O-I-G-0	0% SiO ₂	2.45 ± 0.27	274.1 ± 17.5
O-I-G-5	5% SiO ₂	2.49 ± 0.22	383.6 ± 14.7
O-I-G-10	10% SiO ₂	1.22 ± 0.34	183.8 ± 55.2
O-I-G-15	15% SiO ₂	1.82 ± 0.31	226.7 ± 58.6
O-I-G-20	20% SiO ₂	1.54 ± 0.26	180.2 ± 46.0
O-I-G-25	25% SiO ₂	3.90 ± 1.16	165.1 ± 20.0
O-I-G-30	30% SiO ₂	4.45 ± 2.14	243.4 ± 105.5

Table II
Modulus of elasticity and hardness of foils

	Additive	H_{IT} [MPa]	E_{IT} [MPa]
O-I-F-0	0% SiO ₂	2.70 ± 0.20	162.3 ± 10.1
O-I-F-5	5% SiO ₂	2.77 ± 0.20	231.2 ± 10.7
O-I-F-10	10% SiO ₂	2.59 ± 0.18	233.3 ± 16.9
O-I-F-15	15% SiO ₂	4.21 ± 0.66	265.7 ± 30.3
O-I-F-20	20% SiO ₂	5.98 ± 0.78	269.3 ± 22.0
O-I-F-25	25% SiO ₂	6.32 ± 2.20	300.2 ± 58.3

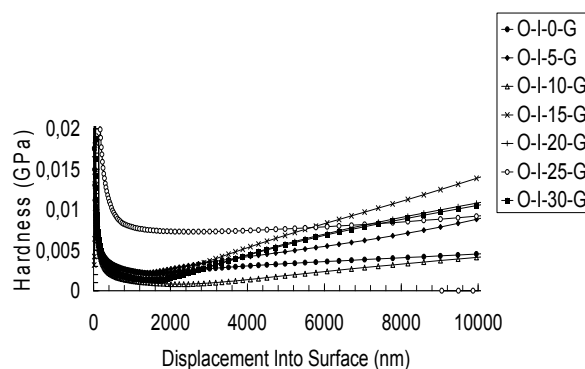


Fig. 3. Dependences of hardness on the indentation depth for samples applied to glass

ected by the substrate and the irregular thickness of the applied layer.

4. Conclusion

The results of this experiment will contribute to the knowledge about materials of this type acquired through other methods^{4,5} thus contributing to the process of optimizing the formation of such coatings for applications requiring increased wear resistance.

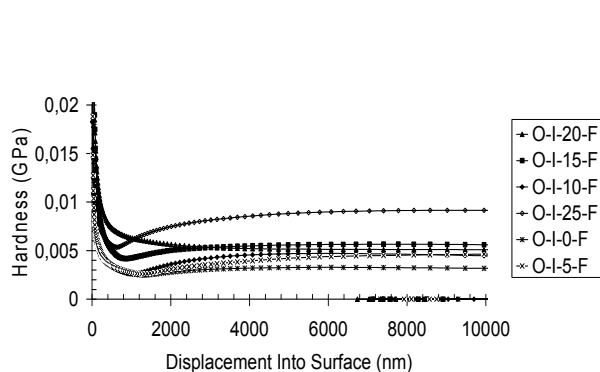


Fig. 4. Dependences of hardness on the indentation depth for samples foils

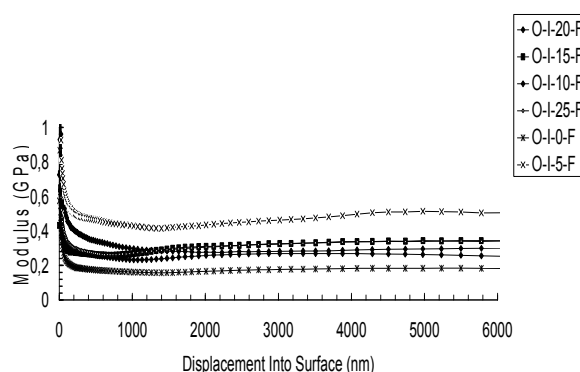


Fig. 6. Dependences of modulus of elasticity on the indentation depth for samples foils

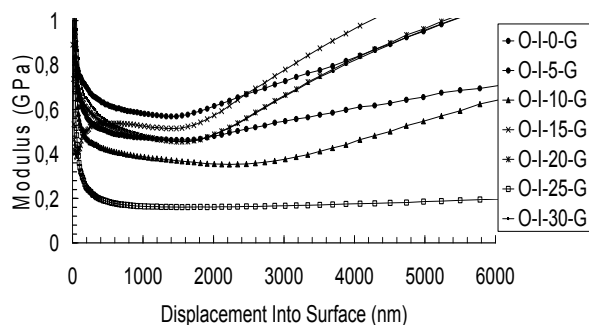


Fig. 5. Dependences of modulus of elasticity on the indentation depth for samples applied to glass

An instrumented hardness test is a suitable method for recognizing the effect of additives on the resulting properties of composite organic-inorganic coatings.

This research was supported by the Academy of Sciences of the Czech Republic, project IAA400500505 and by MŠMT ČR, project MSM 4977751303.

REFERENCES

1. Bláhová O., Špírková M., Vizina M., Skálová J., in: *Nano'03, Brno 2003*, p. 154–159.
2. Špírková M. et al., in: *Nano'03, Brno 2003*, p. 109–114.
3. Špírková M. et al., in: *Nano 02, Brno 2002*, p. 101–104.
4. Špírková M. et al: *Surface Coating Internat.*, B 86, 187 (2003).
5. Špírková M. et al: *J. Appl. Polym. Sci.* 92, 937 (2004).

L. Dajbychová^a, O. Bláhová^a, and M. Špírková^b
^a*New Technology Research Centre, University of West Bohemia, Plzeň,* ^b*Institute of Macromolecular Chemistry, Academy of Sciences of the Czech Republic, Prague, Czech Republic):*
The Influence of Additives on Mechanical Properties of Organic-Inorganic Coatings

This paper focuses on the study of hybrid organic-inorganic nanocomposite materials in the form of coatings applied to a substrate, namely to glass, and separate layers – films. Nanoindentation measuring was used to assess the dependence of mechanical properties (nanohardness and modulus of elasticity) on the amount of additive. Further, these properties are compared for the layer-substrate systems and the layers themselves. Samples in the form of foils confirm the increasing hardness and modulus of elasticity with a higher content of the additive. The results of this work should contribute to optimizing the formation of such layers with respect to applications requiring higher wear resistance.

CONTACT STRENGTH MEASUREMENTS AND CONE CRACK FORMATION OF Si₃N₄ AND SiC BASED CERAMICS

LUCIA HEGEDŮSOVÁ and JÁN DUSZA

Institute of Materials Research, Slovak Academy of Sciences,
Watsonova 47, 040 01 Košice, Slovak Republic
lhegedusova@imr.saske.sk, lucia.hegedusova@yahoo.com

Key words: contact strength, bending strength, Weibull parameters, Fett's theory, crack propagation

1. Introduction

Conventional strength tests describe the failure behaviour of materials under simple stress states to comprise mostly uni-axial stresses with relatively small stress gradients. Considering practical applications^{1–3}, mechanical loading often leads to strongly non-homogeneous and multi-axial stress states to be also induced by contact loading by line or point loads. In principle, the determination of strength under the contact loading results from the Weibull theory to include a multi-axial failure criterion. The contact loading by line and point loads can be induced by opposite rollers and opposite spheres using the devices shown in Figs. 1 and 2, respectively.

Proposed by Fett and illustrated in Fig. 1 (ref.⁴), a device for the contact strength test using rollers with the diameter $D = 2R$ is shown in Fig. 1. Two rollers made of hardened steel are pressed onto the rectangular specimen with the force P . With regard to the Fett's theory⁴, a relationship between the characteristic strength $\sigma_{0,\text{cont}}$ and $\sigma_{0,\text{bend}}$ determined by the contact test using rollers and the four-point bending test, respectively, is derived as

$$\sigma_{0,\text{bend}} \approx \sigma_{0,\text{cont}} \quad (1)$$

where $\sigma_{0,\text{cont}}$ is derived by the Weibull analysis⁵ considering the measured stress σ_{cont} in the form⁴

$$\sigma_{\text{cont}} = 0.98 P / (Ht) \quad (2)$$

Similarly, $\sigma_{0,\text{bend}}$ is determined by the Weibull analysis considering σ_{bend} derived as⁴

$$\sigma_{\text{bend}} = 3P(S_1 - S_2) / (2BW^2) \quad (3)$$

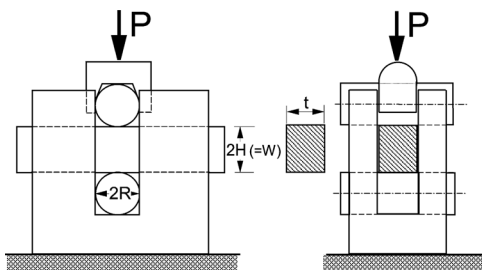


Fig. 1. Schematic illustration of a device for the contact test using rollers⁴

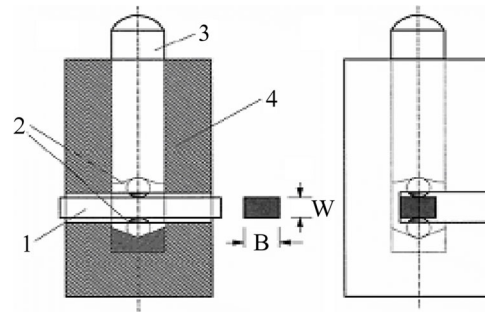


Fig. 2. Schematic illustration of a device for the contact test using spheres⁴

where S_2 and S_1 are inner and outer spans, respectively. Similarly, with regard to the Fett's theory, a relationship between the Weibull moduli m_{cont} and m_{bend} is derived as⁴

$$m_{\text{bend}} \approx 2 m_{\text{cont}} \quad (4)$$

Proposed by Fett, a device for the contact strength test using spheres is shown in Fig. 2 (ref.⁶). The rectangular bar (1) is loaded via two opposing spheres (2) with the radius R which are loaded by the force P . The load P is transferred to the upper sphere by a steel roller (3) guided by the hollow roller (4). The test can be carried out using bending bars of shorter length.

The characteristic strength $\sigma_{0,\text{cont}}$ determined by the contact test using spheres, derived by the Weibull analysis⁵, consider the strength σ_{cont} in the form⁶

$$\sigma_{\text{cont}} = (1 - 2\nu_2)[6P(E'R)^2]^{1/3} / (3\pi) \\ 1/E' = [(1 - \nu_1^2)/E_1] + [(1 - \nu_2^2)/E_2] \quad (5)$$

where E_1 , ν_1 and E_2 , ν_2 are the Young's modulus, the Poisson's ratio for the spheres and an investigated ceramic material, respectively.

2. Experimental procedure and materials

Mechanical tests. The contact tests using rollers and spheres (see Figs. 1, 2) with the diameter $D = 2R = 3$ mm of the rollers and the radius $R = 2$ mm of the spheres were performed by Lloyd LR 5KPlus at room temperature. The rollers and spheres both of standard hardened steel were applied to specimens with the dimensions $W = 3$ mm, $B = 4$ mm, $L = 10$ – 15 mm or $L = 25$ mm. The four-point bending test with $S_1 = 40$ mm, $S_2 = 20$ mm was applied to specimens with dimensions of $W = 3$ mm, $B = 4$ mm, $L = 45$ mm. Specimens used for all mechanical tests were cut by diamond tools, ground and consequently polished with $15 \mu\text{m}$ finish. The specimen edges were chamfered to minimize the influence of the stress concentration. The contact test using rollers and the four-point bending test were realized in such a way that the load P was increased up to the critical load P_c which caused the specimen failure. A part of a number of specimens were

tested in the contact test using spheres in such a way, that the load of the specimens was stopped before the critical load, i.e. before the specimen failure at the load $P = 4.9$ kN, with an aim to investigate a character of the crack growth during the loading regime. These un-failed specimens were cut through the centre of the contact area, ground and polished due to optical electron microscopy for the determination of the crack length c and the angle α between the crack and a contact surface. The rest of a number of specimens was loaded till the specimen failure. All mechanical tests were performed at a loading rate of 0.5 mm min^{-1} .

Experimental materials and microstructure. The following ceramic materials were investigated:

1. Si_3N_4 with the additives 3 % Al_2O_3 and 3 % Y_2O_3 , sintered in the atmosphere N_2 , produced by CeramTec (Plochingen, Germany), and provided in a form of plates with the dimensions $47 \times 11 \times 102$ mm.

2. SiC prepared as a mixture of the commercially available β -SiC powder (HSC-0.59, Superior Graphite) with the additives of 5 % Si_3N_4 , 2.8 % Al_2O_3 and 5.7 % Y_2O_3 , hot pressed at $1870 \text{ }^\circ\text{C h}^{-1}$ in the atmosphere N_2 and subsequently annealed at $1650 \text{ }^\circ\text{C/5 h}$, prepared at Institute of Inorganic Chemistry SAS Bratislava in the form of plates with the dimensions $60 \times 60 \times 6$ mm.

Microstructure of Si_3N_4 (see Fig. 3a) consists of moderately elongated β - Si_3N_4 grains with the aspect ratio of 3–5 and of inter-granular glassy phase with the volume fraction 12 %, and additionally small amount of Fe originating from the used powder for the material preparation. Microstructure of the SiC (see Fig. 3b) consists of fine submicron-sized equiaxed SiC grains with a low aspect ratio and of very thin inter-

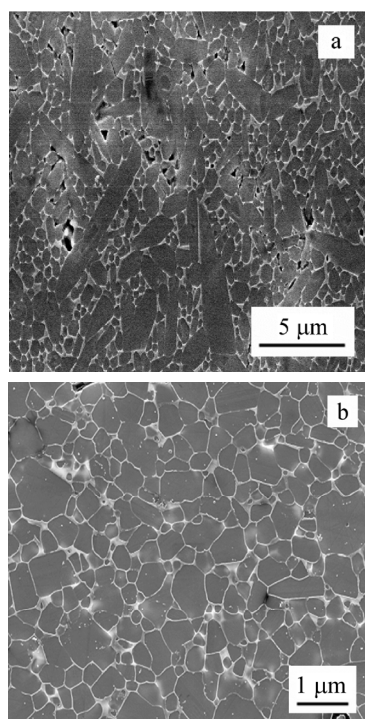


Fig. 3. SEM micrographs of characteristic microstructure of Si_3N_4 (a) and SiC (b), both plasma etched

granular phases/triple points. The average size of the SiC grains is 450 nm.

Material parameters considered in Eq. (5) are as follows: hardened steel of spheres – $E_1 = 200$ GPa, $\nu_1 = 0.29$; Si_3N_4 – $E_2 = 310$ GPa, $\nu_2 = 0.24$; SiC – $E_2 = 400$ GPa, $\nu_2 = 0.24$.

3. Results and discussion

Contact test using rollers and four-point bending test. The characteristic strength $\sigma_{0,\text{cont}}$, $\sigma_{0,\text{bend}}$, the Weibull moduli m_{cont} , m_{bend} determined by the Weibull distribution, and the ratios $m_{\text{bend}} / m_{\text{cont}}$, $\sigma_{0,\text{cont}} / \sigma_{0,\text{bend}}$ are presented in

Table I
The characteristic strength $\sigma_{0,\text{cont}}$, $\sigma_{0,\text{bend}}$ and the Weibull moduli m_{cont} , m_{bend}

Material	m_{cont}	m_{bend}	$m_{\text{bend}} / m_{\text{cont}}$	Eq. (4)
Si_3N_4	7.1	13.9	1.96	2
SiC	8.95	10.6	1.18	2
	$\sigma_{0,\text{cont}}$ [MPa]	$\sigma_{0,\text{bend}}$ [MPa]	$\sigma_{0,\text{cont}} / \sigma_{0,\text{bend}}$	Eq. (1)
Si_3N_4	766.3	727.8	1.05	1
SiC	617.1	437.1	1.41	1

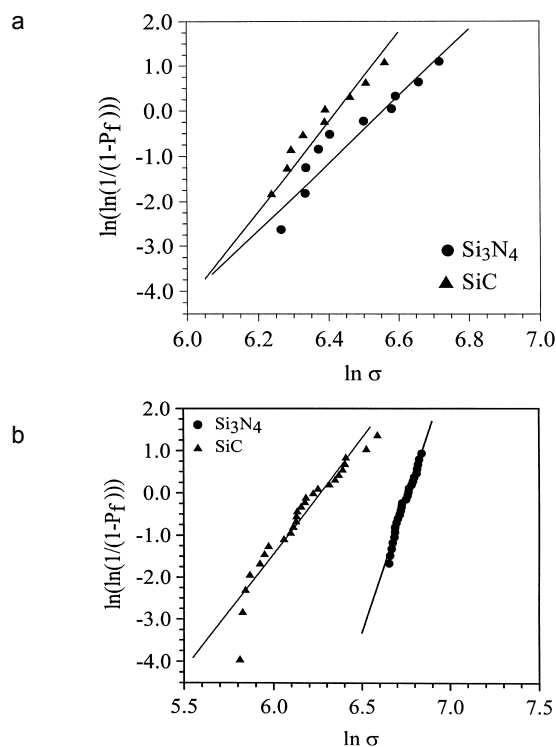


Fig. 4. The Weibull distribution of the characteristic strength $\sigma_{0,\text{cont}}$ [MPa], $\sigma_{0,\text{bend}}$ [MPa], and Weibull moduli m_{cont} , m_{bend} related to the contact test using rollers (a), and to the four-point bending test (b) for the investigated materials

Tab. I, Fig. 4, where m_{cont} , $\sigma_{0,\text{cont}}$ and m_{bend} , $\sigma_{0,\text{bend}}$ are related to the contact test using rollers and the four-point-bending test, respectively.

According to the results, the characteristic strength values for the silicon nitride ceramics were very similar in contact and bending strength tests but for the silicon carbide the characteristic strength in bending test was lower comparing to the value of the contact strength. The Weibull modulus obtained for Si_3N_4 using contact strength method is approximately half of the modulus from the bending method except SiC, where the Weibull modulus in contact mode is similar to the modulus obtained from the bending strength result. The very low characteristic strength in bending mode in the case of SiC is caused by the presence of large processing flaws representing fracture origins. As it was found by fractographical analysis (see Fig. 5b), such flaws with different size (from 5 μm to 100 μm), shape and location (distance from the tensile surface) decrease not only the characteristic bending strength but also lead to the low Weibull modulus for this material. The significantly different Weibull moduli in comparison of the bending and contact strength tests can be explained also by the existence of strong stress gradient near the contact areas, in the case of contact strength test in contrast to the bending test with significantly lower stress gradient. In the case of the silicon nitride ceramics tested in bending test, the fracture origin in the form of processing flaws was identified only randomly as Fe inclusions (see Fig. 5a), and the fracture origin was at the tensile surface and corners of the specimens in the form of small surface defects.

According to the result of ceramographic/fractographic examination, the characteristic damage mechanisms arising during the loading in the contact mode were located below the surface of the specimens in the form of lateral, median and contact end cracks as shown in Fig. 6 for Si_3N_4 . The different

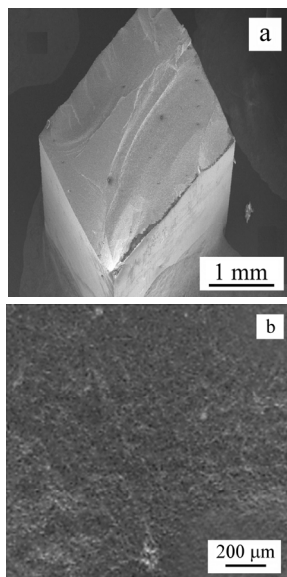


Fig. 5. Fracture surfaces of Si_3N_4 (a) and SiC (b) loaded by the contact test using rollers and the four-point bending test, respectively. Fracture origin in SiC (b)

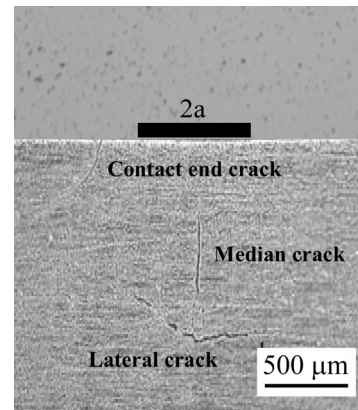


Fig. 6. A cross-section view of a surface between two rollers: lateral, median and contact end cracks in Si_3N_4

crack types could be present at the contact surface and specimen sides of one experiment. A typical order of crack appearance was established by correlating the presence of different cracks and applied load in each experiment. Notably, the first cracks were always found at the specimen sides. At one or both of specimen sides, a surface parallel crack was visible at a depth that was approximately one to two times the contact width $2a$. The crack typically displayed a slightly concave shape with the edges drawn towards the contact surface. In experiments that had proceeded, the cracks of a second type were distinguishable. These cracks were vertical and located between the surface parallel crack and the contact mark. They typically started at the top side of the first crack and grew towards the contact surface. In some experiments, the cracks reached the contact surface at the contact end.

Following the nomenclature that is used for similar sub-surface contact cracks in ceramics, the first crack was named lateral crack and second crack was named median crack. Last cracks were often found together in the contact surface. A few tests did only contain the crack at the corner between specimen side and surface. It was named a contact end crack. Due to the contact symmetry, up to four contact end cracks may appear in one test. They meet the specimen corner at a perpendicular angle in both surface and side views. In the surface, they are curved towards the contact edge.

Table II
The characteristic strength $\sigma_{0,\text{cont}}$, $\sigma_{0,\text{bend}}$ and the Weibull moduli m_{cont} , m_{bend}

Material	m_{cont}	m_{bend}	$m_{\text{bend}} / m_{\text{cont}}$
Si_3N_4	22.6	13.9	0.62
SiC	20.5	10.6	0.52
	$\sigma_{0,\text{cont}}$ [MPa]	$\sigma_{0,\text{bend}}$ [MPa]	$\sigma_{0,\text{cont}} / \sigma_{0,\text{bend}}$
Si_3N_4	3344.2	727.8	4.55
SiC	3327.6	437.1	7.61

Contact test using spheres. The characteristic strength $\sigma_{0,\text{cont}}$, $\sigma_{0,\text{bend}}$ together with the Weibull moduli m_{cont} , m_{bend} determined by the Weibull distribution, and the ratios $m_{\text{bend}}/m_{\text{cont}}$, $\sigma_{0,\text{cont}}/\sigma_{0,\text{bend}}$ are presented in Tab. II, Fig. 7, where m_{cont} , $\sigma_{0,\text{cont}}$ and m_{bend} , $\sigma_{0,\text{bend}}$ are related to the contact test using rollers and the four-point-bending test, respectively. With regard to the higher values of m_{cont} of the contact test using spheres compared to those of both the contact test using rollers and the four-point bending test (see Tab. I), the contact test using spheres is assumed to be the most precise and accordingly the most considerable for the determination of strength of ceramic materials. As assumed in⁶, the preciseness can be explained by stable growth of the cone cracks originating during the contact test using spheres, and not by an initial size distribution of the flaws to originate during the processing.

According to Fig. 8, the damages/fracture origins in contact mode were located at the tensile surface of the sample in the form of similar cone cracks arising to a critical size during the loading, and controlling the fracture, in contrast to the bending mode when the fracture is controlled by processing defects. The radius of the cone crack in Si_3N_4 was significantly larger than that in SiC , and one crack is initiated only (see Fig. 8a). The cone crack was nearly perpendicular to the specimen surface (5–10 μm), then changed its direction and

grew up to the critical size of $\approx 200 \mu\text{m}$. In SiC material the cone crack originated at lower load and therefore the cone crack radius is smaller. In this case, typically multi-cracks are initiating with the first main crack which is longer comparing to the crack in Si_3N_4 (see Fig. 8b). The multi-crack formation is connected with the deformation of the sphere when the load is increasing and with the enlarged contact area between the sphere and specimens. In the tougher Si_3N_4 the cone crack originates at higher loads and the further deformation of sphere is not so significant and does not initiate further crack growth.

Finally, in the case of the contact strength test using spheres, no good correlation between the contact and bending strength values is observed.

This work was supported by the Slovak Research and Development Agency under the contracts No. APVV-0034-07, by the Slovak Grant Agency VEGA 2/7194/27, by NANOSMART Centre of Excellence (1/1/ 2007-31/12/2010) Slovak Academy of Sciences, by HANCOC-MNT.ERA-NET, by NENAMAT INCO-CT-2003-510363.

REFERENCES

1. Ceniga L., in book: *Ceramic and Composite Materials*, chap. 5, p. 147, Nova Science Publishers, New York 2005.
2. Ceniga L., in book: *New Development in Materials Science Research*, chap. 4, p. 139, Nova Science Publishers, New York 2007.
3. Bidulská J., Bidulský R., Ceniga L., Kvačkaj T., Cabibbo M., Evangelista E.: *Metall. Mater.* 46, 151 (2008).
4. Fett T., Munz D.: *Eng. Fract. Mech.* 69, 1353 (2002).
5. Dorčáková F.: *PhD thesis*, Institute of Materials Research, Slovak Academy of Sciences, Košice 2004.
6. Fett T., Ernst E., Munz D.: *J. Mater. Sci.* 21, 1955 (2002).

L. Hegedúsová and J. Dusza (*Institute of Materials Research, Slovak Academy of Sciences, Košice, Slovakia*): **Contact Strength Measurements and Cone Crack Formation of Si_3N_4 and SiC Based Ceramics**

The paper deals with an investigation of contact strength determined by contact tests applied to Si_3N_4 and SiC ceramic materials, where loading of the contact tests is induced by opposite rollers and opposite spheres. Experimental results of the contact tests are compared with those of the four-point bending test, and consequently the comparison of the Weibull parameters in the contact and bending modes results in the verification or the refutation of the Fett's theory. Resulting from microstructural analysis, a reason of deviations from the Fett's theory is determined. In general, the contact tests using rollers and spheres applied to a brittle material induce different types of cracks, i.e. lateral, median, contact end cracks and cone cracks, respectively. In addition to the contact strength determination, an investigation of the crack initiation and propagation is performed.

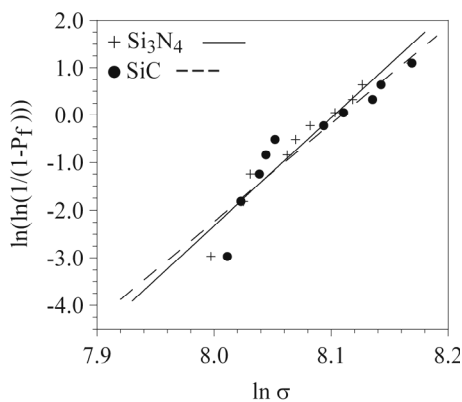


Fig. 7. The Weibull distribution of the characteristic strength $\sigma_{0,\text{cont}}$ [MPa]

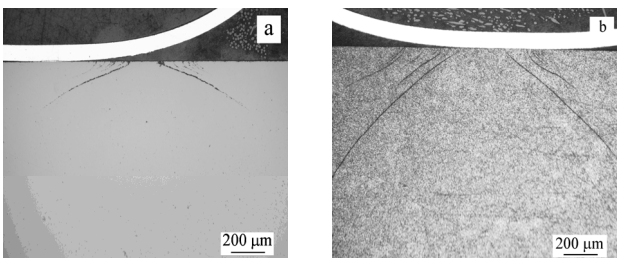


Fig. 8. Optical micrographs of cross-section views of the contact sites in Si_3N_4 (a) and SiC (b)

NANOINDENTAČNÍ MĚŘENÍ HVOF STŘÍKANÝCH POVLAČKŮ

ŠÁRKA HOUDKOVÁ^a, FRANTIŠEK ZAHÁLKA^a, MICHAELA KAŠPAROVÁ^a a OLGA BLÁHOVÁ^b

^a ŠKODA VÝZKUM s.r.o., Tylova 57, Plzeň, 31600, ČR,

^b NTC ZČU, Univerzitní 8, Plzeň, 306 14, ČR

sarka.houdkova@skodavyzkum.cz, blahova@ntc.zcu.cz

Klíčová slova: nanoindentace, HVOF, žárové nástřiky

1. Úvod

Žárový nástřik je částicový proces vytváření povlaků o tloušťce obvykle větší než 50 μm , kdy je nanášený materiál ve formě prášku (případně drátu) přiváděn do zařízení, kde dojde k jeho natavení a urychlení směrem k povlakované součásti. Po dopadu na substrát dojde k výraznému plošnému rozptření částice a k jejímu rychlému utužení. Tím se vytváří povlak s charakteristickou lamelární strukturou a specifickými vlastnostmi. Technologie žárových nástřiků umožňuje vytvářet povlaky z těch druhů keramik, kovů a jejich slitin, u kterých nedochází k rozpadu pod bodem tání, na prakticky všechny typy materiálů substrátu. Technologický proces zaručuje teploty povlakované součásti hluboko pod teplotou fázově-strukturálních přeměn (cca 80–120 °C), což brání nežádoucím deformacím součásti.

Struktura povlaku je tvořena jednotlivými deformovanými částicemi. Míra porozity, stejně jako kvalita zakotvení povlaku k povrchu substrátu a výskyt nenatavených či zoxidovaných částic jsou závislé na teplotě a rychlosti dopadajících částic. Teplota a rychlost částic jsou nejdůležitějšími parametry procesu žárového nástřiku, přímo ovlivňujícími kvalitu výsledného povlaku. Jednotlivé technologie žárového nástřiku dosahují v závislosti na použitém zdroji tepelné energie, konstrukci a nastavení procesních parametrů různých hodnot teploty a rychlosti částic. V případě technologie HVOF (vysokorychlostní nástřik plamenem) je díky unikátní konstrukci hořáku dosahováno vysokých rychlostí letících částic za relativně nízkých teplot (v porovnání např. s plazmatickým nástřikem, viz Smith a spol.¹ (1991)). To umožňuje vytvářet husté povlaky s nízkou mírou dekompozice povlaku během nástřiku a velmi vysokou adhezí k základnímu materiálu.

Technologií žárového nástřiku mohou být připravovány povlaky z různých typů materiálů s rozsahem vlastností vhodných jak pro aplikaci v plynových turbínách, tak např. v elektronickém průmyslu. Velkou skupinou povlaků jsou povlaky určené jako ochrana proti opotřebení, často v kombinaci s odolností proti vysokým teplotám nebo koroznímu napadení.

Tato studie je zaměřena na povlaky, jejichž účelem je zvýšení odolnosti povlakované součásti proti opotřebení. Materiálem těchto povlaků jsou tzv. tvrdokovy, kompozity na bázi kovových slitin vyztužených karbidickými částicemi.

Mikrostruktura HVOF stříkaných cermetových povlaků je tvořena tvrdými, obvykle karbidickými částicemi a kovovou maticí, ve které jsou částice zakotveny. Vlastnosti částic a matrice a jejich vzájemná synergie jsou určující pro celkové vlastnosti povlaku. Studium mechanismů opotřebení cermetových povlaků však prokázalo, že dle způsobu opotřebení a vlastností konkrétních částic a materiálu matrice dochází k opotřebení přednostně u některých strukturálních komponent. Proto byla pozornost zaměřena na zjištění vlastností jednotlivých komponent pomocí nanoindentoru, který umožnil stanovit jejich základní mechanické charakteristiky – tvrdost a modul pružnosti. Jejich vzájemný poměr E/H charakterizuje elastickoplastické vlastnosti hodnocených materiálů. Znalost těchto základních mechanických charakteristik umožňuje nejen přímo predikovat jejich odolnost proti opotřebení a křehkému porušení, ale je nutná i ke stanovení dalších materiálových konstant, jako je například odolnost proti šíření trhlin hodnocená metodou měření indentační lomové houževnatosti. Současně byly zmiňované mechanické charakteristiky hodnoceny u povlaků, které byly vystaveny tepelnému zpracování. Vliv expozice tepelnému namáhání na strukturu a vlastnosti tvrdokovů nanášených technologií žárového nástřiku je tématem celé řady studií^{2–4}.

2. Experimentální podmínky

Mechanické vlastnosti strukturálních komponent byly hodnoceny na dvou různých HVOF stříkaných povlacích na bázi tvrdokovu: $\text{Cr}_3\text{C}_2\text{-NiCr}$ a $(\text{Ti},\text{Mo})(\text{C},\text{N})\text{-NiCo}$. Povlaky byly nástřikány technologií HVOF, systémem TAFA JP-5000 na pracovišti ŠKODA VÝZKUM s.r.o. s využitím standardního postupu přípravy vzorků a optimalizovaných deponičních parametrů. Podmínky depozice jsou uvedeny jinde⁵. Materiál $\text{Cr}_3\text{C}_2\text{-NiCr}$ ve formě prášku je komerčně dostupný pod označením 1375VM, materiál $(\text{Ti},\text{Mo})(\text{C},\text{N})\text{-NiCo}$ s pracovním názvem S49 je experimentálním práškem, vyvinutým v Fraunhofer Institute v Drážďanech.

Část vzorků byla tepelně zpracována ve ŠKODA VÝZKUM s.r.o. žiháním po dobu 8 h na teplotu 700 °C. Mikrostruktura vybraných žárových nástřiků byla hodnocena s použitím SEM na pracovišti ŠKODA VÝZKUM s.r.o.

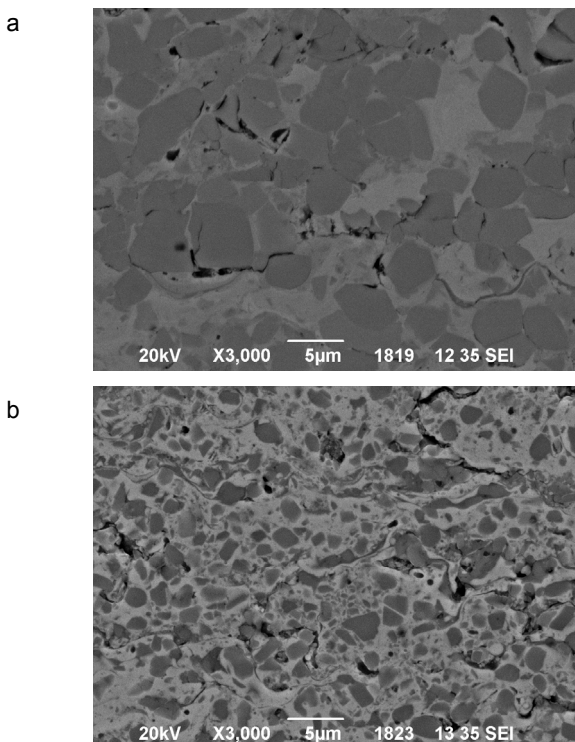
Měření nanotvrdosti bylo realizováno na pracovišti NTC ZČU. Hodnocení mechanických vlastností bylo provedeno na příčném metalografickém výbrusu povlakem. Pro měření byl použit nanoindentor Nano Indenter XP. V povlaku $\text{Cr}_3\text{C}_2\text{-NiCr}$ bylo z důvodu velkého rozptylu naměřených výsledků provedeno celkem 200 měření, 100 v oblasti matrice a 100 v oblasti karbidických částic, v povlaku $(\text{Ti},\text{Mo})(\text{C},\text{N})\text{-NiCo}$ bylo provedeno celkem 60 jednotlivých měření, vždy 30 měření v oblasti matrice a 30 měření v oblastech karbidických částic. Na základě analýzy výsledků, které neprokázaly vyšší spolehlivost měření v případě výběru lokalit, bylo pro měření tepelně zpracovaných povlaků zvoleno hodnocení v náhodných lokalitách. V každém povlaku bylo provedeno 60 měření. V průběhu měření byla snímána velikost tvrdosti,

modulu pružnosti a zatěžování na hloubce proniknutí. Ve všech případech byla použita konstantní hloubka proniknutí indentoru 1 μm , pro indentaci byl použit Berkovichův indentor. Po ukončení měření byla naměřená data tříděna pomocí programu TEST WORKS, kde byla provedena selekce a třídění dat na karbidickou a matriční fázi.

3. Výsledky měření

Mikrostruktura hodnocených žárových nástřiků v tepelně nezpracovaném stavu je zobrazena pomocí SEM na obr. 1.

Mikrostruktura HVOF stříkaného povlaku $\text{Cr}_3\text{C}_2\text{-NiCr}$ je relativně homogenní, s nízkým obsahem pórů. Kromě karbidů Cr_3C_2 a NiCr matrice obsahuje i oxidickou fázi Cr_2O_3 , vzniklou jako produkt oxidace během procesu nástřiku, a pravděpodobně též karbidy Cr_7C_3 a Cr_{23}C_6 s tvrdostí nižší než výchozí Cr_3C_2 , vzniklé oduhličením během nástřiku⁶. Vlivem rozpouštění karbidů v matrici během nástřiku dochází ke zvýšení koncentrace C a Cr v matrici ve srovnání s výchozím práškem. To umožňuje tavenině solidifikovat jako kvaziamorfni nebo nanokrystalická struktura bohatá na Cr a C. Vlivem rychlého tuhnutí se ve struktuře povlaku objevují i další kovové nanokrystalické fáze s velikostí zrna cca 10 nm, tvořené 50 % Ni a 50 % Cr (cit.⁷). Oxidace povlaku $\text{Cr}_3\text{C}_2\text{-NiCr}$ za zvýšených teplot vytváří oxidickou vrstvu Cr_2O_3 , která je velmi dobře adhezně vázána na povrch povlaku a je velmi kompaktní.



Obr. 1. Mikrostruktury žárových nástřiků; a) $\text{Cr}_3\text{C}_2\text{-NiCr}$, b) $(\text{Ti,Mo})(\text{C,N})\text{-NiCo}$

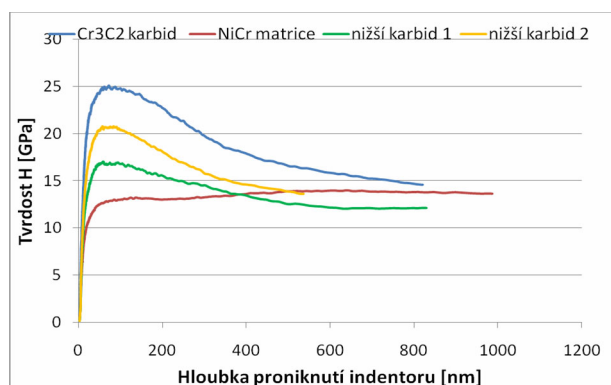
Mikrostruktura HVOF stříkaného povlaku $(\text{Ti,Mo})(\text{C,N})\text{-NiCo}$ je podrobně popsána v cit.⁶. V prášku byly detegovány „core-rim“ kubické fáze, vlivem nedokončené reakce při sintrování se objevuje též Mo_2C . Po nástřiku se v povlaku objevuje též Ti_2O_3 . Oxidací za vyšších teplot vzniká oxidická vrstva, tvořená třemi vrstvami. Vnější je z Co_3O_4 , střední z CoMoO_4 a vnitřní je tvořená částicemi Ti_2O_3 (rutil) v matrici CoMoO_4 . Ti_2O_3 se vyskytuje i v jiné modifikaci, jako tzv. anatas, ale ten je přechodový a objevuje se pouze při teplotách do 500 $^\circ\text{C}$.

Výsledky nanoindentačních měření byly zpracovány do grafů na obr. 2–5, zobrazujících závislost obou sledovaných charakteristik, tvrdosti a modulu pružnosti, na okamžité hloubce proniknutí indentoru. Z grafů je patrné, že snímané charakteristiky se během pronikání indentoru do materiálu a zvětšování oblasti ovlivněné vtiskem mění od vlastností jednotlivých mikrostrukturních součástí (karbidů či karbonitridů a matrice) směrem k hodnotám, vyjadřujícím vlastnosti kompozitu tvrdokovu. U tvrdých fází byla za tvrdost a modul pružnosti brána nejvyšší dosažená hodnota, ke které byl stanoven interval hloubky proniknutí s nejvyšší hodnotou sledované charakteristiky.

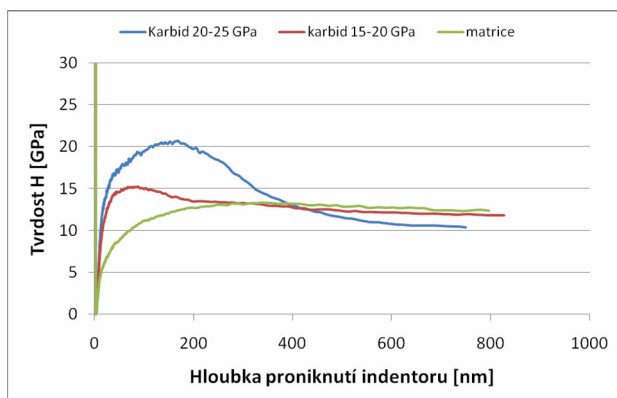
Rozeborem grafů výsledků CSM metody nanoindentačního měření tepelně nezpracovaného povlaku $\text{Cr}_3\text{C}_2\text{-NiCr}$ (obr. 2) byly identifikovány 4 fáze. Na základě³ byl výskyt fází s vlastnostmi mezi vlastnostmi matrice a nejtvrďšího karbidu (pravděpodobně Cr_3C_2) připsán existenci nižších karbidů Cr_7C_3 a Cr_{23}C_6 s tvrdostí nižší než výchozí Cr_3C_2 , vzniklé oduhličením během nástřiku.

Při hodnocení tepelně zpracovaného povlaku $\text{Cr}_3\text{C}_2\text{-NiCr}$ (obr. 3) nebylo možné identifikovat všechny 4 fáze stejně jako u povlaku nezpracovaného. Na základě CSM metody byly identifikovány pouze tři fáze, z nichž jedna odpovídá svým průběhem matrici. Druhé dvě jsou označeny „karbid 20–25 GPa“ a „karbid 25–20 GPa“ dle hodnoty maximální dosažené hodnoty tvrdosti. Spolehlivost identifikace jednotlivých fází je však výrazně závislá na míře rozdílnosti jejich elasticko-plastického chování, a tudíž může být u různých materiálů rozdílná. Značná heterogenita žárově stříkaných povlaků snižuje přesnost identifikace a činí jí značně obtížnou.

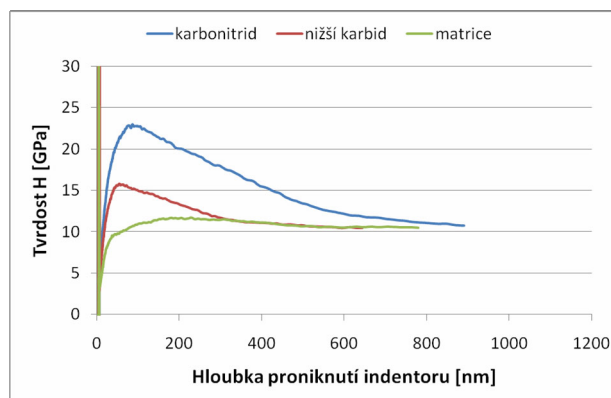
Rozeborem grafů výsledků CSM metody nanoindentačního



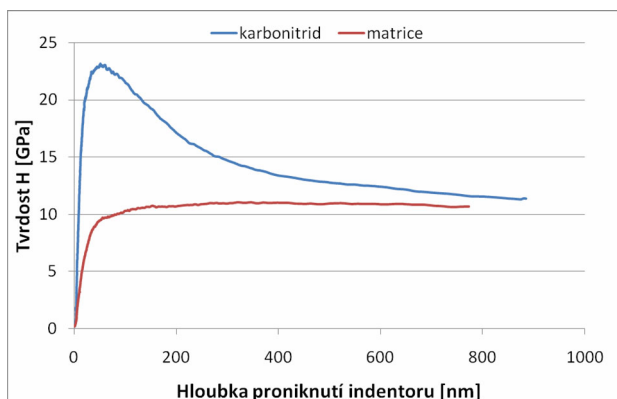
Obr. 2. Průběh tvrdosti v závislosti na hloubce proniknutí indentoru (CSM metoda) tepelně nezpracovaného povlaku $\text{Cr}_3\text{C}_2\text{-NiCr}$



Obr. 3. Průběh tvrdosti v závislosti na hloubce proniknutí indentoru (CSM metoda) povlaku $\text{Cr}_3\text{C}_2\text{-NiCr}$ žíhaného při teplotě $700\text{ }^\circ\text{C}$ po dobu 8 hodin



Obr. 5. Průběh tvrdosti v závislosti na hloubce proniknutí indentoru (CSM metoda) povlaku $(\text{Ti,Mo})(\text{C,N})\text{-NiCo}$ žíhaného při teplotě $700\text{ }^\circ\text{C}$ po dobu 8 hodin



Obr. 4. Průběh tvrdosti v závislosti na hloubce proniknutí indentoru (CSM metoda) tepelně nezpracovaného povlaku $(\text{Ti,Mo})(\text{C,N})\text{-NiCo}$

ho měření tepelně nezpracovaného povlaku $(\text{Ti,Mo})(\text{C,N})\text{-NiCo}$ (obr. 4) byly identifikovány pouze 2 fáze – fáze, jejíž tvar křivky H-h odpovídá matici, a fáze, jejíž tvar křivky H-h odpovídá tvrdé fázi, označené jako karbonitrid.

Při hodnocení tepelně zpracovaného povlaku (Ti,Mo)

Tabulka II

Hodnoty sledovaných mechanických charakteristik povlaku $\text{Cr}_3\text{C}_2\text{-NiCr}$ určených metodou Oliver-Pharr z odlehčovací části zatěžovací křivky při zatížení do hloubky 1 μm

$\text{Cr}_3\text{C}_2\text{-NiCr}$	H [GPa]	E [GPa]	E/H
As-sprayed	$12,3 \pm 2,2$	231 ± 23	18,7
Žíhaný	$10,7 \pm 1,8$	220 ± 10	20,5

$(\text{C,N})\text{-NiCo}$ (obr. 5) byly výsledky měření rozříděny do 3 skupin – jedna odpovídající matici a dvě tvrdé fáze, označené „karbonitrid“ a „nižší karbíd“.

Výsledky měření, hodnoty H a E [GPa] povlaků $\text{Cr}_3\text{C}_2\text{-NiCr}$ a $(\text{Ti,Mo})(\text{C,N})\text{-NiCo}$ v tepelně nezpracovaném i žíhaném stavu jsou pro jednotlivé fáze i pro kompozit uvedeny v tabulce I–IV.

3. Diskuse výsledků a závěr

Výsledky měření pomocí metody CSM, zobrazené

Tabulka I

Hodnoty sledovaných mechanických charakteristik povlaku $\text{Cr}_3\text{C}_2\text{-NiCr}$ naměřených metodou CSM – maximální naměřené hodnoty karbidů (tvrdost H a modul pružnosti E)

$\text{Cr}_3\text{C}_2\text{-NiCr}$		H maximální		H konečná		E maximální		E konečný	
		H [GPa]	h [nm]	H [GPa]	h [nm]	E [GPa]	h [nm]	E [GPa]	h (nm)
As-sprayed	Cr_3C_2	$25 \pm 3,4$	87	$14,6 \pm 2,8$	820	362 ± 45	37	247 ± 24	820
	karbíd 1	$17 \pm 1,5$	93	$12,1 \pm 2,3$	536	255 ± 33	28	235 ± 23	829
	karbíd 2	$21 \pm 2,3$	83	$13,6 \pm 3,1$	829	301 ± 34	28	233 ± 14	713
	matrice			$13,6 \pm 2,8$	986			243 ± 27	986
Žíhaný	karbíd 20-25	$20,6 \pm 0,6$	169	$10,4 \pm 2,3$	750	302 ± 47	23	207 ± 10	750
	karbíd 15-20	$15,3 \pm 2,7$	88	$11,8 \pm 2,1$	827	259 ± 38	31	215 ± 14	827
	matrice			$12,4 \pm 1,9$	796			218 ± 14	796

v grafech na obr. 2–5, dávají dobrou představu o průběhu okamžitých hodnot sledovaných mechanických vlastností v závislosti na hloubce proniknutí indentoru, tzn. v závislosti na velikosti oblasti ovlivněné vtiskem. V případě tvrdých fází je maxima sledovaných hodnot dosahováno pokaždé v jiné hloubce proniknutí indentoru, v závislosti na velikosti strukturální komponenty a jejích vlastnostech.

Informace o hloubkách proniknutí indentoru odpovídajících maximu sledované hodnoty tvrdosti, resp. modulu pružnosti, jsou spolu s dalšími uvedeny v tabulce I a III. V případě povlaku $\text{Cr}_3\text{C}_2\text{-NiCr}$ se hloubka proniknutí indentoru odpovídající maximální naměřené hodnotě tvrdosti pohybovala v rozmezí 80–90 nm, zatímco pro maximální naměřené hodnoty modulu pružnosti v rozmezí 30–40 nm. V případě povlaku $(\text{Ti},\text{Mo})(\text{C},\text{N})\text{-NiCo}$ se hloubka proniknutí indentoru odpovídající maximální naměřené hodnotě tvrdosti pohybovala v rozmezí 45–90 nm, zatímco pro maximální naměřené hodnoty modulu pružnosti v rozmezí 17–65 nm. Rozdíl ve velikosti rozmezí mezi povlakem $\text{Cr}_3\text{C}_2\text{-NiCr}$ a $(\text{Ti},\text{Mo})(\text{C},\text{N})\text{-NiCo}$ je dán rozdílem mikrostruktur obou povlaků. Zatímco mikrostrukturu povlaku $\text{Cr}_3\text{C}_2\text{-NiCr}$ tvoří karbidy Cr_3C_2 , případně karbidy nižší vzniklé vyhoříváním uhlíku při nástřiku s definovaným rozmezím velikosti karbidů ve výchozím materiálu (prášku), obsahuje komplexní mikrostruktura povlaku $(\text{Ti},\text{Mo})(\text{C},\text{N})\text{-NiCo}$ tvrdé částice karbonitridů ve formě tzv. core-rim fází, jejichž velikostní rozmezí je mnohem větší. Z informací o hloubkách proniknutí indentoru se bude vycházet při dalších měřeních vlastností konkrétních fází pomocí nanoindentace. Ani u jednoho materiálu nebyl pozorován vliv žíhání na hloubku proniknutí indentoru odpovídající maximu sledovaných hodnot.

V případě měření nanoindentorem s hloubkou proniknutí 1 μm , což odpovídá zatížení cca 200 mN, se materiálové konstanty měří v rámci jednoho splatu. Na této strukturální úrovni bylo provedeno porovnání hodnot sledovaných vlastností stanovených pomocí různých metod. Ukázalo se, že v případě tvrdosti je dosahováno nejvyšších hodnot použitím metody CSM, metoda Oliver-Pharr dává hodnoty mírně nižší. Tento trend je platný pro oba hodnocené povlaky v tepelně nezpracovaném i žíhaném stavu. V případě modulu pružnosti není situace tak jednoznačná. V tepelně nezpracovaném stavu dosahovaly hodnoty E stanovené metodou CSM vyšších hodnot než použitím metody Oliver-Pharr. U povlaků, které byly žíhány, je však situace opačná: žíhané povlaky dosahovaly vyšších hodnot E, ale rozdíl nebyl velký. Poměr E/H, který

Tabulka IV

Hodnoty sledovaných mechanických charakteristik povlaku $(\text{Ti},\text{Mo})(\text{C},\text{N})\text{-NiCo}$ určené metodou Oliver-Pharr z odlehčovací části zatěžovací křivky při zatížení do hloubky 1 μm

$(\text{Ti},\text{Mo})(\text{C},\text{N})\text{-NiCo}$	H [GPa]	E [GPa]	E/H
As-sprayed	10,1±2	227±23	22,5
Žíhaný	9,7±1,7	219±17	22,5

charakterizuje plasticitu, vychází vyšší, použijeme-li výsledky H a E stanovené metodou Oliver-Pharr.

Vliv tepelného zpracování na sledované hodnoty byl u všech hodnocených vzorků i metod stejný: tvrdost i modul pružnosti byly vyšší u povlaků po nástřiku, tepelné zpracování způsobilo jejich pokles. Tento pokles byl nejvýraznější u karbidů povlaku $\text{Cr}_3\text{C}_2\text{-NiCr}$, kde tvrdost poklesla o 20 až 25 % a modul pružnosti o 15–20 % (stanoveno metodou CSM). Pokles hodnot tvrdosti povlaku v rámci jednoho splatu činil 9 % pro metodu CSM a 14 % pro metodu Oliver-Pharr. Modul pružnosti klesl o 11 % pro metodu CSM a 5 % pro metodu Oliver-Pharr. Pokles u povlaku $(\text{Ti},\text{Mo})(\text{C},\text{N})\text{-NiCo}$ byl v porovnání s $\text{Cr}_3\text{C}_2\text{-NiCr}$ menší: u karbonitridů poklesla tvrdost o 4 % a modul pružnosti 10–24 % (měřeno metodou CSM), v rámci jednoho splatu činil pokles tvrdosti pouhé 1 % metodou CSM a 4 % metodou Oliver-Pharr, pokles modulu pružnosti 7 % metodou CSM a 4 % metodou Oliver-Pharr, což je změna v rámci experimentální chyby téměř zanedbatelná.

Tato práce vznikla za podpory projektu MSM 4771868401 a projektu MSM 4977751303.

LITERATURA

- Smith E. B., Power T. J., Barber T. J.: *United Technology Research Centre Report*, p. 91. East Hartford, CT 1991.
- Berger L.-M., Zieris R., Saaro S.: *Conf. Proc. ITSC 2005, Basel, Switzerland, 2-4 May 2005*, CD, p. 969.
- Enžl R., Fiala P., Houdková Š., Bláhová O.: *Conf. Proc. ITSC 2002*, DVS-Verlag, 2002.
- Houdková Š., Zahálka F., Kašparová M.: *Sborník konference Vrstvy a povlaky 2007, 29.-30. October 2007, Rož-*

Tabulka III

Hodnoty sledovaných mechanických charakteristik povlaku $(\text{Ti},\text{Mo})(\text{C},\text{N})\text{-NiCo}$ naměřených metodou CSM – maximální naměřené hodnoty karbidů (tvrdost H a modul pružnosti E)

$(\text{Ti},\text{Mo})(\text{C},\text{N})\text{-NiCo}$		H maximální		H konečná		E maximální		E konečný	
		H [GPa]	h [nm]	H [GPa]	h [nm]	E [GPa]	h [nm]	E [GPa]	h [nm]
As-sprayed	karbonitrid	23±2,7	45	11,3±1,9	885	396±51	17	232±23	855
	matrice			10,6±2,9	772			232±29	777
Žíhaný	karbonitrid	22,9±2,3	84	10,7±1,8	882	360±48	65	208±23	882
	nižší karbid	15,7±2,4	55	10,4±2,3	643	304±51	30	222±27	643
	matrice			10,5±1,8	779			217±26	779

- nov pod Radhoštěm, p. 49.
5. Houdková Š., Zahálka F., Kašparová M.: *Conf. Proc. ITSC 2008, Maastricht, the Netherlands, 2-4 June 2008*, CD, p. 1497.
 6. Berger L.-M.: *Int. Cong. On Adv. Mater., Proc. and Apl., October 2001, München*, CD, p. 10.
 7. Zimmermann S., Kreye H.: *Proc. of the 9th National Thermal Spray Conf., Cincinnati*, ASM International, Materials Park, Ohio, USA (1996), p. 147.

Š. Houdková^a, F. Zahálka^a, M. Kašparová^a, and O. Bláhová^b (^aŠKODA VÝZKUM s.r.o., Plzeň, Czech Republic, ^bNTC ZČU, Plzeň, Czech Republic): **Nanoindentation Measurement of HVOF Sprayed Coatings**

The influence of high temperature treatment on mechanical properties of Cr₃C₂-NiCr and (Ti,Mo)(C,N)-NiCo HVOF sprayed coatings were evaluated by nanoindentation measurement.

MICROHARDNESS OF PHASE CONSTITUENTS PRESENT IN CREEP-RESISTANT CAST STEEL

MALGORZATA GARBIAK
and **RENATA CHYLIŃSKA**

*Szczecin University of Technology, 70-310 Szczecin,
Al. Piastów 17, Poland
malgorzata.garbiak@ps.pl*

Keywords: microhardness, austenitic cast steel, precipitates

1. Introduction

The performance life of parts of machines and equipment operating at high temperatures depends to a great extent on the structural stability of material. The creep-resistant Ni-Cr cast steels used for operation at high temperatures are enriched with additions of niobium and titanium to improve their creep resistant behaviour. Compared with conventional cast steel, the phase composition of the stabilised cast steel is much more complex. The change of structure consists in partial or complete replacing of complex chromium carbides of the M_7C_3 or $M_{23}C_6$ type with the simple MC type carbides. At an operating temperature and in the presence of silicon, the content of which is higher in cast steel than in steel (for reasons of both technical and useful nature), the MC carbides are losing their stability and undergo phase transformations which result in the formation of a high-silicon $Ni_{16}(Nb,Ti)_6Si_7$ phase, commonly called G phase. Liberated during this transformation, carbon and chromium, whose concentration in the matrix impoverished in nickel is growing, too, get combined to form on the phase boundaries chromium carbides of the $M_{23}C_6$ type^{1,2}. As a result of this effect, after certain time of annealing, complex precipitates composed of several phases start appearing in the alloy structure. Each of these phases has its own hardness, which makes their differentiation by the use of a microhardness tester possible.

An attempt to differentiate the individual phase constituents was made, among others, in study³. Yet, because of a large scatter in the obtained results and small differences in the hardness values obtained for some phases (especially as regards M_7C_3 and $M_{23}C_6$ type carbides), the investigations did not give the expected positive results.

The aim of the investigations undertaken in this study was to use microhardness measurements for the determination of phase constituents included in the composition of complex multi-phase precipitates present in the structure of stabilised austenitic cast steel after the annealing process.

2. Experimental

The choice of material and the method of taking measurements were dictated by the following objectives:

- To produce in alloy structure the precipitates of possibly large dimensions,
- To apply the load of a value such that would produce indentations only within a strictly determined and purposely chosen phase region.

Material for investigations. Creep-resistant cast steel of the chemical composition given in Table I was melted in induction furnace and cast into sand moulds. Then, the specimens cut out from the test ingots were annealed in the atmosphere of air at a temperature of 900 °C for 300 hours. After this time, the structure contained precipitates of dimensions comprised in the range of 10–15 µm, Fig. 1. The „coarseness” of the precipitates was also due to the appropriately high silicon content in alloy⁴.

Table I
Chemical composition of the cast steel, wt.%

C	Ni	Cr	Si	Nb	Ti	Mn	Cu
0.30	29.30	17.80	4.26	1.59	1.07	1.02	0.21

Content of other elements: $P < 0.015$, $S < 0.007$

The cast steel microstructure was examined under an optical microscope and a scanning JEOL 6100 microscope, using polished cross-sections etched with an agent of the following composition: 3 g $FeCl_3$, 10 cm³ HCl, 90 cm³ C_2H_5OH . The chemical composition of the precipitates was determined on a Link ISIS series 300 apparatus. The phase composition was determined on an isolate sample extracted from the cast steel, using Philips PW1710 diffractometer and the method of diffraction analysis. The conditions of the electrolytic extraction were described in⁵.

Microhardness measurements. Microhardness of the precipitates and of the matrix was measured by the Vickers method, pressing statically under a load of 5 gf on the indenter of a Micromet 2100 microhardness tester made by Buehler. The value of the load was chosen basing on the results of the preliminary tests and studies. It was assumed that the load should be such as to enable the indentation to be made in a selected monophase region only. It has been observed that the load higher than 5 gf makes too large indentations, extending through more than one phase which, in turn, gives averaged hardness values not for one but for two phases. The measurements were taken on polished cross-sections of unetched specimens. Mean results from 10 measurements are compiled in Table II.

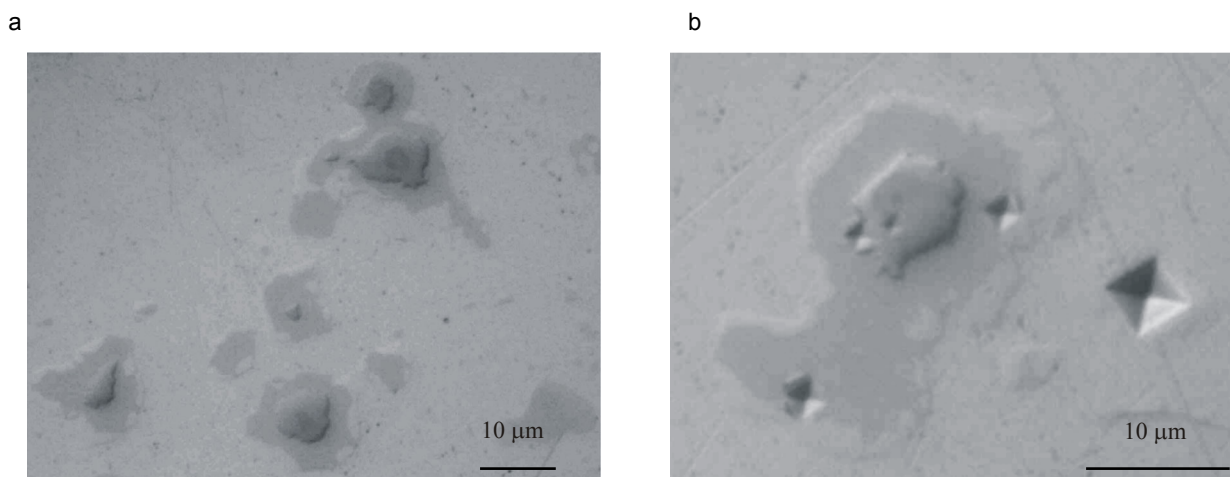


Fig. 1. a) Microstructure of the examined cast steel, b) indentations in precipitate areas and in the matrix

Table II

Results of the Student t test for measurement of microhardness on different phases, $\alpha = 0.05$

Phase	Average, HV	Standard deviation	Number of groups, N	Value test t	df	Probability, p
TiCN	2853	636				
(Nb,Ti)C	1427	275	10	8.612396	9	0.000012
G phase	1127	303	10	4.092959	9	0.002705
M ₂₃ C ₆	774	202	10	2.580205	9	0.029687
matrix	346	46	10	7.960378	9	0.000023

3. Discussion of results

An important consequence of transformations proceeding in the examined alloys due to the annealing process is the complex structure of the formed precipitates, which in their composition may include even four phase constituents.

The sequence in which these precipitates are arranged is the following: the centre is TiCN carbide surrounded by a complex niobium-titanium carbide (Nb,Ti)C, next there is an envelope of the chemical composition corresponding to G phase, while the external layer is composed of the precipitates of chromium carbides of the M₂₃C₆ type, the presence of which is accompanying the MC → G transformation, Fig. 3.

Microhardness was measured in selected areas to which the individual phase compositions were ascribed, basing on the results of the metallographic examinations. The obtained distribution of the hardness values is consistent with the arrangement of phase constituents in a single precipitate, Figs. 2, 3 and 4. The highest hardness, considerably different than the hardness of the remaining carbides, has the TiCN carbide, located in the middle of a complex precipitate. The lowest hardness has the matrix. Very interesting in the obtained results is also the fact that the value of the standard deviation (Table II) is the highest (the largest scatter in re-

sults) in the case of TiCN phase, and the lowest in the case of the matrix. This is due to both the size of an area occupied by these constituents on the metallographic specimen cross-section surface and to the hardness itself possessed by these phases.

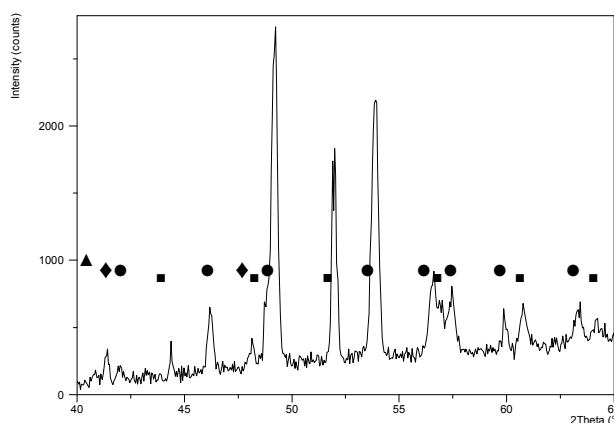
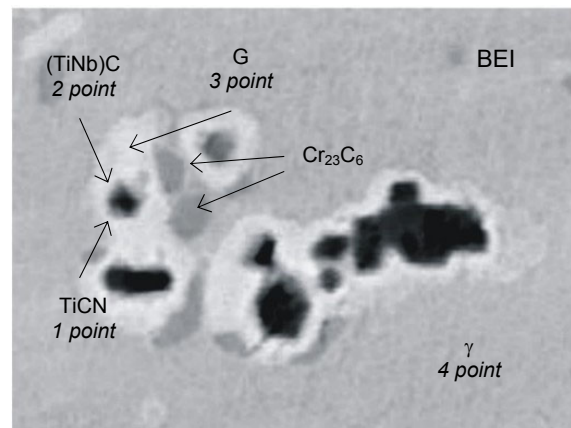
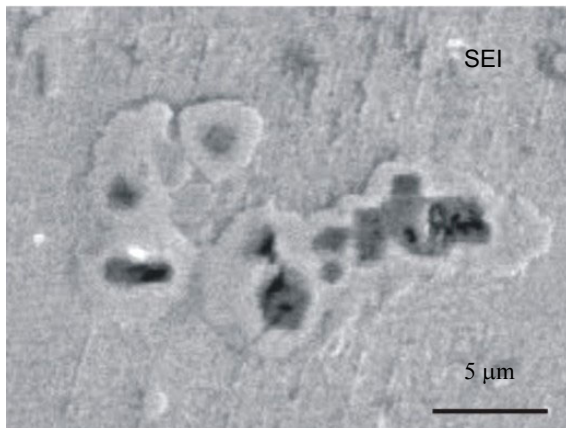
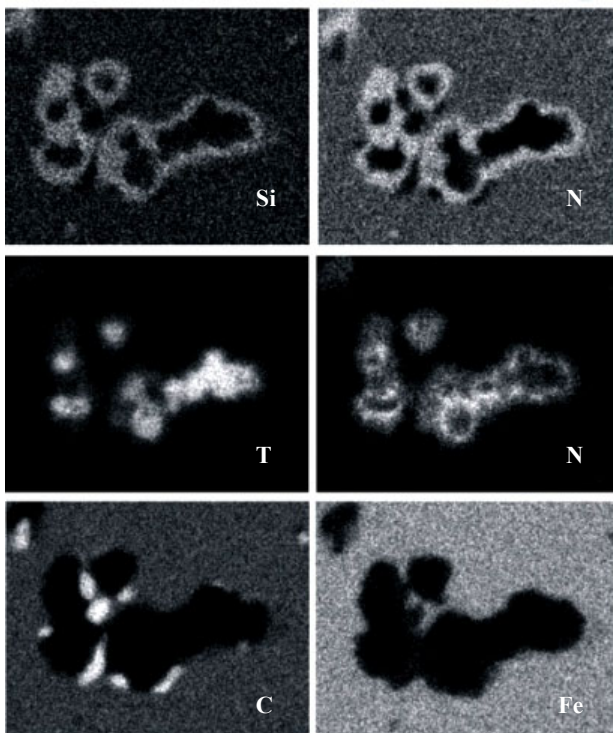


Fig. 2. Phase compositions of precipitates; ◆ (Nb,Ti)C, ● G phase, ■ Cr₂₃C₆, ▲ TiCN

a



b



c

wt.%	Si	Cr	Nb	Ni	Ti	Fe	Mn
1	0.31	1.13	34.55	0.80	62.13	1.20	0.12
2	0.41	1.45	56.58	1.81	38.08	1.57	0.10
3	11.97	2.45	16.47	53.35	8.72	6.88	0.16
4	3.70	18.88	0.18	28.43	0.53	47.51	0.78

Fig. 3. a) Microstructure, b) distribution of elements, c) punctual chemical analysis of precipitates

Of some importance is also the application of small load during the measurements. With increasing load, the error of the measurements of the indentation diameter decreases. Probably, larger number of the measurements would render the same effect, giving smaller standard deviation.

In spite of a large scatter in the results, especially as regards the TiCN phase, and relatively small differences in hardness between the G phase and (NbTi)C carbides, the value of the probability p (the occurrence of test statistics t) is lower than the accepted level of significance $\alpha = 0.05$, which indicates that in all the cases of comparable mean hardness values, the difference between them is still significant enough to enable them to be regarded as the values of the hardness of the individual phase constituents, Fig. 5.

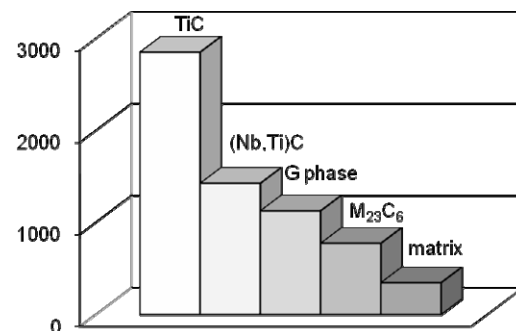


Fig. 4. Distribution of microhardness in phase constituents of the examined cast steel

4. Conclusions

The performed investigations have proved that it is possible to differentiate between the individual phase constituents present in microstructure of the annealed cast steel. The application of statistical analysis enables determining, even when the scatter in results is relatively large, the mean hardness of

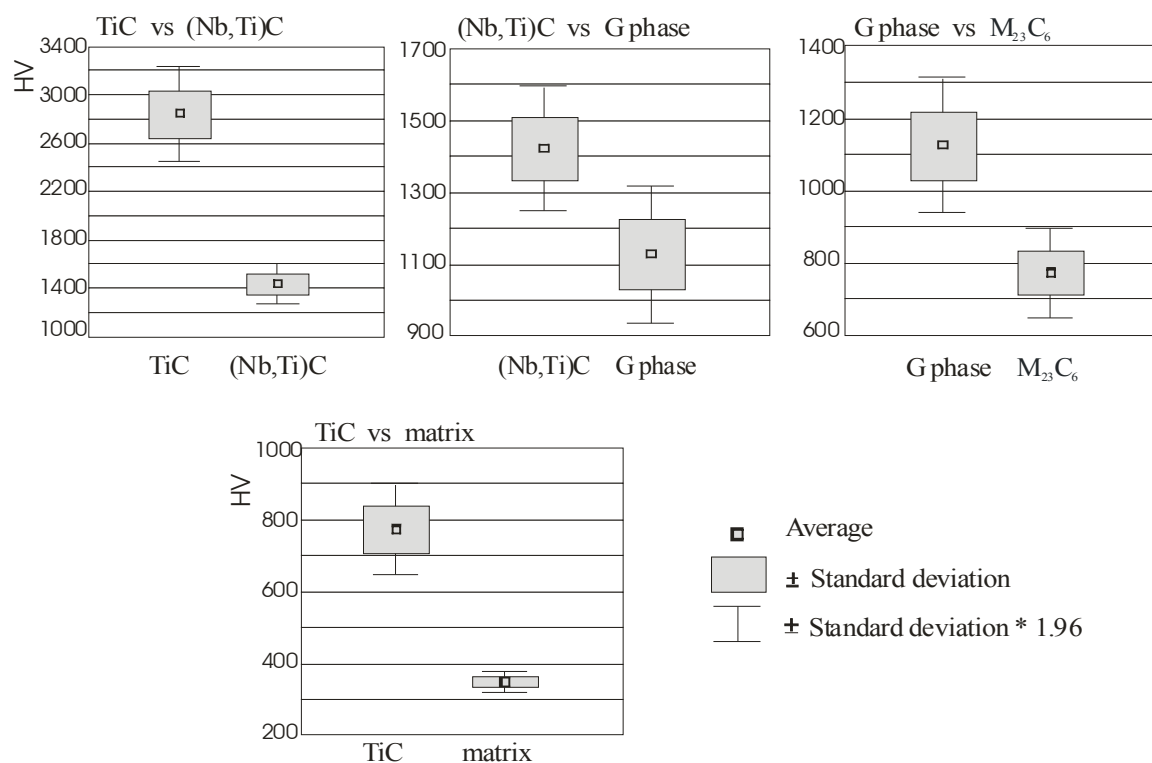


Fig. 5. Comparison of average microhardness between phase constituents of the examined cast steel

each of the phases, providing that these are not the similar values.

So, it is possible to describe the microstructure quantitatively by random measurements of microhardness taken on the metallographic specimen cross-section and their presentation in the form of a distribution of the microhardness values, where the individual phase constituents can be isolated and their quantitative content can be determined – all from the obtained hardness values.

The condition is, however, properly chosen value of the load, which enables eliminating the measurements giving averaged hardness values for two or more phases.

REFERENCES

1. Powell D. J., Pilkington R., Miller D. A.: *Acta Metall.* 713, 36 (1988).
2. Almeida L. H., Ribeiro A. F., Le May I.: *Mat.Char.* 219, 49 (2003).
3. Aydin I., Bühler H.-E., Rahmel A.: *Arch. Eisenhüttenwes.* 421, 310 (1983).
4. Garbiak M., Piekarski B.: *Inż. Mater.* 704, 3 (2006).
5. Chylińska R., Garbiak M., Piekarski B.: *Mat. Sc.* 348, 4 (2005).

M. Garbiak and R. Chylińska (*Szczecin University of Technology, Szczecin, Poland*) **Microhardness of Phase Constituents Present in Creep-Resistant Cast Steel**

The study presents the results of microhardness measurements of the phase constituents present in creep-resistant cast steel. The measurements were taken by the Vickers method, and their main aim was to make a distinction between individual phases included in the composition of complex precipitates formed as a result of ageing the 0.3C-30Ni-18Cr creep-resistant cast steel. The statistical analysis of the results of microhardness measurements has indicated that the averaged values of HV obtained for individual phases are characterised by very significant differences at the adopted level of confidence $\alpha = 0.05$. Hence they can be treated as separate values and as such can be ascribed to the individual phase constituent.

THERMAL SHOCK RESISTANCE OF SiC+Si₃N₄ COMPOSITES EVALUATED BY INDENTATION TECHNIQUE

ALEXANDRA KOVALČÍKOVÁ
and JÁN DUSZA

*Institute of Materials Research, Slovak Academy of Sciences,
Watsonova 47, 040 01 Košice, Slovak Republic
avysocka@imr.saske.sk, jdusza@imr.saske.sk*

Keywords: SiC, SiC+Si₃N₄ composites, mechanical properties, thermal shock resistance

1. Introduction

Silicon carbide and silicon nitride have been recognised as important structural ceramics because of their good combination of mechanical and thermal properties¹. Components to be properly applied in high temperature need to have a high resistance to thermal shock, thermal fatigue, corrosion, and resistance to creep deformation. Si-based ceramics such as silicon carbide and silicon nitride due to their covalent bonding exhibit a high strength at elevated temperature (up to 1000 °C), as well as low thermal expansion coefficient and high thermal conductivity, and therefore a high resistance to thermal shock^{2–4}. A new approach that has received much less attention is the incorporation of Si₃N₄ in SiC with oxide additives. SiC has higher hardness and oxidation resistance, whereas Si₃N₄ has better strength and thermal shock behaviour. Kim et al.⁵ investigated microstructure and mechanical properties of SiC composites that contained up to 50 wt.% of Si₃N₄ particles. The fracture toughness increased as the Si₃N₄ content increased and the effect of Si₃N₄ addition on toughening became apparent as Si₃N₄ contents of ≥ 30 wt.%. The strength increased with Si₃N₄ content and showed a maximum of 1020 MPa at 35 wt.% of silicon nitride. Shaoming⁶ reported maximum strength and toughness values of 810 MPa and 5, 5 MPa m^{1/2} in specimens with different additive compositions of La₂O₃ and Y₂O₃. However, the thermal shock resistance of SiC+Si₃N₄ composites has not yet been reported. Takeda and Maeda⁷ showed that the thermal shock resistance of hot pressed SiC sintered with BeO and AlN depends on the thermal conductivity. At $\lambda \square 100 \text{ W m}^{-1} \text{ K}^{-1}$ was $\Delta T_c = 680 \text{ }^\circ\text{C}$ and at $\lambda = 65 \text{ W m}^{-1} \text{ K}^{-1}$ was $\Delta T_c = 450 \text{ }^\circ\text{C}$. Wang and Singh⁸ measured $\Delta T_c = 500 \text{ }^\circ\text{C}$ at thermal conductivity of $87 \text{ W m}^{-1} \text{ K}^{-1}$ of HP SiC. Pettersson et al.⁹ studied the best parameters for measuring the thermal shock resistance of Si₃N₄ based materials with an indentation-quench method. Many other authors have studied thermal shock resistance of different ceramic materials by water quenching or indentation tests^{10–14}.

Most ceramic materials are sensitive to thermal shock and thermal fatigue. Due to inhomogenous temperature distributions in rapidly cooled or heated ceramic components, high thermal stresses are generated, which are responsible for the extension of existing cracks. The calculation of thermal

stresses is an important step necessary for design with ceramic materials. Thermal stresses depend on physical properties (thermal expansion coefficient α , elastic constants E and ν , thermal conductivity λ , specific heat C_p , density ρ), geometric boundary conditions, and thermal boundary conditions. Failure occurs when the maximum thermal stress reaches a critical value σ_c (strength) or, in terms of fracture mechanics, when the stress intensity factor K_I reaches the fracture toughness K_{IC} . The thermal shock sensitivity of a material consequently depends on the physical properties and on σ_c and K_{IC} . Depending on the special boundary conditions, different shock parameters were defined¹⁵. In addition to these material properties, which can be tabulated, the microstructure character is also of importance and influences the thermal shock behaviour of the material⁹. The investigation of the behaviour of Vickers indentation cracks under quenching condition has raised interest during the last years. An indentation-quench method has been developed by Andersson and Rowcliffe¹⁶. Compared to the Hasselman quench-strength method¹⁷, the evaluation procedure is simple, the sample preparation is easy and only a small number of samples are needed for a series of measurements at different temperatures. The indentation-quench method can be used for the characterization of materials and as a diagnostic tool to predict the thermal shock damage occurrence in a component¹⁸. To evaluate the thermal stress crack initiation and propagation behaviour of ceramics, two thermal shock resistance parameters are usually used¹⁹. First is the resistance to initiation of crack, expressed by parameter R

$$R = \frac{\sigma_f (1-\nu)}{\alpha E} = \Delta T_c$$

where σ_f is the fracture strength, E is the Young's modulus, α is the coefficient of thermal expansion and ν is the Poisson's ratio.

Higher R represents a greater resistance to the initiation of fracture during rapid quenching and during steady-state heat flow down a steep temperature gradient. The second is the resistance to propagation of crack expressed by the parameter R''''

$$R'''' = \left(\frac{K_{IC}}{\sigma_f} \right)^2 (1+\nu)$$

which dedicates the resistance to catastrophic crack propagation of ceramics under a critical temperature difference, ΔT_c .

From the above two equations, it is clearly visible that the thermal shock resistance can be improved by the increased flexural strength and fracture toughness and by decreased Young's modulus and coefficient of thermal expansion.

The main aim of this work is to study thermal shock behaviour of SiC+Si₃N₄ composites using indentation method and to compare to the behaviour of the reference silicon carbide, prepared by the same fabrication route.

2. Experimental procedures

Material preparation

SiC materials were prepared by mixing β -SiC powder (HSC-059, Superior Graphite) with sintering additives Al_2O_3 (A 16 SG, Alcoa) and Y_2O_3 (grade C, H.C. Starck). In the case of composites β -SiC powder was mixed with Si_3N_4 powder (AIY-3/54, Grade C, Plasma & Ceramic Technologies Ltd.), which contained Y_2O_3 and Al_2O_3 sintering additives in weight ratio 6:3. The final chemical compositions of the investigated materials are listed in Table I. The powder mixtures were ball milled in isopropanol with SiC balls for 24 hours. The suspensions were dried and subsequently sieved through 25 μm sieve screen in order to avoid hard agglomerates. The samples were sintered by hot pressing at 1850 °C/1h under mechanical pressure of 30 MPa in N_2 atmosphere. The hot pressed samples were subsequently heat treated at 1850 °C/5 h.

Microstructure and mechanical properties

For microstructural observation the specimens were cut, polished to a 1 μm finish and plasma etched. The microstructures were studied using an SEM (JEOL JSM-7000F). The densities of the sintered and annealed specimens were measured according to Archimedes' principle. Hardness was determined by Vickers indentation (hardness testers LECO 700AT) under a load of 49.05 N with a dwell time of 10 s. In order to determine the indentation toughness at least 15 Vickers indentations per specimen were introduced with the load of 49.05 N. The indentation toughness was calculated from the lengths of radial cracks and indents diagonals using a formula valid for semi-circular crack systems as proposed by Anstis et al.²⁰. The strength was measured using specimens with dimensions 3×4×45 mm, tested in the four point bending mode. They were ground by 15 μm diamond grinding wheel before testing. The two edges on the tensile surface were rounded with a radius about 0.15 mm in order to eliminate a failure initiated from an edge of the specimen. At least ten specimens were tested for each material.

Indentation thermal shock resistance

For the investigation of thermal shock resistance the indentation-quench method was used. The indentations were made, using the load 49.05 N to obtain pre-cracks approxi-

mately in the same length. Four indents were made in each specimen with dimensions 3×4×20 mm. The lengths of the cracks were measured with the same equipment as in the hardness and fracture toughness test. After the indentation the samples were heated in a vertical tube furnace in air to the required temperature and held there for 25 min. Then the specimens were rapidly immersed into a ~20 °C water bath. Final radial crack lengths were again measured. The procedure was repeated at increasing quenching temperatures ΔT , up to the critical value of ΔT_c at which radial crack became unstable and the specimen failed.

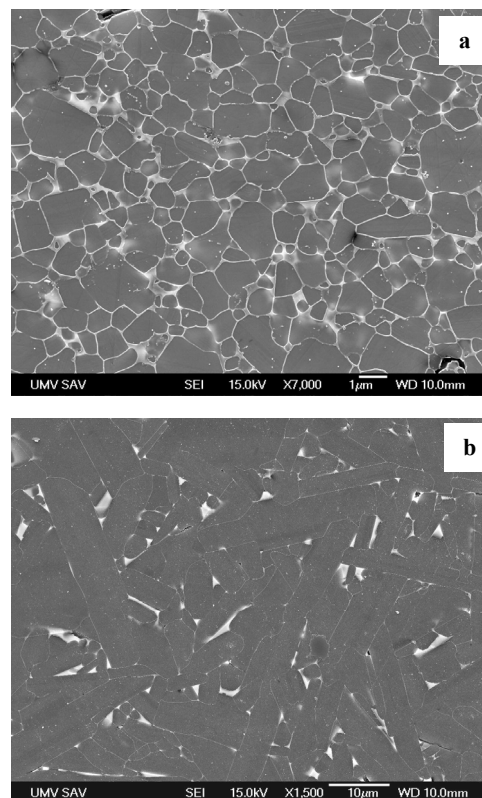


Fig. 1. SEM micrographs of (a) hot pressed SC-N5-HP and (b) annealed SC-N5-1850 composites

Table I
Chemical composition of prepared materials

Samples	Heat treatment	Composition [wt. %]			
		SiC	Si_3N_4	Y_2O_3	Al_2O_3
SC-N0-HP	HP (1850°C/1h)	91.0	0	6.0	3.0
SC-N5-HP	HP (1850°C/1h)	86.5	5	5.7	2.8
SC-N10-HP	HP (1850°C/1h)	81.9	10	5.4	2.7
SC-N0-AN	HP (1850°C/1h) +AN (1850°C/5h)	91.0	0	6.0	3.0
SC-N5-AN	HP (1850°C/1h) +AN (1850°C/5h)	86.5	5	5.7	2.8
SC-N10-AN	HP (1850°C/1h) +AN (1850°C/5h)	81.9	10	5.4	2.7

3. Results and Discussion

Microstructure and mechanical properties

Representative SEM micrographs of a polished and plasma etched surface of the hot pressed and annealed SiC+Si₃N₄ composites are shown in Fig. 1. The microstructures of hot pressed SC-N5-HP (Fig. 1a) consist of fine sub-micron-sized equiaxed SiC grains with a low aspect ratio (~1). The microstructures of the SiC material and SiC+Si₃N₄ composites significantly changed after their post-sintering high temperature treatment at 1850 °C, Fig. 1b. They have a bimodal distribution and consist of elongated SiC grains with higher aspect ratio (4.4) and of smaller SiC grains. In the case of SiC+Si₃N₄ composites the addition of silicon nitride resulted in a finer microstructure of investigated materials.

The basic properties of the materials are summarized in the Table II. All materials are almost full dense (more than 97 % theoretical density). By increasing of Si₃N₄ content the density increased. In our case the addition of Si₃N₄ does not play a role in hardness and fracture toughness values. The effect of Si₃N₄ addition on fracture toughness became apparent at Si₃N₄ content of ≥ 30 wt.% (ref.⁵). The mechanical properties are strongly affected to their microstructural character. For fine-grained globular microstructure of hot pressed SiC and SiC+Si₃N₄ composites the fracture toughness had a value of K_{IC} between 2.8–2.9 MPa m^{1/2}. For annealed materials with plate-like microstructure higher fracture toughness was obtained (4.3–5.4 MPa m^{1/2}). Sciti²¹ showed the increase of K_{IC} from 3 up to 5.5 MPa m^{1/2} after annealing treatment at 1900 °C. In materials with fine microstructure and globular grains, the crack propagates mainly intergranularly with relatively small deflection from the main crack direction. Toughening mechanisms are absent in such microstructures. The crack propagation in the materials with coarse plate-like grains and microstructure is significantly different. The crack deflection is enhanced (often up to approximately 10 μm from the main crack direction). The toughening mechanisms in the form of crack branching and crack deflection have been observed²². Such toughening mechanisms are probably responsible for the increase of fracture toughness. The flexural strength decreases with annealing and aspect ratio of SiC grains but slightly increases with Si₃N₄ addition. Kim⁵ estimated a maximum strength value of 1020 MPa at a Si₃N₄ content of 35 wt.%.

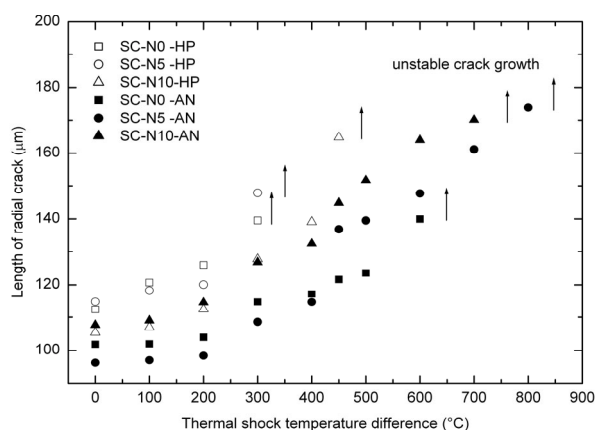


Fig. 2. Crack growth behaviour in the prepared materials after single quenches into water

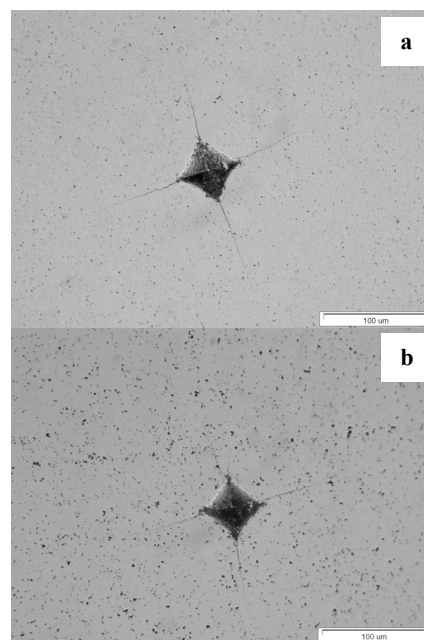


Fig. 3. Optical micrograph of 50 N contact impressions of (a) hot pressed SC-N10-HP and (b) annealed SC-N10-1850 composites

Table II
Selected properties of SiC and SiC+Si₃N₄ composites

Samples	Density [g cm ⁻³]	Hardness HV5 [GPa]	Fracture toughness K _{IC} [MPa m ^{1/2}]	Fracture Strength σ [MPa]	R _{THEORETIC} [°C]	R _{EXPERIMENTAL} [°C]
SC-N0-HP	3.220	20.4 ± 0.9	2.90 ± 0.2	359.2	228	320
SC-N5-HP	3.236	19.7 ± 0.6	2.88 ± 0.2	464.7	333	350
SC-N10-HP	3.249	20.6 ± 0.7	2.89 ± 0.1	541.9	359	500
SC-N0-AN	3.189	20.6 ± 0.3	4.54 ± 0.4	122.6	90	650
SC-N5-AN	3.196	22.5 ± 0.8	5.39 ± 0.3	352.3	206	850
SC-N10-AN	3.204	20.7 ± 1.1	4.38 ± 0.4	193.9	136	760

Further addition of Si_3N_4 up to 50 wt.%, decreased the strength to 855 MPa. To the 10 wt.% of silicon nitride were values of strength less than 700 MPa. In our case the values of flexural strength are significantly lower.

Indentation thermal shock resistance

For all tested specimens the rise in thermal shock resistance with a higher amount of silicon nitride was observed (Fig. 2). This means that the composite $\text{SiC}+\text{Si}_3\text{N}_4$ have better thermal shock resistance than the monolithic silicon carbide. The initiation crack length of annealed materials was 20 μm shorter than to the hot pressed specimens (Fig. 3). Thermal shock tests, studied by indentation-quench method show enhanced resistance of the $\text{SiC}+\text{Si}_3\text{N}_4$ composite and the monolithic SiC material with coarse microstructure, with higher fracture toughness. The explanation of this fact could be described by the R_{th} parameter.²³ This parameter reflects the fact that, to resist a given thermal shock, a material has to exhibit a high resistance to cracking, i.e. a high toughness, and has to have a low thermal stress. Therefore, it is important to design materials with specific microstructures to obtain an optimal state between resistance to initiation (R) and resistance to propagation of crack (R''''). Kalantar and Fantozzi² showed that materials with elongated grains (with higher aspect ratio) had higher ΔT_c . The materials with elongated grains show several mechanisms of toughening, and so they may have stable crack propagation. If the experimental measured ΔT_c values are compared with the calculated R parameter (Table II), in most cases the level of theoretic values is less than measured values and a linear relation exists between them². In our case, the ΔT_c values are lower for all tested specimens, but the largest difference is between theoretical R parameter and experimental estimated ΔT_c of annealed monolithic SiC and $\text{SiC}+\text{Si}_3\text{N}_4$ composites. These materials have lower flexural strength values compared with fine-grained materials because the biggest and more strength degrading flaws were found mainly in form of pores and agglomerates on SiC grains.

4. Conclusions

The Si_3N_4 addition has no influence on the hardness and fracture toughness but the heat treatment at 1850 °C results in the coarsening of the microstructure which leads to the increase of the indentation toughness. This increase is connected with the present toughening mechanisms in the form of crack deflection and crack branching. The flexural strength decreased for annealed materials with increased aspect ratio of their SiC grains, but slightly increased with Si_3N_4 addition.

It was found that both the silicon nitride addition and the heat treatment have a positive effect on the improvement of the thermal shock resistance of the investigated composites. However, more experiments are necessary to understand and explain the effect of the silicon nitride addition on the improvement of the thermal shock resistance.

This work was partly supported by the National Slovak Grant Agency VEGA, project No. 2/7194/27, APVV-0171-06, LPP-0203-07, and NANOSMART, Centre of Excellence, SAS.

REFERENCES

1. Falk L. K. L.: *J. Eur. Ceram. Soc.* 17, 983 (1997).
2. Kalantar M., Fantozzi G.: *Mat. Sci. Eng., A* 472, 237 (2008).
3. Hoffmann M. J., Schneider G. A., Petzow G., in: *The Potential of Si_3N_4 for Shock Applications* (Schneider, Petzow, ed.), 49. Kluwer Academic, Boston 1993.
4. Becher F.: *J. Am. Ceram. Soc.* 74, 255 (1991).
5. Kim Y.-W., Lee Y.-I., Mitomo M., Choi H.-J., Lee J.-G.: *J. Am. Ceram. Soc.* 82, 1058 (1999).
6. Shaoming D., Dongliang J., Shouhong T., Jingkun G.: *Ceram. Int.* 21, 451 (1995).
7. Takeda Y., Maeda K.: *J. Ceram. Soc., Jpn, Intl.* 99, 1113 (1991).
8. Wang H., Singh R. N.: *Intl. Mater. Rev.* 39, 228 (1994).
9. Petterson P., Johnsson P., Shen Z.: *J. Europ. Ceram. Soc.* 22, 1883 (2002).
10. Maensiri S., Roberts S. G.: *J. Am. Ceram. Soc.* 85, 1971 (2002).
11. Hvizdoš P., Jonsson D., Anglada M., Anné G., Van Der Biest O.: *J. Europ. Ceram. Soc.* 27, 1365 (2007).
12. Rui-Xia S., Yan-Sheng Y., Jia L., Dong-Zhi W.: *Mat. Res. Bull.*, 2008, doi: 10.1016/j.mater.resbull.2007.11.001.
13. Yang Z.-H., Jia D.-Ch., Zhou Y., Meng Q.-Ch., Shi P.-Y., Song Ch.-B.: *Mater. Chem. Phys.* 107, 476 (2008).
14. Ding S., Zeng Y.-P., Jiang, D.: *Mat. Sci. Eng., A* 425, 326 (2006).
15. Munz D., Fett T.: In *Springer series in Materials Science*, Hull R., Osgood R. M., Sakaki H., Zunger A. (ed.), *Ceramics*, 229, Springer-Verlag, Berlin 1999.
16. Andersson T., Rowcliffe D. J.: *J. Am. Ceram. Soc.* 79, 1509 (1996).
17. Hasselman D. P. H.: *J. Am. Ceram. Soc.* 52, 600 (1969).
18. Collin M., Rowcliffe D.: *Acta Mater.* 48, 1655 (2000).
19. Hasselman D. P. H.: *Am. Ceram. Soc. Bull.* 49, 1033 (1970).
20. Anstis G. R., Chantikul P., Lawn B. R., Marshall D. B.: *J. Am. Ceram. Soc.* 64, 533 (1981).
21. Sciti D., Guicciardi S., Bellosi A.: *J. Europ. Ceram. Soc.* 21, 621 (2001).
22. Vysocká A., Špaková J., Dusza J., Balog M., Šajgalík P.: *Kovové Materiály* 45, 223 (2007).
23. Tancret F.: *J. Europ. Ceram. Soc.* 26, 1517 (2006).

A. Kovalčíková and J. Dusza (*Institute of Materials Research, Slovak Academy of Sciences, Košice, Slovak Republic*): **Thermal Shock Resistance of $\text{SiC}+\text{Si}_3\text{N}_4$ Composites Evaluated by Indentation Technique**

The thermal shock resistance of $\text{SiC}+\text{Si}_3\text{N}_4$ composites was investigated by indentation technique. The results were compared with thermal shock behaviour of SiC prepared by the same technological route. It was found that the silicon nitride addition has a positive effect in the improvement of the thermal shock resistance of the investigated composites.

HOLOGRAFICKÁ METÓDA URČENIA YOUNGOVHO MODULU PRUŽNOSTI

JOZEF KRAJČOVIČ
a **IGOR JANČUŠKA**

Materiálovotechnologická fakulta STU, Ústav materiálov,
J. Bottu 25, 91724 Trnava, Slovensko
jozef_krajcovic@stuba.sk, igor.jancuska@stuba.sk

Kľúčové slová: optické metódy, deformácia, holografická interferometria, regresná analýza, Youngov modul pružnosti

1. Deformácia ohybom

Mechanické vlastnosti materiálu sa často zisťujú deštruktívnou (trhacou) skúškou v jednoosovom ťahu. Trhací stroj plynulo zvyšuje zaťaženie normalizovanej tyče a zaznamenáva závislosť ťahového napätia σ od pomerného predĺženia ε . Pri skúške možno postupne nájsť napätie σ_U (medzu úmernosti), po ktorých je závislosť lineárna, napätie σ_E (medzu pružnosti), po ktorých je deformácia pružná (elastická), napätie σ_K (medzu klzu), pri ktorom začína plastická deformácia a maximálne napätie σ_P (medzu pevnosti) pri takej skúške. Nás zaujíma prvá oblasť, v ktorej je závislosť ťahového napätia σ od pomerného predĺženia ε lineárna:

$$\sigma = E \cdot \varepsilon \quad (1)$$

Vzťah (1) sa nazýva Hookov zákon a konštanta E je Youngov modul pružnosti v ťahu. V princípe môžeme Youngov modul pružnosti v ťahu určiť aj z iných známych druhov namáhania telesa. Spomedzi základných druhov namáhania telies (ťah, šmyk, krut, ohyb a vzper) sme sa zamerali na ohyb votknutého nosníka pod vplyvom osamelej priechnej vonkajšej sily F pôsobiacej vodorovne vo vzdialenosti l od upevneného konca nosníka, pozri obr. 1.

Pri veľmi malých priehyboch nosníka ($y'^2 \ll 1$) má diferenciálna rovnica priehybovej čiary tvar

$$y'' = \frac{M}{EJ} = \frac{F(l-x)}{EJ} \quad (2)$$

kde $M = F(l-x)$ je ohybový moment vonkajšej sily F vzhľadom na bod osi nosníka vo vzdialenosti x od spodného upevneného konca a J je plošný moment zotrvačnosti kolmého prierezu nosníka. Po dvojnásobnom integrovaní rovnice (2) s využitím okrajových podmienok $y'(0) = y(0) = 0$ získame

$$y(x) = -\frac{F}{6EJ}x^3 + \frac{Fl}{2EJ}x^2 = ax^3 + bx^2 \quad (3)$$

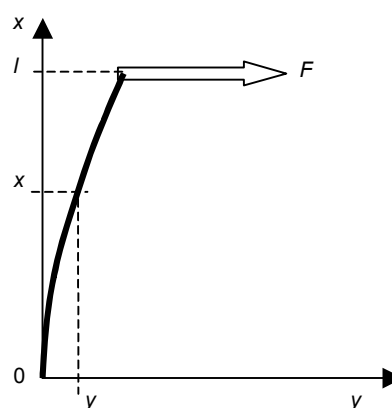
kde $a = -F/(6EJ)$, $b = Fl/(2EJ)$. Ak poznáme hodnoty koeficientov a , b , môžeme podľa vzťahu (3) určiť ohyb y ľubovoľného bodu deformovanej osi votknutého nosníka. Pre ohyb y^*

nosníka v mieste pôsobiska sily ($x=l$) zo vzťahu (3) dostaneme¹

$$y(l) = y^* = \frac{Fl^3}{3EJ} \quad (4)$$

a po úprave

$$E = \frac{Fl^3}{3Jy^*} \quad (5)$$



Obr. 1. Ohyb y nosníka vo vzdialenosti x od upevneného konca nosníka

Hodnoty F a l môžeme merať priamo, hodnotu J môžeme vypočítať z odmeraných rozmerov priechného prierezu nosníka. Na určenie hodnoty y^* možno použiť rôzne metódy. My na to používame citlivú optickú metódu dvojexpozíčnej holografickej interferometrie.

2. Dvojexpozíčná holografická interferometria

Holografickú interferometriu, na rozdiel od klasickej interferometrie, charakterizuje skutočnosť, že aspoň jedna z interferujúcich vln je zrekonštruovaná z hologramu. Interferujú tu dve objektové vlny, prislúchajúce dvom rôznym stavom objektu, napríklad pred deformáciou a po deformácii. Ak na záznamový materiál zaznamenáme dva stavy objektu, hovoríme o dvojexpozíčnej holografickej interferometrii. Pri rekonštrukcii vznikajú súčasne dve objektové vlny, ktoré interferujú a vytvárajú interferogram. Získanie experimentálnych dát v interferometrii spočíva v detekcii štruktúry intenzity svetla v interferograme. Interferenčné extrémny sa nachádzajú v miestach, kde je fázový rozdiel $\Delta\delta$ medzi interferujúcimi vlnami určený známymi podmienkami, napr.

$$\Delta\delta = k \cdot \Delta s = (2m+1)\pi, \quad m = 0, 1, 2, 3, \dots \quad (6)$$

pre interferenčné minimá, pričom $k = 2\pi/\lambda$ je vlnové číslo, určujúce absolútnu hodnotu vlnového vektora k a Δs je roz-

diel optických dráh interferujúcich vlnení. V prípade interferometrie nepriehľadných objektov je veľkosť fázového rozdielu medzi interferujúcimi vlnami $\Delta\delta$ určená vektorom deformácie $\Delta\mathbf{r}$ veľkosťou y v každom mieste sledovaného povrchu, smerom osvetlenia \mathbf{k}_i skúmaného povrchu a smerom pozorovania \mathbf{k}_s interferogramu²

$$\Delta\delta = \Delta\mathbf{r} \cdot (\mathbf{k}_s - \mathbf{k}_i) \quad (7)$$

Symbolom \mathbf{k} sú označené vlnové vektory príslušných svetelných vln. Ich absolútne hodnoty sú rovnaké, nakoľko sú rovnaké vlnové dĺžky svetla. Oba vektory sa líšia len smermi. V našom prípade bol dvojexpozíčný záznam na holografickú dosku vykonaný tak, že vektory \mathbf{k}_s a \mathbf{k}_i boli prakticky nesúhlasne orientované a vektor deformácie $\Delta\mathbf{r}$ bol nesúhlasne orientovaný s vektorom \mathbf{k}_i osvetlenia skúmaného povrchu nosníka so spodným upevneným koncom, preto

$$\Delta\delta = \Delta\mathbf{r} \cdot (\mathbf{k}_s - \mathbf{k}_i) = y2k = \frac{y4\pi}{\lambda} \quad (8)$$

a po dosadení (8) do (6) a úprave pre ohyb y v miestach interferenčných miním platí

$$y = (2m + 1)\frac{\lambda}{4}, \quad m = 0, 1, 2, \dots \quad (9)$$

kde rády $m = 0, 1, 2, \dots$ priradíme minimám na interferograme v smere od upevneného konca k pôsobisku sily. Ak by sa pôsobisko sily nachádzalo presne v minime rádu n , potom

$$y^* = (2n + 1)\frac{\lambda}{4} \quad (10)$$

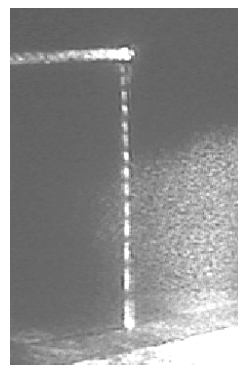
a po dosadení (10) do (5) získame

$$E = \frac{4Fl^3}{3J(2n + 1)\lambda} \quad (11)$$

Ak by sa pôsobisko sily nachádzalo nad interferenčným minimom rádu n , je možné odhadnúť hodnotu rádu v pôsobisku sily reálnym číslom z otvoreného intervalu od n do $n+1$ a toto reálne číslo dosadzovať do vzťahu (11) miesto n . Odhad môže byť založený na meraní priebehu intenzity v interferograme. Rozloženie intenzity je určené funkciou $\cos(\Delta\delta)$. Veľkosť deformačnej sily F spôsobujúcej ohyb predmetu je potrebné voliť tak, aby sa dal jednoznačne určiť počet tmavých interferenčných prúžkov vznikajúcich pri rekonštrukcii interferogramu (obr. 2).

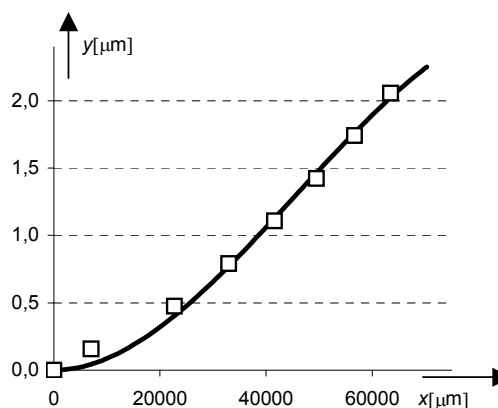
Druhý spôsob, ako môžeme určiť ohyb y^* v pôsobisku sily spočíva vo využití lineárnej regresie. Pomocou softvéru pre obrazové spracovanie môžeme merať vzdialenosť x_m medzi upevneným koncom a minimom rádu m s ohybom y_m vypočítaným podľa vzťahu (9). Takto získame N dvojíc súradníc (x_m, y_m) pre určenie regresných koeficientov a a b v regresnej funkcii (3). Akonáhle sú regresné koeficienty určené, ohyb y^* v mieste pôsobiska sily vypočítame podľa vzťahu

$$y^* = al^3 + bl^2 \quad (12)$$



Obr. 2. Digitálna fotografia interferogramu

a dosadíme do vzťahu (5) pre výpočet Youngovho modulu pružnosti. Regresná krivka poskytuje informáciu o ohybe v ľubovoľnom bode nosníka (obr. 3).



Obr. 3. Regresná krivka regresnej funkcii (3)

3. Analýza experimentálnych výsledkov

Uvedenými spôsobmi sme určovali Youngov modul pružnosti E eutektického kompozitu pripraveného riadenou kryštalizáciou³. Vzorka mala obdĺžnikový prierez. Hrúbku h a šírku δ prierezu sme merali mikrometrom 8-krát v rôznych miestach pozdĺž celej dĺžky vzorky. Prístrojovú chybu mikrometra ($1 \mu\text{m}$) sme zanedbali kvôli pomerne veľkému rozptylu nameraných hodnôt. Stredné hodnoty boli $h = 2937,5 \mu\text{m}$ a $\delta = 2906,6 \mu\text{m}$, so strednými kvadratickými chybami $\Delta h = 20,7 \mu\text{m}$ a $\Delta \delta = 14,0 \mu\text{m}$. Vlnová dĺžka monochromatického laserového žiarenia bola $\lambda = 632,8 \text{ nm}$. Výrobca lasera udáva chybu v určení vlnovej dĺžky $\Delta\lambda = 1 \text{ nm}$. Silu pôsobiacu na nosník sme nastavovali v rozpätí od 30 mN do 80 mN a merali silomerom s chybou $\Delta F = 5 \text{ mN}$. Vzdialenosť l pôsobiska sily od upevneného konca sme merali posuvným meradlom s chybou $\Delta l = 0,1 \text{ mm}$. Kvôli obmedzenej dĺžke vzorky sme vzdialenosť l nastavovali na hodnoty 6 cm a 7 cm. Vzorku sme merali v dvoch pozíciách. V prvej pozícii sila pôsobila

pozdĺžne s hrúbkou, preto bol plošný moment zotrvačnosti prierezu rovný $J = \delta h^3/12$. V druhej pozícii sila pôsobila pozdĺžne so šírkou, preto bol plošný moment zotrvačnosti rovný $J = h\delta^3/12$. Po dosadení momentov do vzťahu (5) získame v adekvátnom poradí pre prvú a druhú pozíciu vzťahu

$$E = \frac{4Fl^3}{\delta h^3 y^*}, \quad E = \frac{4Fl^3}{h\delta^3 y^*} \quad (13, 14)$$

Pri využití lineárnej regresie relatívne chyby $\Delta E/E$ v adekvátnom poradí pre obe pozície odvodíme z vety o prenose chýb

$$\frac{\Delta E}{E} = \sqrt{\left(\frac{\Delta F}{F}\right)^2 + \left(\frac{3\Delta l}{l}\right)^2 + \left(\frac{\Delta \delta}{\delta}\right)^2 + \left(\frac{3\Delta h}{h}\right)^2 + \left(\frac{\Delta y^*}{y^*}\right)^2}$$

$$\frac{\Delta E}{E} = \sqrt{\left(\frac{\Delta F}{F}\right)^2 + \left(\frac{3\Delta l}{l}\right)^2 + \left(\frac{3\Delta \delta}{\delta}\right)^2 + \left(\frac{\Delta h}{h}\right)^2 + \left(\frac{\Delta y^*}{y^*}\right)^2}$$

pričom nevychýleným odhadom pre strednú kvadratickú chybu Δy^* je štatistika

$$\Delta y^* = \sqrt{\frac{\sum_{i=1}^N [y_i - y(x_i)]^2}{N - m}} \quad (15)$$

kde N je počet dvojíc súradníc (x_i, y_i) využitých na nájdenie regresných koeficientov a a b , $y(x_i)$ sú funkčné hodnoty regresnej funkcie (3) v bodoch so súradnicami x_i a $m = 2$ je počet regresných koeficientov.

Pri využití odhadu rádu minima v mieste pôsobiska sily dosadíme plošné momenty prierezu pre prvú a druhú pozíciu vzorky v adekvátnom poradí do vzťahu (11) a získame

$$E = \frac{16Fl^3}{\delta h^3 (2n+1)\lambda}, \quad E = \frac{16Fl^3}{h\delta^3 (2n+1)\lambda} \quad (16, 17)$$

a s využitím vety o prenose chýb získame v adekvátnom poradí vzťahu pre relatívne chyby $\Delta E/E$ merania

$$\frac{\Delta E}{E} = \sqrt{\left(\frac{\Delta F}{F}\right)^2 + \left(\frac{3\Delta l}{l}\right)^2 + \left(\frac{\Delta \delta}{\delta}\right)^2 + \left(\frac{3\Delta h}{h}\right)^2 + \left(\frac{\Delta n}{n}\right)^2 + \left(\frac{\Delta \lambda}{\lambda}\right)^2} \quad (18)$$

$$\frac{\Delta E}{E} = \sqrt{\left(\frac{\Delta F}{F}\right)^2 + \left(\frac{3\Delta l}{l}\right)^2 + \left(\frac{3\Delta \delta}{\delta}\right)^2 + \left(\frac{\Delta h}{h}\right)^2 + \left(\frac{\Delta n}{n}\right)^2 + \left(\frac{\Delta \lambda}{\lambda}\right)^2} \quad (19)$$

Rád interferenčného minima v pôsobisku sily sme odhadovali s chybou $\Delta n = 0,5$. Vzorku sme merali 7-krát v prvej pozícii a 5-krát v druhej pozícii, takže sme mali k dispozícii 12 interferogramov. Z i -teho interferogramu sme modul pružnosti E_i a chybu v jeho určení ΔE_i vypočítali dvomi spôsobmi. Výsledný odhad E modulu pružnosti a chybu odhadu ΔE pre daný spôsob sme stanovili podľa vzťahov

$$E = \frac{1}{12} \sum_{i=1}^{12} E_i, \quad \Delta E = \frac{1}{12} \sqrt{\sum_{i=1}^{12} \Delta E_i^2} \quad (20, 21)$$

Tabuľka I

Odhady a chyby odhadov Youngovho modulu pružnosti eutektického kompozitu

Podľa odhadu rádu minima E [GPa]	Podľa lineárnej regresie E [GPa]
198,5 ± 8,1	204,8 ± 7,9

Výsledky sú uvedené v tabuľke I. Chyby merania pri oboch spôsoboch určenia Youngovho modulu pružnosti sú porovnateľné. Prvou výhodou lineárnej regresie je však to, že umožňuje určiť modul pružnosti aj v prípade, že sa tmavé interferenčné pružky v hornej časti interferogramu vplyvom ich veľkej hustoty zlievajú do tmavého priestoru a nie je možné urobiť odhad rádu minima v mieste pôsobiska sily, resp. nie je možné určiť počet interferenčných miním od upevneného konca po pôsobisko sily. Druhou výhodou lineárnej regresie je to, že regresná krivka poskytuje informáciu o ohybe vzorky v každom bode pozdĺž vzorky. Metóda dvojexpozíčnej interferometrie je pomerne citlivá a je vhodné ju použiť na skúmanie predmetov pravidelných tvarov vyrobených z kovových aj keramických materiálov⁴. Interferogramy, na ktorých boli zjavné nedokonalosti upnutia spodného konca vzorky, sme z merania vylúčili. Metódu je možné využiť aj vtedy, ak má skúmaná vzorka komplikovaný tvar. V takomto prípade je možné metódu doplniť o numerické modelovanie a pomocou programu ANSYS určiť Youngov modul pružnosti a Poissonovo číslo daného materiálu.

Prácu na tomto príspevku podporila Vedecká grantová agentúra projektom č. 1/0173/08.

LITERATÚRA

1. Puchner O. a kol.: *Pružnosť a pevnosť I*. Edičné stredisko SVŠT, Bratislava 1987.
2. Vest Ch. M.: *Holographic Interferometry*. J. Wiley & Sons, New York 1979 (in Russian: Mir, Moskva 1982).
3. Čička R., Trnovcová V., Starostin M. J., Labaš V., Minárik S., Kubliha M., Bošák O.: *Directional solidification in system Al₂O₃-(Y₂O₃)ZrO₂*. Materials science and technology 2 (2004).
4. Balaš J., Szabó V.: *Holografická interferometria v experimentálnej mechanike*. VEDA, Bratislava 1986.

J. Krajčovič and I. Jančuška (*Institute of Materials Science, Faculty of Materials Science and Technology in Trnava, Slovak University of Technology Bratislava, Slovakia*): **Holography Method of Young's Elasticity Modulus Determination**

The paper deals with the comparison of two approaches to the determination of the Young's elasticity modulus. The first approach is based on the determination of number of the interference minima between the fixed end and the force action point. In the second approach the linear regression is used. Both the approaches are based on the application of the two-exposure holography interferometry. The investigated balk shape sample was made from the eutectic Al₂O₃ - (Y₂O₃) ZrO₂ composite. It was shown how the obtained regression curve describes the non-damage deformation of the parallelepiped girder with the fixed down end.

LOCALIZED VISCOUS FLOW IN THE OXIDE AND OXYNITRIDE GLASSES BY INDENTATION CREEP

FRANTIŠEK LOFAJ

*Institute of Materials Research of SAS, Watsonova 47, 040 01
Košice, Slovakia
flofaj@imr.saske.sk*

Keywords: indentation creep, viscosity, oxynitride glass, rare-earth additives

1. Introduction

Vickers, Brinell or Rockwell hardness tests are common methods for the investigation of the hardness, elastic, elastoplastic and plastic behavior, yield strength, etc., of wide range of materials from soft and ductile metals up to brittle and very hard ceramics and glasses¹. These tests are simple and the information is obtained from very small volume of the material. Instrumented indentation developed over last two decades based on the model of Oliver and Pharr² resulted in the measurement of a range of properties and parameters, which are not available from conventional hardness. Besides reduced elastic modulus, elastic and plastic work and several others, indentation creep data became available. However, the indentation creep used in the instrumented indentation is related to the deformation under the sharp indenter over relatively short period of time of tens of seconds up to several minutes at room temperature. Highly localized and concentrated stresses in brittle materials result in the formation of indentation damage, which contributes to the plasticity data. The tests without damage contribution are desirable to obtain concise data on plasticity of the studied materials. Creep resistance, viscous flow as well as time dependence of hardness can be successfully determined at high temperatures using a modified indentation creep, which is a combination of the compressive creep testing and instrumented indentation with blunt indenter^{3–8}. The first tests of this type with hemispherical indenter were performed by Heynes and Rawson in the 60-s to measure the viscosity of glasses³. The theoretical interpretation of this measurement was worked out by Douglas⁴. The flat ended cylindrical punch was used Yu and Li in the 70-s for investigation of creep properties of single crystals and they have proved that its results are equivalent to those of the tensile creep test^{5,6}. During this measurement, a cylinder with the diameter d is pressed with the force F into the flat surface of the sample (Fig. 1) at the test temperature, T , and the depth of the indentation, $h(t)$ is recorded as the function of elapsed time, t . The result is a conventional creep curve with an initial transient stage followed by a stage with the constant impression velocity, $v = dh/dt$. It was shown on various metals, glasses and ceramics that the indentation tests provide the same information on viscosity as tensile tests^{5–8}. Viscosity of the glasses, η , was found to follow the relationship:

$$\eta = d k_1 p/3 k_2 v$$

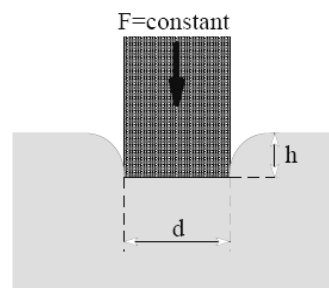


Fig. 1. Schematic representation of the flat cylindrical punch indentation creep geometry

where k_1 and k_2 are the geometrical coefficients and p is the pressure on the indenter. The values of k_1 and k_2 were determined experimentally and by FEM and they are in the range 0.3–0.4 and 0.76–1.0, respectively⁹. Thus, viscosity measured by the indenter with the diameter d and pressure

$$p = 4F/\pi d^2, \text{ is} \quad \eta = c \cdot p/v \quad (1)$$

where $c = k_1/d/3 k_2$. For the FEM values $k_1 = 0.3$ and $k_2 = 0.76$ ⁹, the value $c = 0.13$ d is a constant of the indenter. The activation energy, Q , is given by the formula

$$\eta = \eta_0 \exp(Q/kT), \text{ resp. } \ln v = \ln p - \ln(c\eta_0) - Q/kT \quad (2)$$

where η_0 is a constant and kT has its usual meaning.

Oxynitride glasses present in the advanced structural ceramics at the grain boundaries, originate from sintering additives. Despite being as only 1 nm thin films, they control high temperature behavior of these ceramics and the increase of their viscosity is crucial for the improvement of creep resistance of the whole material. The measurement of the viscosity of such thin films is currently experimentally not possible but it can be measured on the model bulk oxynitride glasses^{10–12}. Viscosities of such glasses were already measured by compressive tests and it was shown that both, rare-earth additives and nitrogen content have significant influence on viscosity and transition temperature of these glasses^{10–12}.

The aim of the current work is to investigate viscosities of the selected oxynitride glasses by indentation method, to compare the obtained results with those from other methods and to prove suitability of indentation method for viscosity measurement of the oxynitride glasses.

2. Experimental part

Glass preparation

Four oxide and four oxynitride glasses were prepared from the mixture of powders of SiO₂ (Aerosil OX 50, Degussa-Hüls AG, Germany), MgO (MgO 500 A, UBE Ind.

Ltd., Japan), α - Si_3N_4 (SN-E10, UBE Ind. Ltd., Japan) and rare-earth oxides RE_2O_3 (RE = La, Sm, Yb, Lu). The ratio Mg: RE of 1:1 was constant and 20 e/o (equivalent %) for each element. The amount of silicon nitride powder was calculated in such a way that the resulting nitrogen contents were 0 e/o in the oxide and 20 e/o in the oxynitride glasses. The powders were homogenized, dried, uniaxially pressed, cold isostatic pressed and finally sintered in gas pressure sintering furnace at 1700 °C under 2 MPa of nitrogen pressure for 0.5 h (ref.^{11,12}). The obtained pellets were cut on 3 mm thick slices ground and polished to obtain two parallel surfaces for the indentation tests.

Indentation creep

The tests were performed in the HTTF2 creep furnace in the temperature range 760–925 °C in air using SiC indenter with the diameter $d = 2.1$ mm under the stress $p = 20$ MPa. Experimental set-up is shown in Fig. 2. Penetration depth was measured as a difference between the data from two linear

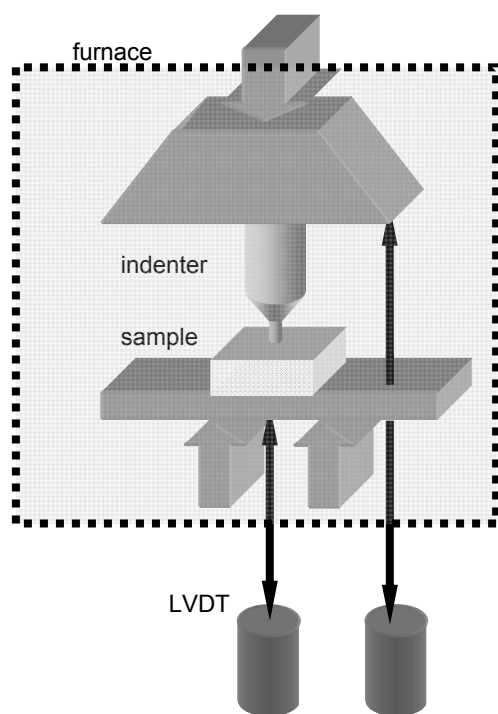


Fig. 2. Schematic representation of the indentation creep test set-up

variable differential transducers (LVDT). They were out of the furnace attached to the loading punches via thin alumina rods to compensate errors due to thermal expansion. The tests run from < 1 min at the highest temperatures up to around 20 hours at the lowest temperatures.

3. Results

Creep curves corresponding to the time dependence of the penetration depth of the indenter in the La-Si-Mg-O glass

are compared in Fig. 3. Penetration rates in the studied temperature range 790–840 °C vary over three orders of magnitude. Similar differences were measured in the case of the corresponding oxynitride glasses, however, with a shift toward higher temperatures. As shown in Fig. 4, penetration rates of around $1 \cdot 10^{-5}$ mm s^{-1} obtained in La-oxide glass at ~ 805 °C occur at around 890 °C in Lu-Si-Mg-O-20 % N glasses.

Penetration rates were transferred into viscosity using Eq. (1) with $c = 0.273$ mm. Fig. 5 shows temperature dependence of viscosity of the La-Si-Mg-O glass. Glass transition temperature, T_g , was determined as a temperature in the middle of the range when viscosity changes from 10^{12} Pa s to $10^{12.6}$ Pa s. The viscosities of all glasses are summarized in Fig. 6. The viscosities of the oxide glasses are significantly lower than those of the corresponding oxynitride glasses. The

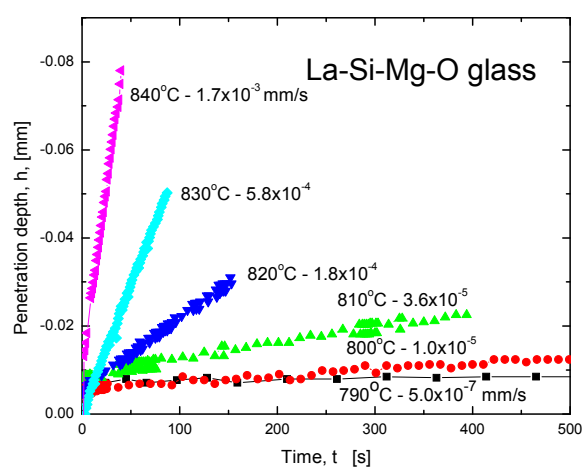


Fig. 3. Time dependence of the penetration depth in La-Si-Mg-O glasses under stress of 20 MPa

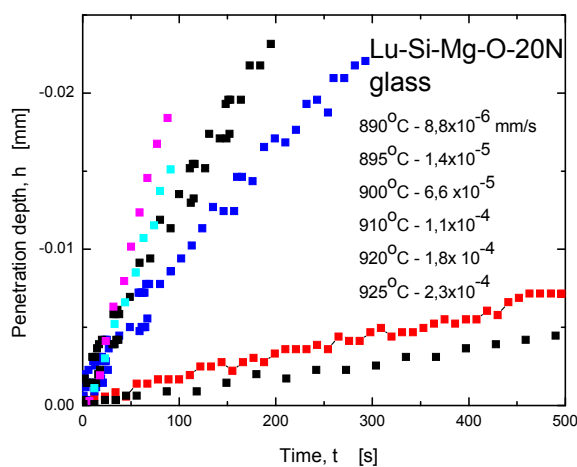


Fig. 4. Indentation creep curves in Lu-Si-Mg-O-N glass under stress of 20 MPa

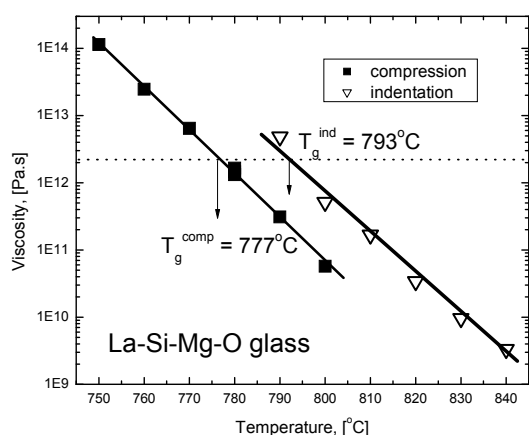


Fig. 5. Temperature dependencies of viscosities obtained by indentation and compressive creep¹¹ methods

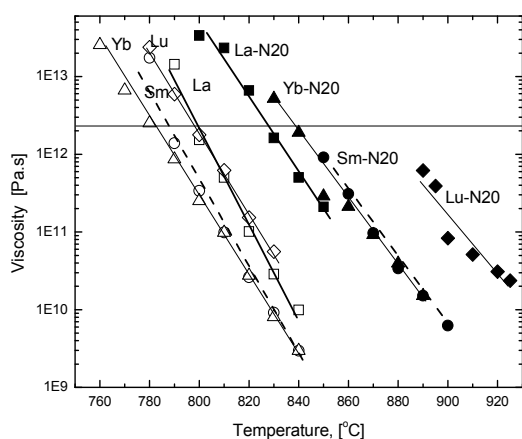


Fig. 6. Summary of the temperature dependencies of viscosities of the studied oxide and oxynitride glasses obtained by indentation creep

differences are up to 70 °C. However, the variations in T_g up to 45 °C can also be seen within each group. The lowest T_g belongs to La- and Yb-containing glasses whereas Lu-containing glasses always exhibit the highest T_g . The values T_g of as well as of the activation energies, which were determined from the Eq.(2), are summarized in Table I and compared with the values obtained earlier from the compressive creep tests on the same materials¹¹.

4. Discussion

The results indicate that the indentation creep method is capable of the determination of the viscosity of oxide and oxynitride glasses over five orders of magnitude and its results are comparable with those obtained by compressive creep method from considerably larger volumes of glass. However, some systematic differences were observed (see Fig. 5). T_g and viscosity from indentation creep are usually higher in the case of oxide and lower in the case of oxynitride

Table I

Summary of the indentation and earlier compressive creep tests in terms of T_g and activation energies

Material	$T_g^{\text{indentation}}$ [°C]	$T_g^{\text{compression}}$ [°C]	Q^{ind} [kJ mol ⁻¹]	Q^{comp} [kJ mol ⁻¹]
La-N0	793 ± 5	777 ± 5	1406±130	1373±129
La-N20	829 ± 6	853 ± 6	1095±91	1151±94
Sm-N0	790 ± 5	773 ± 5	1347±124	1313±122
Sm-N20	841 ± 7	859 ± 6	1096±90	1140±93
Yb-N0	782 ± 6	778 ± 6	1077±95	1097±97
Yb-N20	837 ± 7	857 ± 7	1007±81	1120±91
Lu-N0	800 ± 6	803 ± 6	1167±102	1151±100
Lu-N20	873 ± 7	889 ± 7	1055±82	1110±87

glasses while the activation energies are essentially the same. The differences in T_g are from 3 °C up to 24 °C and can be attributed to the differences in the coefficients k_1 and k_2 and to local inhomogeneities in the glasses. The activation energies obtained by indentation are in the range from 1050 kJ mol⁻¹ up to 1400 kJ mol⁻¹ with the highest values in the case of La- and lowest in Yb- and Lu-containing glasses. Note that these values are considerably higher than 400–550 kJ mol⁻¹ reported for common Mg- or Pb-silicate glasses⁷. Such high activation energies reflect significantly stronger bonds in these glasses when RE and N are incorporated. The data in Table I indicate small but systematic decrease of activation energy of viscous flow in oxide glasses from 1400 kJ mol⁻¹ to 1170 kJ mol⁻¹ when the largest cation La is replaced by the smallest Lu cation, with the exclusion of Yb. Change of the RE type has exactly opposite effect on T_g (Yb is an exclusion¹²). Similar tendencies were observed in the oxynitride glasses and also in compressive creep tests^{10–12}. Thus, viscous flow is influenced by at least three effects:

1. type of the cation modifier
2. RE cation size, and
3. N content.

Chemistry, resp. electronic structure of the RE modifiers seems to weaken the bonding with the ionic size decrease. On the other side, ionic size reduction results in density increase and tightening of the glass network, which partially compensate for the above weakening. Finally, nitrogen significantly increases cross-linking of the network which results in much larger increase of viscosity and transition temperatures than the modification of RE¹². However, the reason why the activation energies of viscous flow in the oxynitride glasses are lower than in the corresponding oxide glasses is not clear.

5. Conclusions

It was shown that the indentation creep method with flat indenter is suitable for the determination of viscosity, T_g and activation energy of oxide and oxynitride glasses. The effects of RE-type and nitrogen content on the viscosity and glass transition temperature, which were measured earlier by the compressive creep method, were also confirmed. The differ-

ences in the measured viscosities result in the differences in T_g values up to 25 °C whereas the values of the activation energy remain identical. The variations in viscosity can be attributed to the differences in the coefficients k_1 and k_2 and to local inhomogeneities in the glasses. The effects of nitrogen and RE-type were attributed to the increase of network cross-linking and tightening of the glass structure when nitrogen and RE with smaller ionic radii are incorporated in the glass network, respectively.

This work was supported by the Slovak Research and Development Agency under the contract No. APVV-0034-07 and Slovak Grant Agency for Science under the contracts No. VEGA 1/4160/07 and VEGA 2/0088/08. The help of F. Dorčáková is appreciated.

REFERENCES

1. O'Neill H.: *Hardness Measurements of Metals and Alloys*, Chapman and Hall, London 1967.
2. Oliver W. C., Pharr G. M.: *J. Mater. Res.* 7, 1564 (1992).
3. Heynes M. S. R., Rawson H.: *Phys. Chem. Glass.* 2/1, 1 (1961).
4. Douglas R. W., Armstrong W. L., Edward J. P., Hall D.: *Glass Tech.* 6/2, 52 (1965).
5. Yu E. C., Li J. C. M.: *Phil. Mag.* 36, 9 (1977).
6. Yu E. C., Li J. C. M.: *J. Mater. Sci.* 12, 2200 (1977).
7. Cseh G., Chinh N.Q., Tasnádi P., Szommer P., Juhász A.: *J. Mater. Sci.* 32, (1997) 1733.
8. Cseh G, Bär J., Gudladt H.-J., Lendvai J., Juhász A.: *Mater. Sci. Eng., A* 272, 145 (1999).
9. Han W. T., Tomozawa M.: *J. Am. Ceram. Soc.* 73, 3626 (1990).
10. Becher P. F., Ferber M. K.: *J. Amer. Ceram. Soc.* 87, 1274 (2003).
11. Lofaj F., Dorčáková F., Hoffmann M. J.: *J. Mat. Sci.* 40, 47 (2005).
12. Lofaj F., Dériano S., LeFloch M., Rouxel T., Hoffmann M. J.: *J. Non-Cryst. Solids* 344, 8 (2004).

F. Lofaj (*Institute of Materials Research of SAS, Watsonova 47, 040 01 Košice, Slovakia*): **Localized Viscous Flow in the Oxide and Oxynitride Glasses by Indentation Creep**

Localized viscous flows in the oxide and oxynitride glasses were investigated by the indentation creep and the results were compared with the data obtained in compression. Despite general agreement between both methods, the observed differences can be attributed to geometrical factors and local inhomogeneities in the glass. RE type and nitrogen content exhibit strong influence on the glass viscosity. Their effects were related to the increase of network cross-linking and tightening of the glass structure when nitrogen and RE with smaller ionic radii are incorporated in the glass network, respectively.

MICROSTRUCTURE AND LOCAL MECHANICAL CHARACTERISTICS OF Zr1Nb ALLOY AFTER HARDENING

**ROSTISLAV MEDLÍN, JAN ŘÍHA,
and OLGA BLÁHOVÁ**

New Technology Research Centre, University of West Bohemia, Univerzitní 8, 306 14 Plzeň, Czech Republic
medlin@ntc.zcu.cz

Key words: Zr1Nb, Zr alloys, LOCA, nanoindentation, X-Ray microanalysis, EPMA, X-Ray diffraction

1. Introduction

Zirconium alloys are used as cladding materials for fissionable fuel in nuclear reactors mainly for their mechanical properties. Their characteristics after long-term oxidation under service conditions in a reactor are intensively investigated. In order to define their fail-safety, it is necessary to know their mechanical characteristics after long-term service and high temperature oxidation, as well as the reasons for changes in those characteristics.

This paper presents the summary of mechanical properties, results of X-ray diffraction and electron microprobe measurements of the Zr1Nb alloy after various exposition time prior to hardening, which simulated the LOCA conditions (Loss Of Coolant Accident). Correlations between the measurements are discussed.

2. Experimental

The samples were small tubes from Zr1Nb material with 600 μm wall thickness, which are identical to actual cladding tubes. LOCA was simulated by heating at 950 $^{\circ}\text{C}$ in steam for 0, 3, 6, 9, 15, 30, 60 and 120 minutes and subsequent hardening in water with ice.

Regarding to the previous results^{1–3}, this article contains new measured data. Samples were examined by X-Ray diffractometer Panalytical X'Pert PRO equipped with high-temperature chamber Anton Paar HTK 1200 N, Nanoindenter XP and scanning electron microscope (SEM) Quanta 200 with EDAX EDS and WDS X-Ray detectors, mostly termed Electron Probe MicroAnalysis (EPMA).

Nanoindentation and microprobe data were measured on the cross-section of the tube wall. Nanoindentation measurements were taken with the load of 8 mN in 5 μm intervals using the Berkovich indenter⁴. The indentation hardness H_{IT} and indentation modulus E_{IT} were measured by the IIT (Instrumented Indentation Testing) method^{5,6}.

As it can be seen in the picture of the cross-section in Fig. 1, there are different layers in the material: an oxide layer under the surface and two different regions in the metal. The picture was taken by the BSE (Back Scattering Electrons) detector in SEM. The various grey levels correspond to various values of atomic weight of elements in the material: lighter elements appear darker.

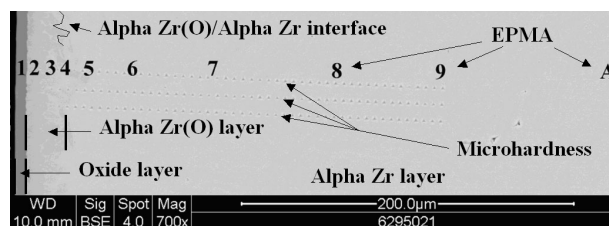


Fig. 1. Typical cross-section of the hardened sample (exposition time 3 min) with marked oxides, Alpha Zr(O) and Alpha Zr phases and locations of hardness and EPMA measurements. The SEM micrograph was taken by the BSE

Under the oxide layer, there is an oxygen-stabilized Zr in the Alpha phase Zr(O). In greater depth, there is Alpha phase where there is not enough oxygen to prevent the phase transformation from Alpha to Beta phase at high temperature. The oxygen-poor structure in the middle of the wall thickness is called the Prior Beta phase⁷.

Problem is that X-Ray diffraction after high-temperature experiments (discussed in other paper⁸) showed certain amount of undissolved Beta phase in that region. That is why calling all the material as Beta phase may cause misunderstanding. Identified Beta phase by X-Ray diffraction was located in Alpha Zr phase region. The oxygen-rich region Alpha Zr(O) phase and the oxygen-poor region Alpha Zr were marked with arrows (Fig. 1).

The differences between the layers correspond to different amounts of oxygen. However, the oxygen solubility is also affected by other influences⁹, such as hydrogen content and its solubility in the material. EPMA results in [au %] percentage represent [wt.%] (weight percentage). Standardized percentage by weight during the low content volume of oxygen has to be compared very carefully with values measured by other methods. This cautions us to be very careful and determine the oxygen content in Auxiliary Units (au). EPMA measurements were carried out from the edging of the sample towards to the centre (Fig. 1).

Lattice parameters and unit cell volumes were calculated by Rietveld's method from diffraction patterns. Biaxial lattice stress was calculated only from the α -Zr diffraction line (102) drift from the reference position according to formula:

$$\sigma_1 + \sigma_2 = -\frac{E}{\mu} \cdot \frac{d - d_0}{d_0}$$

where E is Young modulus, μ is Poisson number, d_0 is reference interplanar distance, d is measured interplanar distance.

3. Results of Measurements

EPMA data measured on the cross-section of samples are shown in Fig. 2 in micrometers from the Alpha Zr(O)/Alpha Zr layer interface. Higher oxygen content in the Al-

pha Zr(O) phase is clearly visible as well as the difference between the distributions of oxygen in dependence on various exposition times prior to hardening.

EPMA values were measured along the same measuring line as the indentation hardness. The summary results for all samples are shown in Fig. 3a–h. The beginning of coordinates is in the Alpha Zr(O)/Alpha Zr layer interface. The correlation between the oxygen content and indentation hardness values in Fig. 3 is evident.

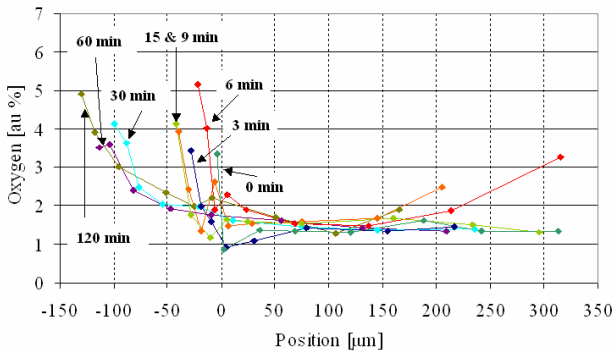
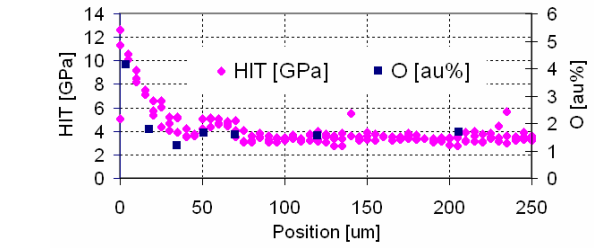
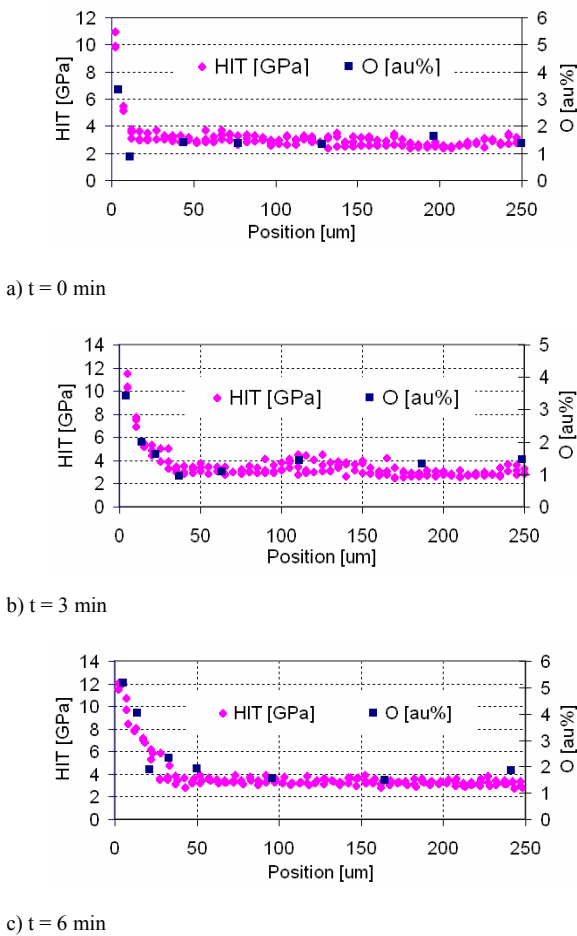
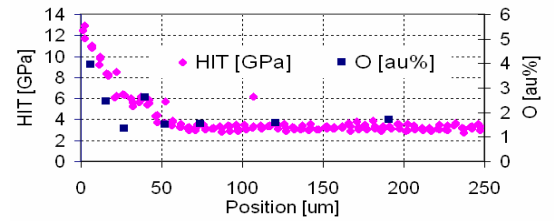


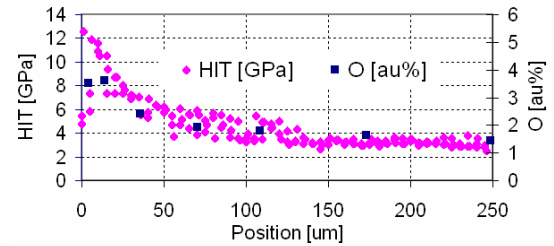
Fig. 2. Oxygen depth-profiles on the cross-sections in dependence on different exposition time prior to hardening



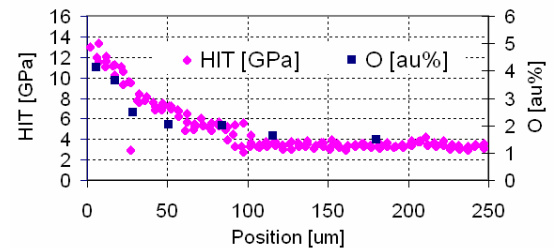
d) t = 9 min



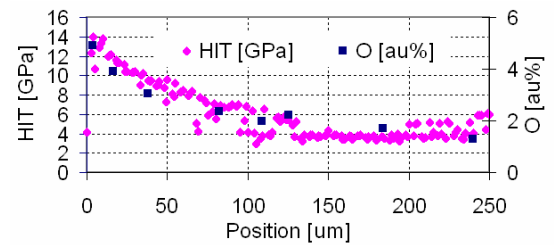
e) t = 15 min



f) t = 30 min



g) t = 60 min



h) t = 120 min

Fig. 3a–h. Oxygen depth-profiles and indentation hardness values measured by the nanoindentation method

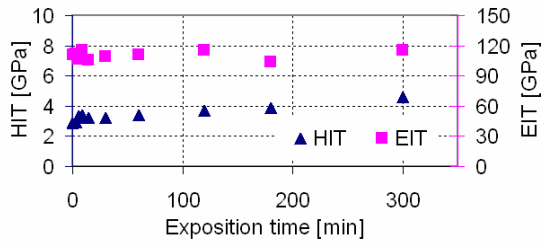


Fig. 4. Indentation hardness and indentation modulus measured in Alpha Zr

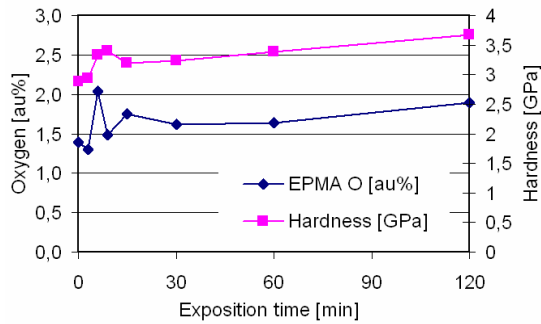


Fig. 5. Indentation hardness measured by nanoindentation and corresponding oxygen content measured by EPMA in Alpha Zr

Fig. 4 shows a comparison of the indentation hardness and indentation modulus values in the Alpha Zr phase in all samples. Fig. 5 contains the EPMA-measured oxygen content compared with corresponding indentation hardness values in the Alpha Zr phase. There is a close correspondence between oxygen content and indentation hardness.

Fig. 6 contains X-ray diffraction patterns (in detail mentioned in⁸) for all samples with very weak oxide signal related to ZrO₂. Quantification of the oxide signal using the phase analysis was attempted, even though this was very difficult due to weak signal. Tab. I shows these results together with the EPMA results from the same region.

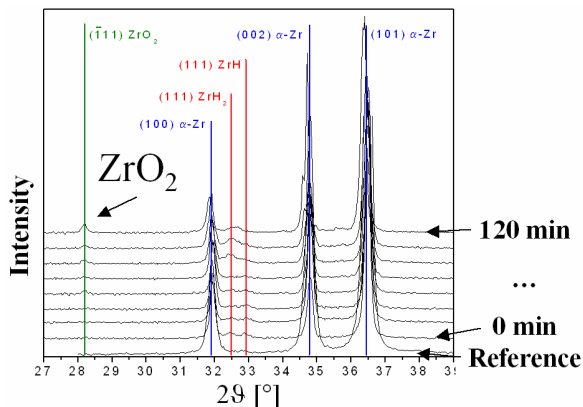


Fig. 6. X-Ray diffraction patterns measured in the centre of each sample. Weak oxide signals are only detectable at the longest exposition times prior to hardening

Table I
X-Ray quantitative phase analysis of ZrO₂ content together with results of EPMA measurement of the oxygen content

Exposition time [min]	X-Ray ZrO ₂ [wt.%]	EPMA O [au.%]
0	0	1.39
3	0	1.30
6	0	2.03
9	0.5	1.49
15	0.28	1.75
30	0.54	1.61
60	0.44	1.64
120	1.35	1.90

High local hardness is accompanied by high local oxygen concentration (Fig. 5). Biaxial stress and unit cell volume determined from X-Ray diffraction have almost the same tendency (Fig. 7). Hardness course have increasing tendency with increasing exposition time except samples exposed for 6 and 9 minutes (Fig. 8). The sample exposed for 6 minutes has the smallest unit cell volume together with the highest amount of oxygen (Fig. 9). This could be caused by presence of oxy-

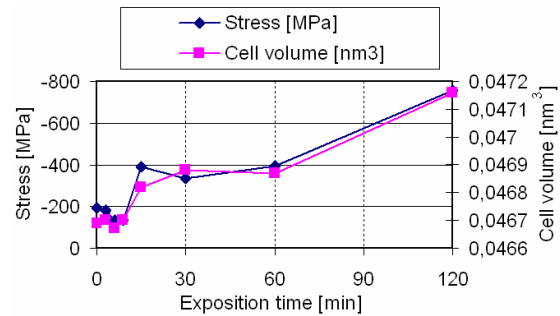


Fig. 7. Cell volume measured by X-Ray together with stress for various exposition times prior to hardening measured in Alpha Zr

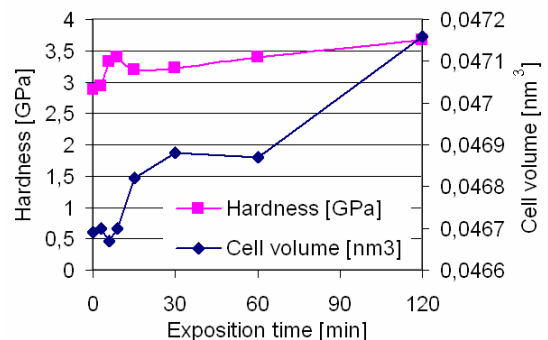


Fig. 8. Cell volume measured by X-Ray together with indentation hardness for various exposition times prior hardening measured in Alpha Zr

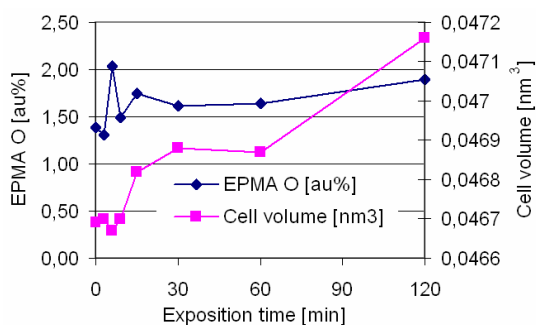


Fig. 9. Cell volume measured by X-Ray together with oxygen content for various exposition times prior hardening measured by EPMA in Alpha Zr

gen in grain boundaries, not in interstitial positions in crystallographic lattice.

Under various conditions⁹, which had been investigated before, there was some amount of hydrogen in the material, which might have changed its mechanical characteristics independently on the oxygen content. However, no such influence was observed in these samples, in which hydrogen content was negligible.

4. Conclusions

This paper is based on a part of long-time investigation and characterization of mechanical and other properties of a new Zr1Nb alloy. In this article were evaluated the relations of oxygen content, unit cell parameters and biaxial stress together with nanoindentation hardness. There is a close correspondence between oxygen volume and microhardness.

This work was supported by the project MPO ČR No. 2A – ITP1/037 and project Kontakt – AIP No. MEB 080869.

REFERENCES

1. Vrtílková, V. et al.: Vliv rozpouštění oxidu vytvořeného na povlakové trubce ze Zr-slitin na termomechanické vlastnosti povlakové trubky po vysokoteplotních přechodech (The Influence of Dissolution of the Oxide Formed on the Fuel-Cladding Tube from Zr-Alloy upon the Ther-

morechanical Properties of the Tube upon High-Temperature Transitions): *Výzkumná zpráva 1164* (Research report). UJP Praha, Praha 2005.

2. Medlín R., Vrtílková V.: *Proceedings of the 12th international workshop on Applied physics of condensed matter. Bratislava, 2006*, pp. 129–132. Slovak University of Technology, Bratislava 2006.
3. Medlín R., Zubko P., Bláhová O.: *Lokální mechanické vlastnosti 2006 (Local Mechanical Properties), Plzeň 2006*, pp. 111–115. ZCU, Plzeň 2006.
4. Bláhová O., Šugár M.: Investigation of Nano-Mechanical Properties of Zirconium Alloys Using Nanoindentation. In this issue.
5. Pešek L., Zubko P., Kalmár P.: *Acta Metallurgica Slovaca spec. iss. 1, 10*, 203–207 (2004).
6. *Metallic materials – Instrumented indentation test for hardness and materials parameters – Part 1: Test method*.
7. Chung H. M.: *Nuclear Eng. Technol.* 37, 327 (2005).
8. Říha J., Bláhová O., Šutta P.: Fázové změny slitiny Zr1Nb a jejich vliv na lokální mechanické vlastnosti (Phase Changes in the Zr1Nb Alloy and their Impact on the Local Mechanical Properties). In this issue.
9. Medlín R., Zubko P.: *Proceedings of the 13th international workshop on Applied physics of condensed matter. Žilina 2007*, pp. 239–242. University of Žilina, Slovakia 2007.

R. Medlín, J. Říha, and O. Bláhová (*New Technology Research Centre, West Bohemia University, Plzeň, Czech Republic*): **Microstructure and Local Mechanical Characteristics of Zr1Nb Alloy after Hardening**

Zirconium alloys are used as cladding materials for atomic fuel in nuclear reactors mainly for their mechanical properties. Their characteristics after long time oxidation under service conditions in a reactor are intensively investigated. In order to define their fail-safety and damage tolerance, it is necessary to know their mechanical characteristics after long-term service and high temperature oxidation as well as the reasons for changes in those characteristics.

This paper presents the summary of mechanical properties, results of X-ray diffraction and electron microprobe measurements of the Zr1Nb alloy after various exposition times prior to hardening, which simulated the LOCA (loss of coolant accident) conditions. Correlations between the measurements are discussed.

STANOVENIE VEĽKOSTI PLASTICKEJ ZÓNY VIDEOEXTENZOMETRICKOU METÓDOU

MÁRIA MIHALIKOVÁ a ĽUBOMÍR AMBRIŠKO

Technická univerzita v Košiciach, Hutnícka fakulta, Katedra náuky o materiáloch, Park Komenského 11, 043 85 Košice, Slovensko

maria.mihalikova@tuke.sk, lubomir.ambrisko@tuke.sk

Kľúčové slová: plastická zóna, videoextenzometrické meranie, hlbokoťažný plech

1. Úvod

Hlbokoťažné ocele považujeme za ocele hromadnej spotreby nielen pre ich priaznivé ekonomické charakteristiky výroby, ale hlavne pre ich dobré pevnostné vlastnosti, všetky poznatky o nich majú veľký praktický význam. Príspevok si kladie za cieľ posúdiť, ako sa dané vlastnosti budú meniť v prípade materiálu s koncentrátormi napätia.

V práci bolo pozorované správanie hlbokoťažnej ocele pri jej zaťažovaní statickým jednoosovým napätím. Videoextenzometrickou metódou bolo stanovené rozloženie deformácií v okolí vrubov.

Videoextenzometria je bezkontaktná metóda merania deformácií, ktorá využíva moderné počítačové a snímacie technológie, ako aj podporu nových programových aplikácií^{1,2}. Vývoj tejto metódy merania je daný vývojom obrazovej analýzy, resp. vývojom programovej metódy vyhodnocovania snímaného obrazu, ale hlavne aplikačnými požiadavkami praxe³.

O vplyve vrubov na deformáciu a vlastnosti konštrukčných ocelí môžeme skonštatovať, že:

- koncentratory napätia spôsobujú viacosový stav napätosti,
- na veľkosť napätí v okolí vrubu vplyva polomer zakrivenia vrubu a jeho hĺbka,
- s väčším polomerom vrubu sa zvyšujú pevnostné vlastnosti R_e a R_m skúšaných ocelí.

Na význam koncentrácie napätia v okolí ostrých vrubov prvý poukázal E. E. Inglis. Dokázal, že najväčšia koncentrácia napätia vzniká v mieste najväčšieho zakrivenia vnútorného povrchu vrubu. Ak bude polomer zakrivenia koreňa trhliny veľmi malý, jednoosové ťahové zaťaženie telesa s trhlinou vyvolá ťahové napätie nielen v smere y , ale aj v smere x , z čoho vzniká kolmá zložka napätia σ_x . Z toho vyplýva, že napätie σ_y bude mať maximálnu hodnotu na hrote trhliny.

Existuje niekoľko metód na snímanie a výpočet deformácií a napätí. V práci boli porovnávané videoextenzometrická metóda a výpočtová metóda získavania hodnôt veľkosti plastickej zóny.

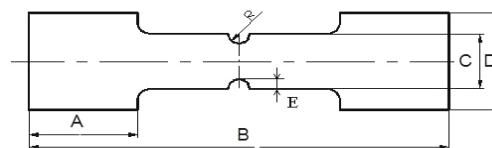
2. Materiál a metodika experimentov

Pre statickú skúšku v ťahu boli použité skúšobné telesá z hlbokoťažnej žiarovo pozinkovanej mikrolegovanej ocele, akosti EN 10292/2000. Plechy hrúbky 1,6 mm boli valcované za studena, ich mechanické vlastnosti sú v tab. I. Skúšobné telesá boli odobraté kolmo k smeru valcovania.

Pre skúšku jednoosovým ťahom boli pripravené telesá podľa STN 42 0321. Telesá mali obojstranný vrub tvaru U.

Tabuľka I
Mechanické vlastnosti skúšaného materiálu

Materiál	Mechanické vlastnosti		
EN	$R_{p0,2}$ [MPa] prične min.	R_m [MPa] prične min.	A_{min} [%] $L_0 = 80$ mm prične
10292/2000	340	410	20



Obr. 1. Tvar skúšobného telesa

Pre vyhodnotenie rozloženia deformácií bola urobená statická skúška jednoosovým ťahom na univerzálnom trhacom stroji FP 100/1 s rýchlosťou posuvu traverzy $1,5 \text{ mm min}^{-1}$, s rozsahom sily 10 kN. Rozmery skúšobného telesa podľa obr. 1 uvádza tab. II.

Tabuľka II
Rozmery skúšobných telie

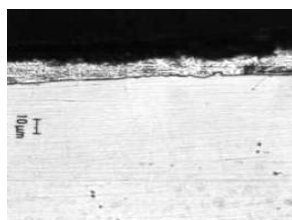
A [mm]	B [mm]	C [mm]	D [mm]	E [mm]	R [mm]
2	134	14	20	2	2

Metalografická analýza

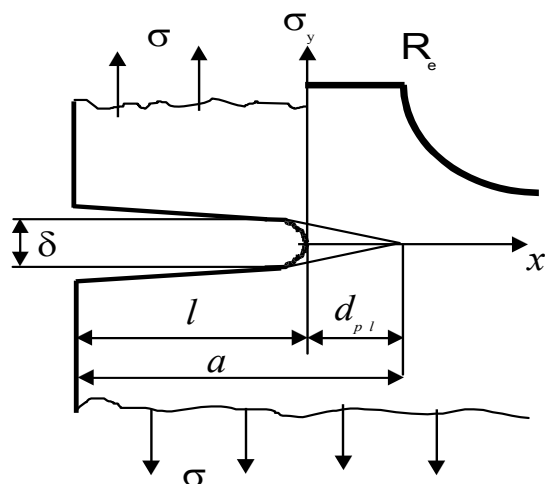
Štruktúra ocele a zinkový povlak (obr. 2 a 3) boli pozorované svetelným mikroskopom OLYMPUS na výbrusoch pripravených za mokra, klasickým brúsením, leštením a leptaním v 2% roztoku nitalu. Ide o oceľ s nízkym obsahom uhlíka (0,10 %), mikroštruktúru tvorí feritické zrnó s malým množstvom perlitu.



Obr. 2. Mikroštruktúra skúšanej ocele



Obr. 3. Zinkový povlak skúšanej ocele



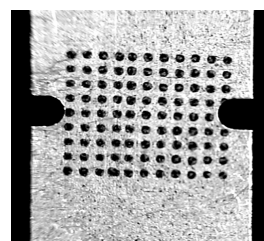
Obr. 4. Otváranie trhliny

Pre otváranie trhliny (obr. 4) dĺžka plastickej zóny pre U vrub sa vypočíta podľa vzťahu (1)⁴.

$$r_{pl} = \frac{d_{pl}}{2} = l \left(\frac{\sigma}{R_e} \right)^2 \quad (1)$$

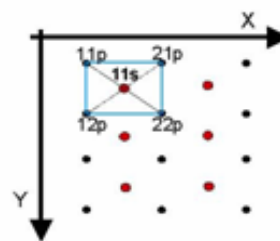
kde d_{pl} – dĺžka plastickej zóny, σ – normálové napätie, R_e – medza klzu materiálu, r_{pl} – polomer plastickej zóny

Na obr. 5 je znázornené skúšobné teleso pripravené na videoextenzometrické meranie⁵. Rozostup bodov bol 1×1 mm. Osvetlené skúšobné teleso upnuté do čelusti trhacieho stroja snímala kamera, ktorá je súčasťou videoextenzometrického systému ME – 46. Snímaný obraz spracovával software Dot-Measuring, ktorý automaticky ukladal snímaný obraz každú sekundu. Počas procesu ťahania skúšobnej tyče sa vo vopred stanovenom okamihu na ťahovom diagrame urobila značka



Obr. 5. Teleso s U vrubom

a zároveň sa jej priradil daný obrázok. Získal sa tak sled obrázkov ako aj záznam ťahového diagramu každého telesa. Obrázky sa vyhodnocovali v programe Ellipse. Stanovovali sa geometrické ťažiská kontrastných bodov na obrázku nedeformovaného a deformovaného telesa, tieto hodnoty boli vstupom pre výpočet pozdĺžnej a priečnej deformácie programom VDTK. Pre jednotlivé deformácie platí výpočet podľa obr. 6.



Obr. 6. Grafické znázornenie výpočtu deformácií

Pre deformáciu v smere osi y (tzn. v smere zaťaženia) pre element 11 v čase t platí vzťah (2):

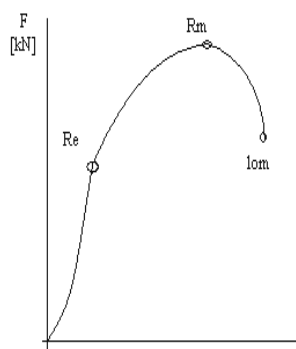
$$\varepsilon_{(Y,11,t)} = \frac{1}{2} \left[\left(\frac{Y_{(12p,t)} - Y_{(11p,t)}}{Y_{(12p,0)} - Y_{(11p,0)}} - 1 \right) + \left(\frac{Y_{(22p,t)} - Y_{(21p,t)}}{Y_{(22p,0)} - Y_{(21p,0)}} - 1 \right) \right] \cdot 100\% \quad (2)$$

Výsledkom programu VDTK sú deformačné mapy, tvorené súradnicami ťažisk bodov a súradnicou z, ktorá v jednotlivých farebných odtieňoch znázorňuje deformáciu.

3. Výsledky experimentov

Rozloženie deformácií

Na telesách s obojstranným vrubom typu U bolo vyhodnotené rozloženie deformácií na dvoch miestach ťahového diagramu: na medzi pevnosti a pred perforáciou (okamih tesne pred roztrhnutím skúšobného telesa). Pre každý stav sa zisťovali štatistické hodnoty ako: maximálna, minimálna a priemerná pre pozdĺžne a priečne deformácie. Výsledky hodnôt zahrňujú priemerné štatistické výsledky z niekoľkých

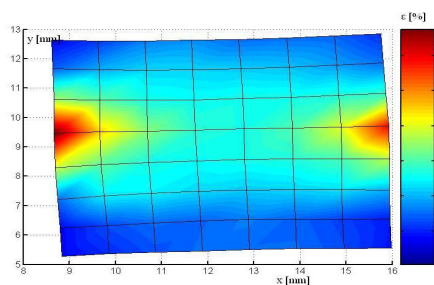


Obr. 7. **Okamihy** vyhodnocovania deformácií; R_m – medza pevnosti; tesne pred lomom

roztrhnutých telies. Číselné hodnoty pozdĺžnych deformácií sú vyhodnocované ako elementy v okolí bodu pre daný stĺpec a vzdialenosť od vrubu. Grafickým zobrazením deformácií a ich rozloženia v okolí vrubov sú deformačné mapy. Program neumožňuje farebne zjednotiť mapy a preto ten istý odtieň farby na jednej mape neznamená tú istú hodnotu deformácie na druhej mape.

Na obr. 7 sú vyznačené okamihy vyhodnocovania deformácií.

Tab. III uvádza podľa vzťahu (2) vypočítané hodnoty pozdĺžnych ε_y a priečných ε_x deformácií zo vstupných údajov, ktoré sme získali z posunutia ťažísk kontrastných bodov na telese s U vrubom. Na ploche medzi vrubmi boli nanosené kontrastné body v 9 radoch a 11 stĺpcoch, vyhodnocovalo sa 9 stĺpcov, obr. 5. Údaje sú z tesnej blízkosti vrubu z ľavej strany telesa, kde došlo skôr ku iniciácii trhliny.

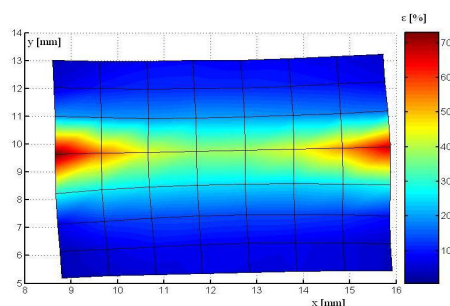


Obr. 8. Deformačná mapa telesa s U vrubom na R_m

Tabuľka III

Deformácie na telese s U vrubom

Teleso s U vrubom	R_m		lom	
	ε_x	ε_y	ε_x	ε_y
Max.	2,04	42,4	2,3	89,94
Mín.	-4,68	2,54	-6,3	2,62
Priemer	1,37	11,93	-	-



Obr. 9. Deformačná mapa telesa s U vrubom tesne pred lomom

Tabuľka IV

Veľkosť plastickej zóny pre teleso s U vrubom

U-vrub	r_{pl} [mm]	
	vypočítané	odmerané
R_m	2,88	3,05
lom	3,86	3,5

Rozloženie pozdĺžnej deformácie na telesách s U vrubom zobrazujú deformačné mapy na obr. 8 a 9.

Aplikáciou vzťahu (1) pre výpočet veľkosti plastickej zóny pre vruby typu U a stanovením polomeru plastickej zóny s využitím deformačných máp pre skúšaný materiál sme dospeli k výsledkom uvedeným v tab. IV. Pri určovaní plastickej zóny sme zmerali na deformačných mapách maximálnu deformáciu vykreslenú červenou farbou, pričom za plastickej zónu sme považovali 60 % z maximálnej deformácie.

4. Závěry

- Rozloženie deformácie u hladkých skúšobných telies na medzi pevnosti je homogénne. V práci boli sledované telesá s U vrubom, pričom nehomogenita rozloženia deformácií bola ovplyvnená vrubom, rozpätie hodnôt pozdĺžnych deformácií na R_m bolo od 2,54 do 42,4 %.
- Aplikáciou vzťahu pre výpočet veľkosti plastickej zóny pre vruby typu U a odmeraním plastickej zóny pre skúšaný materiál na medzi pevnosti sme dospeli k výsledkom, ktoré sa vzájomne odlišujú o 6,6 %. V prípade stavu tesne pred lomom sa výsledky líšia o 9,3 %.

Prezentované výsledky boli získané v rámci riešenia projektov VEGA 1/4149/07 a APVV 0326-07.

LITERATÚRA

1. Mihaliková M., Gazdag Š.: *Metalurgija* 47, 203 (2008).
2. Mihaliková M., Pešek J.: *Acta Metallurgica Slovaca* 13, 151 (2007).
3. Mihaliková M.: *Strojárstvo* 12, 66 (2006).
4. Kučera J.: *Úvod do mech. lomu*, VŠB, Ostrava 2006.
5. Marušiaková A., Pešek L., Gazdag Š.: *Acta Metallurgica Slovaca* 13, 438 (2007).

M. Mihaliková and Ľ. Ambriško (*Department of materials science, Faculty of metallurgy, Technical university of Košice, Slovakia*): **Size of the Plastic Zone Determined by Videoextensometric Method**

This work deals with determination of deformations distribution. The deep - drawing steels with notches was loaded by static uniaxial tension. By videoextensometric method was established the size of plastic zone near notches. The size of plastic zone was rated with calculation too. Results of both methods are identic.

FÁZOVÉ ZMĚNY SLITINY Zr-1Nb A JEJICH VLIV NA LOKÁLNÍ MECHANICKÉ VLASTNOSTI

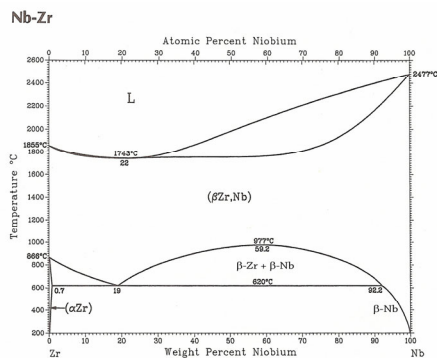
JAN ŘÍHA, OLGA BLÁHOVÁ a PAVOL ŠUTTA

Výzkumné centrum - Nové technologie, Západočeská univerzita v Plzni, Univerzitní 8, 306 14 Plzeň, Česká republika
janriha@ntc.zcu.cz

Klíčová slova: slitiny zirkonia, difrakční fázová analýza *in situ*, indentační tvrdost, fázové transformace

1. Úvod

Slitiny zirkonia jsou v jaderné energetice používány již více než 50 let. Je to především díky jejich vysoké korozní odolnosti ve vodě i mnoha dalších agresivních prostředích a velmi malému příčnému profilu záhytu tepelných neutronů. Jsou tedy ideálním materiálem pro výrobu ochranných povlaků palivových tyčí, vystavených extrémním podmínkám aktivní zóny jaderného reaktoru. Pro tyto účely je rozhodující minimální obsah hafnia, které se v zirkoniu běžně vyskytuje a má asi 600× vyšší příčný průřez pro záchyt tepelných neutronů. Vlivem přímého styku s chladicí vodou o cca 320 °C a tlaku 16 MPa dochází k tvorbě povrchové oxidické vrstvy, která ovšem výrazně zpomaluje rychlost další oxidace². V současné době je předmětem výzkumu chování slitin při haváriích typu LOCA (loss of coolant accident), při nichž vlivem úniku chladicího média dochází k prudkému ohřevu na přibližně 1000 °C, s následným velmi rychlým ochlazením. Ve struktuře materiálu pak dochází k výrazným změnám, vedoucím ke zhoršení mechanických vlastností – zejména snížení tažnosti a maximální síly do porušení. Tento příspěvek je zaměřen především na popis fázových transformací za vysokých teplot a jejich vliv na indentační tvrdost a modul pružnosti.



Obr. 1. Binární diagram soustavy Zr – Nb (převzato z citace⁴)

2. Experiment

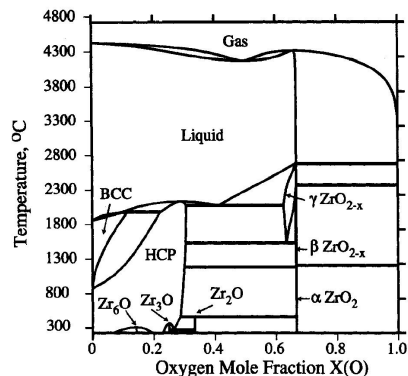
Jako experimentální materiál byla použita slitina zirkonia a niobu (obr. 1) s malým obsahem kyslíku (obr. 2). Chemické složení je uvedeno v tab. I.

Původním polotovarem byla tažená bezešvá trubka s vnějším průměrem 9 mm a tloušťkou stěny zhruba 0,7 mm. Pro sledování fázových transformací byla využita rentgenová difrakční analýza prováděná *in situ*. Měření probíhala na automatickém práškovém difraktometru Panalytical X'Pert PRO osazeném měděnou rentgenovou lampou ($\lambda_{\text{K}\alpha 1} = 0,15405980$ nm) a ultra-rychlým polovodičovým detektorem PIXcel s vysokou rozlišovací schopností.

Ohřev vzorku byl zajištěn vysokoteplotní komorou Anton Paar HTK 1200N s maximální pracovní teplotou 1200 °C. Komora je vybavena indukčním ohřevem zajišťujícím rovnoměrné prohřátí vzorků prakticky bez teplotních gradientů. Změna rozměrů vzorku vlivem teplotní roztažnosti je kompenzována speciálním držákem, který změnou výšky udržuje povrch vzorku stále v přesné poloze zajišťující splnění Braggova zákona:

$$n\lambda = 2d \cdot \sin \vartheta \quad (1)$$

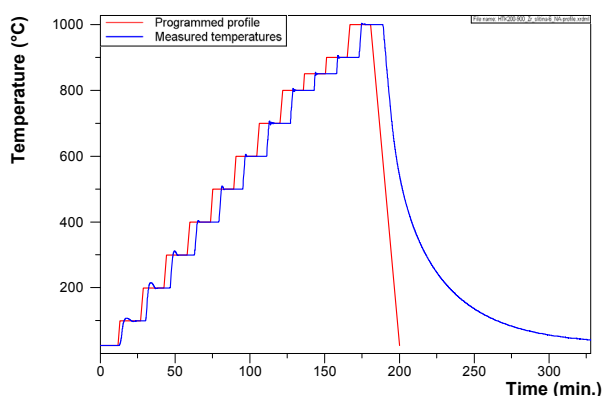
kde n je řád reflexe, λ je vlnová délka RTG záření, d je mezirovinná vzdálenost a ϑ je Braggův úhel. V opačném případě by došlo k posunu difrakčních linií, a tím ke zkreslení výsledků. Komora byla vakuována rotační olejovou vývěvou



Obr. 2. Binární diagram soustavy Zr – O (převzato z citace³)

Tabulka I
Chemické složení experimentálního materiálu

Nb	H	N	C	O	Zr
[hm. %]	[ppm]	[ppm]	[ppm]	[ppm]	
1,0 ± 1,1	3	20	100	840	zbytek



Obr. 3. Průběh ohřevu vzorku

Tabulka II

Hodnoty indentační tvrdosti a indentačního modulu pružnosti experimentálního materiálu

Stav vzorku	Tvrdost [GPa]	Modul pružnosti [GPa]
Výchozí stav – broušeno	5,70 ± 1,32	125,2 ± 20,6
Výchozí stav – leptáno	3,59 ± 0,96	96,0 ± 9,0
Po expozici – s vrstvou oxidu	10,51 ± 3,19	180,3 ± 38,0
Po expozici – odbroušený oxid	7,63 ± 1,43	131,0 ± 14,5

BOC Edwards RV3 vytvářející hraniční tlak přibližně 0,2 Pa. Difraktogramy byly snímány vždy v rozsahu $2\theta = 28 \div 72^\circ$. Ohřev vzorku probíhal stupňovitě od pokojové teploty až do 1000 °C. V intervalu 100 ÷ 800 °C probíhal ohřev vždy po 100 °C, po dosažení 800 °C byl jeden difraktogram změřen při 850 °C, vzhledem k přibližnému dosažení teploty fázové přeměny α -zirkonia (hexagonální, těsně uspořádaná mřížka) na β -zirkonium (kubická, prostorově centrovaná mřížka) při 862 °C. Další difraktogramy byly snímány při 900 a 1000 °C. Celý průběh ohřevu je uveden na obr. 3.

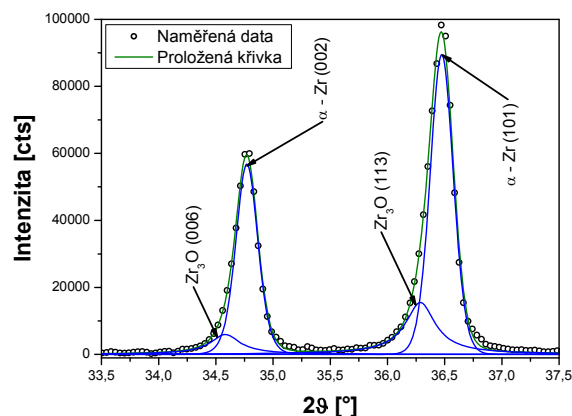
Pro potřeby měření byly původní trubičky kruhového průřezu podélně rozříznuty na polovinu a poté mechanicky slisovány do tvaru destičky. Plocha ozářená RTG zářením byla 10 × 10 mm. Vliv zdeformované struktury byl minimální, protože s rostoucí teplotou došlo k rekrystalizaci.

Měření probíhala také na přístroji AXS Bruker D8 Discover s kobaltovou rentgenovou lampou ($\lambda_{K\alpha 1} = 0,1789010$ nm) a plošným detektorem Hi-Star.

Indentační měření bylo provedeno na přístroji NanoIndenter XP Berkovičovým indentorem se zatížením 8 mN. Měření bylo provedeno vždy na několika místech po celé ploše povrchu vzorku a hodnoty byly poté zprůměrovány. Výsledky jsou uvedeny v tab. II.

3. Diskuse výsledků

Na difraktogramu měřeném při pokojové teplotě je patrné, že se ve slitině nevyskytovalo pouze α -zirkonium, ale

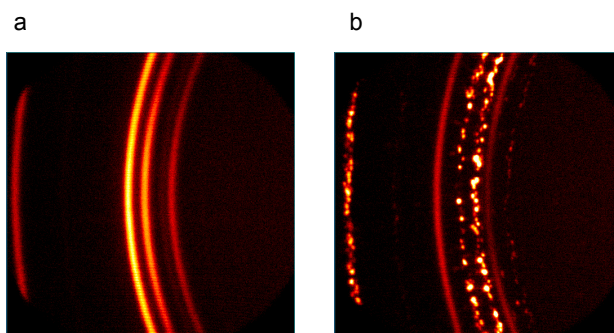


Obr. 4. Částečný difraktogram slitiny při 25 °C s proloženými liniemi jednotlivých fází

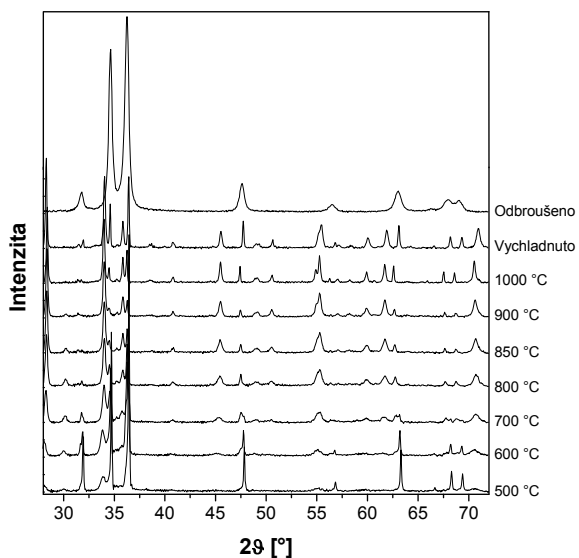
i fáze, která byla s odvoláním na práci³ identifikována jako oxid Zr_3O s trigonální krystalovou mřížkou. Přítomnost této fáze se projevila pouze mírnou nesymetrií linií čistého zirkonia (obr. 4). Během dalšího ohřevu zůstalo toto složení zachováno až do 400 °C, kdy se na pozici přibližně $2\theta = 33,93^\circ$ objevila linie odpovídající nejsilnější difrakční linii (444) oxinitridu zirkonia $ZrON$ s kubickou krystalovou mřížkou (obr. 8).

Při 500 °C je na pozici $2\theta = 30,02^\circ$ patrná nejsilnější linie (111) oxidu zirkonia ZrO_2 s ortorombickou krystalovou mřížkou (obr. 6, 7). Při dosažení teploty 600 °C již začíná docházet k fázové transformaci samotného zirkonia z fáze α (HCP) na fázi β (BCC), což také odpovídá binárnímu diagramu soustavy Zr – Nb (obr. 1). Je zde rovněž patrné, že fáze β -Zr zůstala v oxidické povrchové vrstvě zachována i při pokojové teplotě, což bude předmětem dalšího zkoumání.

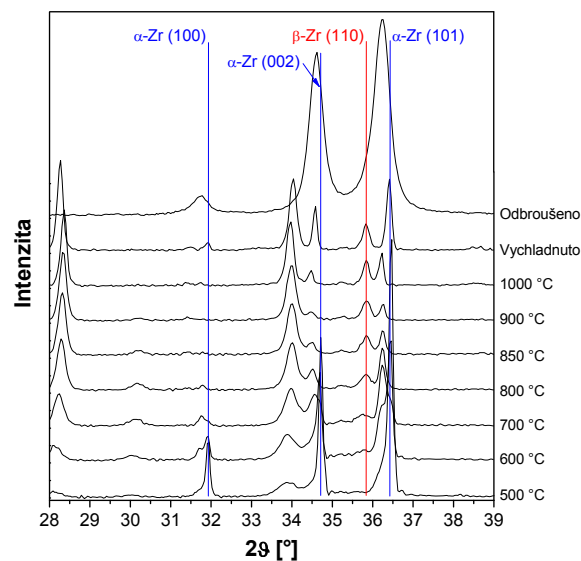
V difraktogramu snímaném při 500 °C je vidět, že v tomto stádiu dochází již k dosti výrazné oxidaci povrchu. Je zde patrné zvyšování množství oxidu Zr_3O a ZrO_2 s ortorombickou mřížkou, stejně jako oxinitridu zirkonia $ZrON$. Vzhledem k dosažené hodnotě vakua 0,2 Pa to může být způsobeno zbytkovým obsahem vzduchu, resp. kyslíku v komoře. Při atmosférickém tlaku je počet částic vzduchu na



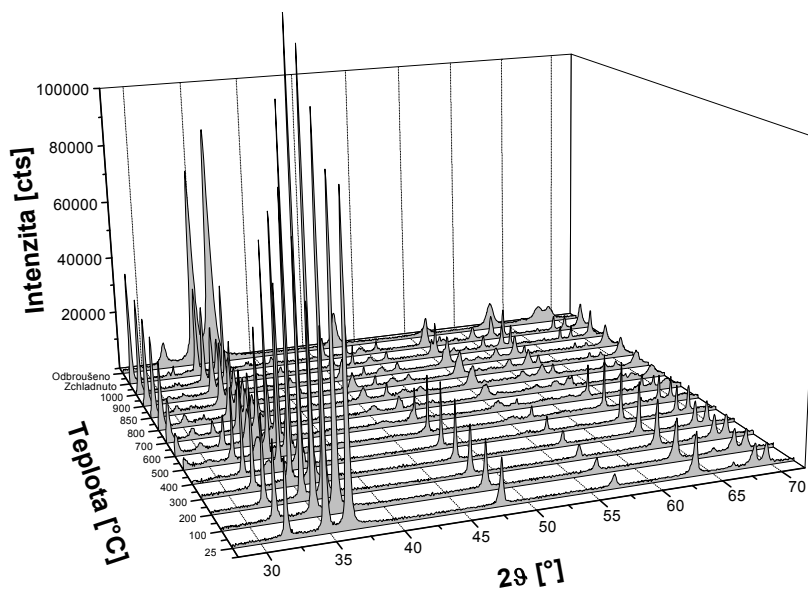
Obr. 5. 2D Difraktogram výchozího stavu (a) a stavu po expozici (b)



Obr. 6. Difraktogramy vzorku při vysokoteplotním ohřevu a po ochlazení



Obr. 7. Detail difraktogramů vzorku při vysokoteplotním ohřevu a po ochlazení



Obr. 8. Difraktogramy experimentálního vzorku

1 cm^3 přibližně $29 \cdot 10^{18}$, při námi dosaženém vakuu $0,2 \text{ Pa}$ je to asi $37 \cdot 10^{12}$, počet molekul kyslíku je tedy zhruba $7 \cdot 10^{12}$.

Z měření provedených na přístroji Bruker je patrné výrazné zhrubnutí materiálu během expozice. Vzorek ve výchozím stavu je takřka ideálně jemnozrný, s hladkými, spojitými liniemi (obr. 5a). Po expozici jsou vlivem zhrubnutí tyto linie tvořeny pouze body, představujícími koherentně difraktující oblasti. Spojité linie patří oxidům (obr. 5b).

Z výsledků měření indentační tvrdosti a modulu pružnosti je patrný nárůst hodnot obou veličin po vysokoteplotní expozici, viz tab. II. Při dřívějších experimentech prováděných ve spolupráci ÚJP Praha s Výzkumným centrem – Nové technologie bylo prokázáno, že je tento nárůst způsoben difúzí kyslíku do povrchových vrstev slitiny, kdy potom přímo na povrchu vzniká tenká oxidická vrstva. Kyslík zároveň proniká hlouběji do materiálu slitiny, kde se usazuje v intersticiálních

polohách krystalové mřížky^{6,7}. Toto bylo potvrzeno i nyní, kdy je patrný pokles tvrdosti i modulu pružnosti po odbroušení povrchové vrstvy oxidů (tab. II). Zároveň je také vidět rozdíl hodnot tvrdosti a modulu pružnosti u vzorku ve výchozím stavu s povrchem broušeným a odleptaným. Je to způsobeno vnesením plastické deformace do povrchové vrstvy během broušení.

4. Závěr

Mechanické vlastnosti slitin zirkonia jsou rozhodující měrou ovlivněny množstvím kyslíku ve struktuře. Se zvyšováním obsahu kyslíku při vysokoteplotní expozici dochází k markantnímu nárůstu tvrdosti a modulu pružnosti. Zároveň se ovšem výrazně snižuje tažnost a houževnatost slitin. Difrakční fázovou analýzou *in situ* byl sledován jednak vznik povrchové vrstvy oxidů, ale také fázové transformace zirkonia při vysokých teplotách. Z výsledků je patrné, že při teplotách do zhruba 400 °C k výrazné oxidaci nedošlo. Od 500 °C již byla materiálu dodána dostatečná aktivační energie ke vzniku oxidů a oxo-nitridu zirkonia. Od 600 °C je patrný počátek přeměny α -fáze zirkonia na fázi β , která je ukončena přibližně při 850 °C, což dosti přesně odpovídá binárnímu fázovému diagramu soustavy Zr – Nb. Při dalších experimentech zaměřených na studium těchto fázových přeměn bude nutné zapojit do vakuové soustavy vymrazovačku, popřípadě použít výkonnější typ vývěvy. Vymrazovačka jednak zhruba o jeden řád zlepší současné vakuum 0,2 Pa, ale také zamezí zpětnému pronikání uhlíkových par z vývěvy do vysokoteplotní komory. Provedené experimenty zároveň ukázaly, že RTG difrakce *in situ* je velice účinná metoda sledování fázových transformací, která může být využita i pro tvorbu pseudo-fázových diagramů.

Práce byla podpořena výzkumným projektem MPO ČR 2A – ITP1/037.

LITERATURA

1. Bláhová, O., Šutta, P., Říha, J., Šugár, M., Medlín, R., Savková, J.: Zvýšení bezpečnosti jaderných elektráren při haváriích typu LOCA, Výzkumná zpráva NTC ZČU, Plzeň, 2008.
2. Koutský, J., Kočík, J.: *Radiation Damage of Structural Materials*. Academia, Praha 1994.
3. Arroyave, R., Kaufman, L., Eagar, T. W.: *Thermodynamic Modeling of the Zr-O System*, Calphad, Vol. 26, sv. 1, s. 95–118, March 2002.
4. Baker H. (ed.): *ASM Handbook*, vol. 3, Alloy Phase Diagrams, ASM International, Materials Park, Ohio 1992.
5. Říha J., Vincze A., Šutta P.: *Proceedings of the 14th International Conference on Applied Physics of Condensed Matter* (s. 195–198), Liptovský Ján, 2008.
6. Vrtílková V., Novotný L.: Vliv rozpouštění oxidu vytvořeného na povlakové trubce ze Zr-slitin na termomechanické vlastnosti trubky po vysokoteplotních přechodech, Výzkumná zpráva UJP Praha 1164, 2005.
7. Vrtílková V., Novotný L.: Vliv rozpouštění oxidu vytvořeného na povlakové trubce ze Zr-slitin na termomechanické vlastnosti trubky po vysokoteplotních přechodech, Výzkumná zpráva UJP Praha 1165, 2006.
8. Kaddour D., Frechinet S., Gourgues A. F., Brachet J. C., Portier L., Pineau A.: *Scr. Mater.* 51, 515 (2004).

J. Říha, O. Bláhová, and P. Šutta (*New technologies – research centre, University of West Bohemia, Plzeň, Czech Republic*): **Phase Transformations of Zr-1Nb Alloy and Its Influence on Local Mechanical Properties**

Zirconium alloys are very important materials used in nuclear water reactors. Due to their high corrosion resistance and low capture cross section of thermal neutrons are these alloys ideal for production of protective layers of the nuclear fuel rods. This work deals with zirconium phase transformations at high temperatures and their influence on indentation hardness and modulus of elasticity of Zr-Nb alloy. For phase transformations observation *in situ* XRD analysis was used. The measurements were carried out with the aid of high-temperature chamber, in which 0.2 Pa vacuum was created. The sample was gradually heated up to 1000 °C.

SCRATCH RESISTANCE OF TiAlSiN COATINGS

JARMILA SAVKOVÁ
and **OLGA BLÁHOVÁ**

Department of Material Science and Technology, University of West Bohemia, Universitní 8, 306 14 Plzeň, Czech Republic
savkova@kmm.zcu.cz

Key words: scratch test, TiAlSiN coating

1. Introduction

Scratch test is one of the most used methods for adhesion testing of thin coatings. In common devices a diamond indenter is pulled along the substrate surface, while the normal force on the indenter is steadily increased (Fig. 1) and the lateral force is measured. At the so called critical load (L_{C1} , L_{C2} , ..., L_{CN}) the indenter breaks through the coating into the substrate material^{1,2}. At this point the lateral force is increased and acoustic emission is observed which both can be recorded. Many different failures are observed which include coating detachment, through-thickness cracking and plastic deformation or cracking in the coating or substrate. In fact it is usual that several different failure modes occur at the same time and this can make the results of the test difficult to interpret. The failure modes observed in the scratch test depend on many factors and are most easily characterised in terms of the hardness of both substrate and coating. The failure events are detected by examination of the scratch track after scratching using an optical microscope¹⁻³.

With this critical load the scratch test is nearly the only method that delivers a numeric value for the adhesion of hard PVD coatings²⁻⁵.

The normal load during the test is either kept constant or progressively increased. Progressively increasing scratch load eventually induces a critical point of damage such as coating delamination, coating cracking (in the case of brittle coatings) or whitening (in the case of polymeric coatings) in a single

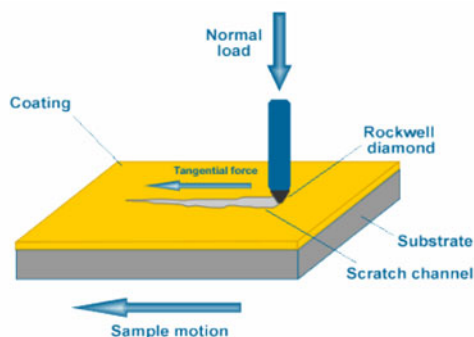


Fig. 1. Scratch test principle¹

test. In the constant-load test, multiple tests at increased constant-load levels are needed in order to determine the critical scratch load. In any case, the critical load itself or its derivative (e.g. scratch hardness, defined as the load divided by indented area) is used to compare the performance of different coatings. A number of ASTM and ISO standards are available for the scratch test of coatings. ASTM C 1624 describes a standard test method for hard (Vickers hardness $HV \geq 5$ GPa) ceramic coatings, while ASTM D 7027 is for the evaluation of polymeric coatings and plastics. Nano-scratch of soft coatings is described by ASTM D EN 1071 standard includes a comprehensive atlas of scratch test failure modes^{1,6}.

Three different scratching procedures are described in the standard EN 1071-3:

A. Progressive load scratch test – recommended operating parameters are 100 N min^{-1} (loading rate) and 10 mm min^{-1} (lateral displacement speed).

B. Constant load scratch test – recommended operating parameters are 10 mm min^{-1} (lateral speed) and 10 mm scratch length. Normal load increases in increments between successive scratches carried out under constant load at different locations on the sample surface. It is also recommended that one fifth of the critical load (determined by progressive load mode) will be used for the indenter load step size between consecutive tests.

C. Multipass scratch test – standard-operating parameters are the same as in B and it is recommended to use 50 % of critical load determined by progressive load mode. In this test the number of scratches until failure is determined⁶.

2. Experimental procedure

Coatings were produced by a multi-source PVD system, using cathodic arc-evaporation, in an industrial vacuum chamber. Cathodes were made from pure Ti and Al/Si. The TiAlSiN layers with same overall thickness of $2,5 \mu\text{m}$ were deposited on substrates of tool steel from Böhler-Uddeholm, VANADIS 4 – V (C 1.4 %, Cr 4.7 %, Mo 3.5 %, V 3.7 %, Si 0.4 %) and Sverker 21 – S (C 1.55 %, Cr 11.8 %, Mo 0.8 %, V 0.8 %, Si 0.3 %, Mn 0.4 %). Steel samples ($\varnothing 40 \times 5 \text{ mm}$) were hardened and annealed at $550 \text{ }^\circ\text{C}$, ground

Table I
Deposition parameters

Coating	Al/Si [V]	Ti [V]	Bias [V]	Pressure [mbar]
1	120	50	20	0.05
2	50	120	80	0.05
3	120	120	80	0.05
4	nACo® LISS a.s. Rožnov p. Radhoštěm			

and polished to mirror-like state (roughness $< 0.02 \mu\text{m}$). Steel surface was cleaned by ion bombard just before deposition. TiN interlayer with a thickness of about $0.1 \mu\text{m}$ were deposited between the substrate and film. The deposition parameters are listed in Tab. I.

A Hommel tester T1000 waveline profilometer with diamond stylus was used for determination of roughness after deposition. A standard Rockwell hardness tester was used for evaluation of adhesion between coating and substrate. Standard test parameters were used – Rockwell C type diamond cone indenter with an applied load of 1500 N.

Scratch testing was carried out using the Scratch tester CSEM Revetest. ASTM D EN 1071 method A (progressive load scratch test) was used with a Rockwell C diamond indenter with radius of $200 \mu\text{m}$. The load increased from 0 to 80 N at a specified loading rate. Generally a loading rate of 10 N mm^{-1} was used for the scratch tests. Load can be measured at any place, as we know the loading rate and the length of the track. The friction force was measured and a piezoelectric accelerometer detects the acoustic emission produced as the coating is damaged. The value of the critical load is then determined using these traces in conjunction with an optical microscope. All scratches were carried out at least two times and in the same direction. Critical loads according ASTM standard, L_{C1} (first lateral cracking), L_{C2} (first severe cracking and delamination at track border), L_{C3} (first delamination within the scratch track) and L_S (total delamination) were determined.

3. Results and discussion

Surface after deposition was characterized by three roughness parameters: R_a – roughness average, R_t – maximum height of the profile and R_z – average distance between highest peak and lowest valley, Tab. II.

Coatings were observed by optical microscope to characterize quality of coatings surface, Fig. 2.

The adhesion from Rockwell hardness indentation test is analysed with optical microscope and classified with A

Table II
Roughness parameters

Coating	Steel ^a	R_a [μm]	R_t [μm]	R_z [μm]
1	S	0.06 ± 0.01	2.37 ± 0.27	1.29 ± 0.11
	V	0.07 ± 0.01	2.53 ± 0.65	1.48 ± 0.30
2	S	0.09 ± 0.01	3.16 ± 0.35	2.10 ± 0.28
	V	0.09 ± 0.01	2.98 ± 0.68	2.18 ± 0.45
3	S	0.10 ± 0.01	3.76 ± 0.41	2.23 ± 0.34
	V	0.07 ± 0.01	3.04 ± 0.62	1.78 ± 0.39
4	S	0.10 ± 0.01	2.89 ± 0.41	1.76 ± 0.24
	V	0.10 ± 0.01	2.59 ± 0.32	1.75 ± 0.23

^a S – Sverker 21, V – Vanadis 4

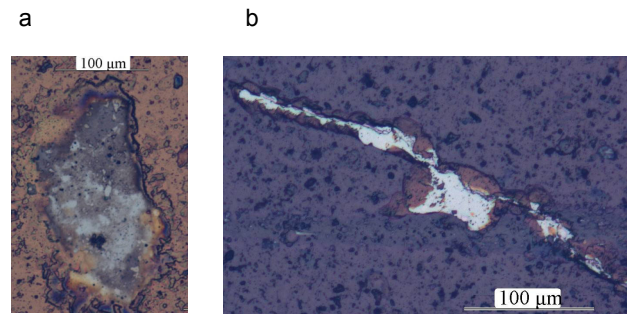


Fig. 2. Surface defects on coating 2 (a) and 4 (b)

(adhesive failure) and K (cohesive failure) number according to the level of cracking or coating delamination around the indent, Fig. 3 (ref.⁷). Only indents classified as A/K 1-2 correspond to acceptable adhesion.

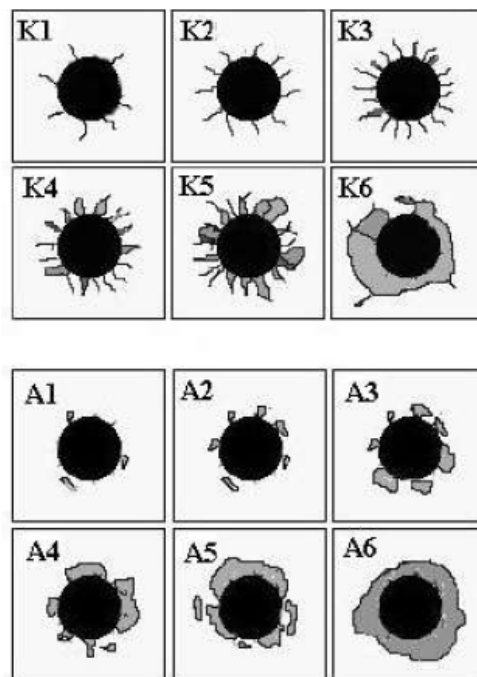


Fig. 3. Comparison chart – grades of failure mechanism⁷

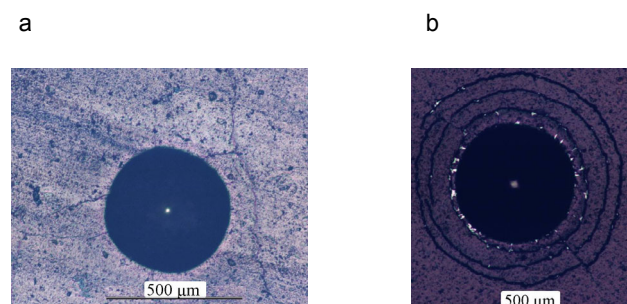


Fig. 4. Coating 3 (a) and 4 (b) after Rockwell test

Coatings adhesion was classified: 1 – A1/K1, 2 – A0/K1, 3 – A0/K2, 4 – A2/K2, Fig. 4.

The four coating types, all deposited onto hard metal substrates and of thickness 2.5 μm , were tested using the Revetest with progressive loading from 0 to 80 N. The load rate was set at 10 N mm^{-1} and the table speed at 10 mm min^{-1} . Two scratches in the same direction were made on every sample and critical loads were determined from each scratch, without calculating the mean value, Tab. III. Optical microscope with image analysis (NIKON NEOPHOT 200 with LUCIA 4.81) was used to investigate the critical points along each scratch and thus determine the critical loads at which first failure (partial delamination) and total failure of the coating occurs (L_S).

Table III
Critical loads

Coating	Steel ^a	L_{C1} [N]	L_{C2} [N]	L_{C3} [N]	L_S [N]
1	S	19.5	20.8	53.4	–
		21.4	31.7	51	–
	V	27	46	60	–
		30	50	63	–
2	S	19.7	26.9	50.4	–
		18.5	23.2	63.8	–
	V	43.2	47.4	61.6	–
		40.7	47.3	68.6	–
3	S	8.8	8.8	35.3	–
		10.1	10.7	41.8	–
	V	17.3	21	48.7	–
		17.9	20.4	27.3	–
4	S	10.5	19	31	70.6
		11.6	17.2	30.8	69.6
	V	7.6	12	35.8	64
		9	21	36.7	57.1

^a S – Sverker 21, V – Vanadis 4

Coating 1: an adhesive failure occurs at load lower than 10 N for all 4 tests due to the surface defects, Fig. 5. This failure wasn't used for determining critical loads. Fewer defects were observed for coating on Vanadis 4 steel. Tensile Hertzian crack within the scratch track is the main failure type from load 20 N, Fig. 6.

Interfacial spallation at the track border occurs about load 30 N. Discontinuous ductile perforation of the coating was when load reached 65 N, Fig. 7.

Coating 2: cracking on steel Sverker 21 starts by tensile Hertzian failure mode at load cca 20 N. Few failures occur at beginning of scratch track on steel Sverker 21 because of surface defects. Coating on steel Vanadis 4 was without failures before 20 N. After increasing load up to 25 N (S) and 40 N (V) deformation rises and first adhesive failure occurs

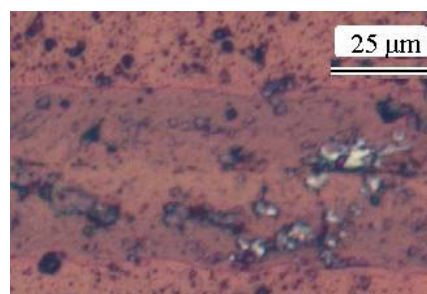


Fig. 5. Coating 1, steel Sverker 21, load 10 N

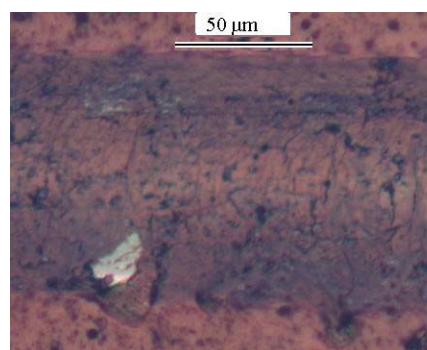


Fig. 6. Coating 1, steel Sverker 21, load 20 N

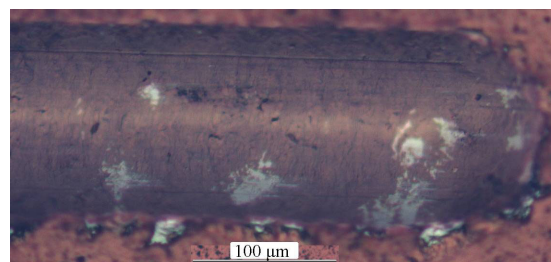
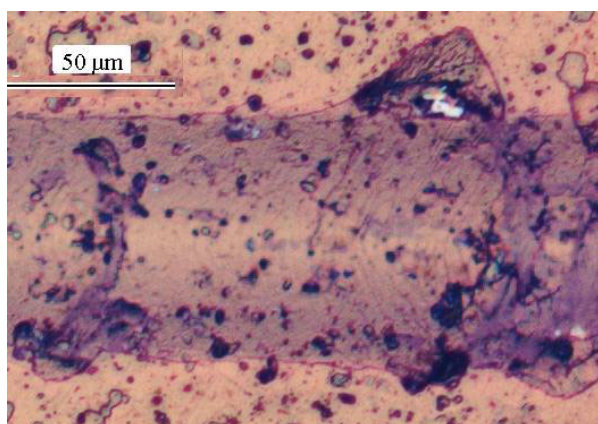
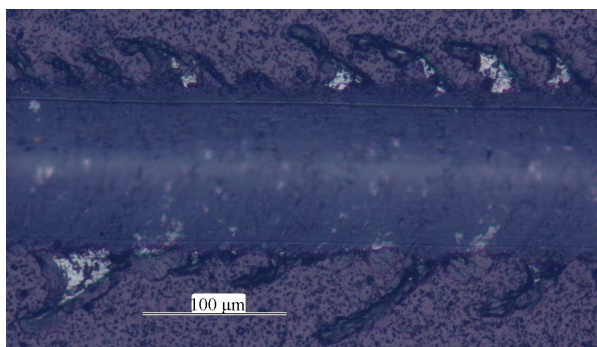
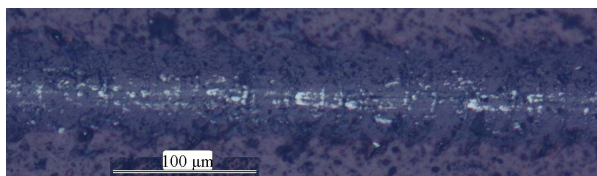
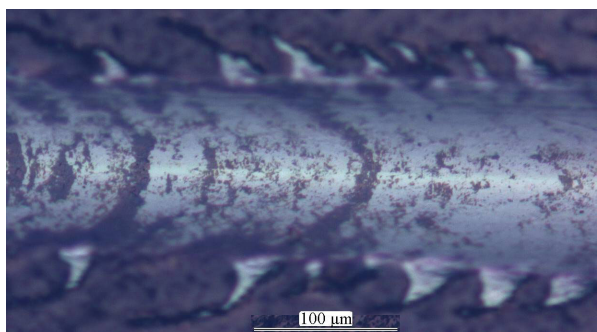


Fig. 7. Coating 1, steel Sverker 21, load 80 N

by spallation along the scratch track borders – cohesive and interfacial, Fig. 8. Coating on Vanadis 4 has very few discontinuous ductile perforations at load 80 N.

Coating 3: very similar failure on both substrates. First failures both adhesive and cohesive occur at relatively low load, 8 N for Sverker 21 and 17 N for Vanadis 4. Coatings were practically without perforation within scratch track, Fig. 9.

Coating 4: similar failure as for coating 3 with larger adhesive failure along scratch border, Fig. 11. Load 60 N caused complete uncovering of the substrate. Critical loads for Sverker 21 are lower than that for Vanadis 4. Discontinuous ductile perforation starts from L_{C1} for all four scratches, Fig. 10. Cracks are with long area interfacial spallation.

Fig. 8. **Coating 2**, steel Sverker 21, load 25 NFig. 9. **Coating 3**, steel Vanadis 4, load 58 NFig. 10. **Coating 4**, steel Vanadis 4, load 10 NFig. 11. **Coating 4**, steel Vanadis 4, load 60 N

4. Conclusions

The coatings on Vanadis 4 steel have generally better adhesion than coatings deposited on Sverker 21. For coatings on Sverker 21 first failure occurs at load 10 N (coatings 3 and 4) or 20 N (coatings 1 and 2).

Lowest adhesion and lowest critical loads were observed for coating with highest surface roughness – coating 4 on both steels and coating 3 on Sverker 21.

For coating 4 (both steels) loads higher than 50 N caused complete delamination.

Failure at beginning occurs for all scratches because of higher roughness and surface defects, Fig. 2b. This failures wasn't used for determination of critical loads.

Best adhesions have coatings 1 and 2, first uncovering of substrate occurs at load higher than 50 N.

This work was supported by Kontakt-AIP No. MEB 080869.

REFERENCES

1. www.csm-instruments.com. downloaded 28th October 2008.
2. Chen Z., Wu L. Y. L., Chwa E., Tham O.: Mater. Sci. Eng., A 493, 292 (2008).
3. <http://www.irg-woem.org/pdfs/13.pdf>. downloaded 28th October 2008.
4. Hoy R., Kamminga J. D., Janssen G. C. A. M.: Surf. Coat. Technol. 200, 3856 (2006).
5. Beegan D., Chowdhury S., Laugier M. T.: Surf. Coat. Technol. 20, 5804 (2007).
6. EN 1071-3: Advanced technical ceramics – Method of test ceramic coatings – Part 3: Determination of adhesion and other mechanic failures modes by a scratch test.
7. www.ateam.cz. downloaded 28th October 2008.

J. Savková and O. Bláhová (*Department of Material Science and Technology, University of West Bohemia, Plzeň, Czech Republic*): **Scratch Resistance of TiAlSiN Coatings**

Hard coatings are applied to the surfaces of mechanical components subjected to wear in order to increase their durability and performance. One main application is hard coatings for cutting tools such as drills, end mills and indexable cutting inserts. Superhard nanocomposite coatings comprise two or more phases that are either a nanostructured phase embedded in another amorphous phase, such as nanocrystalline (nc-) TiN and amorphous (a-)Si₃N₄ (nc-TiN/a-Si₃N₄), or two nanocrystalline phases such as nc-TiN/BN. One of the most important characterizations of coating-substrate system is adhesion. Scratch test is one of the most used methods for adhesion testing. In our paper adhesive properties of four TiAlSiN coatings were characterized, one commercially used and three “laboratory” coatings.

INDENTATION LOAD/SIZE EFFECT OF STRUCTURAL CERAMIC MATERIALS

**JANA ŠPAKOVÁ, FRANTIŠKA
DORČÁKOVÁ, and JÁN DUSZA**

*Institute of Materials Research SAS, Watsonova 47, 040 01
Košice, Slovakia
jsparkova@imr.saske.sk, fdorcakova@imr.saske.sk,
jdusza@imr.saske.sk*

1. Introduction

Indentation tests like hardness measurement are perhaps the most commonly applied methods for measuring the mechanical properties of materials. The utility of hardness is further enhanced by the fact that it is obtained by a simple test that can be rapidly performed using small samples at moderate cost. However, this utility is partly compromised by the often complex and variable dependence of hardness on several factors such as surface finish, microstructure, indenter load and configuration. Hardness is conventionally determined by applying a load to a material via a geometrically defined indenter, and defined as the ratio of the applied load “P” to the contact area, “A”, of the resultant indent

$$H = \frac{P}{A} = \beta \frac{P}{d^2} \quad (1)$$

where “d” is the characteristic size of resultant indent and “β” is a constant which depends only on the indenter geometry. Two major indenter geometries, Vickers and Knoop, are widely used for hardness testing of structural ceramics. In general, the Vickers hardness “HV” is calculated using the contact area of the indent and the parameter “d” in Eq. (1) is defined as the average of the two diagonals of the square – shaped indent which results in a β-value of 1.8544. In the case of Knoop hardness, the parameter “d” is defined as the length of the long diagonal of the resultant rhombic impression and “β” has a value of 14.229. Moreover investigations have confirmed that the apparent hardness of a given ceramic material is a function of the applied test load, and the measured hardness increases with decreasing test load. To explain this so called “indentation load/size effect – ISE” intensive research has been performed during the last decade and several theories have been occurred for explanation of this. The most common explanation concerns the experimental errors resulting from the limitations of the resolution of the objective lens and the sensitivity of the load cells^{1–3}. According to Bückle² the ISE is directly related to the intrinsic structural factors of the test materials, including indentation elastic recovery, work hardening during indentation, surface dislocation pinning, etc.^{4–6}. It was found that dislocation and twin activities may results in ISE in alumina ceramics with different grain size, too. Another explanation of ISE is the formation of cracks⁷, small ratios of grain size to the indentation size⁸. Conse-

quently, several empirical or semi-empirical equations, including the Mayer’s law^{5,9}, the Hays-Kendall approach¹⁰, the elastic recovery model⁴, the energy-balance approach¹¹, the proportional specimen resistance (PSR) model¹², etc. were proposed for describing the variation of the indentation size with the applied test indentation load. Except of the Mayer’s law, all other approaches involve the determination of a so-called true-hardness, i.e., a load-independent hardness number. It should be mentioned that Hays-Kendall approach frequently gives unrealistic values of load necessary to induce plastic deformation¹², energy-balance approach is essentially a modified form of the empirical Mayer’s law, while the elastic recovery model applies only to plastic materials where slip bands with a particular spacing d_0 between them are produced by indentation. Therefore Hays-Kendall approach and elastic recovery model are not considered here. The most widely used empirical equation for describing the ISE is the Mayer’s law, which gives an expression relating load and size of indentation,

$$P = A \cdot d^n \quad (2)$$

where the exponent “n”, i.e. Mayer’s index, is a measure of the ISE, and “A” is a constant. Parameters “n” and “A” can be derived directly from the curve fitting of the experimental data. When $n < 2$ there is ISE behaviour and when $n = 2$, the hardness is independent of applied load. On the other hand, ISE behaviour may be described by the PSR model¹². In this model, the test – specimen resistance to permanent deformation is assumed not to be a constant, but to increase linearly, and is the directly proportional.

$$W = a_1 d \quad (3)$$

To a first approximation, the form of Eq. (3) can be considered to be similar to the elastic resistance of a spring with the opposite sign to the applied test load. Then, the effective indentation load and the indentation dimension can be related as:

$$P_{\text{eff}} = P_{\text{max}} - W = P_{\text{max}} - a_1 d = a_2 d^2 \quad (4)$$

Eq. (4) means that the proportional specimen resistance (PSR) described by the “ a_1 ”-value and the second coefficient “ a_2 ” can be readily evaluated through the linear regression of “P/d” versus “d”. Thus the applicability of the PSR model to describe the observed ISE in a relatively wider range of applied test load can be examined by testing the linearity between “P/d” and “d”. Eq. (4) can be rearranged as:

$$\frac{P}{d} = a_1 + a_2 \cdot d \quad (5)$$

which enables us to calculate “ a_1 ” and “ a_2 ” from the plots of “ P/d ” against “ d ”. According to the Li and Bradt¹², the parameters “ a_1 ” and “ a_2 ” can be related to the elastic and the plastic properties of the test material, respectively. Especially, a_2 was suggested to be a measure of the so-called true hardness, i.e., load-independent hardness “ H_0 ” ($H_{0(V)}$ -true Vickers hardness, $H_{0(K)}$ -true Knoop hardness)

$$H_{0(V)} = 1,8544 \cdot a_2 \quad H_{0(K)} = 14,229 \cdot a_2 \quad (6)$$

There have been several studies^{13,14} concerning the applicability of the PSR model to describing the ISE of brittle materials.

2. Experimental materials and methods

Three monolithic Al_2O_3 , Si_3N_4 , Si_3N_4 -SiC nanocomposites and ceramic-metal composite WC-Co have been investigated. The monolithic Si_3N_4 was pressure sintered with addition of 3 wt.% Y_2O_3 and 3 wt.% Al_2O_3 by CeramTech (Plochingen, Germany). This monolithic Si_3N_4 is a reference material for European research program ESIS (European Structural Integrity Society) for evaluation of mechanical and physical properties. Pure Al_2O_3 was cold isostatic pressed at 150 MPa and sintered at 1600 °C for 1 h in Faensa (Italy). Si_3N_4 -SiC nanocomposite was prepared by carbothermal reduction from the starting mixture 83.12 wt.% Si_3N_4 , 4.43 wt.% Y_2O_3 , 7.39 wt.% SiO, 4.05 wt.% C in Bratislava (Slovakia). The samples were hot-pressed under a specific heating regime, atmosphere and mechanical pressure at 1750 °C for 2 h. The WC-Co specimens were prepared using standard preparation technique in Šumperk (Czech Republic).

The surface of specimens was ground and polished to 1 μm finish before the mechanical tests. Macrohardness has been measured in a wide range of applied loads from 50 N to 200 N using the testing device HPO 250 for both Vickers and Knoop indenter geometries, and dwell time of 10 seconds. The average values for macrohardness were calculated from 10 measurements. For measuring microhardness by Vickers indenter in load range from 2 N to 10 N a microhardness tester LECO LM 700AT was used. For estimating microhardness by Knoop indenter in the same load range a Zwick/materialprüfung grün Systemtechnik Wetzlar was used and dwell time of 10 seconds. The average values for microhardness were calculated from 20 measurements.

3. Results and discussion

The present data and Mayer’s law

Table I summarizes the Mayer’s law parameters determined by the regression analyses of the results shown in Fig. 1.

The analysis of results listed in Tab. I indicates that, among all test materials, the most significant ISE for Vickers microhardness was observed in Si_3N_4 -SiC nanocomposite ($n = 1.897$) while the ISE in WC-Co (1.922) is negligible. In the case of Knoop microhardness the most significant ISE was observed for Al_2O_3 ($n = 1.746$) while the ISE in Si_3N_4

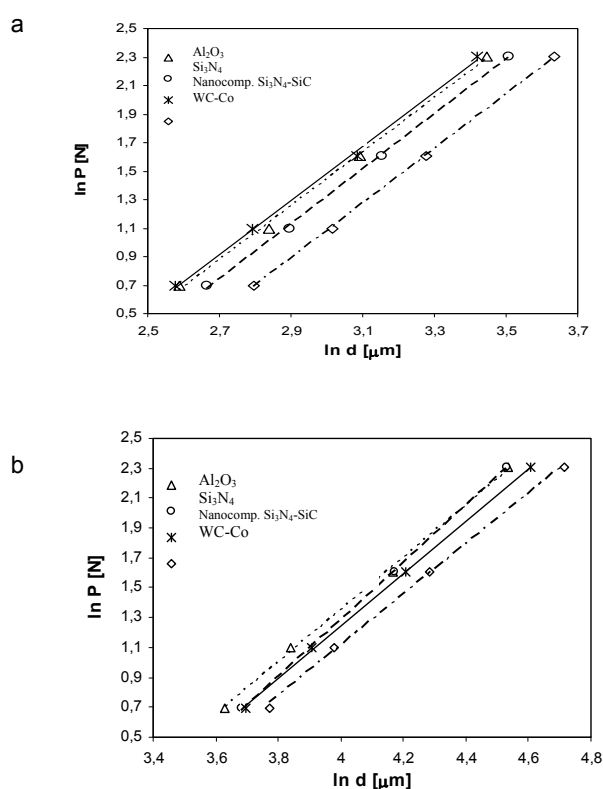


Fig. 1. Dependency of $\ln P$ on $\ln d$ according to the Mayer’s law for tested materials from a) Vickers hardness b) Knoop hardness

Table I

Regression analysis results of the experimental data according to Mayer’s law for Vickers hardness (a) and Knoop hardness (b)

a) Vickers hardness			
Material	n	A	R ²
Si_3N_4	1.922	4.45	0.9994
nanocomp. Si_3N_4 -SiC	1.897	4.21	0.9985
Al_2O_3	1.898	4.25	0.9983
WC-Co	1.922	4.69	0.9999
b) Knoop hardness			
Material	n	A	R ²
Si_3N_4	1.908	6.35	0.9995
nanocomp. Si_3N_4 -SiC	1.749	5.76	0.9996
Al_2O_3	1.746	5.63	0.9986
WC-Co	1.761	5.92	0.9271

($n = 1.908$) is negligible.

It can be seen that the ISE for the Knoop microhardness may be slightly greater than the ISE for the Vickers indentation microhardness. Due to the nature of intrinsic brittleness, Vickers indentation may result in microfracture around the

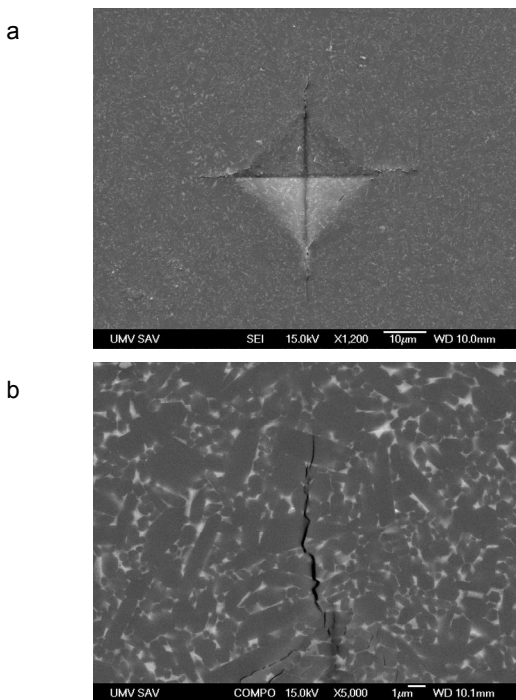


Fig. 2. Formation of indentation radial cracks in Si_3N_4 at 10 N by Vickers indenter (a) detail of indentation radial crack

impression in the surface and/or subsurface of ceramics when the load is high enough¹⁵. Since microfracture occurs mainly during the loading, a portion of energy, which is used to create the indentation deformation will be dissipated by the crack formation shown in Fig. 2.

Thus, one can expect that, for a given material, the hardness value measured with a cracking indentation will be higher than that measured with a crack-free indentation at the same load¹⁶. It seems to be impossible to avoid the effect of microstructure on the hardness measurements in low-load range, in which the ISE is significant, for microcracking can occur in most ceramics even at loads lower than 50 N. On the other hand, when tested below such a low load, the experimental errors related to the small size of the indentation will be significant, sometimes making it impossible to conduct repeatable measurements.

Sargent and Page¹⁷ considered several “n value versus ln A” relationships in an attempt to ascertain any possible microstructural effects on those power law parameters. The knowledge of the correlation between “n” and “A” seems to be of little significance for understanding the ISE, because Gong et al.¹⁸ found that the best-fit value of the Mayer’s law coefficient depends on the units system used for recording the experimental data and completely different trends of “n” versus “A” may be observed in different units systems. Previous studies^{19,20} also tried to relate Mayer’s index “n” to the microstructural features. However, knowledge of the generality of the correlation between “n” and grain size is still lacking. In fact, previous studies^{16,21} have pointed out that as pure empirical equation, Mayer’s law cannot provide any knowledge of the origin of ISE.

Proportional specimen resistance “PSR” model

Fig. 3 shows the P/d curves for the tested materials (a—from HV, b—from HK). The best-fit values of the parameters included in Fig. 3 for each material are listed in Tab. II.

Table II

The best-fit results of the PSR model parameters for Vickers hardness (a) and Knoop hardness (b)

a) Vickers hardness				
Material	a_1	a_2	HV ₀ [GPa]	R ²
Si_3N_4	0.0136	0.0086	15.95	0.9986
nanocomp. Si_3N_4 -SiC	0.0182	0.01	18.54	0.9942
Al_2O_3	0.0177	0.0096	17.80	0.9965
WC - Co	0.013	0.0066	12.24	0.9999
b) Knoop hardness				
Material	a_1	a_2	HK ₀ [GPa]	R ²
Si_3N_4	0.0062	0.0011	15.65	0.9991
nanocomp. Si_3N_4 -SiC	0.0186	0.0008	11.38	0.9969
Al_2O_3	0.0187	0.0009	12.81	0.9965
WC - Co	0.0218	0.0006	8.54	0.9823

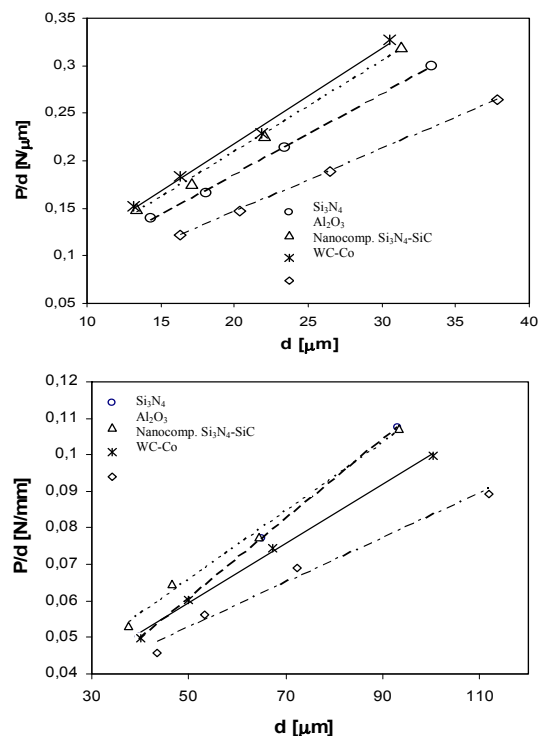


Fig. 3. Dependency of P/d on d according to the PSR model for tested materials from a) Vickers hardness b) Knoop hardness

Dependency of “P/d” on “d” of WC-Co from Knoop hardness reveals nonlinearity. Different behaviour of WC-Co can be explained by the presence of ductile binder phase Co and the significantly lower elastic recovery. The applicability of the PSR model in analyzing the ISE, true hardness was calculated for each material. The results are given in Tab. II, too. As can be seen from Tab. II, it can be concluded, that PSR model may provide a satisfactory explanation for the origin of ISE in microhardness test for various materials. Similar conclusion has been obtained by Li et al.¹². PSR model describes two distinctive regimes of hardness, the indentation load-dependent regime, or ISE regime and the indentation load-independent regime, and Eq. (2) is suggested to be valid in the ISE regime²².

On the other hand, several authors^{21,23} concluded that using the PSR model for ceramics in relatively wide range of applied load can produce several inconsistencies. Experimental results of Gong et al.²⁴ show that at least in some situations, the P/d-d linear relationship can be observed only in a narrow range of applied load. Recently, Sangwal et al.²⁵ and Sahin et al.²⁶ found that behaviour of “P/d” against “d” exhibits two different slopes. The transitions suggests that the phenomenon of the appearance of discontinuities in the conventional P(d) plots for single crystalline samples is connected with the characteristics such as defect structures and grain sizes of the samples. Sangwal et al.²⁷ described that this transition is associated with the processes of relaxation of indentation stresses. Several differences are evident in Tab. II. The slope of the line for the Vickers microhardness is greater than the slope for the Knoop microhardness results. This indicates that the load independent Vickers microhardness for all tested materials is greater than the Knoop values. The values of a_1 are also different. This suggests that ISE for the Vickers microhardness may be greater than that for Knoop microhardness. These results are contrary to the ISE prediction from the n-values of the previous Mayer’s law analysis. Similar conclusion has been obtained by Li et al.²⁸. This is because the Knoop indentation is shallower and has a larger ratio of indentation surface area to the displaced area volume than Vickers indentation. Knoop indentations exhibit much less cracking than Vickers indentation at the same load. Any possible constant hardness threshold due to change in cracking scale may be suppressed until much higher loads, and in any case, any not even be noticeable²⁹. Knoop hardness gradually reaches constant values at very high loads and the Knoop plateau is usually lower than the Vickers plateau values¹⁶. Thibault and Lyinquist³⁰ noted that the onset of serious cracking led to a decrease in the apparent Knoop hardness. This may have been due in part to displacement of the indentation tips or sides, or Swain and Wittling³¹ have recently argued, the crack opening displacement under the Knoop indentation leading to greater indenter penetration. Another reason is that PSR model has been attributed to the elastic properties of the specimens and also to the friction between the indenter facets and the specimen.

4. Conclusions

Independent Knoop and Vickers indentation hardness data of the monolithic Al_2O_3 , Si_3N_4 , Si_3N_4 -SiC nanocomposite

and hardmetal WC-Co have been presented and analyzed by the Mayer’s law and also by application of a proportional specimen resistance (PSR) model. Differences and similarities between the Vickers and Knoop indentation hardness have been observed and discussed.

1. In the test load range, from 2 to 10 N, all the tested materials exhibit a significant indentation load/size effect.
2. Mayer’s law was proved to be sufficient for the description of experimental data. However, no useful knowledge of the origin of the observed ISE may be provided based on this empirical data.
3. The PSR model can be used to analyze the ISE observed in all of tested materials. The PSR model is recommended for determination of load-independent or true hardness.
4. According to PSR model, true Knoop hardness, in comparison with true Vickers hardness exhibits lower value due to cracking. Knoop indentations exhibit much less cracking than Vickers indentation at the same load.

The paper was supported by NANOSMART, Centre of Excellence, SAS, by the Slovak Grant Agency for Science, grant No. 2/7914/2, APVV-0171-06.

REFERENCES

1. Brown A. R. G., Ineson E.: *J. Iron Steel Institute* 169, 376 (1951)
2. Bückle I. H.: *Metall. Rev.* 4, 49 (1959).
3. Mason W., Johnson P. F., Varner J. R.: *J. Mater. Sci.* 26, 6576 (1991).
4. Tarkanian M. L., Neumann J. P., Raymond L., in: *The Science of Hardness Testing and Its Research Applications*, (J. H. Westbrook, H. Conrad, ed.), p. 187. American Society for Metals, Metal Park, OH 1973.
5. Mott B. W.: *Microindentation Hardness Testing*. Butterworths, London 1956.
6. O’Neil H.: *The Hardness of Metals and Its Measurement*. Sherwood, Cleveland 1934.
7. Li H., Bradt R. C.: *J. Mat. Sci.* 31, 1065 (1996).
8. Elmustafa A. A., Eastman J. A., Rittner M. N., Weertman J. R., Stone D. S.: *Scr. Mater.* 43, 951 (2000).
9. Tabor D.: *The Hardness of Metals*. Oxford University Press, Oxford 1951.
10. Hays C., Kendall E. G.: *Metall.* 6, 275 (1973).
11. Quinn J. B., Quin G. D.: *J. Mater. Sci.* 32, 4331 (1997).
12. Li H., Bradt R. C.: *J. Mater. Sci.* 28, 917 (1993).
13. Quinn G. D., Green P., Xu K.: *J. Am. Ceram. Soc.* 86, 441 (2003).
14. Kim H., Kim T.: *J. Europ. Ceram. Soc.* 22, 1437 (2002).
15. Lawn B. R., Wilshaw T. R.: *J. Mater. Sci.* 10, 1049 (1975).
16. Li Z., Ghosh A., Kobayashi A. S., Bradt R. C.: *J. Am. Ceram. Soc.* 72, 904 (1989).
17. Sargent P. M., Page T. F.: *Proc. Brit. Ceram. Soc.* 26, 209 (1978).
18. Gong J. H., Zhao Z., Guan Z. D., Miao H. Z.: *J. Eur. Ceram. Soc.* 2000, 1895.
19. Babini G. N., Bellosi A., Galassi C.: *J. Mater. Sci.* 22, 1687 (1987).
20. Gong J. H., Miao H. Z., Guan Z. D.: *Mater. Sci. Eng., A*

- 303, 179 (2001).
21. Gong J., Wu J., Guan Z.: *J. Eur. Ceram. Soc.* 19, 2625 (1999).
 22. Li H., Han Y. H., Bradt R. C.: *J. Mater. Sci.* 29, 5641 (1994).
 23. Peng Z., Gong J., Miao H.: *J. Eur. Ceram. Soc.* 24, 2193 (2004).
 24. Gong J., Wu J., Guan Z.: *J. Eur. Ceram. Soc.* 19, 2625 (1999).
 25. Sangwal K., Surowska B., Blaziak P.: *Mater. Chem. Phys.* 80, 428 (2003).
 26. Sahin O., Uzun O., Kolemen U., Duzgun B., Ucar N.: *Chin. Phys. Lett.* 22, 3137 (2005).
 27. Sangwal K., Surowska B., Blaziak P.: *Mater. Chem. Phys.* 77, 511 (2003).
 28. Li H., Bradt R. C.: *J. Mater. Sci.* 28, 917 (1993).
 29. Quinn J. B., Quin G. D.: *J. Mater. Sci.* 32, 4331 (1997).
 30. Thibault N. W., Lynquist H. L.: *Trans. ASM* 38, 271 (1947).
 31. Swain M., Wittling M.: *Fracture Mechanics of Ceramics*, 11, (Bradt R. C., Hasselman D. P. H., Munz D., Sakai M., Schevchenko, ed.). Plenum, NY 1996.

J. Špaková, F. Dorčáková, and J. Dusza (*Institute of Materials Research SAS, Watsonova 47, 040 01 Košice, Slovakia*): **Indentation Load/Size Effect of Structural Ceramic Materials**

The Vickers and Knoop hardness of monolithic Al_2O_3 , Si_3N_4 , Si_3N_4 -SiC nanocomposites and a ceramic-metal composite WC-Co in the load range from 2 N to 200 N have been investigated. The experimental results revealed that for each material the Vickers and Knoop hardness in the load range from 2 N to 10 N exhibits a load dependence, i. e. indentation load/size effect (ISE). ISE was analyzed using the Mayer's law and the Proportional Specimen Resistance (PSR) model. Analysis based on Mayer's law can not provide any useful information about the cause of the observed ISE, while true hardness H_0 , which is load independent, can be deduced from the PSR model. According to PSR model, true Knoop hardness, in comparison with true Vickers hardness exhibits lower value due to cracking. The aim of this contribution is to describe indentation load/size effect at Vickers and Knoop hardness test of structural ceramics using the Mayer's law and the Proportional Specimen Resistance (PSR) model.

VPLYV FOSFORU NA LOKÁLNE MECHANICKÉ VLASTNOSTI A VÝVOJ ŠTRUKTÚRY IF OCELÍ

PETER ZIMOVČÁK^a, ONDREJ MILKOVIČ^b, PAVOL ZUBKO^b
a MAREK VOJTKO^b

^a U. S. Steel Košice, s.r.o, Vstupný areál U. S. Steel, 044 54 Košice, ^b Katedra náuky o materiáloch, HF TUKE, Park Komenského 11, 043 85 Košice, Slovenská republika
pzimovcak@sk.uss.com, ondrej.milkovic@tuke.sk, pavol.zubko@tuke.sk, marek.vojtko@tuke.sk

Kľúčové slová: IF oceľ, precipitácia, segregácia

1. Úvod

Ocele bez interstícií (IF ocele) predstavujú jednu z hlavných skupín ocelí aplikovaných v automobilovom priemysle. Tieto ocele vykazujú vysokú mieru tvárniteľnosti, ktorá je zabezpečená vyviazaním interstícií (uhlíka a dusíka) z tuhého roztoku do disperzných častíc pomocou titánu a nióbu. S ohľadom na svetový trend znižovania emisií sú výrobcovia automobilov nútení do výroby ľahších komponentov s vyššou pevnosťou, ktoré zabezpečia zníženie hmotnosti automobilu a tým aj celkovú spotrebu paliva. Preto, jednou z možností zvyšovania pevnosti IF ocelí je využitie legúr, ktoré zabezpečujú spevňovanie mechanizmom tvorby substitučného tuhého roztoku^{1–3}.

V tejto práci sú skúmané IF ocele, do ktorých boli pridané rôzne množstvá fosforu a mangánu. Práve fosfor patrí medzi prvky, ktoré výrazne zvyšujú pevnostné vlastnosti roztoku, pričom z cenového pohľadu je taktiež najefektívnejší. Na druhej strane je známy nepriaznivý vplyv fosforu na krehkosť ocelí, ktorá je spôsobená segregáciou fosfou na hraniciach zŕn. Tento efekt má za následok náchylnosť plechov na interkryštalický lom počas sekundárnych lisovacích operácií s hlbokým ťahom alebo počas prevádzky. Preto na zvýšenie pevnosti IF pri zachovaní plastických vlastností ocelí je najvhodnejšie nájsť optimálny pomer legujúcich prvkov^{2,4,5}.

2. Experimentálny materiál a metodika

Pre experimenty boli pripravené tri druhy ocelí v prevádzkovom toku zloženého z valcovania za tepla, valcovania

Tabuľka I

Parametre procesu výroby ocelí

Valcovanie za tepla [°C]	Teplota zvinovania [°C]	Úber za studena [%]	Teplota žihania [°C]
940	640	74	600–900

Tabuľka II

Chemické zloženie ocelí

Oceľ	Obsah [hm. ppm]							
	C	Mn	Si	P	S	Ti	Nb	N
10	50	6640	100	1020	50	330	410	50
11	41	5340	100	660	60	300	390	64
12	51	2730	110	500	51	360	380	42

za studena a laboratórneho žihania na zariadení Hot Dip Process Simulator. Teplotné priebehy a parametre valcovania jednotlivých operácií sú zaznamenané v tabuľke I. Chemické zloženie skúmaných ocelí a ich označenie je uvedené v tabuľke II.

Analýza disperzných fáz v oceliach bola študovaná pomocou metodiky extrakčných replík v transmisnom elektrónovom mikroskope JEOL JEM 2000 FX s použitím EDX analyzátoru Link 860. Vzorky boli mechanicky brúsené a leštené. Výbrusy boli elektrolyticky leptané v elektrolyte HClO₄ + CH₃CH₂OH (v pomere 1 : 10) pri konštantnom napätí 15 V. Na naleptaný povrch bola naparená uhlíková vrstva, ktorá bola následne odleptaná z povrchu v rovnakom elektrolyte.

Lomové plochy vzoriek, ako aj analýza metalografických výbrusov boli pozorované v rastrovacom elektrónovom mikroskope JEOL JSM 7000 F s použitím EDX analyzátoru firmy Oxford Instruments.

Mikrotvrdosť HV 0,01 bola meraná na metalografických výbrusoch chemicky leštených v roztoku (100 g l⁻¹) kyselina šťavelová, H₂O₂ a H₂O v pomere 7:1:20, prístrojom Hanne-mann.

3. Výsledky a diskusia

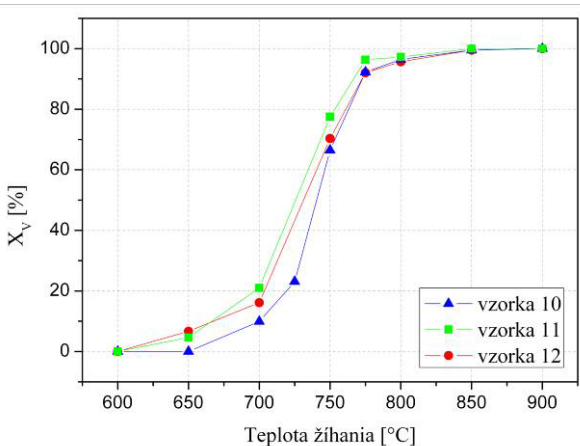
Pre stanovenie vhodnej teploty žihania IF ocelí v prevádzkových podmienkach boli vykonané experimentálne žihania, z ktorých bol vypočítaný podiel rekryštalizovaných zŕn (obr. 1) podľa vzorca:

$$X_V = \frac{R_{p0,2}0 - R_{p0,2}X}{R_{p0,2}0 - R_{p0,2}1} \cdot 100$$

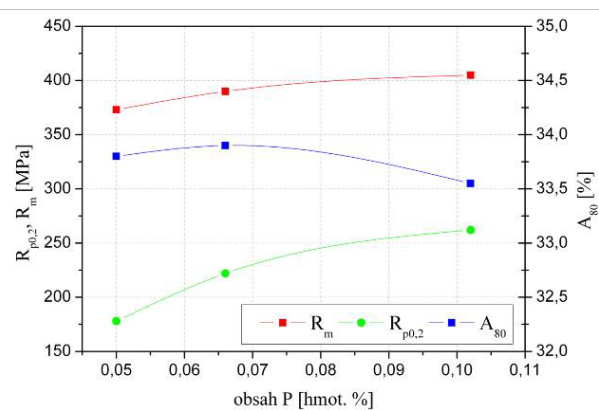
kde R_{p0,2}0 – hodnota medze klzu neprežíhaného materiálu, R_{p0,2}1 – hodnota medze klzu 100 % prežíhaného materiálu, R_{p0,2}X – hodnota medze klzu X % prežíhaného materiálu

Z kinetiky rekryštalizácie bola stanovená teplota žihania na 850 °C, pri ktorej došlo k úplnej rekryštalizácii ocelí.

Mechanické vlastnosti ocelí (obr. 2) po kontinuálnom žihaní pri teplote 850 °C boli hodnotené zo statickej skúšky v ťahu. Namerané hodnoty poukázali, že s rastúcim obsahom fosforu a mangánu v oceliach rastie medza klzu o 80 MPa a taktiež medza pevnosti o 30 MPa, pričom ťažnosť materiálu sa takmer nemení a koliše pri hodnote 34 %.



Obr. 1. Závislosť podielu rekryštalizovaných zŕn v oceliach od zvolenej teploty žihania

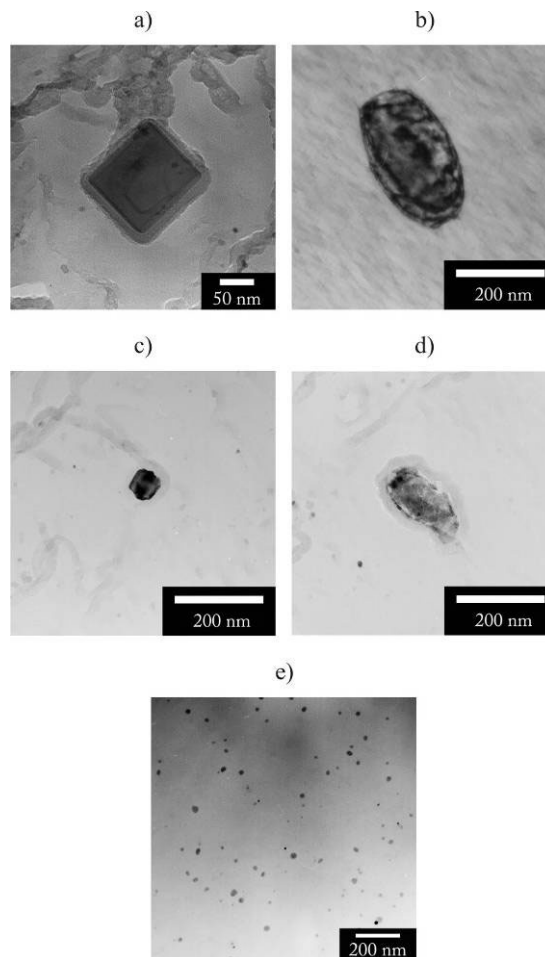


Obr. 2. Mechanické vlastnosti skúmaných IF ocelí v závislosti od obsahu fosforu v oceliach

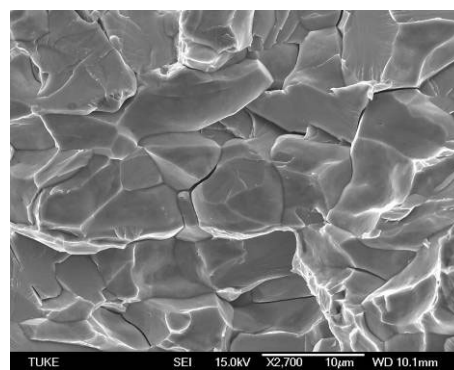
Vzhľadom na pozitívny vplyv fosforu a mangánu na zvýšenie pevnostných vlastností popri zachovaní ťažnosti boli ocele podrobené TEM analýze disperzných fáz. Vo všetkých oceliach boli nájdené častice TiN, MnS, NbC, TiC, (Ti+Nb)C a častice na báze Ti a S, ktoré sú zdokumentované na obr. 3. (Bližšia charakterizácia častíc bola zdokumentovaná v práci⁶.) Výskyt jednotlivých typov častíc odpovedal obsahu prítomnosti mangánu v oceliach, pričom najvyšší počet MnS častíc bol v oceli 11, s čím súvisí aj najvyšší podiel síry v tejto oceli. Výskyt častíc na báze Ti a S klesal so zvyšujúcim sa obsahom Mn v oceliach. Napriek vysokému obsahu fosforu neboli častice typu FeTiP a Fe(Ti+Nb)P v oceliach identifikované. Neprítomnosť fosfidických častíc môže byť pripísaná vysokej teplote žihania, pri ktorej nedochádza k ich precipitácii, resp. pri teplote žihania 850 °C je rozpustnosť fosforu v tuhom roztoku vyššia ako koncentrácia, ktorú obsahovali skúmané ocele. Podobnú skutočnosť precipitácie fosfidických častíc v IF oceliach potvrdili autori prác^{5,7}, ktorí identifikovali vyprecipitované fosfidické častice hlavne v blízkosti oblasti hraníc zŕn v oceliach žihanych pri teplote 700 °C. Avšak po žihaní pri

800 °C ocele neobsahovali fosfidické častice².

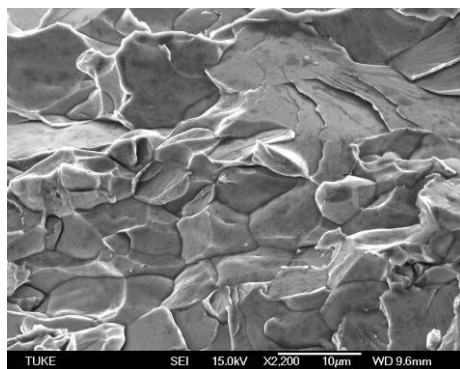
Z dôvodu absencie fosfidických častíc vo všetkých skúmaných oceliach a taktiež z dôvodu, že fosfor patrí medzi povrchovo aktívne prvky v oceliach, bol vykonaný experiment, pri ktorom boli rázom zlomené vzorky ochladené



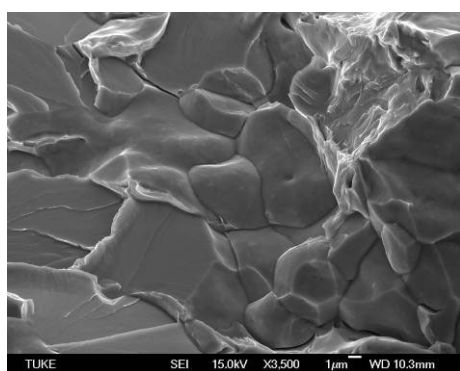
Obr. 3. TEM fotografie disperzných fáz extrahovaných z ocelí: a) TiN, b) MnS, c) (Ti+Nb)C, d) častica na báze Ti a S, e) karbidy NbC a TiC



Obr. 4. SEM fotografia lomovej plochy ocele 10

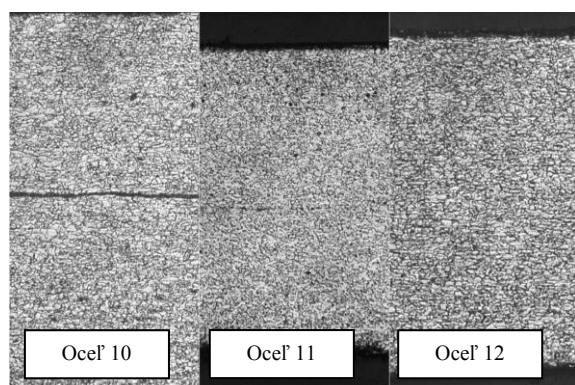


Obr. 5. SEM fotografia lomovej plochy ocele 11



Obr. 6. SEM fotografia lomovej plochy ocele 12

v tekutom dusíku. SEM pozorovania lomových plôch jednotlivých typov ocelí sú zdokumentované na obr. 4–6. Lomové plochy ocelí charakterizujú prevažne transkrystalické štiepne fazety, avšak na lomových plochách je možné zo snímkov pozorovať oblasti interkrystalického štiepného porušenia. Všetky druhy ocelí mali oblasti interkrystalického štiepenia rozložené po celej lomovej ploche a podiel interkrystalického štiepenia sa zvyšoval s rastúcim obsahom fosforu v oceliach, pričom výskyt oblastí interkrystalického štiepenia sa sústre-

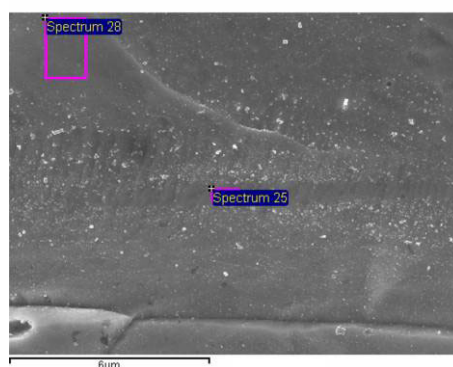


Obr. 7. Mikroštruktúry ocelí v kolmej rovine na smer valcovania (63×)

d'oval v stredovej oblasti hrúbky vzoriek.

Keďže v stredovej oblasti hrúbky vzoriek bol pozorovaný zvýšený výskyt interkrystalického štiepenia, boli vyhotovené metalografické výbrusy v rovine kolmej na smer valcovania ocelí. Na mikroštruktúrach zdokumentovaných na obr. 7 je vidieť zvýraznenie stredovej oblasti leptaním, ktoré je v oceli 12 nepozorovateľné a naopak v oceli 10 výrazné.

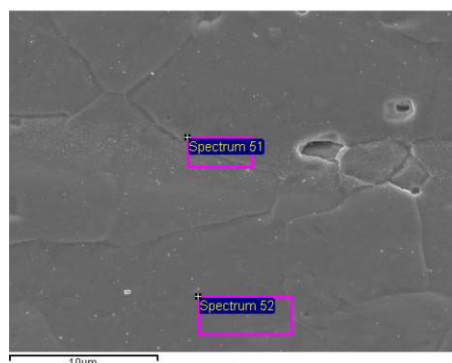
EDX analýza naleptaných výbrusov ocelí 10 a 11 (obr. 8 a 9) poukázala, že v stredových oblastiach sa nachádza zvýšené množstvo fosforu, ktoré po kvantitatívnej analýze dosahovalo vyššie hodnoty (tab. III, IV) ako sa nachádza v zložení ocelí. V oblasti obohatenej fosforom je možné taktiež pozorovať zvýšenú hustotu disperzných častíc. TEM analýzou častíc extrahovaných v uhlíkových replikách bola pozorovaná vyššia početnosť častíc TiC, TiNbC a NbC. Napriek vysokému obsahu fosforu v tejto oblasti, fosfidické častice neboli nájdené.



Obr. 8. Detail stredovej analýzy

Tabuľka III
Kvantitatívne vyhodnotenie EDX analýzy z obr. 8

Element	Spectrum 51	Spectrum 52
	[hm. %]	[hm. %]
P	0,34	0
Mn	0,79	0,86
Fe	98,88	99,14

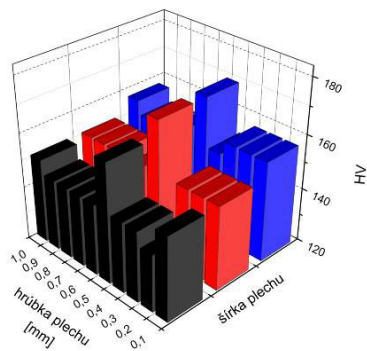


Obr. 9.

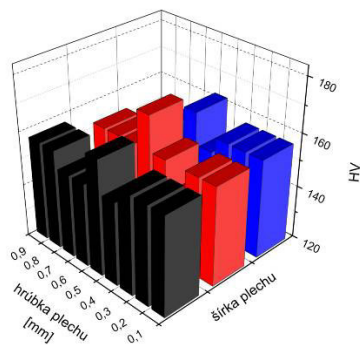
Tabuľka IV

Kvantitatívne vyhodnotenie EDX analýzy z obr. 9

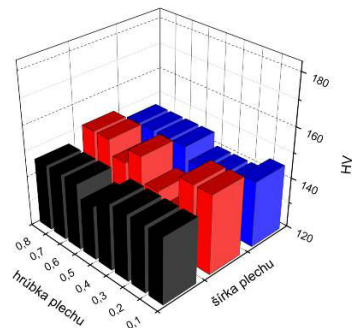
Element	Spectrum 25	Spectrum 28
	[hm. %]	[hm. %]
P	0,34	0
Mn	0,50	0,36
Fe	99,16	99,64



Obr. 10. Mikrotvrdoť HV 0,01 vzorky 10



Obr. 11. Mikrotvrdoť HV 0,01 vzorky 11



Obr. 12. Mikrotvrdoť HV 0,01 vzorky 12

Na metalografických výbrusoch bola meraná mikrotvrdoť HV 0,01 po hrúbke materiálu (obr. 10–12) s cieľom zistenia zmeny mechanických vlastností v závislosti od zmeny rozloženia fosforu v materiále. Namerané hodnoty poukazujú na zvýšenie tvrdosti ocele 10 a tiež miernejšie zvýšenie tvrdosti ocele 11 v stredovej oblasti plechu. Okrem ovplyvnenia stredovej oblasti došlo u ocelí 10 a 11 k celkovému miernemu nárastu tvrdosti matrice oproti oceli 12.

4. Závěry

Z výsledkov experimentov možno usudzovať, že fosfor v oceli má priaznivý vplyv na pevnostné vlastnosti, ktoré sa prejavili nárastom medze klzu, medze pevnosti a taktiež miernym nárastom tvrdosti matrice, pričom ťažnosť materiálu bola zachovaná. Analýzou precipitátov bolo zistené, že fosfor ostal v tuhom roztoku a neprecipitoval vo forme fosfidických častíc. Avšak, EDX analýza a hodnoty mikrotvrdoty oceľových plechov preukázali na zvýšenie fosforu v stredovej oblasti hrúbky plechu a ovplyvnenie stredovej oblasti oceli so zvýšením obsahu fosforu v oceliach. Efekt stredovej segregácie pravdepodobne súvisí s nízkym rozdeľovacím koeficientom fosforu, ktorý počas tuhnutia ocele pri kontinuálnom liatí ostáva v oblastiach, ktoré kryštalizujú ako posledné.

LITERATÚRA

1. Alaoua D., Lartigue S., Larere A., Priester L.: Mater. Sci. Eng., A 189, 155 (1994).
2. Ghosh P., Ray R. K., Ghosh C., Bhattacharjee, D.: Scr. Mater. 58, 939 (2008).
3. Ramos A. S., Sandim H. R. Z., Hashimoto T. M.: Mater. Characterization 45, 171 (2000).
4. Feliu S., Pérez-Revenga M. L.: Appl. Surf. Sci. 229, 112 (2004).
5. Ghosh P., Ray R. K., Bhattacharya B., Bhargava S.: Scr. Mater. 55, 271 (2006).
6. Milkovič O.: Výskumná správa č. P – 102 – 00057/08. Technická univerzita v Košiciach, Košice 2008.
7. Ghosh P., Ray R. K., Bhattacharjee D.: Scr. Mater. 57, 241 (2007).

Prezentované výsledky boli získané v rámci riešenia projektu APVV 0326-07.

P. Zimovčák^a, O. Milkovič^b, P. Zubko^b, and M. Vojtko^b (^a U. S. Steel Košice, Slovakia, ^b Department of materials Science, Technical University of Košice, Faculty of Metallurgy, Slovakia): **Influence of Phosphorus on Local Mechanical Properties and Structure Evolution of IF Steels**

Three interstitial free steels stabilized by Ti and Nb, with different content of phosphorus, have been studied. The minimal differences in precipitation behavior and no phosphides particles in steels processed by continuous annealing at 850 °C were observed. The finer mechanical properties and the similar drawability with higher content of phosphorus have been measured.

DETERMINATION OF MECHANICAL PROPERTIES OF MoSi_2 COMPOSITES BY NANOINDENTATION

PAVOL ZUBKO^a, BEÁTA BALLÓKOVÁ^b, LADISLAV PEŠEK^a,
and OLGA BLÁHOVÁ^c

^a Technical university of Košice, Faculty of metallurgy, Department of material science, Park Komenského 11, 043 85 Košice, Slovakia, ^b Slovak Academy of Science, Institute of Materials Research, Watsonova 13, 040 01 Košice, Slovakia, ^c New Technologies, Research Center, Universitní 8, 306 14 Plzeň, Czech Republic
pavol.zubko@tuke.sk, bballokova@imr.saske.sk,
ladislav.pesek@tuke.sk, blahova@ntc.zcu.cz

Key words: ceramic composites, hardness, Young modulus, depth sensing indentation

Introduction

The MoSi_2 phase is a borderline ceramic–intermetallic compound with both covalent and metallic atomic bonds. Besides traditional use as heating elements, materials based on MoSi_2 appear to be promising candidates for wide variety of high-temperature structural applications, where high strength and temperature durability is required^{1,2}.

The main disadvantage of MoSi_2 -based composites is low fracture toughness, low hardness in lower temperatures. Several ways of improving the performance of MoSi_2 -based composites have been developed by incorporating SiC , ZrO_2 or HfO_2 particles into the matrix.

The aim of this work was to investigate mechanical properties of MoSi_2 -based composites with reinforced 10 wt.% of ceramics particles: SiC , nano SiC , Si_3N_4 , ZrO_2 , HfO_2 particles were used.

Depth sensing indentation technique³ was used to determine mechanical properties in local scale represented by indentation depth of 100 nm and in global scale represented by the depth of 1000 nm.

2. Materials and experimental procedure

The materials were prepared by powder metallurgy technology using a high-energy milling process. The mechanical treatment was started from coarse-grained elemental powders (Mo and Si) with diameters of 100–500 μm and reinforced materials in order to prepare materials with 10 % of SiC , nano SiC , ZrO_2 , HfO_2 and Si_3N_4 . The powders were milled using the steel ball milling set in argon environment. The milled powders were densified by hot pressing at 1550 °C in vacuum.

The experimental materials, incorporated with secondary

particles were supplied in the form of bars. For investigation were samples mounted, grinded and polished.

The microstructures of investigated materials are shown in Fig. 1–6. Fig. 1 shows material of monolithic MoSi_2 in cross-polarized illumination. The average grain size of mono-

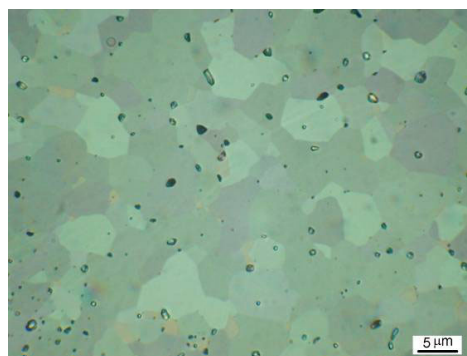


Fig. 1. The microstructure of monolithic MoSi_2

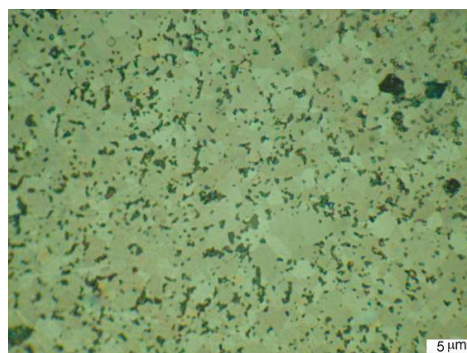


Fig. 2. The microstructure of MoSi_2 -based composites with incorporated 10 wt.% nano SiC particles

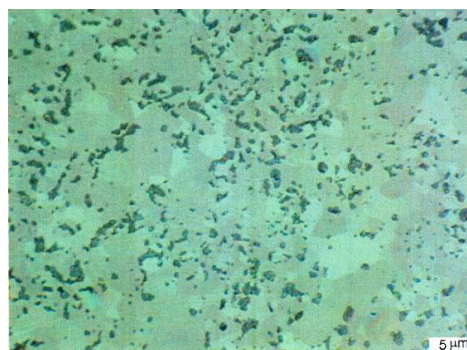


Fig. 3. The microstructure of MoSi_2 -based composites with incorporated 10 wt.% SiC particles

lithic MoSi_2 is $5 \mu\text{m}$. Incorporation of particles (SiC , ZrO_2 , Si_3N_4) causes reduction of grain size growing, increasing ratio of pores, while HfO_2 particles cause opposite behaviour. The glassy SiO_2 phase was found in the microstructure in both cases too.

Depth sensing indentation tests were carried out using Nanoindenter XP with Berkovich tip. Over 50 indents were placed on each of investigated materials. The CSM (Continuous Stiffness Measurement) was used to show difference between properties measured in local and global scale. In the case of local properties the mean indent area is smaller

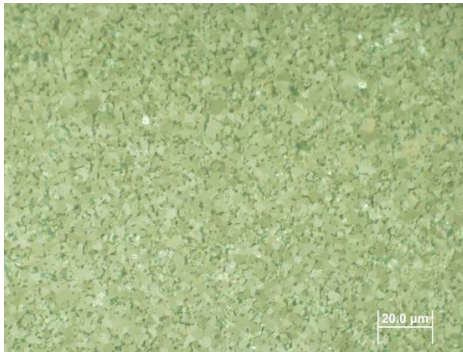


Fig. 4. The microstructure of MoSi_2 -based composites with incorporated 10 wt.% ZrO_2 particles

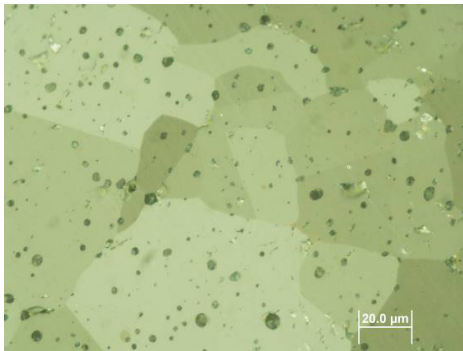


Fig. 5. The microstructure of MoSi_2 -based composites with incorporated 10 wt.% HfO_2 particles

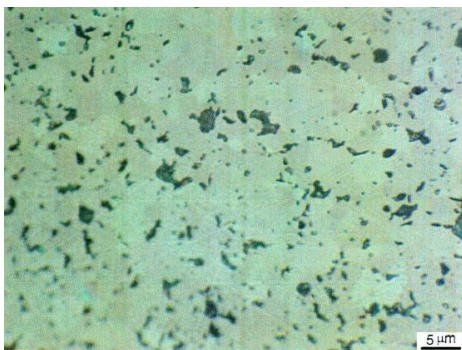


Fig. 6. The microstructure of MoSi_2 -based composites with incorporated 10 wt.% Si_3N_4 particles

then the area of one grain, while the global properties represent two and more grains.

The instrumented hardness (H_{IT}) and indentation modulus (E_{IT}) were evaluated in two indentation depths. The influence of incorporated particles on the properties of particular grains was investigated in the depth of 100 nm. The influence of grains boundaries and pores on properties was investigated in global scale of 1000 nm.

The goal of this contribution is to describe the effect of incorporated particles on the hardness and modulus for different scales.

3. Results and discussion

The results of indentation experiments presented as: Hardness (H_{IT}) vs. indentation depth and modulus (E_{IT}) vs. indentation depth relations are shown in Fig. 7 and Fig. 8. The hardness and modulus values decrease with increasing indentation depth. The pores were observed in the microstructure of investigated materials. Therefore the hardness and modulus values decrease because of plastic zone under the tip closes to a phase intersection. The presence of pores and their size distribution are documented in Fig. 1–6 and in the Table I. Hardness and modulus values were extracted from the depth of 100 nm to avoid the influence of pores on the improvement of mechanical properties by incorporation of particles. The modulus values and hardness values are summarized in the Table II and III. The hardness and modulus values were extracted from the depth of 1 μm in order to describe the effect of pores.

Both, hardness and modulus values in 100 nm depth are the highest for composites with 10 % Si_3N_4 and with 10 % nanoSiC particles. Similar results were measured for the maximum depth, too. The smallest difference between the average hardness and modulus values determined in local and global scale was measured in the material with ZrO_2 particles, but the scatter of the results was the highest. The grain size of

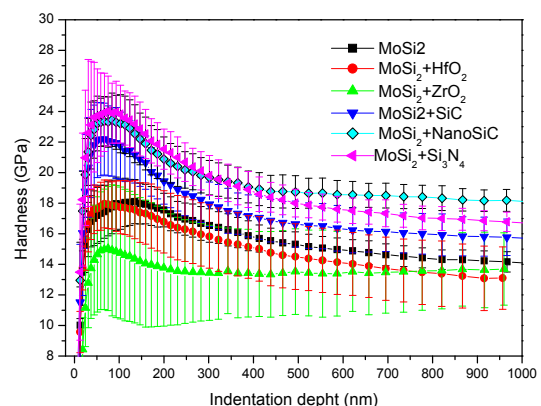


Fig. 7. Hardness (H_{IT}) – indentation depth dependence of investigated materials

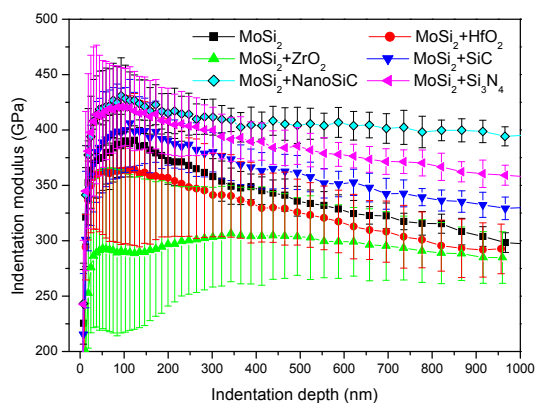


Fig. 8. Indentation modulus (E_{IT}) – indentation depth dependence of investigated materials

Table I
The size and area ratio of pores found in investigated materials

10 %	MoSi ₂ +					
	HfO ₂	ZrO ₂	nano SiC	SiC	Si ₃ N ₄	monolith
Pore size, μm	1–2	2–4	–	1–2	–	0.1–1
Area ratio, %	10	5.6	–	10	–	0.7

Table II
Modulus of elasticity (GPa) determined in the depth 100 nm (E_{IT100}) and 1000 nm (E_{IT1000})

10 %	MoSi ₂ +					
	HfO ₂	ZrO ₂	nano SiC	SiC	Si ₃ N ₄	monolith
E_{IT100}	352	294	414	398	415	385
STD	65	86	41	31	33	24
% COV	18	29	10	7	8	6
E_{IT1000}	295	294	395	331	357	297
STD	30	22	12	10	9	9
% COV	10	8	3	3	3	3

this material is the smallest. The measured results in local scale are therefore strongly affected by both grain boundaries and pores.

Table III
Hardness (GPa) determined in the depth 100 nm (H_{IT100}) and 1000 nm (H_{IT1000})

10 %	MoSi ₂ +					
	HfO ₂	ZrO ₂	nano SiC	SiC	Si ₃ N ₄	monolith
H_{IT100}	18	15	23	22	24	18
STD	1.8	5	1.7	1.8	1.6	1.4
% COV	19	32	8	8	7	8
H_{IT1000}	12	13	18	16	16	14
STD	2	2	0.8	1	0.6	0.7
% COV	17	15	4	7	4	5

4. Conclusions

The depth sensing indentation method is usable to determine mechanical properties of composite materials; however it is very important to take in account the microstructure inhomogeneities, like pores, etc.

It is possible to determine the homogeneity of materials based on the scatter of measured results.

The highest hardness and modulus values were measured on materials with incorporated nanoSiC and Si₃N₄ particles.

This work was supported by the VEGA Grant No. 1/3210/06 and partly by the SK-CZ project SK-CZ-0108-07.

REFERENCES

- Hvizdoš P., Besterčí M., Ballóková B., Sholl R., Bohm A.: *Mater. Lett.* 51, 485 (2001).
- Ballóková B., Hvizdoš P., Ivan J., Zumdíck M., Besterčí M.: *Int. J. Mat. Product Technology* 22, 322 (2005).
- Oliver W. C., Pharr G. M.: *J. Mat. Res.* 7, 1564 (1992).

P. Zubko^a, B. Ballóková^b, L. Pešek^a, and O. Bláhová^c
^aDepartment of Material Science, Technical university of Košice, Košice, ^bSlovak Academy of Science, Institute of Materials Research, Košice, Slovakia, ^cNew Technologies Research Center, West Bohemian University, Plzeň, Czech Republic): **Determination of Mechanical Properties of MoSi₂ Composites by DSI**

The paper deals with the determination of mechanical properties of MoSi₂ composites with incorporated SiC, nanoSiC, Si₃N₄, HfO₂ and ZrO₂ particles. The hardness and modulus of the investigated composite materials were determined. The highest hardness and modulus values were obtained in the case of MoSi₂ with nanoSiC and Si₃N₄ particles. The great influence of pores was detected.

Author Index

- Ambriško L. s150, s206
- Ballóková B. s227
Bídulská J. s155
Bídulský R. s155, s159
Bláhová O. s98, s132, s136, s140, s163, s175, s182, s202, s210, s214, s227
Březina M. s167
Buršík J. s98
Buršíková V. s98, s129, s132, s171
- Ciupinã V. s132
Contulov M. s132
- Čech J. s129
- Dajbychová L. s175
Dorčáková F. s218
Dusza J. s191, s178, s218
- Ferdinandy M. s112
Forstová K. s123, s146
Fořt T. s102
Franta D. s98
- Garbiak M. s187
Grande M. A. s155, s159
Grossman J. s102
- Hegedúsová L. s178
Houdková Š. s105, s182
- Chylińska R. s187
- Jančuška I. s109, s195
Jašek O. s98, s171
Juhász A. s112
- Kabátová M. s159
Kandra T. s150
Karásková M. s98
Kašparová M. s105, s182
Klapetek P. s98
Kloc P. s129
Kočiško R. s155
Kollárová M. s136
Kovalčíková A. s191
- Krajčovič J. s109, s195
Kučerová Z. s171
Kudrle V. s171
Kupča L. s167
Kvačkaj T. s155
- Lofaj F. s112, s198
- Matějková J. s171
Medlín R. s202
Menčík J. s115, s143
Mihalíková M. s206
Milkovič O. s223
Musa G. s132
- Navrátil Z. s129
Němeček J. s120, s123, s146
Novák R. s102
- Odrášková M. s125
- Pešek L. s136, s150, s227
- Ráheľ J. s125
- Říha J. s202, s210
- Savková J. s214
Sobota J. s102
Sřahel P. s125, s129
Stoica A. s132
Synek P. s171
- Špaková J. s218
Špírková M. s140, s175
Šutta P. s210
- Vadasová Z. s136
Vítů T. s102
Vlãdoiu R. s132
Vojtko M. s223
Vyskočil J. s102
- Zahálka F. s105, s182
Zajičková L. s98, s171
Zimovčák P. s223
Zubko P. s136, s223, s227



Projekt MICRONETWORK

Partnerská síť pro spolupráci vysokých škol, výzkumných ústavů a průmyslu pro rozvoj mikroelektroniky a nanotechnologií

Cíle projektu

- posílení spolupráce vysokých škol a výzkumných ústavů s průmyslovou sférou
- vybudováním komunikační platformy
- další vzdělávání v oblasti komunikace a argumentace, ekonomiky a legislativy vysokých škol, projektového řízení
- propagace zúčastněných subjektů a jejich výstupů

<http://www.micronetwork.cz/>

Partneři projektu

Fakulta elektrotechniky a komunikačních technologií VUT v Brně – Ústav mikroelektroniky

Přírodovědecká fakulta MU - Ústav fyzikální elektroniky

Evropský polytechnický institut, s.r.o.

CSRC, spol. s r.o.

IQI s.r.o.

BD SENSORS s.r.o.

Institut mikroelektronických aplikací s.r.o.

ASICentrum spol.s.r.o.



evropský
sociální
fond v ČR



EVROPSKÁ UNIE



MINISTERSTVO ŠKOLSTVÍ,
MLÁDEŽE A TĚLOVÝCHOVY



OP Vzdělávání
pro konkurenceschopnost



VYSOKÉ
UCENÍ
TECHNICKÉ
V BRNĚ



INVESTICE DO ROZVOJE VZDĚLÁVÁNÍ

CHEMICKÉ LISTY • ročník/volume 105 (S), čís./no. Symposia • LISTY CHEMICKÉ roč./vol. 135, ČASOPIS PRO PRŮMYSL CHEMICKÝ, roč./vol. 121 • ISSN 0009-2770, ISSN 1213-7103 (e-verze), ISSN 1803-2389 (CD verze) • evidenční číslo MK ČR E 321 • Vydává Česká společnost chemická jako časopis Asociace českých chemických společností ve spolupráci s VŠCHT Praha, s ČSPCH a ÚOCHB AV ČR za finanční podpory Nadace Český literární fond a kolektivních členů ČSCH • IČO 444715 • Published by the Czech Chemical Society • VEDOUCÍ REDAKTOR/EDITOR-IN-CHIEF: B. Kratochvíl • REDAKTORI/ EDITORS: J. Barek, Z. Bělohlav, P. Drašar, J. Hetflejš, P. Holý, J. Horák, P. Chuchvalec, J. Podešva, P. Rauch, J. Volke; Bulletin: I. Valterová; Webové stránky: R. Liboska, P. Zámstný • ZAHRANIČNÍ A OBLASTNÍ REDAKTORI/FOREIGN AND REGIONAL EDITORS: F. Švec (USA), Z. Kolská (Ústí nad Labem) • KONZULTANT/CONSULTANT: J. Kahovec • TECHNICKÁ REDAKTORKA/EDITORIAL ASSISTANT: R. Řápková • REDAKČNÍ RADA/ADVISORY BOARD: K. Bláha, L. Červený, E. Dibuszová, J. Hanika, Z. Havlas, J. Káš, M. Koman, J. Koubek, T. Míšek, V. Pačes, O. Paleta, V. Růžička, I. Stibor, V. Šimánek, R. Zahradník • ADRESA PRO ZASÍLÁNÍ PŘÍSPĚVKŮ/MANUSCRIPTS IN CZECH, SLOVAK OR ENGLISH CAN BE SENT TO: Chemické listy, Novotného lávka 5, 116 68 Praha 1; tel./phone +420 221 082 370, +420 222 220 184, e-mail: chem.listy@csvts.cz • INFORMACE O PŘEDPLATNÉM, OBJEDNÁVKY, PRODEJ JEDNOTLIVÝCH ČÍSEL A INZERCE/INFORMATION ADS: Sekretariát ČSCH, Novotného lávka 5, 116 68 Praha 1; tel. +420 222 220 184, e-mail: chem.spol@csvts.cz, chem.ekonom@csvts.cz • PLNÁ VERZE NA INTERNETU/FULL VERSION ON URL: <http://www.chemicke-listy.cz> • TISK: Rodomax s.r.o., Rezecká 1164, 549 01 Nové Město nad Metují • Redakce čísla Symposia (ISSUE EDITOR): L. Pešek, V. Buršíková, O. Bláhová • SAZBA, ZLOM: ČSCH, Chemické listy • Copyright © 2011 Chemické listy/Česká společnost chemická • Cena výtisku 170 Kč, roční plné předplatné 2011 (12 čísel) 1730 Kč, individuální členské předplatné pro členy ČSCH 865 Kč. Roční předplatné ve Slovenské republice 92 EUR (doručování via SCHS), individuální členské předplatné pro členy ČSCH 70 EUR (doručování via SCHS), 258 EUR (individuální doručování), ceny jsou uvedeny včetně DPH • DISTRIBUTION ABROAD: KUBON & SAGNER, POB 34 01 08, D-80328 Munich, FRG; Annual subscription for 2011 (12 issues) 225 EUR • This journal has been registered with the Copyright Clearance Center, 2322 Rosewood Drive, Danvers, MA 01923, USA, where the consent and conditions can be obtained for copying the articles for personal or internal use • Pokyny pro autory najdete na <http://www.chemicke-listy.cz>, zkratky časopisů podle Chemical Abstract Service Source Index (viz <http://cassi.cas.org/search.jsp>) • Chemické listy obsahující Bulletin jsou zasílány zdarma všem individuálním a kolektivním členům ČSCH a ČSPCH v ČR i zahraničí, do všech relevantních knihoven v ČR a významným představitelům české chemie a chemického průmyslu; v rámci dohod o spolupráci i členům dalších odborných společností • Molekulární námět na obálce: P. Holý • Dáno do tisku 28.2.2011.